THEORIES AND EXPERIMENTS ON THE ELECTRO-CHEMO-MECHANICS OF BATTERY MATERIALS

by

Rong Xu

A Dissertation

Submitted to the Faculty of Purdue University

In Partial Fulfillment of the Requirements for the degree of

Doctor of Philosophy

School of Mechanical Engineering

West Lafayette, Indiana

December 2018

THE PURDUE UNIVERSITY GRADUATE SCHOOL

STATEMENT OF COMMITTEE APPROVAL

Dr. Kejie Zhao, Chair

School of Mechanical Engineering

Dr. Ganesh Subbarayan

School of Mechanical Engineering

Dr. Thomas Siegmund

School of Mechanical Engineering

Dr. Wenbin Yu

School of Aeronautics and Astronautics

Approved by:

Dr. Jay P. Gore

Head of the Graduate Program

To my family,

for their support and encouragement throughout my life

ACKNOWLEDGMENTS

First, I would like to express my heartiest gratitude to my advisor, Dr. Kejie Zhao, for his advising throughout my graduate study at Purdue University. Dr. Zhao is the person who guided me into the science world. He develops my research interest on the electrochemistry and mechanics in Li-ion batteries, provides me insightful guidance and constant support via his vast knowledge and sharp insight in mechanics and materials, and, most importantly, keeps training me to be an independent researcher which is of great significance for a graduate student who wants to survive in the academia. I am so fortunate to have Dr. Zhao to steer me in the right direction. I also need to thank my advisor for his support in my life at Purdue. Dr. Zhao is a friendly person who always shows his great patience and encouragement to me. It seems like it was only yesterday that we were meeting in his office. He encouraged me to use English in our conversation, even though my speaking was poor at that time. I believe it was hard for him to understand what I was saying, but he was patient and enthusiastic to help improve my speaking. I really got many confidence and benefits from his patience and encouragement.

Deep appreciation should also go to my thesis committees, Dr. Ganesh Subbarayan, Dr. Thomas Siegmund and Dr. Wenbin Yu, for their helpful suggestions and comments throughout the development of this thesis. Their deep understanding of mechanics provides me a lot of enlightenment in my research. Furthermore, they are gracious and enthusiastic, no matter in their classes, in our communication or in my exams. I also appreciate their consideration and time in the schedule of my defense exam.

Special thanks to my colleague, Luize Scalco de Vasconcelos. We joined the Zhao's group at almost the same time and both spend our four years studying here. It is so unforgettable on the days that we gradually filled our empty lab with a variety of equipment. We took trainings, solved

troubles and upgraded equipment all together. Without her help, I couldn't have finished my research. Furthermore, both of us are involved in each other's research. She always shows utmost responsibility, carefulness and enthusiasm in our research which significantly inspire me and help higher my research standard. I learn a lot from her, a sincere thank you.

I would like to thank every person in Zhao's group, Hong Sun, Xiaokang Wang, Nikhil Sharma, Xianyang Wu, Ram Kishore Venkatesan, Pengfei Liu, Haijun Ruan, Shadad Hassan, Dong-Liang Wu, Yanfei Liu, Yang Ding, Jincheng Lei and Junzhe Shi. Our group is full of vigor and vitality, and everyone in the group is talented and diligent. They help improve my research skills, polish my academic work and enlighten me with numerous amazing ideas. I am so glad to have this opportunity to work with them.

I am fortunate to have so many wonderful collaborators and friends, Biwei Deng, Jiazhi He, Dr. Fei Yin, Dr. Tao Song, Dr. Qingqing Sun, Dr. Yaowu Hu, Dr. Ze Liu at Purdue University, Dr. Jianlin Li at Oak Ridge National Laboratory and Fang Hao at Houston University. They are responsible and full of creativity in the projects we collaborated. I really enjoy collaborating with them and hope to work with them in future.

Last, I am extremely thankful to my family. My great parents, Mr. Julian Xu and Mrs. Lifang Huang, always offer me ceaseless care and support. Without their support, my thesis would never have been accomplished. I also need to specially thank my wife, Yue Zhang, who has accompanied me for more than three years at Purdue. To stay with me, she abandoned many opportunities in her study and career. Appreciate my wife for her huge sacrifice and support.

TABLE OF CONTENTS

LIST OF TABLES

LIST OF FIGURES

ABSTRACT

Author: Xu, Rong. PhD
Institution: Purdue University
Degree Received: December 2018
Title: Theories and Experiments on the Electro-Chemo-Mechanics of Battery Materials
Major Professor: Kejie Zhao

Li-ion batteries is a system that dynamically couples electrochemistry and mechanics. The electrochemical processes occurring during battery operation induces a wealth of elemental mechanics such as deformation, plasticity, and fracture. Likewise, mechanics influences the electrochemical processes via modulating the thermodynamics of Li reactions and kinetics of ionic transport. These complex interrelated phenomena are far from being well understood and need to be further explored. This thesis studies the couplings between the mechanical phenomena and electrochemical processes in Li-ion batteries using integrated theories and experiments.

A continuum model coupling the kinetics of Li diffusion and kinematics of large elasto-plastic deformation is established to investigate the coupling between Li transport and stress evolution in electrodes of Li-ion batteries. Co-evolutions of Li distribution, stress field and deformation in the electrodes with multiple components are obtained. It is found that the Li profile and stress state in a composite electrode are significantly different from that in a free-standing configuration, mainly due to the regulation from the mechanical interactions between different components. Chemomechanical behaviors of the heterogeneous electrodes in real batteries are further explored. Three-dimensional reconstructed models are employed to investigate the mechanical interactions of the constituents and their influence on the accessible capacity of batteries.

Structural disintegration of the state-of-art cathode materials $LiNi_xMn_yCo_zO_2$ (x+y+z=1, NMC) during electrochemical cycling is experimentally revealed. Microstructural evolution of different marked regimes in electrodes are tracked before and after lithiation cycles. It is found that the decohesion of primary particles constitutes the major mechanical degradation in the NMC materials. Electrochemical impedance spectroscopy (EIS) measurement confirms that the mechanical disintegration of NMC secondary particle causes the electrochemical degradation of the battery. To reveal the reasons for particle disintegration, the dynamic evolution of mechanical properties of NMC during electrochemical cycling is explored by using instrumented nanoindentation. It is found that the elastic modulus, hardness, and interfacial fracture strength of NMC secondary particle significantly depend on the lithiation state and degrade as the electrochemical cycles proceed, which may cause the damage accumulation during battery cycling.

Corrosive fracture of electrodes in Li-ion batteries is investigated. Li reaction causes embrittlement of the host material and typically results in a decrease of fracture toughness. The dynamics of crack growth depends on the chemomechanical load, kinetics of Li transport, and the Li embrittlement effect. A theory of coupled diffusion, large deformation, and crack growth is implemented into finite element program and the corrosive fracture of electrodes under concurrent mechanical and chemical load is simulated. The competition between energy release rate and fracture resistance as crack grows during both Li insertion and extraction is examined in detail, and it is found that the corrosive fracture behaviors of the electrodes rely on the chemomechanical load and the supply of Li to the crack tip. The theory is further applied to model corrosive behavior of intergranular cracks in NMC upon Li cycles. The evolving interfacial strength at different states of charge and different cycle numbers measured by in-situ nanoindentation is implemented in the numerical simulation.

1. INTRODUCTION

1.1 Li-ion batteries

Energy is essential to all of us. However, energy may not be always available at times and places that we want to utilize it, thus, methods to transport and store energy are important. Among all energy conversion and storage systems, electrochemical system that can inexpensively and efficiently convert the energy between electrical and chemical forms has attracted most of the interest in this century [1-3]. Li-ion batteries, one of the most promising electrochemical systems for energy conversion and storage, have become the dominant power source for portable electronics and electric vehicles/plug-in hybrid electric vehicles [4-6]. In the future, the global Li-ion battery market will keep growing, partially because of the increasing demand for portable electronics, and partially because of the strict government regulations to reduce the pollution from combustion of fossil fuels [7, 8]. According to a new report by Variant Market Research Inc., the global Li-ion battery market is expected to reach USD 56 billion by 2024, growing at a CAGR of 10.6% from 2016 to 2024, Figure 1.1.

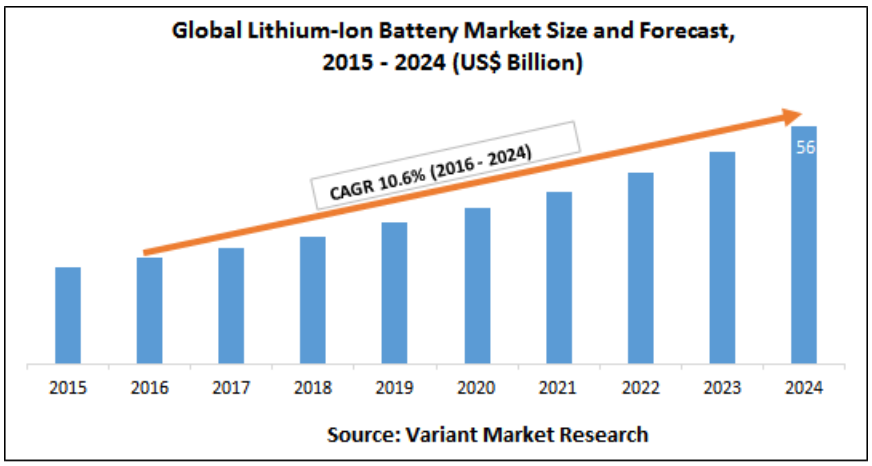

Figure 1.1. Global Li-ion battery market size and forecast, 2015-2024 (US$ Billion), (Source: Variant Market Research, Inc).

The widespread use of Li-ion batteries in commercial and industrial applications is mainly owing to their unique advantages [9-11], including high energy density (~600Wh/kg) [12], high power density [13], high working voltage (~3.6V) [14], long cyclic life (~10000 times, $LiFePO_4$) [15], and environmental sustainability. However, several concerns about the reliability of Li-ion batteries in such large-scale applications, particularly the safety issues caused by battery failure, have not been addressed and may hinder the market growth in the coming years. For instance, the Li-ion battery package of a Tesla Model S reignited twice in a crash that killed two teens and injured one other in Florida, according to a report released by federal investigators. The reliability of Li-ion batteries during operation are believed to be determined by the complex interrelated phenomena including the electricity, chemistry, mechanics and design [4, 16].

1.2 Electrochemistry in Li-ion batteries

Li-ion batteries are basically an electrochemical system that can convert the electrical energy into chemical energy, and *vice versa*. The energy conversion in Li-ion batteries occurs via the electrochemical reaction between two electronically conducting electrodes. Before introducing the electrochemical reaction in Li-ion batteries, a simple chemical reaction between two elements *A* and *B* is first considered,

$$A + B = AB. \tag{1.1}$$

For a chemical reaction, the reactant *A* and *B* must contact each other to form the product *AB*, and then either *A* or *B* diffuses through *AB* to contact with the other reactant on the other side. For an electrochemical system like the Li-ion batteries, an additional component, electrolyte, is present in-between two reactants (i.e. two electrodes), as schematically shown in Figure 1.2. The electrolyte must contain ions of either *A* or *B*, or both, and be ionic conductive but not electronic conductive such that it can serve as a carrier of ions and a blocker of electrons. In the

electrochemical reaction, reactant *A* and *B* do not contact each other, instead, ions of *A* or *B* diffuse through the electrolyte and contact with the other reactant on the other side to form the product *AB*. Since an electrochemical reaction mush maintain the electrical neutrality but the electrolyte hinders the transport of electrons, another path, usually an external circuit, is required whereby the electrons can move through the system, as shown in Figure 1.2.

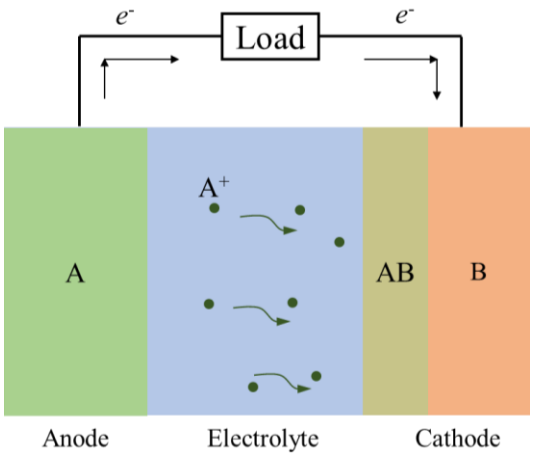

Figure 1.2. Basics of battery operation and major components of Li-ion batteries.

An important feature of the electrochemical reaction is that ions and electrons must pass through the electrolyte and the external circuit, respectively, at an equal rate, to match the charge neutrality. Consequently, when the external circuit is open, electrons cannot follow through the system and thus ions in the electrolyte stop moving, which inhibits the entire electrochemical reaction. In this case, chemical driving force for the Reaction (1.1) is balanced by an electrostatic driving force in the opposite direction. Based on thermodynamics, the chemical driving force of a reaction is determined by the standard Gibbs free energy change per mole of reaction, ΔG_r°, as [3]

$$\Delta G_r^\circ = \sum \Delta G_f^\circ(\text{products}) - \sum \Delta G_f^\circ(\text{reactants}) \qquad (1.2)$$

where $\sum \Delta G_f^\circ$(products) and $\sum \Delta G_f^\circ$(reactants) are the Gibbs free energies of formation of all products and reactants, respectively. The electrostatic driving force is determined by the voltage *E* between the electrodes as, –*zFE*. Here *z* is the charge number of the mobile ions involved in the reaction and *F* is the Faraday constant (96,500 Coulombs per mole) that represents the magnitude of electric charge per mole of electrons. The balance between chemical driving force and electrostatic driving force can be expressed as,

$$\Delta G_r^\circ = -zFE. \tag{1.3}$$

Equation (1.3) indicates there is an external voltage *E* between two electrodes that represents the total electrical work done by electrons flow through the external circuit. If two electrodes are good electronic conductors and the electrolyte is a perfect ionic conductor but an electronic insulator, this external voltage *E* is uniquely determined by the specific reactions between two electrodes while independent of the identity of the species in the electrolyte.

Note that the reactions occurring in the electrochemical system are reversible, although they usually have a preferable direction along which the reactions can spontaneously take place. Therefore, if a voltage larger than the *E* in Equation (1.3) is applied in the opposite direction of the electronic path, the electrochemical reactions can be reversed. In this case, electrical energy from the external source is converted back to the chemical energy stored in electrochemical system, so-call, recharging the system.

In principle, Li-ion batteries can maintain a high energy/power density during the repeated charging and discharging. Unfortunately, electrochemical aging of Li-ion batteries is always occurring during the cycling [16-18]. Battery degradation and failure can take place either in the anodes, cathodes and electrolyte, or at their interfaces. Figure 1.3 summaries the main aging mechanisms occurring in Li-ion batteries. They can be categorized into several classes: (i) Film

formation on the surface of electrodes, such as solid electrolyte interface (SEI) formation caused by the irreversible reactions between electrode materials and liquid electrolyte, and Li plating due to a too large Li influx [19, 20]; (ii) Structural changes of electrode materials, such as the atomic structural disordering caused by repetitive cation mixing or irreversible phase transition [21]; (iii) Parasitic reactions such as the local corrosion of current collector and dissolution of binders [22]. These degradations occurring during the cycling deteriorate the electrochemical performance of Li-ion batteries including available capacity and rate performance. For example, the formation of SEI film on the surface of electrodes consumes the available Li ion in electrolyte, leading to a loss of battery capacity, and, furthermore, the passive SEI film impedes the transport of Li into electrode materials, decreasing the rate preformation of batteries [19].

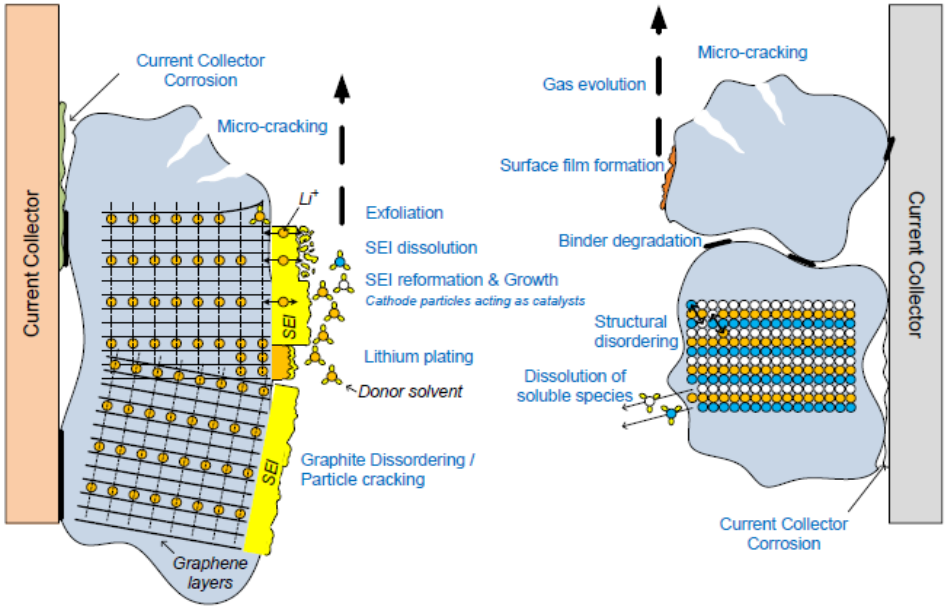

Figure 1.3. Main mechanisms for eletrochemical degradation and failure in Li-ion batteries [22].

Many designs or modifications in recent years have been made to mitigate the eletrochemical degradations of Li-ion batteries. For example, a surface modification through

depositing an atomic layer of metal oxides such as TiO_2 [23], Al_2O_3 [24] or solid-state electrolyte [25] on the active paticles of electrodes is able to mitigate the structural disording of active materials and meanwhile suppress the formation of SEI film. Another way to mitigate the degradations is to use the addictives [26-29]. A series of addictives such as fluoroethylene carbonate (FEC) and vinylene carbonate (VC) have been proven to help stablize the SEI film and thus remarkably improve the capacity retention and coulombic efficiency of Li-ion batteries [28]. Nevertheless, mitigating the electrochemical degradations is still a grand challenge, mainly owing to the fact that the degradations do not originate from one single cause, but from a number of various processes and their interactions [30].

1.3 Mechanics in Li-ion batteries

Electrochemical processes in Li-ion batteries have been quite well studied; less understood is the phenomena of mechanics associated with battery operation, such as deformation [31], stress evolution [32], fracture [33, 34], and fatigue [35]. When Li-ion batteries are cycling, Li atoms are repetitively inserted (extracted) into (out of) electrode materials, inducing a deformation of electrode materials that ranges from a few percent to a few hundred percent (depending on the specific reaction types and electrode materials [36], Figure 1.4). This deformation is often constrained by surrounding inactive materials (i.e. binders, conductive matrix and current collector), or mismatched due to the anisotropic volume change of grains with different orientations [37] and the inhomogeneous Li distribution [32]. In this case, a field of mechanical stresses will develop in electrodes and cause a wealthy of phenomena of mechanics.

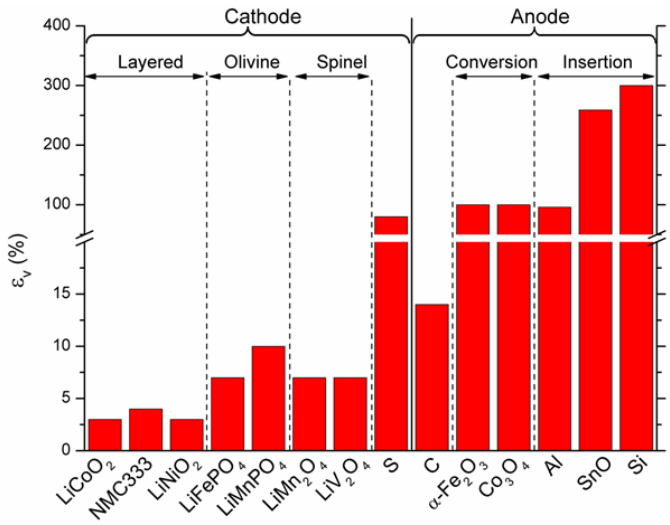

Figure 1.4. A survey of volumetric strain of different types of cathode and anode materials [36].

Mechanical stresses developed during battery cycling may cause the morphological changes of electrodes such as bending of electrodes and close of pores [38]. Meanwhile, stresses often lead to various mechanical degradations, including fracture of active materials [39-41], crack of inactive conductive matrix [42], buckling and debonding of thin films [43, 44], breakage of SEI [45] in both anode and cathode. Among them, fracture of active materials constitutes the major mechanical degradation of Li-ion batteries. Recent experiments have shown that the class of electrode materials with an intercalation-type Li reaction (i.e. $LiCoO_2$ (LCO) [46], Li_2MnO_4 (LMO) [47], $LiNi_xMn_yCo_zO_2$ (NMC, x+y+z=1) [41, 48] and graphite [40]) often experiences the fracture after a number of cycles, albeit of only a few percent of volumetric change associated with battery cycling, Figure 1.5a-e. As expected, the high-capacity electrodes with a conversion- or insertion-type reactions suffers a much heavier fracture due to their huge volumetric change associated with lithiation/delithiation. For instance, with a ~300% volumetric expansion after fully lithiated, Si based electrode often experiences a catastrophic mechanical failure in the very early cycles [39], Figure 1.5f. In addition to the fracture of active materials, various other forms of mechanical

degradation have been also observed, such as wrinkle of Si thin film electrode [44], breakage of SEI in Co_3O_4 particles [45] and cracks in conductive matrix [43], Figure 1.6a-c.

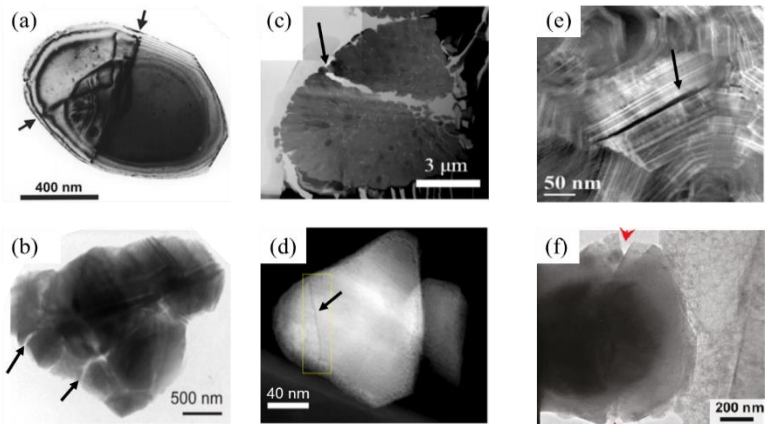

Figure 1.5. Fracture of active materials after battery cycling, (a) LCO [46], (b) LMO [47], (c, d) NMC [41, 48], (e) graphite [40] and (f) Si [39].

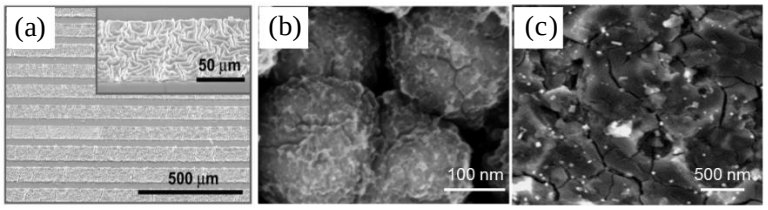

Figure 1.6. Various forms of mechanical degradation in Li-ion batteries including (a) wrinkle of Si thin film electrode [44], (b) breakage of SEI in Co_3O_4 particles [45] and (c) cracks in conductive matrix [43].

Mechanical degradation is a critical issue for Li-ion batteries. For example, cracks (Figure 1.5) impede the electron conduction in electrodes, and thus significantly increase the electric and ohmic resistances of batteries. As a result, working voltage of the batteries dramatically drops and the rate capability decreases [49]. Moreover, repetitive formation and breakage of SEI film (Figure 1.6b) constantly consume the available Li ions in electrolyte and thus persistently decreases the cyclic efficiency of Li-ion batteries [45]. In recent years, many clever designs have been developed

to mitigate the mechanical failure of batteries, such as creating open spaces to accommodate volumetric swelling [50-53], compositing active phase and inactive components [54, 55], constructing hierarchal structures [56], and manipulating geometries and patterns at the nanoscale [57-59]. All these designs have proven that mechanics perspectives can provide important insight in the course of developing reliable batteries [60, 61].

1.4 Electro-chemo-mechanics in Li-ion batteries

To better understand the complex interrelated phenomena in Li-ion batteries, researchers now are trying to consider the Li-ion batteries as a system that dynamically couples electrochemistry and mechanics. The electrochemical process of Li insertion and extraction induces rich phenomena of elemental mechanics [31-35]. Meanwhile, mechanical stresses modulate the thermodynamics and kinetics of ionic transport, surface charge transfer, interfacial reaction, and phase transition of materials [62, 63]. While the mechanical deformation and failure in the cycles of batteries are well known, the influences of stresses on the electrochemical reactions are less obvious and are much less studied. In fact, for a system involving multi-physical processes, a conventional wisdom is that "chemistry always win" simply because the energy scales in the chemical reactions are usually orders of magnitude higher than the mechanical energies [64]. Li-ion batteries might be an exception in that the chemical driving force (bonding energy) in the lithiation/delithiation reactions is relatively weak in order to maintain a good cyclability, while the mechanical deformation and stresses are usually significant that leverages the mechanical energy to a level comparable with the chemical energies [31, 65-67]. A few recent theories or observations originates from the coupling of electrochemistry and mechanics [63], including diffusion-induced stresses [32], stress regulated surface charge transfer [68], interfacial reaction [69-71], as well as

lithiation induced corrosive fracture [40, 72, 73]. Most of the phenomena are at early stage of study and are to be further explored.

1.4.1 Stress regulated Li diffusion

Diffusion of Li atoms into an electrode material is accompanied by a change of volume. This volumetric change may induce stresses if the deformation is constrained. The diffusion-induced stresses in the electrode materials is now well recognized. Maybe less understood is the impact of stress on the transport of Li within the host, and hence on the electro-chemical potential of the cell. When Li is inserted into a host, locally generated stresses due to strain mismatch modify the energy cost associated with further insertion. In other words, stress affects the chemical potential of Li in the host, whose gradient drives diffusion. The modeling of the coupling between mechanics and chemistry is thus twofold: diffusion induces stresses, and stresses affect diffusion. The stress-diffusion coupling is sketched in Figure 1.7. For a free-standing spherical particle, the inhomogeneous distribution of Li induces a field of stress within the particle. For a given Li flux prescribed at the outer shell of the particle, the shell region (Li rich) is under compression and the core region (Li poor) is under tension, as shown in Figure 1.7a. Stress modifies the chemical potential of Li and drives Li migrate from the compressed part to the tensed core. Figure 1.7b sketches the comparison of radial distribution of Li in the spherical particle with and without accounting for the stress effect. Overall, the stress gradient tends to homogenize the Li distribution.

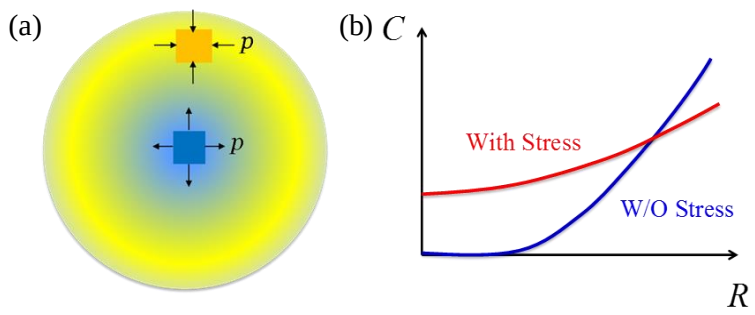

Figure 1.7. (a) Schematic of diffusion-induced stresses in a free-standing spherical particle. Li insertion causes deformation of the host material and the inhomogeneous distribution of Li induces a field of stress within the particle. The shell region (Li rich) is under compression and the core region (Li poor) is under tension. (b) Sketch of the stress effect on radial distribution of Li in the spherical particle. The stress gradient tends to homogenize the Li distribution. The red line represents the Li profile calculated by considering both effects of stress and Li concentration gradient, while the blue line represents the case that Li diffusion is driven only by the concentration gradient [63].

Continuum models coupling deformation to diffusion of atoms in a solid solution are certainly not new. A fundamental idea of most models is the representation of the deformation induced by insertion of guest species as an eigenstrain (stress-free strain). The analogy with thermal strain is then obvious, and dates back at least to the work of Prussin [74], who analyzed stresses generated in Si wafers due to solute diffusion. Fundamental contributions to the thermodynamics of solid solutions under stresses are those of Larché and Cahn [75, 76], and Li [77], who independently derived expressions for the chemical potential of diffusing species into a solid host. A comprehensive framework for diffusion coupled to large, inelastic deformations was proposed by Stephenson [78]. By contrast, analyses focusing on electrochemical insertion in electrode materials are relatively new. Relying on the analogy with thermal strains but neglecting stress effects on diffusion, early work was done to estimate the stress generated in carbon anodes [32], $LiMn_2O_4$ [79], $LiCoO_2$ [80, 81] cathode, and Si anode particles [82]. The effect of stress on the activation energy for diffusion was studied by Gao et al., Cheng et al., and others [66, 83-85]. The stochastic methodology has also been adopted to study the intercalation induced stresses and

damages in electrodes by Mukherjee et al. [86-88]. For high-capacity electrodes, lithiation-induced strains are often accommodated by inelastic deformation. Continuum models that account for large elasto-plastic deformation of the electrode have appeared more recently [31, 36, 89]. The simplest formula, regardless the deformation kinematics and constitutive behaviors of the electrodes, may be following,

$$\mu = \mu_0 + kT\ln\left(\frac{C}{C_{\max} - C}\right) - \Omega\sigma_m, \tag{1.4}$$

which neglects the variation of the elastic constants with composition and assumes purely volumetric strain induced by lithiation. Here, k is the universal gas constant, T is the temperature, μ is the chemical potential of Li in the host, μ_0 is a reference value, $C_{\max}$ is the maximum Li concentration in the host materials, $\sigma_m = \sigma_{kk}/3$ is the mean stress and Ω represents the partial molar volume of Li in the host. The first two terms on the right-hand side of Equation (1.4) are the familiar expressions of the chemical potential for a species in non-ideal solution. The third term in Equation (1.4) represents the change in elastic energy upon insertion under stress.

1.4.2 Stress regulated surface charge transfer

In addition to the effect on Li diffusion, mechanical stresses influence the electrical response of electrode materials [90, 91]. Sethuraman et al. [90] reported that the stress affects the equilibrium potential of Si electrodes with an estimate that 1 GPa stress changes the electrical potential by ~ 60 mV. Piper et al. [91] found that a compressive stress leads to a higher overpotential and a lower saturation capacity at the cut-off voltage during galvanostatic operations. Stress has a similar effect of electrical overpotential and modulates the driving force of charge transfer at the electrode surface. Butler-Volmer relationship is the most common equation describing the charge transfer rate in terms of the thermodynamic driving force (i.e. overpotential).

However, the stress effect is ignored in the traditional Butler-Volmer equation. Recently, researchers modified Butler-Volmer equation by incorporating the stress effect into the free energy and activation energy for the surface charge transfer process [92]. Figure 1.8 shows the free energy diagram altered by the applied electrical potential and mechanical stresses. The activation energies of the redox reactions at equilibrium states are identical, $\Delta G_{0O} = \Delta G_{0R}$, (black solid lines). The chemical equilibrium will be broken by the electrical overpotential $E - E_0$ as well as the mechanical stress, where E represents the electrical field and E_0 the equilibrium potential. The electrical overpotential promotes electron transfer and decreases the free energy of the oxidized state by $F(E - E_0)$ (red dashed line). The tensile stress in the surface layer, on the other hand, causes a change of elastic energy $\Delta W = \sigma_m \Omega$ (blue dashed line) that promotes the formation of neutral Li. The change in the total free energy of the reduced state relative to the oxidized state is $F(E - E_0) - \sigma_m \Omega$. Therefore, the stress effect is included in the Butler-Volmer equation as,

$$i = i_0 \left\{ \exp\left[(1-\alpha) \frac{F(E - E_0) - \sigma_m \Omega}{kT} \right] - \exp\left[\alpha \frac{F(E - E_0) - \sigma_m \Omega}{kT} \right] \right\}, \qquad (1.5)$$

where α is the charge transfer coefficient and i_0 is the exchange current density. The modified Butler-Volmer equation indicates that tensile stresses would facilitate the combination of Li ions and electrons, and thus lithiation reactions.

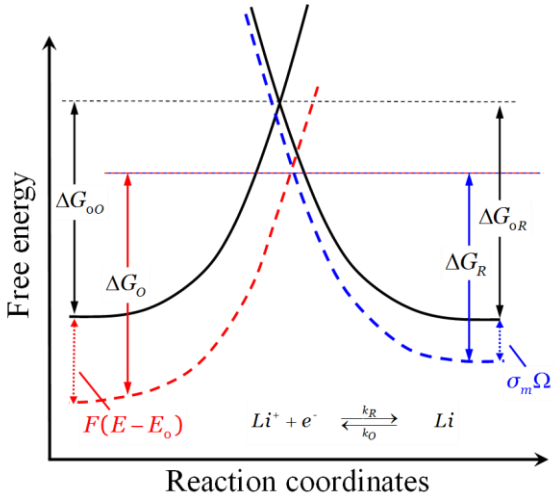

Figure 1.8. Free energy diagram for the surface charge transfer process altered by the applied electrical potential and mechanical stresses. The activation energies of the redox reactions at equilibrium states are identical, $\Delta G_{0O} = \Delta G_{0R}$, (black solid lines). The chemical equilibrium will be broken by the electrical overpotential as well as the mechanical stress. The electrical overpotential E-E_0 promotes electron transfer and decreases the free energy of oxidized state by $F(E\text{-}E_0)$ (red dashed line). The tensile stress in the surface layer causes a change of elastic energy $\Delta W = \sigma_m \Omega$ (blue dashed line) and promotes the formation of neutral Li atoms. The change in the total free energy of reduced state relative to oxidized state is $F(E\text{-}E_0)\text{-}\sigma_m\Omega$.

In a recent report, Kim et al. [93] made an ingenious use of the principle of stress-driven diffusion to design a novel class of mechanical energy harvesters. The experimental setup is schematically shown in Figure 1.9a. Two identical partially lithiated Si films serve as electrodes separated by electrolyte-soaked polymer membranes. Bending-induced asymmetric stresses generate chemical potential difference, driving Li ions migrate from the compressed electrode (red) to the tensed side (blue) to generate electrical current. By removing the bending stress ion flux and electrical concurrent are reversed. The device can sustain more than a thousand cycles with nearly constant current output. Furthermore, the device exhibits higher average energy output than most piezoelectric generators when operating at low frequencies. In this design, the electrical current density depends on the magnitude of bending-induced asymmetric stresses. The characteristic of the output electric current is determined by the concurrent surface charge transfer and Li bulk

diffusion in the electrodes – both processes are dependent on the bending stresses. Figure 1.9b shows the schematic of the current density upon release of bending. At the short-range time scale, the peak of output current is limited by the Butler-Vomer surface charge transfer process. In the following stage, the bulk transport of Li through the electrodes becomes the rate-limiting step. The current density eventually diminishes to zero until new equilibrium state is reached. By examining the experimental measurement of the current density, it is able to identify the surface charge transfer-controlled or diffusion-controlled regime. This feature also enables one to control the current density of mechanical energy harvesters through manipulating the geometry of the electrodes in order to optimize the energy efficiency of the device. The work by Kim et al. is a clear demonstration of interactions between stresses and electrochemistry, and opens the avenues of optimizing electrochemical devices for mechanical sensing and actuation.

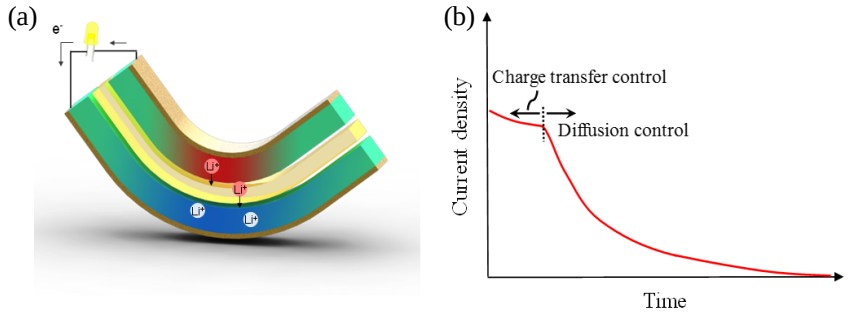

Figure 1.9. (a) Design of mechanical energy harvester based on the stress-driven Li diffusion. Two identical partially lithiated Si films act as electrodes, separated by electrolyte-soaked polymer membranes (the size of the electrodes and electrolyte are not in scale). Bending-induced asymmetric stresses generate chemical potential difference, driving Li ions migrate from the compressed electrode (red) to the tensed side (blue).[93]. (b) Schematic of short circuit current density during release of bending. The peak current is determined by the Butler-Volmer surface charge transfer process and the subsequent stage is controlled by Li diffusion in the electrodes.

1.4.3 Stress regulated interfacial reaction

The operation of an electrochemical cell involves a number of kinetic processes, including Li diffusion through the electrodes and the electrolyte, electron transport, redox reactions at the interface, lithiation at the reaction front, and phase transition of the electrode materials. Lithiation reaction involves short-range processes, such as breaking and forming of atomic bonds. It is now evident that lithiation of some systems results in interfacial reaction-controlled kinetics. For instance, initial lithiation of crystalline Si generates an atomically sharp planar interface separating crystalline Si from amorphous lithiated Si and the deformation is highly anisotropic [94]. Meanwhile, to accommodate the large volumetric expansion associated with the lithiation process, the host material must deform plastically. By considering the interfacial reaction and the elasto-plastic deformation, a theory has been constructed which accounts for concurrent reaction kinetics and plasticity that allows people to explore the stress regulated interfacial reactions, inhomogeneous growth of lithiated phase, as well as the instability of solid state reaction front. In the following sub-sections, respective theories and quote experimental observations that verify those ideas will be briefly introduced.

The most dramatic effect of stress on electrochemical reactions may be the stress-induced stagnation of reaction front during lithiation of Si spherical particles. To establish a theoretical basis, the authors identify the driving force for the reaction – the change in the free energy associated with the reaction that converts one Li atom and $1/x$ number of Si atoms into lithiated Si [65]. Let ΔG_r be the free energy when both the stress and the applied voltage vanish. When the conducting wire is connected through a voltage source, associated with converting one Li atom into lithiated Si, one electron passes through the conducting wire, so that the external voltage source does work $e\Phi$, where Φ is the voltage, and e is the elementary charge. The driving force

is modified when the two phases, the crystalline Si and the lithiated Si, are stressed. The stresses come from the mismatch strain between the crystalline Si and lithiated Si. During the lithition, the lithiated Si experiences a volume expansion while the crystalline Si does not, which generates a compressive stress in lithiated Si and a tensile stress in crystalline Si. The mean stresses in lithiated Si and crystalline Si at the reaction front are denoted as $\sigma_m^{\mathrm{Li}_x\mathrm{Si}}$ and σ_m^{Si}, respectively. Associated with converting one Li atom into lithiated Si, the crystalline Si phase loses $1/x$ number of Si atoms, and the stress in silicon does work $-\sigma_m^{\mathrm{Si}}\Omega^{\mathrm{Si}}/x$, where Ω^{Si} is the volume per Si atom. The amorphous phase gains $1/x$ number of Si atoms and one Li atom, so that the stress in the amorphous phase does work $\sigma_m^{\mathrm{Li_xSi}}\Omega^{\mathrm{Li_xSi}}/x$, where $\sigma_m^{\mathrm{Li_xSi}}$ is the mean stress in the amorphous phase at the reaction front, and $\Omega^{\mathrm{Li_xSi}}$ is the volume per unit of $\mathrm{Li_xSi}$. Combining the above contributions, the authors find that, when the reaction advances, the net change in the free energy is [65]

$$\Delta G = \Delta G_r - e\Phi + \frac{1}{x}\left(\sigma_m^{\mathrm{Si}}\Omega^{\mathrm{Si}} - \sigma_m^{\mathrm{Li_xSi}}\Omega^{\mathrm{Li_xSi}}\right), \tag{1.6}$$

The authors have neglected the dissipation at electrolyte/electrode interfaces, as well as inside the electrodes and electrolytes. In the sign convention, a negative ΔG drives lithiation, and a more negative value represents a larger driving force. The free energy of reaction ΔG_r takes a negative value. The authors also take the polarity of the voltage source in the direction that drives lithiation. As expected, a compressive mean stress in the crystalline Si promotes lithiation, but a compressive mean stress in the lithiated Si retards lithiation.

The authors derive the stress field in a spherical Si particle [65] and examine how the stress field modifies the driving force for the lithiation reaction. The free energy contributed by stresses is plotted in Figure 1.10a. The horizontal axis represents the normalized radius of the crystalline core, where *a* represents the radius of the crystalline Si core, and *b* the outer radius of the Si particle.

As expected, the contribution due to the stresses is positive and retards lithiation. The magnitude of the contribution increases as the crystalline core shrinks. Recall that the free energy of formation of lithiated silicon is small; for example, ΔG_r = -0.18 eV for amorphous $Li_{2.1}Si$ [95]. Consequently, the reaction can readily generate large enough stress to counteract the electrochemical driving force, stalling the reaction. Such a stagnation effect was observed in a recent experimental study of the kinetics of crystalline Si particle lithiation with in situ transmission electron microscopy (TEM). McDowell et al. monitored the propagation of the lithiation reaction front described by the ratio *a/b*, Figure 1.10b [96]. This figure shows that the propagation of the reaction front is significantly slowed at similar ratios of a/b for particles with different sizes, which suggests that the large compressive stress built up as the ratio *a/b* decreases retards the lithiation reaction.

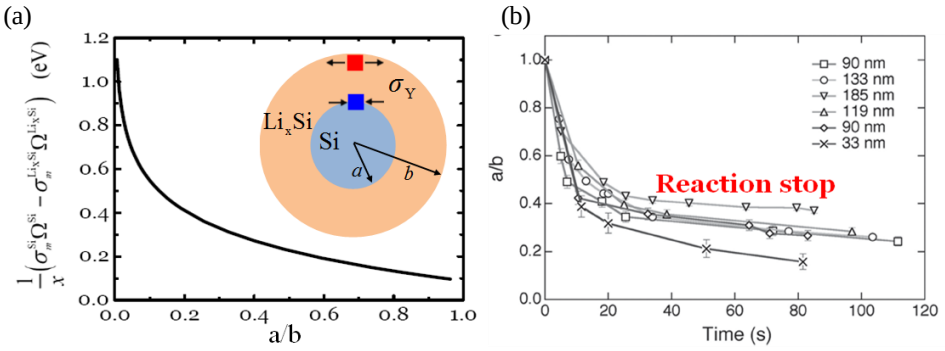

Figure 1.10. (a) Stress-regulated interfacial reaction during lithiation of a crystalline Si spherical particle. Stress modifies the free energy associated with the reaction that converts one Li and 1/*x* Si atoms into lithiated Si at the reaction front. The figure plots the evolution of the free energy contributed by mechanical stresses as a function of the position of the reaction front. The inset shows the schematic of the stress field within the particle [65]. (b) Experimental evidence of the stagnation of lithiation reaction due to the stress effect. Lithiation in the particles of different sizes significantly shows down at similar *a*/*b* ratios suggesting that stress gradually builds up as the *a*/*b* ratio decreases and retards the progression of the reaction front [96].

For the system with interfacial reaction controlled kinetics, the stress field will be modified by the geometric factor of surface curvature [70]. When the reaction front is flat (e.g. thin film

case), the volumetric expansion associated with the reaction is accommodated by elongating the lithiated phase in the direction normal to the reaction front, while maintaining the geometric compatibility between the two phases in the directions tangential to the reaction front. As the reaction front advances, previously lithiated material recedes by rigid-body translation with no further deformation. The stresses in the lithiated phase remain compressive state. When the reaction front is convex (e.g. lithiation on the surface of nanowires, spherical particles), the lithiated phase recedes as the reaction front advances. An element of lithiated material at the front initially undergoes compressive stress in the hoop directions. While upon subsequent lithiation, the element is pushed away and then develops a tensile stress in the hoop directions. The tensile stress may increase the solubility of Li and facilitate Li transport through the lithiated material. On the contrary, when the reaction front is concave (e.g. lithiation on the inner face of the nanotubes), the stress field is reversed and the lithiated phase is subjected to compressive stresses. For a system with alternative convex and concave surface curvatures, Figure 1.11a, the lithiated phase may grow to a wavy morphology because of the asymmetric field of stresses. In a recent study, Zhang et al. used *in situ* TEM to observe the lithiation behavior of SiO_2 coating on SiC nanowires [70]. SiC is inert to Li reaction so the entire deformation is due to the lithiation of SiO_2 thin coating. Figure 1.11b shows the inhomogeneous growth of SiO_2 during the cycle of lithiation and delithiation. It forms a wavy structure that parts of the surface grow thicker than others. In a high-resolution TEM image (details in the reference [70]), the pristine SiO_2@SiC nanowire has a twinning microstructure that induces alternative convex and concave curvatures. It is plausible that the tensile stress field associated with the convex surface grows a thicker layer of the lithiated phase. Such a stress-mediated growth shows an interesting mechanism of non-uniform morphology, and

may also provide an alternative way to fabricate complex patterned nanostructures in other electromechanical systems [97, 98].

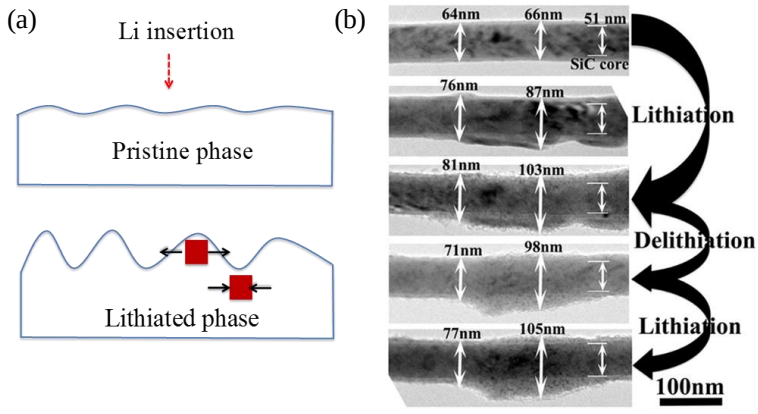

Figure 1.11. (a) Schematic of inhomogeneous growth of lithiated phase due to the stress regulated lithiation reaction. The lithiated phase of convex curvature develops a field of tensile stresses, facilitating Li transport through the lithiated material and promoting the interfacial reaction at the phase boundary. On the contrary, the lithiated phase of concave curvature is under a field of compressive stresses, retarding the electrochemical growth of the layer. (b) In situ TEM observation of the inhomogeneous growth of the SiO_2 layer during the cycle of lithiation and delithiation [70].

1.4.4 Corrosive fracture of electrodes

Fracture and fatigue occur in most of electrode materials and numerous models have been developed to analyze fracture in Li-ion batteries. Different approaches were adopted in literature [32, 34, 99, 100]. Several groups incorporated diffusion-induced stress calculations and used a stress criterion to predict the onset of fracture [32, 89, 100]. Another set of literature have studied lithiation-induced fracture by applying Griffith fracture mechanics [33, 99]. To date, few studies have looked into the concurrent Li transport and crack propagation. Fracture in electrochemical systems is often corrosive in nature. Corrosive fracture is also known variously in the mechanicscommunity as environment-sensitive fracture, subcritical crack growth, or stress-corrosion cracking, which differs from the conventional sense of corrosion in electrochemistry. Li

is like a corrosive species. Li insertion breaks the host atomic bonds and forms weaker bonds between Li and host atoms, decreasing both elastic modulus and fracture strength of the host material [101-103]. The dynamics of crack propagation should be coupled with the redistribution of Li. In particular, Li diffuse quickly on the crack surface because of the high surface diffusivity, and is accumulated at the crack tip due to the large tensile stresses ahead of the crack. In a recent work, it is found that local tensile stress field around the crack tip decreases the chemical potential and attracts Li accumulation at the crack tip [104]. As a result, aggregated Li reduces the fracture toughness of the host material, acting as a corrosive agent that accelerates crack nucleation and propagation [105]. This phenomenon is a reminiscence of corrosive fracture of metals induced by oxygen or moisture at the crack tip. However, different from oxygen, Li might be a more corrosive species because the formation of oxides at the crack tip may shield further oxygen transport and protect unstable crack propagation [106, 107], while lithiated alloys do not usually have such an effect.

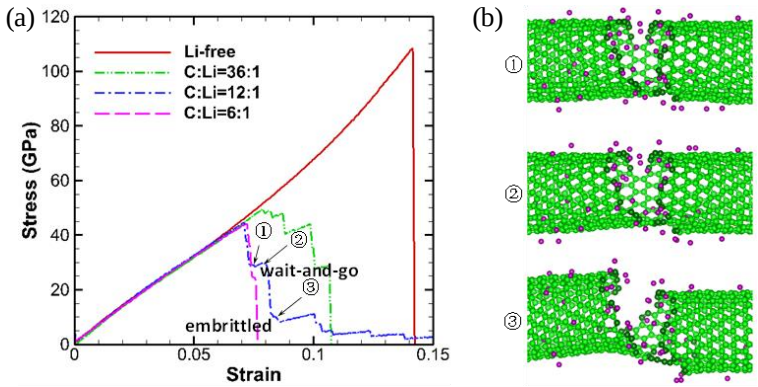

Figure 1.12. (a) Stress-strain curves of the SWCNTs containing a hole-like defect. (b) Three stages of SWCNTs showing the corrosive fracture behavior of SWCNTs studied by molecular dynamics simulations [72].

Huang et al. [72] recently investigated lithiation-mediated corrosive failure in defective single-walled carbon nanotubes (SWCNTs) using molecular dynamics simulations. They found that the coupling between fracture and Li diffusion would cause two distinct fracture modes: abrupt and retarded fracture. Abrupt fracture involves spontaneous Li weakening of the propagating crack tip, while retarded fracture features a "wait-and-go" crack extension process in which the crack tip periodically arrests and waits to be weakened by diffusing Li before extension resumes. Initially the crack maintains a steady state under a given external tension load. When lithiation proceeds, Li ions accumulate around the crack tip, weakening the fracture strength of the material around the crack tip. If fracture strength drops to be lower than the energy release rate, crack starts propagating which creates fresh surfaces without Li. Without the participation of Li at the crack tip, fracture strength of the material recovers and the crack will stop and wait to be weakened again by Li diffusion before the propagation resumes. Depends on the times scales of Li diffusion and crack propagation, Li may always catch up the crack propagation when it extends, inducing an abrupt fracture of the electrodes. Figure 1.12a shows stress-strain curves of SWCNTs containing a hole-like defect. Figure 1.12b provides three fractural states of SWCNTs that show the corrosive fracture behavior of SWCNTs based on molecular dynamics simulations. More recently, Klinsmann et al. studied fracture-diffusion coupling using a phase field approach [108]. Similar abrupt and "wait-and-go" fracture behaviors were reported in their model.

1.5 Thesis outline

The overarching goal of this thesis is to understand the couplings between mechanics and electrochemistry in Li-ion batteries using integrated theories and experiments. This thesis is organized as follows. Chapter 2 establishes a continuum model coupling the diffusion and large elasto-plastic deformation and its numerical implements. The governing equations for the

kinematics of an elasto-plastic solid and the kinetics of Li transport in a chemomechanical system under both mechanical and chemical load are listed. Chapter 2 also presents the theories of nanomechanical quantification using instrumented nanoindentation. The classical Oliver-Pharr method is employed to determine the elastic modulus and hardness of battery materials, and the indentation cracking method as well as the improved pop-in method are used to determine the fracture toughness. Chapter 3 explores the couplings between the lithiation kinetics and stresses in three-dimensional electrodes that are composed of multiple components. This chapter studies the regulations from the mechanical interactions between different components on the Li chemical potential, Li concentration, stress field and elasto-plastic deformation of the electrodes. Chapter 4 further studies the chemomechanical behaviors of the highly heterogeneous electrodes in real batteries. The finite element program, derived from the continuum theory coupling diffusion and large elasto-plastic deformation, and the three dimensional (3D) reconstructed model of both cathode and anode materials from the practical batteries are combined in this chapter. The main goal of this chapter is to investigate the mechanical interactions of the constituents and their influence on the accessible capacity of batteries.

Chapter 5 experimentally reveals the structural disintegration of the state-of-art cathode materials NMC during electrochemical cycling. The microstructural evolution of different marked regimes in electrodes after lithiation cycles is tracked. It is found that the decohesion of primary particles constitutes the major mechanical degradation in the NMC materials. The electrochemical degradation caused by the mechanical disintegration is examined by the electrochemical impedance spectroscopy (EIS) measurement. A finite element program is employed to study the evolution of Li concentration and stresses in a NMC secondary particle and employ the cohesive zone model to simulate microcracks accumulate and propagate during the cycling. Chapter 6

explores the dynamic evolution of mechanical properties of NMC during electrochemical cycling. Instrumented nanoindentation in an inert environment is employed to measure the elastic modulus, hardness, and interfacial fracture strength of NMC with a hierarchical meatball structure as a function of the state of charge and cycle number. The mechanical properties significantly depend on the lithiation state and degrade as the electrochemical cycles proceed.

Chapter 7 investigates the corrosive fracture of electrodes in Li-ion batteries. Li reaction causes embrittlement of the host material and typically results in a decrease of fracture toughness of anodes when Li inserts and a reduction of fracture toughness of cathodes when Li extracts. The dynamics of crack growth depends on the chemomechanical load, kinetics of Li transport, and the Li embrittlement effect. A theory of coupled diffusion, large deformation, and crack growth is implemented into finite element program to simulate the corrosive fracture of electrodes under concurrent mechanical and chemical load. The competition between energy release rate and fracture resistance as crack grows during both Li insertion and extraction is examined in detail. It is found that the corrosive fracture behaviors of the electrodes rely on the chemomechanical load and the supply of Li to the crack tip. This model is further applied to simulate corrosive behavior of intergranular cracks in NMC upon Li cycles. The evolving interfacial strength at different states of charge and different cycle numbers measured by in-situ nanoindentation is implemented in the numerical simulation.

2. THEORETICAL FRAMWORK AND EXPERIMENTAL METHOD

2.1 Coupled chemomechanical theory and computation framework

The continuum theory of coupled Li diffusion and large elasto-plastic deformation is described in this chapter. Governing equations for the kinematics of an elasto-plasticitic solid and the kinetics of Li transport in a chemomechanical system are listed in the following.

2.1.1 Kinematics of deformation

When a solid deforms by mechanical forces under constraint conditions, each material particle retains its material coordinates **X** and its spatial coordinates **x** is determined by the displacement vector $\mathbf{u}(\mathbf{X}, t)$, pointing from the reference position to the current configuration,

$$\mathbf{x}(\mathbf{X}, t) = \mathbf{X} + \mathbf{u}(\mathbf{X}, t) . \tag{2.1}$$

The deformation gradient **F** includes the complete information about the local strain and rotation of the material. **F** can be written in terms of the displacement gradient,

$$\mathbf{F} = \frac{\partial \mathbf{x}}{\partial \mathbf{X}} = \nabla \mathbf{u} + \mathbf{I} . \tag{2.2}$$

A theory of the multiplicative decomposition of the deformation gradient is used,

$$\mathbf{F} = \mathbf{F}_{\text{el}} \mathbf{F}_{\text{inel}} , \tag{2.3}$$

where $\mathbf{F}_{\text{e}}$ represents the reversible elastic distortion and $\mathbf{F}_{\text{inel}}$ represents the inelastic distortion of the material. The ratio of the current to the initial volume (or mass density) is given by

$$\frac{\partial V}{\partial V_0} = \det(\mathbf{F}) = J > 0 , \tag{2.4}$$

and hence

$$J = J_{\text{el}} J_{\text{inel}} , \qquad J_{\text{el}} = \det(\mathbf{F}_{\text{el}}) > 0 , \qquad J_{\text{inel}} = \det(\mathbf{F}_{\text{inel}}) > 0 . \tag{2.5}$$

The inelastic deformation can be further decomposed into two parts: a volumetric change caused by Li insertion or extraction, and plastic deformation of the material due to the irreversible shape change,

$$\mathbf{F}_{\text{inel}} = \mathbf{F}_{\text{Li}}\mathbf{F}_{\text{pl}}\,, \tag{2.6}$$

where $\mathbf{F}_{\text{Li}}$ represents the eigen deformation induced by the insertion or extraction of Li atom into the host material, and $\mathbf{F}_{\text{pl}}$ represents the irreversible plastic deformation that dictates the shape change of the body.

Let J_{Li} denotes the volume change per unit reference volume, it is assumed that this change is entirely due to the change of Li concertation in the host frame, so that the volumetric change is written as follows

$$J_{\text{Li}} = \det(\mathbf{F}_{\text{Li}}) = (1 + \Omega C), \tag{2.7}$$

where Ω is the partial molar volume of Li atom in the host material and $C(\mathbf{X}, t)$ is the number of Li atom per unit volume in the reference state (i.e. nominal Li concentration). The Li insertion-induced linear deformation gradient is

$$\mathbf{F}_{\text{Li}} = {J_{\text{Li}}}^{1/3}\mathbf{I} = (1 + \Omega C)^{1/3}\mathbf{I}\,, \tag{2.8}$$

Here an isotropic expansion in each direction upon Li reactions is assumed. This assumption is not necessarily correct, for instance, in the layered cathode, the deformation is highly anisotropic. An anisotropic deformation will be considered when the theory is applied in the later modeling of NMC aggregated particles.

The stress tensor satisfies the mechanical equilibrium condition,

$$\nabla \cdot \mathbf{P} + \mathbf{B}_{\text{v}} = \mathbf{0}\,, \tag{2.9}$$

where **P** represents the first Piola-Kirchhoff (PK) stress that relates forces in the current configuration with respect to the area in the reference configuration (nominal stress). The volume

force vector $\mathbf{B}_v$ is also determined with respect to the reference volume, and the tensor divergence operator ∇ is computed in the Lagrangian (reference) coordinates. The first PK stress **P** is calculated from the second Piola-Kirchhoff stress as

$$\mathbf{P} = \mathbf{FS}\,, \tag{2.10}$$

where **S** represents the second PK stress where both force and area are represented in the material configuration. **S** is related to the symmetric Cauchy stress $\boldsymbol{\sigma}$ in the deformed body by

$$\boldsymbol{\sigma} = J^{-1}\mathbf{FSF}^{\mathrm{T}}\,. \tag{2.11}$$

It would be convenient to introduce the elastic second PK Stress, [109]

$$\mathbf{S}_{\mathrm{el}} = J_{\mathrm{el}}\mathbf{F}_{\mathrm{el}}^{-1}\boldsymbol{\sigma}\mathbf{F}_{\mathrm{el}}^{-\mathrm{T}}\,. \tag{2.12}$$

A constitutive model proposed in the prior work is adopted [92, 109]. The elastic second PK stress is related to the elastic Green-Lagrange strain tensor $\mathbf{E}_{\mathrm{el}}$ by

$$\mathbf{S}_{\mathrm{el}} = J_{\mathrm{el}}\mathbf{F}_{\mathrm{el}}^{-1}\boldsymbol{\sigma}\mathbf{F}_{\mathrm{el}}^{-\mathrm{T}} = \mathbf{C} : \mathbf{E}_{\mathrm{el}}\,, \tag{2.13}$$

where **C** is the elastic constant matrix for the material in the reference configuration. The elastic Green-Lagrange strain tensor is computed from the elastic right Cauchy-Green deformation tensor

$$\mathbf{E}_{\mathrm{el}} = (\mathbf{C}_{\mathrm{el}} - \mathbf{I})/2\,, \tag{2.14}$$

where the elastic right Cauchy-Green deformation tensor is determined by

$$\mathbf{C}_{\mathrm{el}} = \mathbf{F}_{\mathrm{el}}^{\mathrm{T}}\mathbf{F}_{\mathrm{el}}\,, \tag{2.15}$$

The material element yields under the von Mises criterion and the plastic deformation follows the J_2 flow theory. The von Mises criterion suggests that the yielding of the material begins when the second deviatoric stress invariant J_2 reaches a critical value. The yield function F_{y} is written as,

$$F_{\mathrm{y}} = \sigma_{\mathrm{mises}} - \sigma_{\mathrm{y}} \tag{2.16}$$

where σ_{y} is the yield stress and σ_{mises} is the von Mises stress, defined as,

$$\sigma_{\text{mises}} = \sqrt{3J_2(\boldsymbol{\sigma})} = \sqrt{3\text{dev}(\boldsymbol{\sigma}):\text{dev}(\boldsymbol{\sigma})/2} \tag{2.17}$$

Since a multiplicative decomposition of deformation is used, the associated plastic flow rule can be written as [110]

$$\dot{\mathbf{C}}_{\text{pl}}^{-1} = -2\lambda \mathbf{F}^{-1} \frac{\partial F_{\text{y}}}{J\partial \boldsymbol{\sigma}} \mathbf{F} \mathbf{C}_{\text{pl}}^{-1} \tag{2.18}$$

where the plastic multiplier λ and the yield function F_{y} satisfy the Kuhn-Tucker condition,

$$\lambda \geq 0, \qquad F_{\text{y}} \leq 0, \qquad \lambda F_{\text{y}} = 0 \tag{2.19}$$

$\boldsymbol{C}_{\text{pl}}^{-1}$ and $\dot{\boldsymbol{C}}_{\text{pl}}^{-1}$ are the plastic right Cauchy-Green and plastic right Cauchy-Green rate, respectively,

$$\mathbf{C}_{\text{pl}}^{-1} = \mathbf{F}_{\text{pl}}^{-1}\mathbf{F}_{\text{pl}}^{-\text{T}}, \qquad \dot{\mathbf{C}}_{\text{pl}}^{-1} = \dot{\mathbf{F}}_{\text{pl}}^{-1}\mathbf{F}_{\text{pl}}^{-\text{T}} + \mathbf{F}_{\text{pl}}^{-1}\dot{\mathbf{F}}_{\text{pl}}^{-\text{T}} \tag{2.20}$$

The governing equations for the kinematics of deformation is strongly nonlinear. Their weak formulations are rewritten and integrated into the finite element program COMSOL Multiphysics™ (COMSOL Multiphysics, Sweden) within a Lagrangian setting. The coupled equations for mechanical equilibrium and Li diffusion will be solved simultaneously at every time step. The weak form for the mechanical equilibrium is obtained by multiplying Equation (2.9) by a test function and integrating it over the volume of the material

$$\int_{V_0} (\nabla \cdot \mathbf{P} + \mathbf{B}_{\text{v}}) \cdot \mathbf{v}\, dV_0 = 0\,, \tag{2.21}$$

where **v**(**X**, t) is a test function that vanishes on the boundary. Integrating the equation by parts it gives

$$\int_{V_0} \mathbf{P} \cdot \nabla \mathbf{v}\, dV_0 - \int_{V_0} \mathbf{B}_{\text{v}} \cdot \mathbf{v}\, dV_0 - \int_{A_0} \mathbf{T} \cdot \mathbf{v}\, dA_0 = 0\,, \tag{2.22}$$

where $\mathbf{T}$ represents the nominal surface traction that is related to the first PK stress via the formula $\mathbf{T} = \mathbf{P} \cdot \mathbf{N_0}$, where the normal vector $\mathbf{N_0}$ corresponds to the undeformed surface element.

2.1.2 Kinetics of diffusion

The mass conservation requires

$$\frac{\partial C}{\partial t} + \nabla \cdot \boldsymbol{J} = 0 \,, \tag{2.23}$$

where $\boldsymbol{J}(\mathbf{X}, t)$ is the number of the Li atom per unit time crossing a unit area in the reference state (i.e. nominal Li flux). Fick's law is adopted to describe the kinetics of Li atoms diffusing in the host material,

$$\boldsymbol{j} = -\frac{cD}{kT}\nabla_{\mathbf{x}}\mu \,, \tag{2.24}$$

where $c(\mathbf{X}, t)$ is the number of Li atoms per unit volume in the current state (i.e. true concentration), $\boldsymbol{j}(\mathbf{X}, t)$ is the number of Li atoms per unit time crossing a unit area in the current state (i.e. true flux), and $\mu(\mathbf{X}, t)$ represents Li chemical potential in the host material. *D*, *k*, and *T* are Li diffusivity, the gas constant, and temperature, respectively. Here it is assumed that the Li diffusivity in the host is isotropic and is independent of the deformation gradient **F** and Li concentration *C*.

Equation (2.24) describes Li diffusion in the current state (Eulerian coordinate) such that the quantities are written in terms of the true form and $\nabla_{\mathbf{x}}$ represents the gradient with respect to the Eulerian coordinate on the spatial frame. Using the standard transformation rules of continuum mechanics, the relationship between the nominal flux $\boldsymbol{J}$ and true flux $\boldsymbol{j}$ can be obtained. Consider a material element of normal vector $\mathbf{N_0}$ and area *dA* in the reference state deforms to a configuration of $\mathbf{n_0}$ and *da* in the current state, Nanson derived the formula

$$\mathbf{F}^{\mathrm{T}}\mathbf{n_0}da = \det(\mathbf{F})\mathbf{N_0}dA \,. \tag{2.25}$$

Note that the rate of Li diffusion should be independent of the description system, thus, the following condition must hold

$$\boldsymbol{j} \cdot \mathbf{n_0}da = \boldsymbol{J} \cdot \mathbf{N_0}A \,. \tag{2.26}$$

Combining Equations (2.25) and (2.26), the relationship between the flux vectors in the two coordinates can be obtained,

$$\boldsymbol{j} = \frac{\mathbf{F}}{\det(\mathbf{F})}\boldsymbol{J}\,. \tag{2.27}$$

The true concentration c relates to the nominal concentration C as

$$c = \frac{C}{\det(\mathbf{F})}\,. \tag{2.28}$$

The chain rule of partial derivatives is used here,

$$\nabla_{\mathbf{x}}(\quad) = \mathbf{F}^{-\mathrm{T}}\nabla(\quad)\,. \tag{2.29}$$

Combining Equations (2.25) to (2.29), the relationship between the nominal flux and the chemical potential in the Lagrangian frame can be written as

$$\boldsymbol{J} = -\frac{CD}{kT}\mathbf{F}^{-1}\mathbf{F}^{-\mathrm{T}}\nabla\mu\,. \tag{2.30}$$

It is assumed that the Helmholtz free energy per unit reference volume $\phi(\mathbf{F}, C)$ is a function of the deformation gradient and the nominal Li concentration. Derived from the thermodynamic imbalance, the chemical potential of Li can be expressed as [111]

$$\mu = \frac{\partial\phi(\mathbf{F}, C)}{\partial C} - \Omega\sigma_m\,, \tag{2.31}$$

where $\sigma_m = (\sigma_1 + \sigma_2 + \sigma_3)/3$ is the mean stress. $\frac{\partial\phi(\mathbf{F},C)}{\partial C}$ represents the isothermal chemical potential of Li at zero stress state. It is assumed that the elastic strains are small compared to the Li-induced deformation, and neglect the dependence of elastic moduli on Li concentration. The free energy is adopted from a prior work, [31]

$$\phi(\mathbf{F}, C) = \phi_0(C) + W(\mathbf{F})\,, \tag{2.32}$$

where $\phi_0(C)$ and $W(\mathbf{F})$ are the free energies contributed by the stress-free chemical potential and the strain energy, respectively. The simplified form adopts the stress-free chemical potential of

diffusing species into an ideal solid solution, originally proposed by Larché and Cahn and subsequently used by others [112, 113],

$$\frac{\partial \phi_0(C)}{\partial C} = \mu_0 + kT\ln\left(\frac{C}{C_{\max} - C}\right), \tag{2.33}$$

where $C_{\max}$ is the maximum Li concentration in the reference state and the constant μ_0 is a reference chemical potential. Combining Equations (2.31) to (2.33), the chemical potential is written as follows,

$$\mu = \mu_0 + kT\ln\left(\frac{C}{C_{\max} - C}\right) - \Omega\sigma_m\,, \tag{2.34}$$

In writing the weak formula, the chemical potential $\mu(\mathbf{X}, t)$ is used as the field variable. Following the similar procedure in Equations (2.21) and (2.22), the weak form for the mass transport is obtained as follows,

$$\int_{V_0} \left(\frac{\partial C}{\partial t} + \nabla \cdot \boldsymbol{J}\right)\hat{\mu}\, dV_0 = 0\,, \tag{2.35}$$

where $\hat{\mu}(\mathbf{X}, t)$ is a test function. Integrating the equation by parts, it yields

$$\int_{V_0} \frac{\partial C}{\partial t}\hat{\mu} dV_0 - \int_{V_0} \boldsymbol{J}\cdot\nabla\hat{\mu}\, dV_0 + \int_{A_0} \left(\boldsymbol{J}\cdot\mathbf{N_0}\right)\hat{\mu} dA_0 = 0\,, \tag{2.36}$$

where $\boldsymbol{J}\cdot\mathbf{N_0} = J_0$ is the nominal Li influx into the host material.

2.1.3 Implementation in finite element program

The coupled diffusion-deformation theory in Chapters 2.1.1 and 2.1.2 are implemented into a finite element program using the commercial software COMSOL. Solid Mechanics Modulus in COMSOL is utilized to solve the solid deformation. Lithiation induced volume change is simulated using the thermal expansion function in which the temperature field is replaced by the Li concentration field. Weak form of the governing equation for Li transport (Equations (2.34)) is

implemented into the Weak Form PDE Modulus in COMSOL to solve the Li concentration. It is noted that the chemical potential is used as the field variable for Li transport, which is beneficial for the numerical convergence. Li concentration can be computed from the chemical potential and the mean stress through Equations (2.34). The built-in time-dependent solver MUMPS (MUltifrontal Massively Parallel sparse direct Solver) is used to solve the weak formulations of kinematics of deformation in Equation (2.22) and kinetics of Li diffusion in Equation (2.36). Segregated approach is adopted to improve the convergence. The test functions $\mathbf{v}(\mathbf{X}, t)$ and $\hat{\mu}(\mathbf{X}, t)$ are selected as quadratic Lagrange and linear Lagrange, respectively, to save the computational cost and retain the numerical accuracy at the same time. The co-evolution of Li concentration and stresses are calculated from the field variables $\mathbf{u}(\mathbf{X}, t)$ and $\mu(\mathbf{X}, t)$ via the approaches described in Chapters 2.1.1 and 2.2.2

2.2 Instrumented nanoindentation

Mechanical properties of electrode materials are essential for the design of Li-ion batteries with a good mechanical resilience. However, experimental characterization on mechanical properties of the electrode materials used in practical batteries is a challenge, partially because of the difficulty of mechanical measurement for air-sensitive electrode materials, and partially because of the high anisotropy and heterogeneity of electrode materials at microscopic level. Instrumented nanoindentation that can measure the mechanical properties of heterogeneous samples at the micron- or nano-scale serves as a good platform for the mechanical characterization of electrode materials [114-121]. Instrumented nanoindentation typically includes a displacement monitor, a force controller, and an indenter with a specific geometry (usually a Berkovich tip with a three-sided pyramid geometry). During the indentation, movement of the indenter is precisely controlled by the force controller via an electromagnetic field, Figure 2.1. The depth of penetration

into the sample and the associated reaction force are simultaneously recorded and constitute a load-displacement curve from which the local mechanical properties of the sample can be extracted [122, 123].

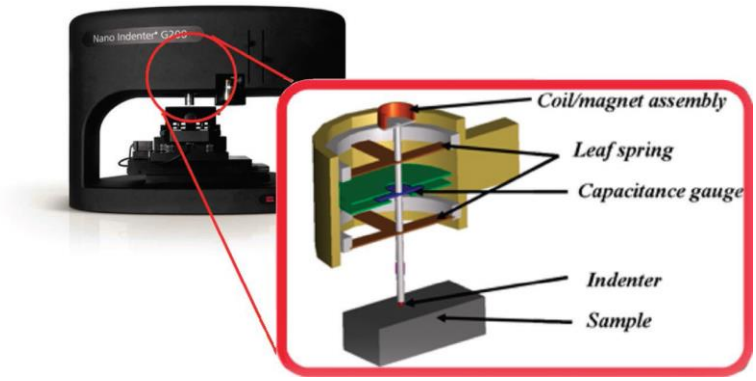

Figure 2.1. Nanoindenter G200 equipped with the XP transducer that combines superb load and displacement resolutions [124].

2.2.1 Elastic modulus and hardness

Elastic modulus E and hardness H of the sample can be extracted from the load-displacement curve of the indentation using Oliver-Pharr method [125]. The hardness H is defined as the maximum applied load $P_{\max}$, as shown in Figure 2.2a, divided by the corresponding contact area A,

$$H = \frac{P_{\max}}{A_{(h_c)}}, \tag{2.37}$$

where $P_{\max}$ is directly obtained from the prescribed load and the contact area A is calculated from an empirical function of the contact depth h_c at the maximum applied load $P_{\max}$. As illustrated in Figure 2.2b, h_c is estimated from the geometric relation with the depth of penetration h at the $P_{\max}$, (i.e. $h_{\max}$) and the corresponding sink-in depth h_s,

$$h_c = h_{\max} - h_s\,, \tag{2.38}$$

where $h_{\max}$ is recorded by the displacement controller and the sink-in depth h_s is calculated by an empirical function $h_s = \epsilon P_{\max}/S$. ϵ is a constant that depends on the geometry of indenter (ϵ = 0.75 for the Berkovich tip), and *S* is the slope of the initial unloading curve during indenter removal. Usually, the upper portion of unloading curve within the load range 70~100% $P_{\max}$ is used to estimate the *S*.

Follow by contact mechanics, the reduced elastic modulus E_r is expressed as

$$E_r = \frac{S\sqrt{\pi}}{2\beta\sqrt{A}}, \tag{2.39}$$

where β is a dimensionless parameter depending on the geometry of the indenter tip. Considering the deformation of both the indenter and sample, elastic modulus of the sample *E* can be converted from the reduced elastic modulus of E_r,

$$\frac{1}{E_r} = \frac{1-v^2}{E} + \frac{(1-v_i^2)}{E_i}, \tag{2.40}$$

where Young's modulus and Poisson's ratio of the diamond indenter (E_i, v_i) are 1141 GPa and 0.07, respectively; and v is the Poisson's ratio of the sample to test.

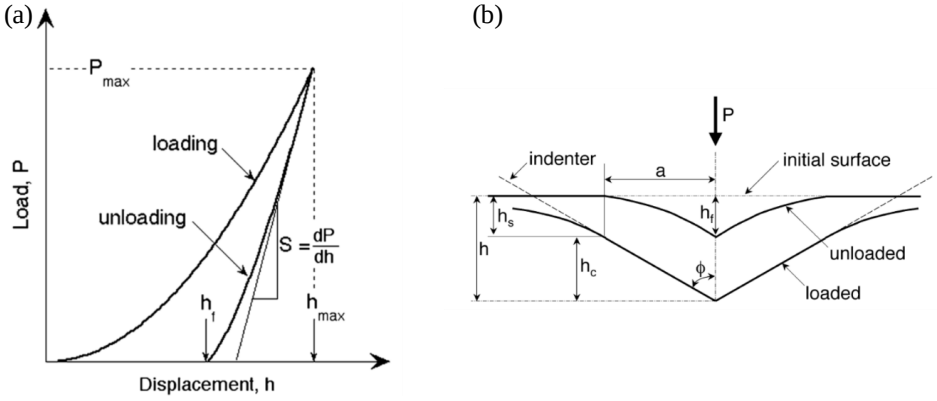

Figure 2.2. Schematics of (a) the load–displacement curve from an indentation and (b) the unloading process and the contact geometry [126].

2.2.2 Fracture toughness

Fracture toughness K_c is a property representing the ability of a material to resist fracture, and is one of the most important material properties for many design applications. In fracture mechanics, K_c is defined as the magnitude of the stress intensity factor at the point of crack extension [127], and is typically measured by the crack tip opening displacement (CTOD) test. In CTOD test, the sample is cut with a sharp notch of known length and applied by a load increased during the test until the specimen fails [128]. The stress intensity factor at the time of crack extension (i.e. fracture toughness K_c) can be easily calculated from the applied load, crack length and sample geometry. Although the fracture toughness measurement using CTOD test is simple and efficient, the samples for CTOD test have to be macroscopic in scale, which limits the application of this method on the measurement for the samples with a small characteristic size such as the thin films or particles. Nanoindentation is now widely accepted as a novel tool for measuring the fracture toughness at a small scale (micro- to nano-scale). During the indentation of elastic/plastic materials, the sharp indenter penetrates into the materials, inducing a field of stress below the loading zone [129, 130]. It has been proved that the high stress singularity at the corners of indents may initiate the radial cracks, Figure 2.3a, and the lengths of the surface traces of the radial cracks correlate with the fracture toughness of the testing material. By implementing the indentation induced stress field into the standard fracture mechanics analysis, fracture toughness K_c can be expressed from a combination of the modulus, hardness, applied load and radial crack length,

$$K_c = \alpha \left(\frac{E}{H}\right)^{\frac{1}{2}} \left(\frac{P}{c^{\frac{3}{2}}}\right), \tag{2.41}$$

where α is an empirical constant depending on the geometry of the indenter (0.036 for cube corner indenter). The E and H are elastic modulus and hardness measured from the Oliver-Pharr method

described in Chapter 2.2.1. The fracture toughness K_c can be determined by simply measuring the length of radial cracks c.

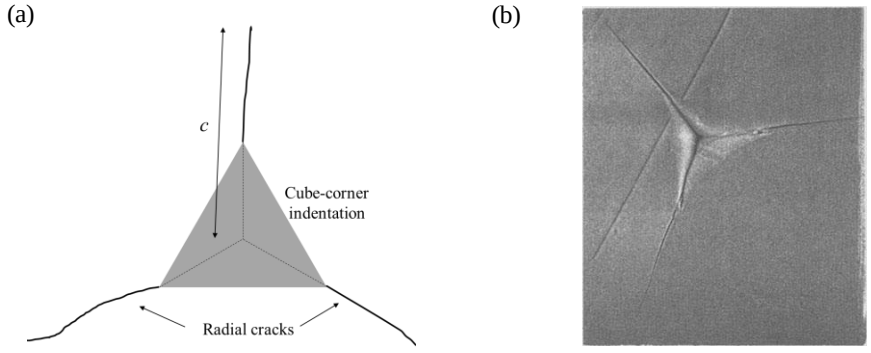

Figure 2.3. (a) Schematic illustration and (b) SEM images of indentation with radial cracks induced by a cube-corner indenter [131].

In the fracture toughness measurement, a cube-corner indenter with a sharp semiapex angle (apical face angle 35.3°) is usually used to initiate the radial cracks at a low applied load. As presented by a prior study, the cube corner indenter displaces more than 3 times the volume of the Berkovich indenter, and thus produces much higher stresses to initiate the crack [131]. Therefore, the cracking load for a material can be significantly reduced by using a cube-corner indenter (around 0.5 grams for most brittle materials), enabling the fracture toughness measurement for the samples with a small characteristic size. Another merit from the indentation cracking method is that no special sample geometry is required, which saves the time and cost for the fracture toughness measurement.

If the sample size is very small, the indentation load should be limited at a sufficiently low level, presumably producing the cracks that are short and difficult to measure by conventional methods such as optical microscopy and electron microscopy, Figure 2.3b. However, the initiation of radial cracks at low indentation load can be still detected by a sharp increase of penetration

depth in the load-displacement curve, referred as a "pop-in" [132]. Pop-in appears to occur when a median crack is nucleated at the boundary of the plastic zone immediately below the point of contact of the indenter. This is followed by immediate propagation upward to join with existing, or lead to the formation of, radial cracks at the surface. The pop-in event is associated with a change of crack morphology such that the pop-in length can be used to estimate the length of indentation-induced radial crack [132],

$$c = \sqrt{2h_m} + \left(Q\frac{E}{H} - \sqrt{2}\right)h_x, \tag{2.42}$$

where Q is a material-independent constant of 4.55; h_x is the pop-in length obtained from the relation $h_x = h_m - h_t$; h_m is the penetration of indentation with pop-in and h_t is the anticipated penetration in the hypothetical absence of pop-in; The values of h_m and h_t can be easily obtained from the load-displacement curve of indentation tests, as shown in Figure 2.4.

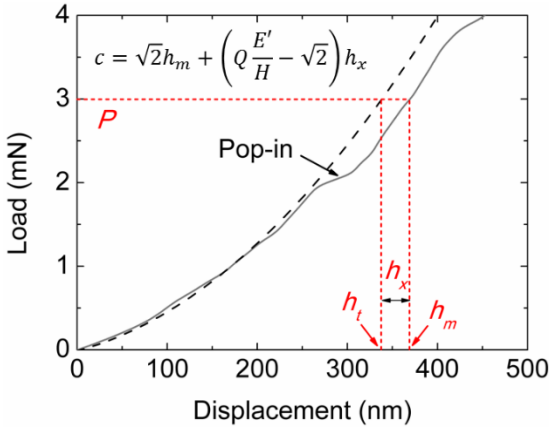

Figure 2.4. Load-displacement curve showing the pop-in event and the h_x, h_m, h_t and P in the calculation of K_c [133].

3. MECHANICAL INTERACTIONS REGULATED KINETICS AND MORPHOLOGY OF COMPOSITE ELECTRODES IN LI-ION BATTERIES

3.1 Introduction

Li-ion batteries are a key technology for portable electronics and electric vehicles [10, 12, 15]. The demand of light-weight, high-energy-density batteries has stimulated tremendous efforts from virtually all engineering disciplines. Mechanical degradation has become a limiting factor for the commercialization of high-capacity electrodes [60, 61]. Such effects are exemplified in high-capacity anodes and Li-rich cathodes – large volumetric swelling and shrinking ranging from tens of percent to a few hundred percent occurs repetitively during the charge and discharge cycles [134]. Averting the mechanical degradation remains one of the major challenges for the development of high-performance batteries. On the frontier of mechanics, the kinetics of diffusive and interfacial reactions in the electrodes induces a wealth of intriguing phenomena, including cavitation [135], reactive plasticity [136, 137] and corrosive fracture [72]. The electrochemical processes of Li insertion and extractions modulate large deformation and stress generation in the electrodes. Meanwhile, mechanical stresses significantly influence the thermodynamics and kinetics of lithiation reactions, ion diffusion, and phase transitions [65, 96, 138].

Numerical modeling is a common exercise to study the evolution of Li diffusion and the stress field in Li-ion batteries. However, prior research has been extensively focused on single particles or two-dimensional structures [32, 80, 82, 139, 140]. Bower and Guduru developed a finite element method to model diffusion, large deformation, and fracture [92], and the method was applied for a thin-film Si electrode [111]. Brassart et al. developed a finite element program to model the cyclic behavior of single spherical particles [141]; similar approach was adopted by

Cui et al. [142]. An and Jiang reported a numerical implement in finite element package ABAQUS, and studied the failure mechanism in Si thin film bonded to a metal current collector [143]. Stein and Xu used isogeometric analysis to model the mechanical behaviors of single particles with different shapes [144]. Yang et al. recently developed a finite element program by manipulating the stress effect on Li diffusivity, and studied the lithiation behavior of Si nanowires [69, 145]. There are a few attempts in recent studies that incorporate a secondary component in the material model. Higa et al. simulated stresses in a two-dimensional cylindrical model that consists of a well-bonded binder with a cylindrical particle [146]. Rahani et al. studied the role of plastic deformation of binders on the stress evolution in the distributed spherical particles in a porous electrode by using a two-dimensional microstructural resolved model [147]. Nevertheless, the mechanical interactions among the different components and the stress effect on Li transport have not been considered. There has been a lack of computation tools to investigate the fully coupled diffusion and stress in three-dimensional composite configurations. Herein, a finite element program based on a continuum theory of coupled diffusion and large elasto-plastic deformation is developed. It enables people to model the complex behaviors of three-dimensional objects that are composed of multiple components and to explore the kinetics and morphological evolution of composite electrodes coupled with the mechanical interactions.

As pointed out by a recent experimental study on Si nanowires, lithiation often occurs simultaneously in a cluster of active materials in a mechanically confined medium [100]. The mechanical interactions among the individual Si structures in the closed space alter the reaction mechanisms along the various crystallographic orientations and enhance the fracture resistance of lithiated Si by mediating the stress concentrations. Indeed, distinct from the simplified single-particle or free-standing models, a battery electrode usually consists of multiple components with

a large variation of mechanical properties [102]. The different components interact with each other during lithiation reactions and raise a complex field of stresses. It is demonstrated that single-particle models are unable to capture the mechanical behaviors of a composite electrode due to the strong coupling between Li transport and stresses. In a model of multiple particles embedded in a matrix, it is found that Li profiles and the stress field are highly asymmetric due to the matrix confinement and particle interactions. In another example of multiple Si nanowires in a confined space, the mechanical stress regulates the Li chemical potential, redistributes the Li concentration, and transforms the anisotropic deformation of nanowires to an isotropic behavior and *vice versa*. Such findings are in good agreement with the experimental report [100].

3.2 Li diffusion and stresses in particle/matrix composite electrodes

As the first attempt to model the composite electrodes, three-dimensional material models consisting of two components – active and inactive materials is considered, where Li diffusion only occurs in the active material while the inactive material provides mechanical confinement. This is an assumption based on the fact that the kinetics in batteries is often limited by the diffusion in the active materials while Li transport through the porous matrix is usually a faster process. In the reference state, both components are free of Li and stresses. Lithiation is induced by imposing a nominal influx J_0 of Li on the surface of the active material. The concurrent diffusion and large elasto-plastic deformation is described by a previous developed theory in Chapter 2.1.

Three sets of material models are simulated to assess the effect of mechanical interactions on the co-evolution of Li diffusion and the stress field – a single free-standing particle, a particle embedded in a matrix, and multiple particles confined in a matrix. Amorphous Si is taken as the model system for the active material and typical polymer binders are taken as an example of inactive matrix. The radius of Si spherical particles is set to be A=1 μm. The size of the matrix and

the spacing between the particles are varied to tune the mechanical interactions. The material parameters are adopted as follows. For Si particles, Young's modulus E_P=80 GPa, Poisson's ratio υ_P=0.3, yield strength σ_Y=0.5 GPa, Li diffusivity D=10^{-16} m^2/s, partial molar volume of Li in Si Ω=1.36×10^{-29} m^3, and temperature T=300 K [90, 101, 148]. It is worth noting that Young's modulus, yield strength, and Li diffusivity of lithiated Si may depend on the Li composition. Here the material parameters are considered as constants to reduce the complexity of the modeling. For the matrix, Poisson's ratio υ_M=0.3, and Young's modulus E_M are varied in the range of 260 MPa to 2.6 GPa. The volumetric strain of Si upon full lithiation is about 300% which sets the relationship ΩC_{max}=3, where C_{max} represents the maximum Li concentration. The charging time to reach the theoretical capacity of Si is set to be τ =1 h. The nominal flux J_0 is then determined through the relationship $4\pi A^2 J_0 \tau = (4\pi A^3/3) C_{max}$. At the charging rate τ =1 h, $J_0 = 2.8D/A\Omega$. Li insertion is terminated when the concentration on particle surface reaches C_{max}.

Single free-standing particles have been examined in several past studies which often treat a spherical particle as a one-dimensional model by taking into account the symmetry. A full three-dimensional spherical model is used to verify the finite element program and to demonstrate the different features of single particles versus composite configurations. Figure 3.1a and b show the distribution of Li concentration and the corresponding equivalent stress along the radius of the Si particle at the normalized charging time $\bar{t} = Dt / A^2$. The chemical potential of Li in the particle drives Li diffusion from the surface toward the center. At a fast charging rate relative to the diffusion rate of Li, the particle expands more near the surface than at the center, resulting in a compressive stress field near the surface and a tensile stress field at the center. For the spherical particle, the equivalent stress is $\sigma_e = |\sigma_\theta - \sigma_r|$, which is bounded in the interval $0 \le \sigma_e \le \sigma_Y$. Figure 3.1b shows the evolution of the equivalent stress. The gradient of the mean stress promotes Li

diffusion toward the center and tends to homogenize the Li distribution. Such a homogenization effect consequently reduces the stresses and induces elastic unloading in the plastic regime. As evident in the Figure 3.1b, the spherical particle experiences plastic yielding and elastic unloading in the course of Li insertion. The results are compared with that from a previous study by Brassart et al. which used one-dimensional finite element formulation [141]. The Li profiles and stress states at each time step are in excellent agreement.

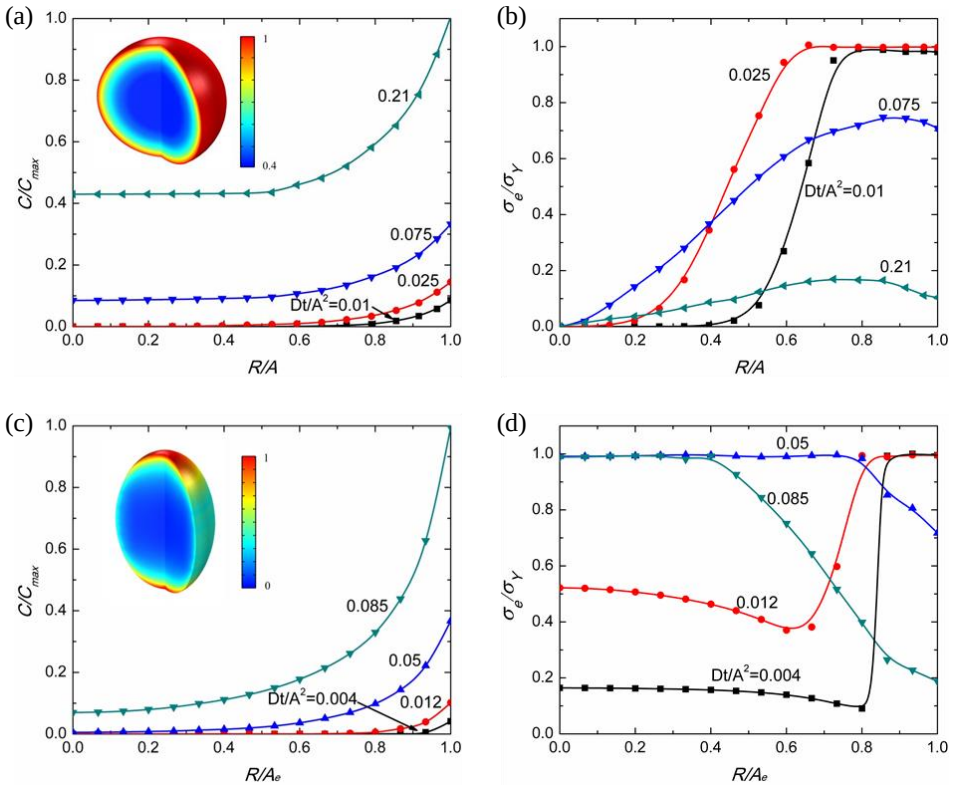

Figure 3.1. (a) Distribution of Li concentration along the radius of a three-dimensional spherical Si particle under the lithiation rate τ=1 h, (b) The corresponding evolution of the equivalent stress. The particle experiences plastic yielding and elastic unloading in the course of Li insertion. (c) Distribution of Li concentration along the semi-major axis of a three-dimensional elliptical Si particle, (d) The corresponding evolution of the equivalent stress. The elasto-plastic behavior is distinct from that of spherical particles due to the geometric asymmetry.

For comparison, the lithiation behavior of an elliptical Si particle is also studied to demonstrate the geometric effect. The two semi-minor radii of the ellipse are set as A and the semi-major radius being $A_e=1.5A$. The charging time to reach the theoretical capacity remains t=1 h. Figure 3.1c shows the distribution of Li concentration along the semi-major axis. The Li profile is inhomogeneous within the elliptical particle as indicated by the inset figure of Figure 3.1c – the area near the end of the semi-major axis is fully lithiated in a short time while other regimes remain at fairly low Li concentrations. Such inhomogeneity is dominated by the geometric effect that the uniform influx J_0 leads to a larger Li concentration near the semi-major axis which has a smaller effective radius. The geometric asymmetry also results in different elasto-plastic behaviors. The center of the elliptical particle is subjected to non-hydrostatic stresses. Figure 3.1d plots the evolution of the equivalent stress. The equivalent stress at the center steadily increases until it reaches the yield strength. The outer shell experiences plastic yielding and then elastic unloading due to the homogenization effect of the stress gradient to the Li distribution.

The diffusion kinetics in composite electrodes coupled with the mechanical interactions has not been explored in prior studies. A simple case that a spherical particle is embedded in a matrix are considered here to demonstrate the distinct behaviors of composite structures versus the single particles. It is noted that the material models considered here are yet to be close to the real configurations in commercial batteries, however, the examples can be used to uncover the elementary coupling between the lithiation kinetics and mechanical stresses in three-dimensional structures. Figure 3.2a sketches the different elasto-plastic behaviors of a spherical particle embedded in a matrix of different stiffness and of different boundary conditions. For a single free-standing Si particle, Figure 3.1d shows that the outer shell experiences a transition of plastic yielding to elastic unloading while the center remains elastic. Such a behavior is expected for a

spherical particle embedded in a sufficiently compliant matrix of free boundary conditions. When the stiffness of the matrix increases, the matrix imposes a strong mechanical constraint to the deformation of the particle. The constraint imposes a hydrostatic stress to the center of the particle. However, for the outer shell, the compressive stress induced by the matrix may override the stress relaxation caused by the homogenization of Li distribution and lead to a permanent plastic deformation. The stress evolution will be altered by prescribing a periodic boundary condition (P. B. C) along the horizontal direction as if the interactions between the particles are considered. The simultaneous swelling of the neighboring particles in the confined space results in a non-hydrostatic stress field that effectively promotes the plastic yielding of the particles. As a result, the entire particle will reach plasticity progressively from the surface toward the center during the Li insertion. Figure 3.2b shows an example of the equivalent stresses for E_M/E_P= 0.032 and $2A/L$=0.67. The mechanical interactions are dependent on the stiffness ratio E_M/E_P and the size ratio $2A/L$ between the matrix and the particle. For a particle-matrix composite of small values of E_M/E_P and $2A/L$, the elasto-plastic behavior reduces to that of a single free-standing particle.

For the composite electrodes in batteries, mechanical failure often occurs by the structural disintegration due to the fracture of the conductive matrix or interfacial debonding between the active material and the matrix. Such failure mechanisms may be dictated by the tensile and shear stresses in the matrix. Figure 3.2c shows the profiles of the maximum tensile and shear stresses in the matrix as a function of $2A/L$ at the time that the particle is fully lithiated. It is found that the maximum stresses in the matrix are always located near the particle/matrix interface during lithiation. The tensile stress may cause fracture of the matrix initiated from the interface, and the shear stress may cause the interfacial debonding between the particles and the matrix. Figure 3.2c shows that, for $2A/L$=0.71, the maximum tensile and shear stresses in the matrix reach peak values,

which are on the same magnitude of the yield strength of the active particle. Such large stresses are hardly sustainable for the polymer matrix.

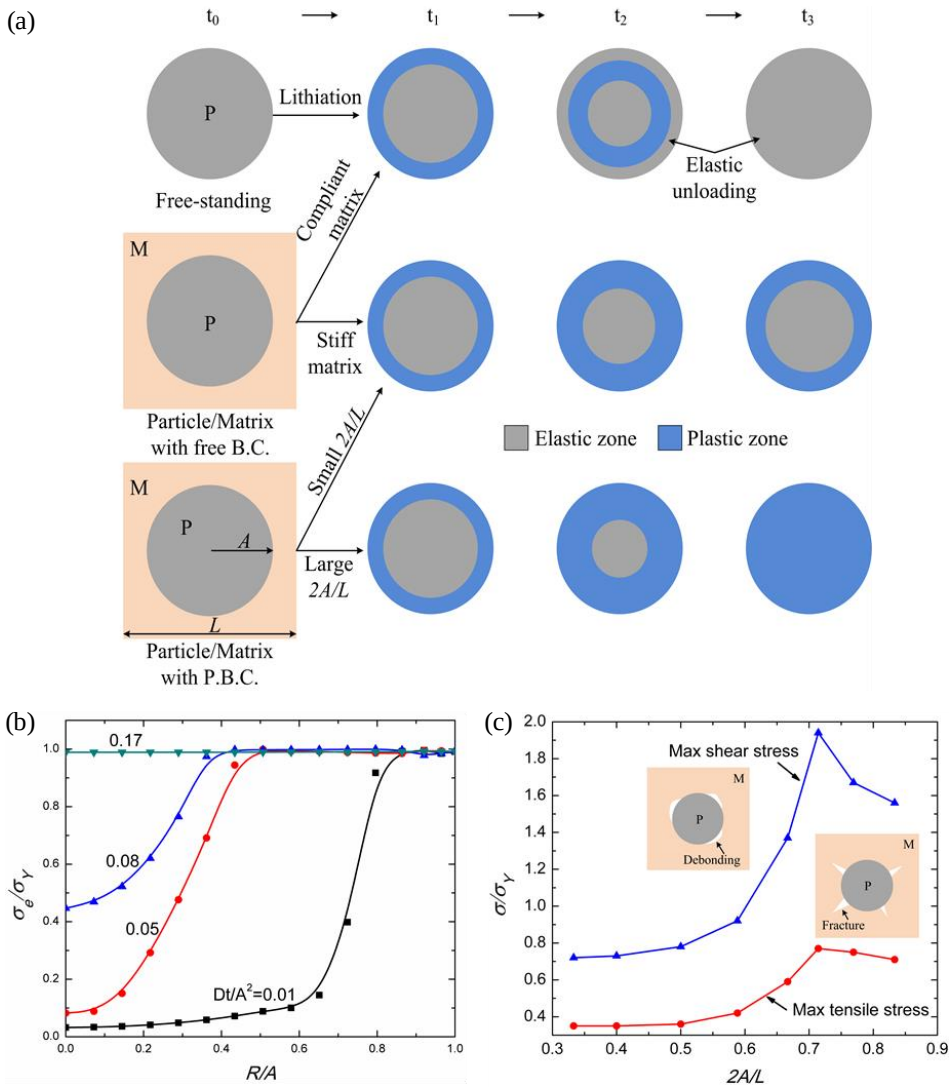

Figure 3.2. (a) Schematic of the stress evolution in a single free-standing particle versus a particle embedded in a matrix of different stiffness and under different boundary conditions. The particle is subjected to a constant charging rate. (b) Evolution of the equivalent stress in a particle embedded in a matrix of stiffness E_M/E_P= 0.032. The size ratio is $2A/L$=0.67. Periodic boundary condition is applied along the horizontal direction. The charging rate is τ= 1 h. (c) The profile of the maximum tensile and shear stresses in the matrix as a function of $2A/L$. The particle is at the fully charged state. The tensile stress may cause fracture of the matrix, and the shear stress may cause interfacial debonding between the particle and the matrix.

In the next example, multiple particles embedded in a matrix is considered to demonstrate the inhomogeneity of Li distribution regulated by the mechanical stresses. Figure 3.3a shows three particles of a relatively large spacing in between. Li concentration shows a homogeneous distribution as there are minor mechanical interactions between the particles. As the particle distance decreases, Figure 3.3b, a highly asymmetric stress field develops in the particles which consequently redistributes the Li concentrations. The largest compressive stress occurs at the point in a particle of the shortest distance to the neighboring particles, so does the Li chemical potential. The variation of the Li chemical potential depends on the magnitude of the local compressive stress. Li atoms are then accumulated in the region of the lowest Li chemical potential. $C_{\min}/C_{\max}$ is used to dictate the inhomogeneity of Li distribution, where $C_{\min}$ represents the minimum Li concentration on the surface of the particle at the fully lithiated state. The inhomogeneity quantity depends on a set of dimensionless parameters $\left(A/L,\ E_{\mathrm{M}}/E_{\mathrm{P}}, L^2/D\tau, t/\tau\right)$, where A/L, $E_{\mathrm{M}}/E_{\mathrm{P}}$, $L^2/D\tau$ and t/τ represent the normalized particle spacing, matrix stiffness, charging rate, and charging time, respectively. Through parametric studies, the inhomogeneity can be obtained in terms of E_M/E_P and A/L, as shown in Figure 3.3c. As expected, for the small values of E_M/E_P and A/L, the particles approach to a homogeneous lithiation. In the other limit of large E_M/E_P and A/L, the effect of the mechanical interactions on the Li distribution becomes dominant and the Li profiles are highly inhomogeneous. In this case, insertion of Li is blocked by the local high compressive stress that significantly reduces the effective capacity of the Si particles. It shows the fact that the capacity of the composite electrodes is not linearly scaled with the mass of the active materials but is rather limited by the inhomogeneous storage of Li.

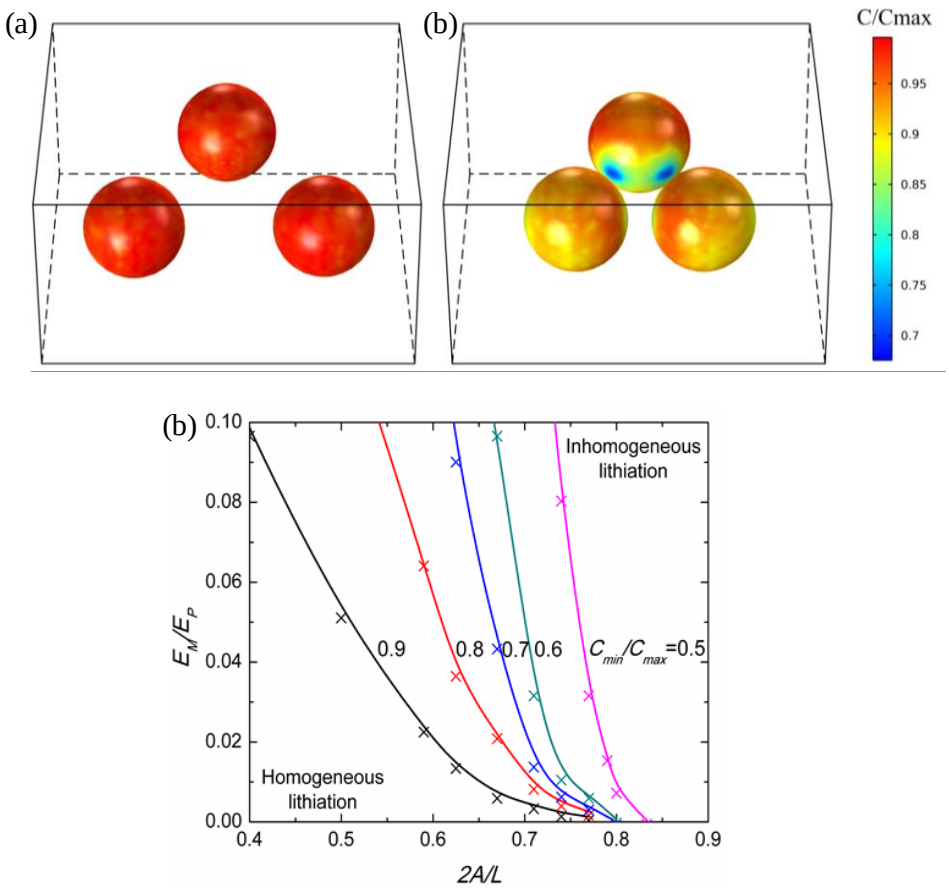

Figure 3.3. (a) The homogeneous distribution of Li concentration in three particles with a relatively large space in between. (b) The highly inhomogeneous distribution of Li concentration due to the mechanical interactions between particles when they are close. (c) The inhomogeneity of Li concentration distribution in terms of non-dimensional quantities E_M/E_P and $2A/L$.

3.3 Lithiation of Si nanowires

The mechanical degradation of high-capacity electrodes motivated researchers to seek solutions from the nanotechnology, which has enabled low-cost, fast fabrications of nanostructured materials with nanoscale controls on the size, shape, and chemical compositions. As the characteristic size of the electrode materials scales down to the nanometer range, it can mitigate mechanical degradation through manipulating the deformation pattern. Furthermore, the small feature size enables flaw tolerance, facilitates ion and electron conduction, and promotes the rate capability by increasing the surface area of the electrodes to react with Li. Nanoelectrodes of

different geometrical shapes have been assessed in a variety of electrodes, including nanowires [51], nanotubes [149], thin films [44], and nanoparticles [150]. The finite element program is employed to model the lithiation behavior of nanowires which have shown a great promise for the commercialization of Si electrodes. Two example systems are studied – a single amorphous Si nanowire as well as a cluster of crystalline Si nanowires both lithiated in a confined space. The goal is to demonstrate the mechanical stresses regulated lithiation kinetics and morphological evolution of the nanowires, that is, the local contact force drives Li flux and dynamically changes the composition in the contact area and therefore modulates the deformation behavior. Understanding such a coupling effect is significant for the design of nanostructures to reach the optimum capacity and for the assessment of the mechanical performance of the electrodes.

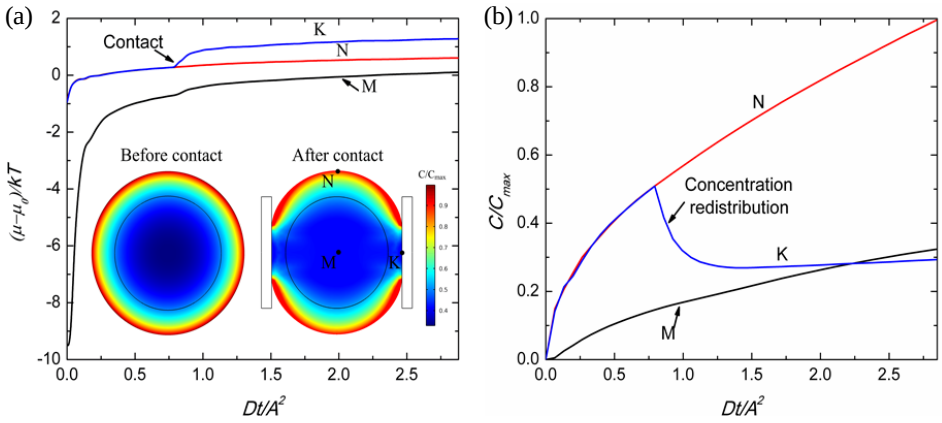

Figure 3.4. The morphological evolution of a single amorphous Si nanowire regulated by the contact force. The compressive force between the nanowire and the rigid wall modulates the Li chemical potential and distribution of Li concentration, and thus transfer the isotropic deformation to an anisotropic behavior. (a) The distribution of Li chemical potential at different locations, marked by M, N, and K, before and after the Si nanowire contacts the rigid wall. (b) The evolution of Li profiles at the different locations. The contact force at K redistributes the Li concentration and leads to the anisotropic deformation.

The lithiation-induced deformation in an amorphous Si nanowire is confined by the side rigid walls by the mechanical contact. The radius of the nanowire is 275 nm. Figure 3.4a and b

show the distributions of Li chemical potential and Li concentrations at the different locations, marked by M, N, and K, as a function of the charging time. In Figure 3.4a, the jump in the Li chemical potential at K indicates the initial contact of the nanowire with the rigid wall. The confinement generates a large local compressive stress and drastically alters the profile of the Li chemical potential as shown in Figure 3.4a. The local contact force drives Li flux away from the stressed area. Li concentration at K gradually decreases until it reaches a steady state as shown in Figure 3.4b. This behavior infers that any contact forces, such as the mechanical load in the indentation experiments, may dynamically change the local composition at the measured regime. In order to accurately map the Li profile and the mechanical properties, one needs to consider the dynamic nature of Li diffusion, the stress-relaxation mechanisms in the electrodes, as well as the magnitude of the local forces. The morphological evolution is associated with the redistribution of Li concentrations. The contact force transfers the isotropic deformation of an amorphous nanowire to an anisotropic behavior, as shown in the inset figures of Figure 3.4a.

The lithiation mechanism of crystalline Si is different from that of amorphous Si. The reaction front separating the crystalline Si and lithiated amorphous phase is atomically sharp which is indicative of distinction from the diffusive behavior. The rate of lithiation in crystalline Si is limited by the short-range processes of interfacial reactions and the deformation is governed by the concurrent reaction and plasticity [94]. The sharp interface is simulated by adopting a step function of Li diffusivity $D_L/D_C=10^4$, where D_L represents Li diffusivity in the lithiated phase, and D_C the diffusivity in the pristine core. Meanwhile a constant velocity V is prescribed to the step function along the radial direction of the Si nanowire to represent the propagation of the reaction front. Since the reaction rates along various crystallographic orientations are different, the reaction rates along the <110> and <100> direction are set as $V_{110}/V_{100}=5$ [151]. It is worth noting that such

a numerical approach is not aiming to incorporating a physical model on the short-range processes of bond switching, instead it serves as a means to model the kinetics of lithiation that is limited at the reaction front. The anisotropic deformation of a single crystalline nanowire and the movement of the sharp interface in the course of lithiation are shown in Figure 3.5a. The corresponding Li profiles at different charging time are plotted in Figure 3.5b.

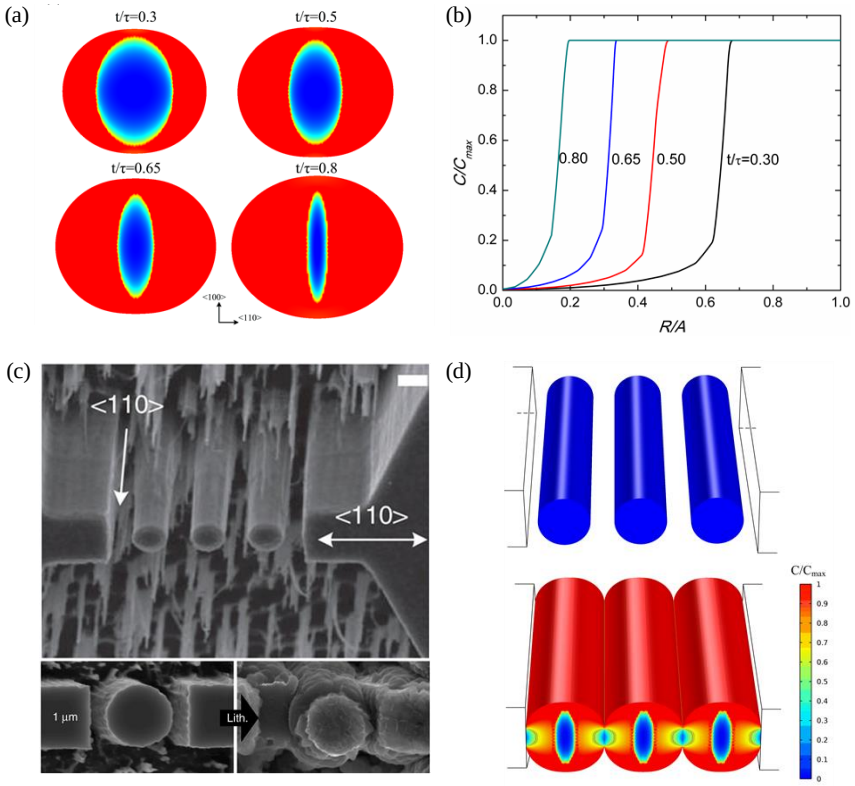

Figure 3.5. The morphological evolution of a single crystalline Si nanowire versus multiple nanowires. (a) The anisotropic deformation of a single crystalline nanowire induced by the concurrent interfacial reaction and plasticity. The propagation of the sharp lithiation front is simulated by setting $V_{110}/V_{100}=5$ and $D_L/D_C=10^4$. (b) The corresponding Li profiles at different charging time. (c) An experimental study of multiple nanowires shows that the mechanical interactions regulate the kinetics of lithiation and morphological evolution of the nanowires [100]. (d) Finite element simulations on the experimental setting capture the transition from the anisotropic deformation to an isotropic behavior due to the stress effect.

Next lithiation of a cluster of Si nanowires - three crystalline nanowires confined by rigid walls is simulated to compare with the recent experimental study. Figure 3.5c reproduces the experimental figure that the mechanical interactions among the individual nanowires and the confined medium regulate the morphological evolution of the nanowires [100]. The numerical results shown in Figure 3.5d are in excellent agreement with the experimental finding. The contact forces transfer the anisotropic deformation of crystalline nanowires to an isotropic behavior due to the redistribution of Li concentrations. Such transition mitigates the stress concentrations in single nanowires and thus results in a higher fracture resistance in the cluster of nanowires.

3.4 Conclusions

A finite element program based on a theory of coupled diffusion and large elasto-plastic deformation is developed. The program enables people to model the chemomechanical behaviors of three-dimensional composite electrodes and to explore the intimate coupling between the lithiation kinetics and mechanical stresses. It is found that the Li profiles and stress states in multiple particles constrained by a matrix are significantly different from that in a free-standing configuration. The capacity and stresses of the composite electrodes can be optimally designed by tuning the size, shape, and pattern of the active particles, as well as the stiffness, geometry, and porosity of the matrix. The mechanical interactions regulate Li chemical potential in Si nanowires and transform the isotropic deformation to an anisotropic behavior and vice versa. The modeling highlights the strong coupling between the electrochemistry of lithiation and mechanical stresses in the composite electrodes and provides important insight on the design of resilient Li-ion batteries.

4. COMPUTATIONAL ANALYSIS OF CHEMOMECHANICAL BEHAVIORS OF COMPOSITE ELECTRODES IN LI-ION BATTERIES

4.1 Introduction

Li-ion batteries are the major power source in portable electronics and electric vehicles [152, 153]. Innovation in the battery technology has been driven by the imperative demand of materials of light weight, high energy density, fast charging, long lifespan, and low cost [4, 10, 154]. Mechanical degradation of batteries caused by the repetitive swelling and shrinking of electrodes in the lithiation cycles is now well recognized [60, 155]. The stress induced structural disintegration impedes electron conduction and causes persistent loss of capacity of batteries in the long-term cycles. In particular, the mechanical failure has become the bottleneck in the commercialization of high-capacity electrodes because of the massive volumetric deformation associated with the electrochemical processes. Figure 1.4 gives a brief survey of the volumetric strain of different types of cathode and anode materials. It is evident that drastic deformation is inherent to the high-capacity electrodes, such as S cathode as well as conversion and insertion type anodes [79, 156-158]. The repetitive volumetric change in the active materials generates a complex field of stresses in the electrodes and leads to various sources of mechanical degradation including fracture [34, 39, 94], plasticity [31, 65, 141] and cavitation [135, 159].

While mechanical failure of batteries is frequently observed, maybe less understood is the impact of stresses on the electrochemical processes, that is, how the locally generated stresses modify the energy landscape and kinetics of Li transport, interfacial reactions, and hence the capacity and potential of batteries [65, 96, 138, 160]. Developing continuum models and numerical methods for the coupled Li diffusion and large deformation has been a topic of intense interests in

the past few years, especially for the application of Si anode [32, 58, 80, 82, 89, 92, 139, 140, 145]. Nevertheless, most of prior research has been focused on idealized structures of single, isolated particles or two-dimensional structures. In commercial batteries, both the cathode and anode are composites of high heterogeneity at the nano- to microscale. A composite electrode is usually consisted of active particles of different sizes and irregular shapes, a matrix composed of polymer binders and additives, and pores filled with the electrolyte [102]. The components intimately interact with each other during the lithiation cycles and raise a complex field of stresses within the electrodes. Although the simplified models of single particles are useful to capture the first-order coupling effect between diffusion and stresses, the predictions on Li concentrations, stress field, and mechanical failure from the idealized models can be substantially different from that of the composite configurations. Relying on the techniques of X-ray tomographic microscopy and focused ion beam scanning electron microscope (FIB/SEM), the microstructure of composite electrodes in commercial batteries can be reconstructed with sufficient details and imported into the computational programs such as finite element methods (FEM) and finite volume methods (FVM) [161-163]. Several groups have recently utilized the reconstructed 3D models to simulate the stress generation and electrochemical behaviors in more realistic configurations. The major findings, in comparison with the single-particle models, are as follows. (i) The stress field, Li concentration, and mechanical failure are strongly affected by the local details of the microstructure. (ii) The bicontinuous network of reconstructed particles show significantly higher stresses than that in single isolated particles. (iii) The mechanical properties of binders, particularly the yield stress and elastic modulus, play an important role in determining the average stresses developed in the electrodes [163-167].

Here, 3D composite models of $LiNi_{0.3}Mn_{0.3}Co_{0.3}O_2$ (NMC333, simplified as NMC in the following text) cathode and SnO anode are reconstructed based on extensive X-ray tomographic microscopy data. The models are implemented into a developed finite element program that computes the coupled Li diffusion and stresses. The finite element program is then used to investigate the evolution of the stress field and the mechanical interactions regulated Li distribution and capacity of the electrodes. The state of charge in the active particles is highly inhomogeneous depending on the distribution of the active particles and properties of the matrix. The effective capacity is limited by the inhomogeneous storage of Li and significant capacity loss is possible due to the particles contact and mechanical confinement of the surrounding medium. A map of the specific capacity of the composite electrodes in terms of the volume fraction and volumetric strain of the active particles is constructed. An ample space of optimization on the capacity and mechanical performance of electrodes could be further constructed through tuning the size, shape, and pattern of the active particles, as well as the stiffness, geometry, and porosity of the matrix.

4.2 Numerical modeling

The composite electrodes composed of two general components, active particles which store Li and inactive matrix which provides mechanical confinement to the deformation of the active materials. The inactive matrix is a representation of the effective medium including the polymer binders, conductive agents, and porosity in commercial batteries. The kinetics in batteries is often limited by Li diffusion in the active materials while Li transport through the porous matrix is usually a faster process. Here Li diffusion is considered to only occur in the active material. The continuum theory of coupled diffusion and large elasto-plasticity and its implementation into the finite element program are is described in Chapter 2.1.

4.3 Reconstruction of 3D composite electrodes and statistical analysis

The microstructure of NMC cathode and SnO anode are reconstructed from experimentally segmented images and implement the reconstructed geometries into the finite element computational program. The 2D binarized images for the NMC and SnO electrodes are generously provided by Dr. Martin Ebner from the Wood group at ETH Zurich, who obtained these images using the synchrotron radiation X-ray tomographic microscopy technique, Figure 4.1 [168]. Interested readers may be referred to the open-source database hosted by ETH Zurich which provides the microstructural data for 16 different NMC-based electrodes with various degrees of compositions and morphologies [168, 169]. The 2D binarized images are compiled into Avizo 8.1 (FEI; Hillsboro, OR) to generate the 3D voxel data set in which the active particles and the inactive matrix are separately defined. Relying on the 3D voxel representation, a surface description (surface mesh with triangular grid) for both active particle and inactive particles can be created in Avizo. Default surface meshes are often far too fine for the subsequent operations; The surface mesh is simplified and the major blemishes, such as triangles with poor aspect ratios, intersections, or acute dihedral angles of the surface mesh are corrected, using Avizo's surface editor. Then a volumetric tetrahedral grid can be generated based on the previously created triangular surfaces. The tetrahedral grid mesh is the basis for producing different geometries of the electrode microstructure including the boundary, edges and points, etc. Finally the open-source tool MeshLab is employed to smooth the volumetric tetrahedral grid using the Laplacian Smoothing Filter, and export the smoothed tetrahedral grid mesh in a Standard Tessellation Language (STL) file format that can be imported into the geometry module of COMSOL. The build-in mathematical models in COMSOL are applied to the reconstructed domains.

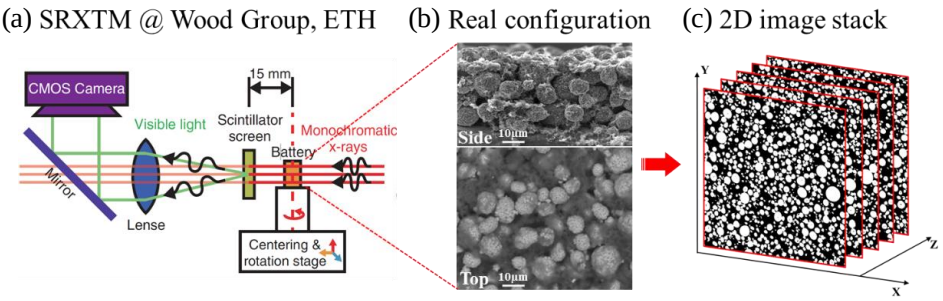

Figure 4.1. X-ray tomography used to obtain the X-ray tomograms of electrodes in Li-ion batteries. (a) Sketch of the x-ray tomography setup [168]. (b) Scanning electron micrograph of NMC cathode (c) 2D binarized tomograms of NMC cathode.

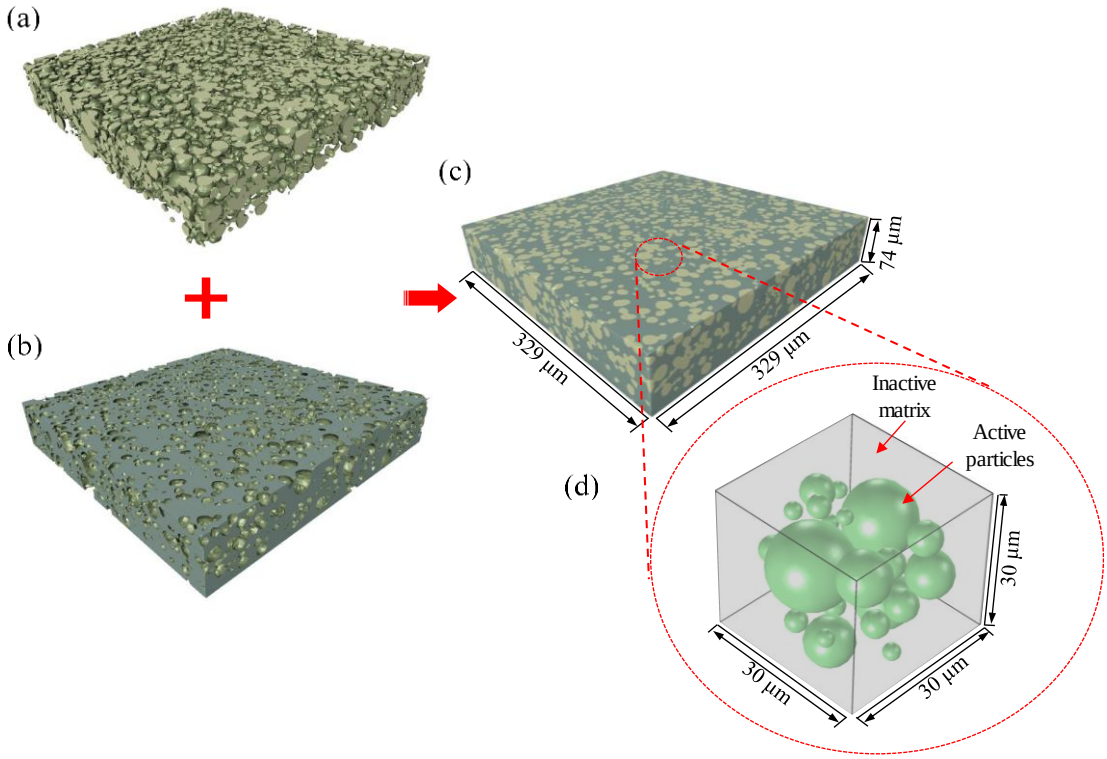

Figure 4.2. Reconstruction of NMC composite electrodes. The electrodes are serial-sectioned and 2D images from each layer are aligned, segmented, and stacked into 3D configurations. (a) Active spheroidal NMC particles. (b) Inactive matrix. (c) Reconstructed NMC electrodes composed of active particles and inactive matrix. (329×329×74 μm^3). (d) Representative volume element (RVE) of the reconstructed NMC electrode (30×30×30 μm^3), where the green spheres represent the active materials and the grey medium represents the inactive components. Li diffuse in the active particles and the surrounding matrix provides mechanical confinement to the deformation of the active materials.

Figure 4.2a-c show the active spheroidal NMC particles, the inactive matrix, and the reconstructed NMC electrode, respectively. The NMC electrode is reconstructed by Avizo 8.1 (FEI; Hillsboro, OR) based on a stack of 8-bit black and white binarized images of 889×889 pixels in which each of pixel size is 0.37 μm. The total volume of the reconstructed electrode is 329×329×74 μm^3. Statistics analysis on the particle size distribution and particle distances is performed for the entire NMC electrode and is used to create the representative volume element (RVE). The RVE is a volume of heterogeneous objects representative to the geometric features of the entire electrode and affords the balance between the computational cost and statistical accuracy [170, 171]. For NMC, the particles are spherical in nature as is observed in the majority of the particles of the reconstructed electrode (7752 particles). Therefore, a RVE with the size of 30×30×30 μm^3 that contains 27 spherical particles is built, Figure 4.2d. The coordinate of the center of NMC particles as well as their radius are extracted from a local volume of the reconstructed NMC electrode, Figure 4.2c. This information is then used as the input to build the RVE with spherical NMC particles. As stated earlier, the details of the microstructure determine the stress field and the electrochemical behaviors of the composite electrodes. The statistical features of the RVE versus the entire reconstructed volume are carefully compared. Figure 4.3a shows the particle size distribution. The probability is calculated by the sum of the volumes of the particles within a given size interval divided by the total volume of all the particles. Figure 4.3b and c show the distance (surface to surface) of the nearest neighbors and the average and standard deviation of the distance from the 1^{st}, 2^{nd}, and 3^{rd} neighbors for individual particles, respectively. The statistical analysis of the RVE for the NMC electrode compressed by 2000 bar after fabrication is shown in Figure 4.4. In addition, Table 4.1 provides further information on the volume fraction of the active particles V_f, the average diameter of the particles A, as well as the number of particles

in the RVEs of uncompressed/compressed samples. The selected RVEs indeed show the same statistical features of the entire NMC electrodes and thus are representative to microstructure of the composite electrodes.

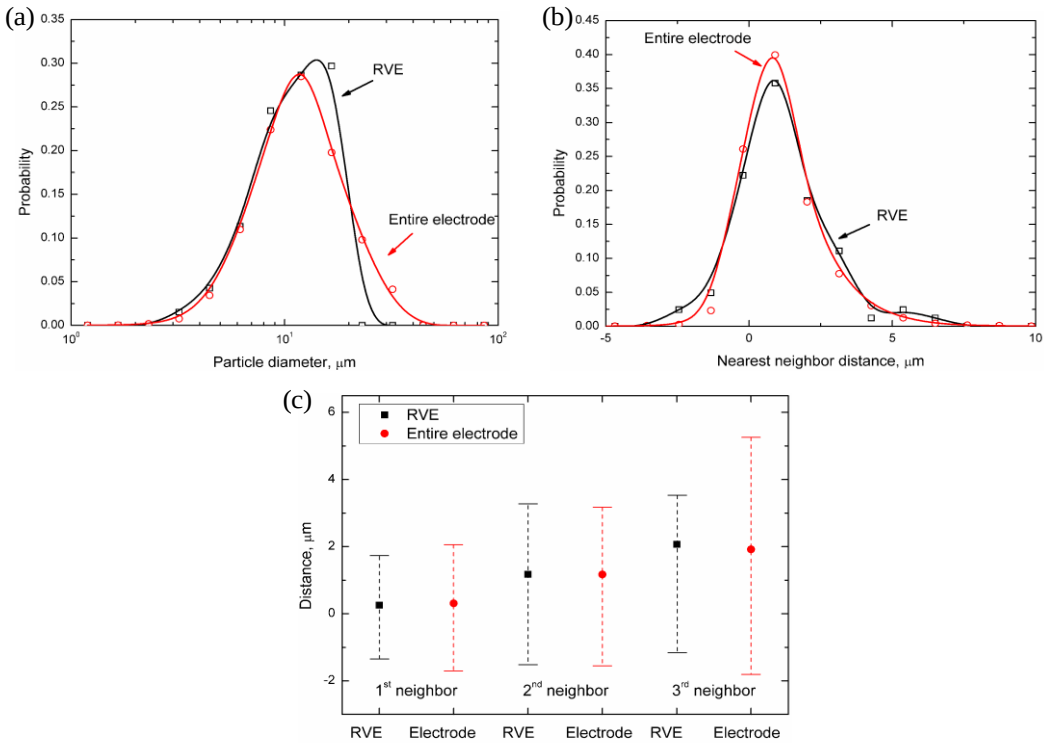

Figure 4.3. Statistical analysis of RVE in comparison with the entire NMC electrode. (a) Particle size distribution. (b) Probability distribution of the distance from the nearest neighbor for individual particles. (c) The average and standard deviation of the distance from the 1st, 2nd, and 3rd neighbors for individual particles in the RVE and reconstructed NMC electrodes.

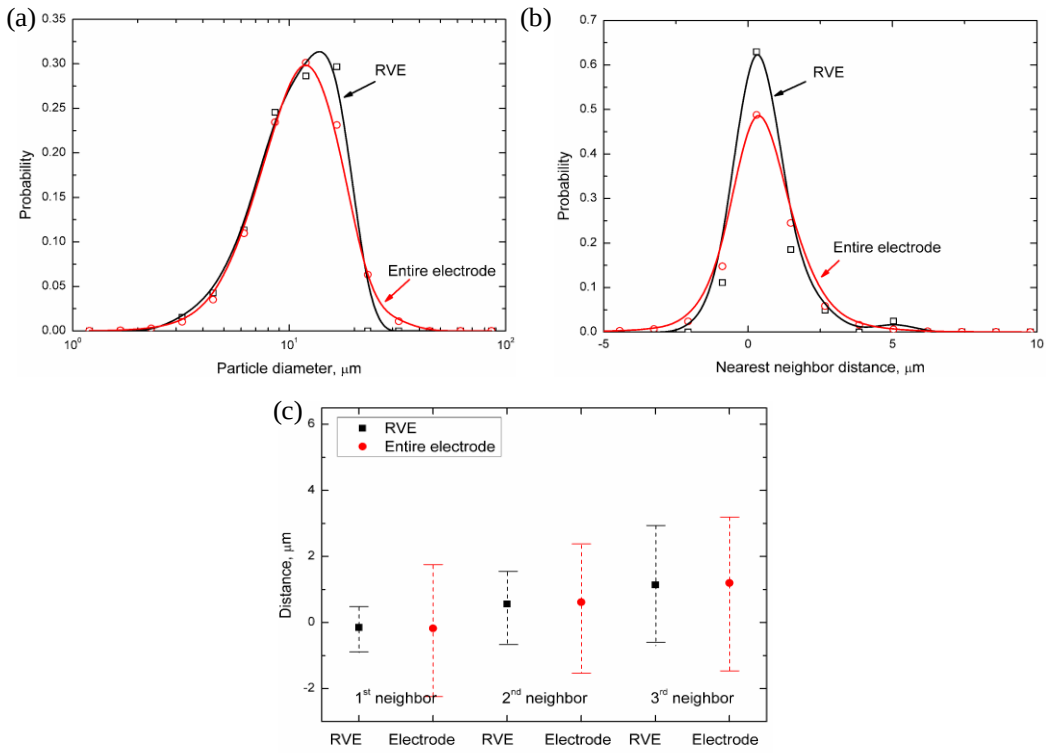

Figure 4.4. Statistical analysis of (a) particle size distribution, (b) distance between the nearest neighboring particles, and (c) distance from the 1st, 2nd, and 3rd neighbor for individual particles in the RVE of compressed NMC electrodes and reconstructed compressed NMC electrodes.

Table 4.1. Statistic data for the NMC electrodes and RVEs.

	Uncompressed RVE	Uncompressed NMC electrode	Compressed RVE	Compressed NMC electrode
Volume fraction V_f, %	27.03	26.85	38.74	38.62
Average radius A, μm	3.08	3.03	3.08	2.78
Number of particles	27	7752	27	13993

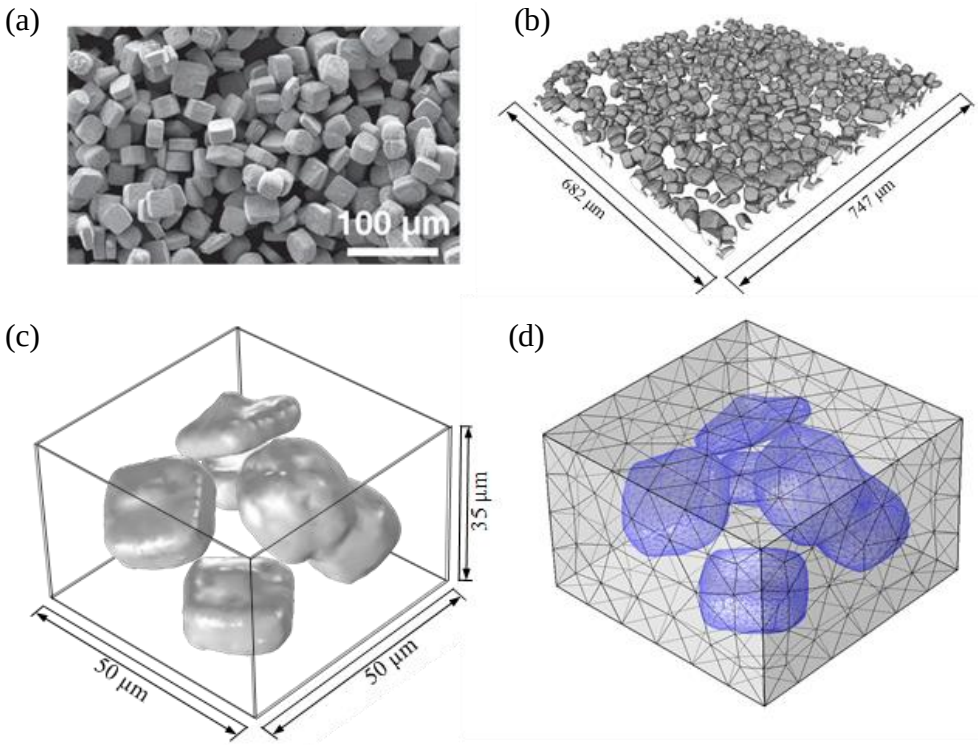

Figure 4.5. Reconstruction of SnO composite electrodes. (a) SEM image of SnO particles [168]. (b) 3D visualization of reconstructed SnO particles (682×747×85 μm^3). (c) RVE of the reconstructed SnO electrode (50×50×35 μm^3). (d) Mesh of the SnO RVE after surface smoothing.

In another sample, the SnO electrode is selected as a representative of high-capacity electrodes that undergoes large elasto-plastic deformation upon lithiation. Figure 4.5a shows the scanning electron microscopy (SEM) image of the SnO particles with an estimated average diameter of 30μm. The reconstructed model (682×747×84 μm^3, Figure 4.5b) shows that a large portion of the particles have irregular shapes and particles in local regions are aggregated. Since the complexity of particle geometries places a challenge in the selection of the RVE, a local collection of RVE whose volume fraction of active particles is close to that in the entire electrode is used. Figure 4.5c shows the RVE which has rough particle surfaces, aggregated particles, and initial defects of voids and cracks. To avoid the computational singularity, the Laplacian

smoothing method is utilized to smooth the particle surface and delete those structural defects. The RVE after surface smoothing has a size of 50×50×35 μm ^{3} and the mesh is shown in Figure 4.5d. Albeit relatively small size, the RVE is a reasonable representation of the microstructural feature of the SnO electrodes.

4.4 Results and discussion

NMC is a class of cathode materials attractive for the application of electric vehicles. Therefore, the NMC is adopted as an example to examine the mechanical behaviors of intercalation-type electrodes which usually undergo relatively small volumetric strain upon lithiation (<10%). In the numerical modeling, a perfect bonding between the active particles and the inactive matrix is assumed. The stress field in the composite electrode is induced by the coexistence of inhomogeneous distribution of Li and thus mismatch strains in the active particles, the mechanical confinement of the matrix against the volumetric change of the particles, and the contact of neighboring particles. Li distribution and the stress field dynamically co-evolve because of the coupling effect of diffusion and stresses. The radii of the NMC particles vary from 1.49 μm to 7.67 μm with an average value of A=3.08 μm. The size of the matrix for the uncompressed sample is 30×30×30 μm^3, and its size in the compressed sample decreases to 30×30×21 μm^3 while the volume of the active particles remains the same. The material properties are adopted as follows. For NMC, elastic constitutive behavior is adopted and the mechanical properties are considered to be independent of the Li composition. The material properties are set as, Young's modulus E_{NMC}=120 GPa [102], Poisson's ratio v_{NMC}=0.3, Li diffusivity D=10^{-15} m^2/s [172], partial molar volume of Li in NMC Ω=1.3×10^{-30} m^3 [173], and temperature T=300 K. The constitutive behavior of inactive matrix is described by a Neo-Hookean material model with the Young's modulus E=4.2

GPa and Poisson's ratio v=0.3 [102]. The volumetric strains of NMC materials upon full lithiation are in the range of 4% ~ 10% [173]. The volumetric strain is set as 9% at the fully lithiated state in the numerical calculations and the deformation is assumed to be linearly proportional to the Li concentration. Therefore, the maximum Li concentration can be calculated as $C_{\max}=0.09/\Omega$. In addition, the volumetric strain is systematically varied to study its influence on the mechanical and electrochemical performance of the electrodes. To model the potentiostatic lithiation process, a constant chemical potential μ_S is applied on the surface of active particles. The magnitude of μ_S is equal with the chemical potential of Li at the fully lithiated state of NMC without the influence of mechanical stresses, $\mu_S = \mu_0 + kT\log\left(\Omega C_{\max}/\det(\mathbf{F})\right)$. For simplification, the interfacial charge-transfer kinetics at the interface between NMC particles and matrix is ignored so that the insertion of Li is only governed by the chemical potential gradient at the interface. For the galvanostatic lithiation, the time φ to reach the theoretical capacity of NMC is used to represent the charging rate. The nominal flux J_0 is then determined through the relationship $V_{NMC}C_{\max} = S_{NMC}J_0\varphi$. At the charging rate φ=1 h, J_0 =5.54×10^{-5} mol/m^2.

The stress field and Li concentration within the composite electrode are solved simultaneously. It is demonstrated that the evolution of stresses and the mechanical interactions regulated Li transport under the potentiostatic lithiation condition. Figure 4.6a shows the sectional view of Li profiles in the uncompressed RVE at different dimensionless time steps $\bar{t} = Dt/A^2$. As expected, lithiation proceeds at different degrees in the particles of different sizes. Particles of small size are lithiated much faster than those large particles. Within individual particles, Li distribution is highly inhomogeneous where the outer shell region is Li rich and the inner core is Li poor. The gradient of Li concentration induces mismatch strains and generates compressive stresses in the outer shell regions and tension around the inner core. Meanwhile, the expansion of

particles is constrained by the inactive matrix as well as neighboring particles, inducing an extra compressive stress field in the particles. The magnitude of this additional compressive stress depends on the Li concentration in the active particles, the size and pattern of the active particles, as well as the mechanical properties of the active and inactive materials. The stresses influence the Li transport in the way that the stress gradient within a particle tends to homogenize the distribution of Li and drives Li diffusion from the compressed region (Li rich) to the tensed side (Li poor).

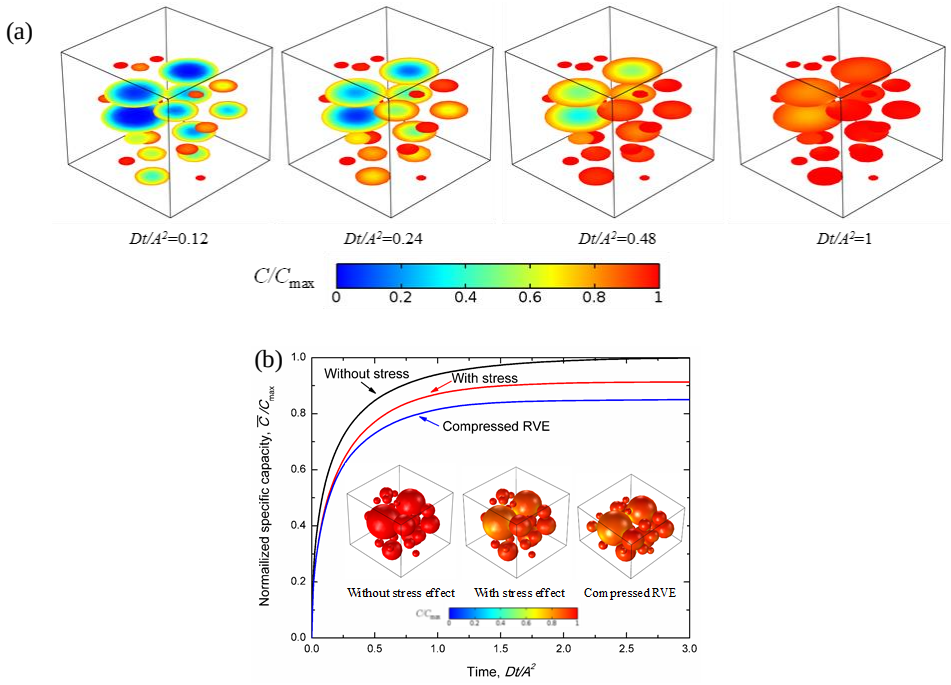

Figure 4.6. The effect of mechanical interactions on Li distribution and capacity of the RVE. (a) The sectional view of Li profiles at different time steps during potentiostatic lithiation of the RVE. Li diffusion is driven by both the Li concentration gradient and the stress field. (b) Normalized specific capacity as a function of the lithiation time for the uncompressed RVE with (red line) and without (black line) including the stress effect on diffusion and for the compressed RVE including the stress effect (blue line), respectively. Inset figures show the Li distribution at the fully lithiated state for the three cases.

The inhomogeneity of Li distribution reduces the effective capacity of the composite electrodes. With regard to the stress effect on the capacity, the local compressive stresses increase

the chemical potential of Li, impeding the Li insertion and thus reducing the deliverable capacity. To demonstrate the extent of the stress modulated capacity, lithiation in three sets of samples are simulated: uncompressed RVE with and without including the stress effect on Li diffusion, and compressed RVE with the stress effect. Figure 4.6b plots the normalized specific capacity $\overline{C}/C_{\max}$ as a function of the lithiation time in the three cases where $\overline{C}$ represents the average Li concentration over all the NMC particles. The specific capacity increases quickly at the initial stage of lithiation because of the large driving force of chemical potential, and then gradually approach to the steady state. Without considering the stress effect on Li diffusion (black line), the normalized capacity reaches the unit at the fully lithiated state and Li insertion in each single particle is saturated. In comparison, the uncompressed RVE shows a significant loss of capacity (~10%) at the fully lithiated state if the stress effect on Li diffusion is accounted (red line). For compressed RVE (blue line), the capacity is reduced to an even larger extent. This is due to the fact that the smaller particle spacing in the compressed samples induces a higher compressive stress filed in both the active particles and the inactive matrix. More discussions about the stress evolution within the particles upon lithiation can be found in Chapter 3. The inset snapshots in Figure 4.6b show the Li profiles in the three configurations upon full lithiation. It is evident that Li insertion is blocked in the regions where large compressive stresses develop. Figure 4.7 shows the local microstructural details and the correspondence between the Li distribution and mean stresses in the uncompressed RVE without and with the stress effect in comparison with the results of the compressed RVE.

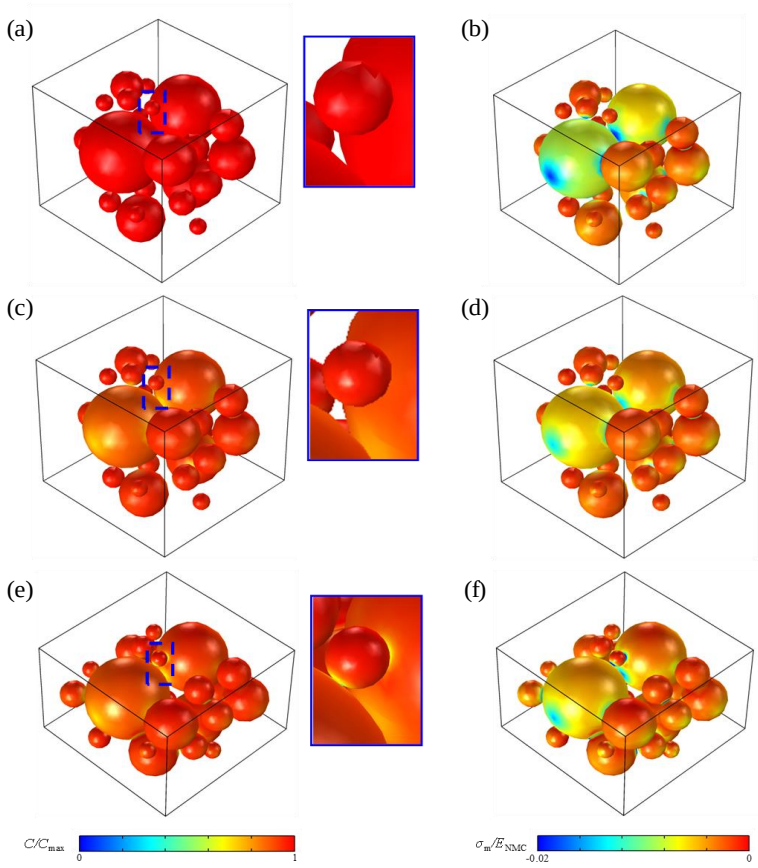

Figure 4.7. The left column shows the Li profiles at the fully lithiated state (Dt/A^2=1) after potentiostatic lithiation of the uncompressed RVE without (a) and with (c) the stress effect, and of the compressed RVE with the stress effect (e), respectively. The right column ((b), (d), and (f)) shows the corresponding distribution of mean stresses. The mechanical interactions among the particles (local view in the middle column) regulate Li distribution and the large compressive stresses impede Li insertion into the particles.

To further examine the compressive stress induced capacity loss, the individual contributions due to the matrix confinement and particles contact are investigated. Figure 4.8a plots the distribution of Li concentration along the radius of a particle which is free of contact with its neighbors. The solid and dashed lines represent the Li profile at different lithiation steps without and with including the stress effect on Li diffusion, respectively. The compressive stresses developed by the mechanical constraint of the inactive matrix smooth the Li concentration gradient in the particle. At the fully lithiated state, the compressive stress exerted on the outer surface of

the particle counterbalances the driving force of concentration gradient for Li diffusion and blocks further insertion of Li. The ~ 10% capacity loss at the terminal state of lithiation is attributed to the mechanical confinement of the matrix. In another particle, Figure 4.8b plots the Li distribution along two radii, where R_1 represents the direction along which the particle is free of contact with others (solid line), and R_2 represents the direction along which the particle is in contact with its neighbor (dashed line). The difference of Li concentrations along the two orientations represents the capacity loss due to the particles contact. The local contact generates a large magnitude of compressive stresses that cause deficiency of Li storage around the outer regime of the particle. The inhomogeneity of Li profiles also induces anisotropic deformation of the particle that the spherical particle may evolve into non-spherical shapes.

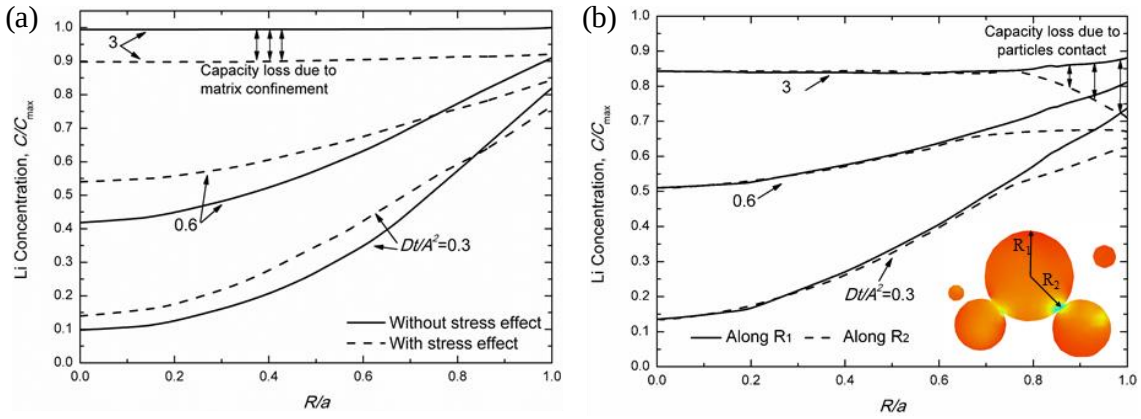

Figure 4.8. Capacity loss due to the mechanical confinement of the matrix and particles contact. (a) Radial distribution of Li in a particle which is free of contact with its neighbors. The mechanical confinement is provided only by the matrix. The solid and dashed lines represent the results calculated with and without accounting for the stress effect on Li diffusion, respectively. The compressive stresses developed by the matrix confinement tend to homogenize the Li distribution within the active particles and decrease the effective capacity. (b) Li profiles along two radii of different orientations. R_1 represents the direction along which the particle is free of contact, and R_2 represents the direction along which the particle is in contact with its neighbor.

The accessible capacity of the composite electrodes depends on the internal stresses. The stress field in the active particles dynamically evolves in the electrochemical processes of Li insertion and extraction, and is further determined by the geometric features of the particles, the volume fraction of the active materials, the volumetric expansion during lithiation, and the effective properties of the matrix. The specific capacity of the electrodes is screened in terms of the variation of the volume fraction of the active particles V_f and the volumetric strain upon full lithiation ε_V. Figure 4.9 shows the contour plot of the normalized specific capacity $\overline{C}/C_{\max}$. The capacity decreases as V_f and ε_V increase (upper right regime in Figure 4.9) because both the higher occupancy and larger deformation of the active material result in severe mechanical interactions among the constituted components which in turn reduce the effective capacity. The dependence on V_f indicates that the effective capacity of the composite electrode is not linearly scaled with the mass of the active material, but is limited the inhomogeneous storage of Li that is modulated by the mechanical stresses. In terms of the volumetric strain ε_V, albeit smaller values compared to that in high-capacity electrodes, the stress can still be significant because the active particles are usually ceramic-like materials with high stiffness. In addition to the two studied parameters, the contour plot of capacity can be extended to multi-dimensions by including, for instance, the stiffness ratio of the active and inactive materials, the sphericity of the particles, the distance of neighboring particles, among others. There is a wide spectrum in the design of composite electrodes to reach the optimum electrochemical behaviors and mechanical performance. The computational program provides a viable tool in the selection of materials and design of the geometries of the constituted components. For the interest of different boundary conditions, Figure 4.10 shows the results of galvanostatic lithiation including the specific capacity of the electrodes at different charging rates and the influence of the stress field on the capacity

retention. Same conclusions is drawn that the stress field regulates Li transport and large compressive stresses may significantly reduce the capacity of the composite electrodes.

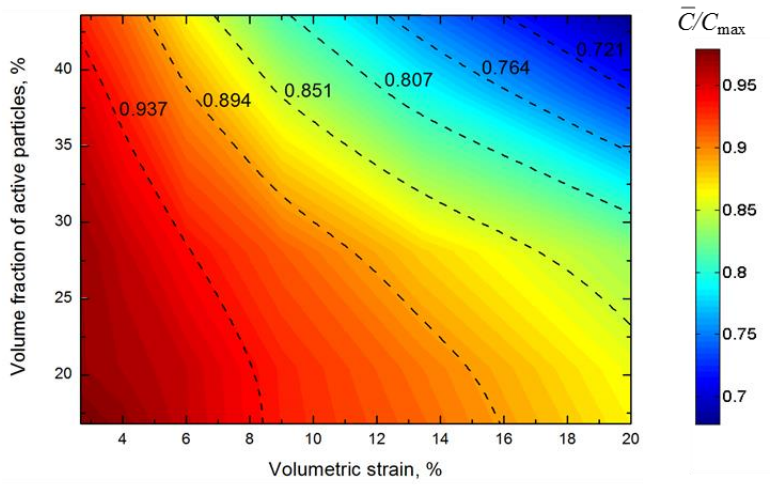

Figure 4.9. Contour plot of specific capacity of the composite electrode in terms of the volumetric strain and volume fraction of the active particles. Higher values of the volume fraction and the volumetric strain (upper right region) significantly reduce the effective specific capacity because of the mechanical interactions of the constituent components.

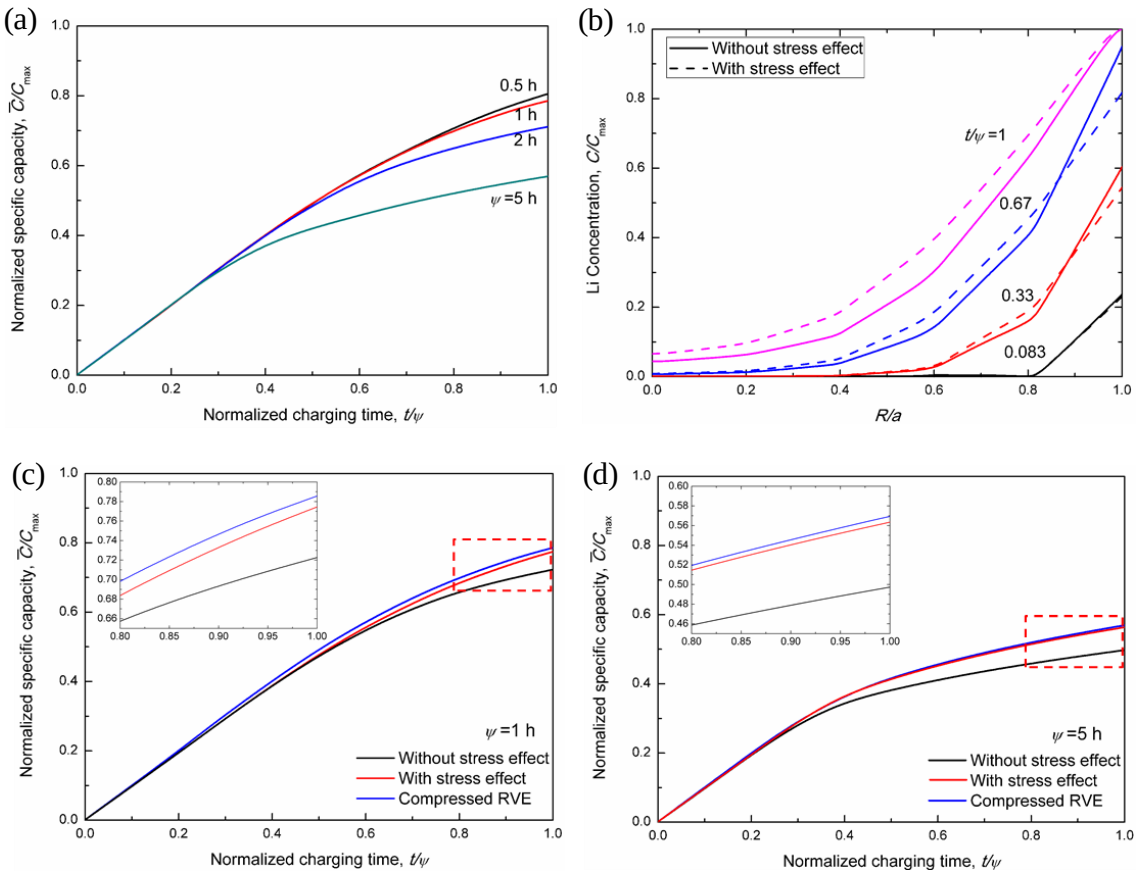

Figure 4.10. (a) Specific capacity of the composite electrode lithiated at different galvanostatic rates. (b) Li concentration profiles in the composite electrode at different time steps of galvanostatic lithiation. (c) and (d) The influence of stresses on the specific capacity of the composite electrode for the galvanostatic lithiation rate φ = 1 *h* and φ = 5 *h*, respectively.

Another important aspect in the design of composite electrodes is to avoid the structural disintegration due to the fracture of the conductive matrix or interfacial debonding between the active material and the matrix. The potential failure can be dictated by the stresses in the matrix. Figure 4.11a and b show the distribution of the first principal stress and shear stress in a cross section of the inactive matrix at fully lithiated state. The maximum stresses in the matrix are located at the regimes in between the close particles. The normal stress may cause the tear of the polymer matrix or irreversible morphology changes. On the other hand, the shear stress is the major cause of the interfacial debonding between the particles and the matrix. The disconnection

of the particle network ultimately isolates the active particles and increases the ohmic and thermal resistance of the electrodes – another known factor that causes persistent capacity loss of the electrodes over cycles. Figure 4.11c and d plot the quantitative characterization of the stresses (maximum shear stress, equivalent stress, and mean stress) in the matrix as a function of the volume fraction V_f and the volumetric strain ε_V, respectively. The magnitude of the three stress components increases with an almost proportional relationship with the two variables. In the limiting cases of V_f =40% and ε_V =20%, the stresses reach the value of the stiffness of the matrix. Such large stresses are hardly sustainable for the polymer matrix.

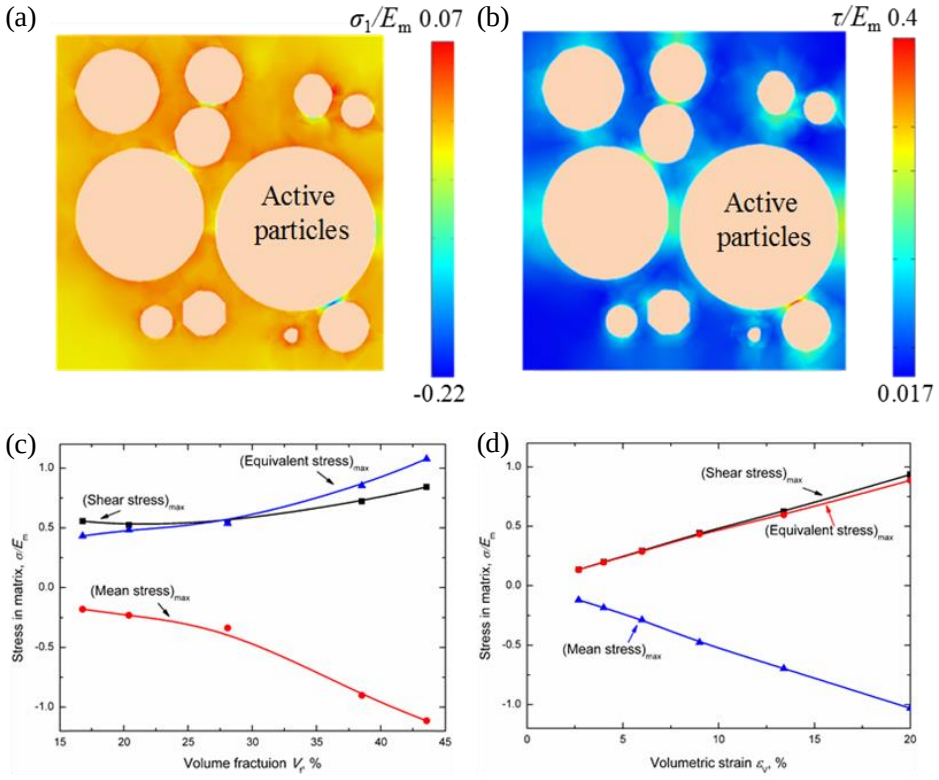

Figure 4.11. Plots of (a) first principal stress and (b) shear stress in the matrix. The regions in between two particles are subject to large stresses that might lead to fracture or debonding of inactive matrix during lithiation. The maximum shear stress, equivalent stress, and mean stress in the matrix as a function of (c) volume fraction and (d) volumetric strain of the active particles.

Large deformation and geometric nonlinearly are challenging topics in continuum mechanics. To demonstrate the capability of the computational program for the materials experiencing large elasto-plasticity during Li insertion, mechanical behaviors and stress modulated Li transport in SnO composite electrodes are simulated. Metal oxides hold the great promise of high-capacity anodes to replace the conventional graphite materials. Most studies on metal oxides have been focused on their electrochemical performance and the reaction mechanisms. On the mechanical aspect, a large volumetric strain (~ 100%) is often associated with the lithiation process in metal oxides that challenges the structural stability in the long-term cycles. However, the mechanical behaviors of oxide electrodes have been rarely explored. 3D model of SnO composites is reconstructed and then imported into the finite element program. Details are described in Chapter 4.3. The material properties for SnO particles are assumed to be constant. The material properties are set as, Young's modulus E_{SnO}=50 GPa, Poisson's ratio ν_{SnO}=0.3, yield strength σ_Y=200 MPa , Li diffusivity D=10^{-13} m^2/s [174, 175], partial molar volume of Li in SnO Ω=1.35×10^{-29} m^3 [168], and the temperature T=300 K. Experimental results show that the volume strain of SnO is proportional to the lithiation state and reaches to 258% upon fully lithiated [158, 168]. Therefore, the volume expansion of SnO is assumed as a linear function of Li concentration and set the maximum Li concentration C_{max}=$2.6/\Omega_{SnO}$. An elastic and perfect plastic constitutive model is adopted such that SnO particles yield when the equivalent stress reaches the yield strength σ_Y. The galvanostatic lithiation is simulated where the time to reach the theoretical capacity of SnO is set to be φ, and the nominal flux J_0 is determined through the relationship $V_{SnO}C_{\max} = S_{SnO}J_0\varphi$. For the lithiation rate φ=2 h, J_0 =$1.32\text{x}10^{-4}$ mol/m^2.

Different from the spherical NMC particles, the fabricated SnO shows irregular shapes and rough surfaces. The geometric features will influence the Li distribution and determine the stress

field. Li tends to accumulate at the regions of smaller surface curvature. Meanwhile, stresses are concentrated at the edges and corners which place a strong driving force of Li diffusion. Figure 4.12a and b show the Li distribution in the SnO particles before lithiation and after Li insertion for 1 h. It is evident that lithiation in different particles proceeds at different stages. Within individual particles, Li distribution is highly inhomogeneous that Li is concentrated in the bulged regimes of smaller surface curvature. The particles are color coded by the magnitude of the mean stress in Figure 4.12c and the red arrows show the direction of local Li flux. Li flow corroborates with the stress field that local tensile stress attracts Li insertion while compressive stresses drive Li away. Figure 4.12d shows the cross-sectional view of Li profiles in the reconstructed RVE at different time steps. The aggregated particles of irregular shapes show higher concentration of Li because of the effects of both the surface curvature and the mechanical stress. The high disparity of Li concentration over the active particles generally compromises the electrochemical performance of the battery packages. Recent studies [169, 176] have also pointed out that the mechanical and electrochemical performance of electrodes can be improved if the active particles are synthesized with the control of size, shape, and alignment.

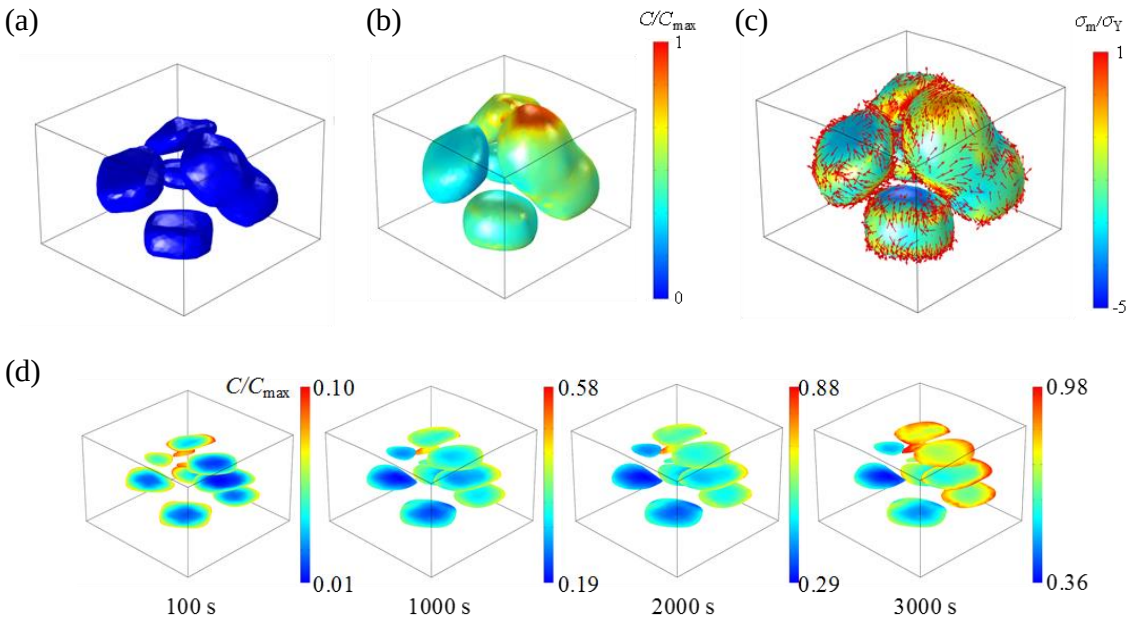

Figure 4.12. Li distribution in the SnO particles (a) before lithiation and (b) after galvanostatic lithiation for 1 h (b). (c) The profiles of mean stresses and Li flux within the particles. The particles are color coded by the magnitude of mean stresses where blue color represents the regimes under large compressive stresses and red color shows the regimes under large tensile stresses. The direction of local Li flux is represented by the red arrows. It is evident that local tensile stresses attract Li while the compressive stresses drive Li away. (d) Cross-sectional visualization of Li profiles in the reconstructed RVE at different time steps during the galvanostatic lithiation.

4.5 Conclusions

The mechanical stresses and electrochemical behaviors of Li-ion batteries are intimately coupled. While the mechanical failure of batteries is well recognized in the research community, the stress regulated Li transport and thus the deliverable capacity of batteries have been overlooked. The dynamic nature of mechanical interactions in the heterogeneous composite electrodes adds a further challenge in characterizing the stress effect. A finite element program that computes coupled Li diffusion and stresses for three-dimensional composite electrodes is developed. Reconstructed models for commercial batteries are employed to study the co-evolution of stresses and Li storage. The NMC cathode represents the intercalation-type electrodes of spherical shape

and small deformation, while the SnO anode represents the high-capacity materials of irregular shapes and dramatic volumetric change upon Li insertion. The state of charge in the active particles is highly inhomogeneous regulated by the stress field. Significant capacity loss is possible due to the mechanical confinement of the inactive matrix and particles contact. A multi-dimensional space of design is open for the optimization of the mechanical and electrochemical performance of composite electrodes by the selection of the geometry, network, and properties of the active particles and the surrounding medium.

5. DISINTEGRATION OF MEATBALL ELECTRODES FOR $LINI_XMN_YCO_ZO_2$ CATHODE MATERIALS

5.1 Introduction

Mechanical stability is one of the key criteria in the selection of electrode materials for high-performance Li-ion batteries [4, 60, 61, 153]. The stress-induced structural disintegration of electrodes impedes electron conduction and increases the electric and thermal resistances. Furthermore, mechanical deformation of the active material interferes with the stability of solid electrolyte interface (SEI) which results in a persistent decrease of cyclic efficiency [177, 178]. Mechanics of both anode and cathode materials has been extensively studied in recent years [46, 47, 179-183]. Various forms of mechanical degradation are revealed including fracture [34, 39, 46], plasticity [31, 136], and cavitation of active particles [135, 159], crack of inactive conductive matrix [42, 85], debonding of thin films [43], and breakage of SEI [45].

This chapter is to study the mechanical degradation of NMC cathode materials by tracking the microstructural evolution of the electrodes after electrochemical cycles. NMC is the current choice of cathode for high-capacity batteries in the electric vehicle applications [184, 185]. It is formed by partially replacing Co in $LiCoO_2$ by Ni and Mn to achieve the improved electrochemical performance while reducing the material cost. The composition of Ni, Mn, and Co can be tuned to optimize the capacity, rate performance, electrochemical stability, and lifetime [173]. Distinct from the typical microstructure of single particles embedded in a conductive matrix, the as-synthesized NMC particles have a hierarchical meatball structure - small primary particles of submicron size aggregate and form the secondary spherical particles (~ 10 m) [186]. The primary particles are hold together by weak van der Waals interactions. Therefore, the mechanical strength of the NMC secondary particles, determined by the adhesion of the constituent primary particles,

is much lower than the intrinsic material strength of single particles. Decohesion of the primary particles attributes to the major cause of mechanical degradation in NMC materials as is schematically shown in Figure 5.1a. A few recent studies revealed fragmentation of the NMC secondary particles induced by the disassembly of the primary particles [36, 187, 188]. For example, Sun et al. observed extensive fracture and amorphization in Li-rich NMC particles [189]. They used numerical modeling to analyze the conditions for crack initiation at the interfaces between primary particles in reconstructed models. Li et al. compared the cyclic performances of two groups of NMC electrodes, one is homogeneous NMC single particles and the other is secondary particles assembled by many primary particles [187]. They attributed the accumulated capacity fade to the fracture of NMC secondary particles upon electrochemical cycles at high C-rate, high cutoff voltage, and high operation temperature. The mechanistic understanding on the disintegration of the meatball structure, the track of morphological evolution, its influence on the electrochemical performance, and development of engineering solutions to enhance the mechanical stability of NMC materials warrant further systematic studies.

The electrochemical conditions which lead to the disintegration of NMC particles are investigated. Coin cells using NMC cathode and Li anode (half cells) are cycled at different charging rates and voltage windows. Post-mortem imaging using scanning electron microscope (SEM) is performed on the cycled NMC electrodes. Direct comparison of the microstructural features in different regimes before and after lithiation cycles reveal that severe fracture of the meatball structure at the interface of primary particles occur at a slow charging rate. Such an observation runs counter to a well-developed theory of fast-charging induced extensive stresses and fracture in single particles [34]. Electrochemical impedance spectroscopy (EIS) analysis confirms that charging rate is a controlling factor resulting in the accumulated disintegration of

NMC particles. A numerical model is built to investigate the evolution of Li concentration and stresses within NMC secondary particles. Cohesive zone model (CZM) integrated in ABAQUS is utilized to simulate crack formation and propagation at the interface of primary particles. The theoretical modeling is in good agreement with the experimental results and provides understanding on the mechanical behaviors of NMC cathode materials.

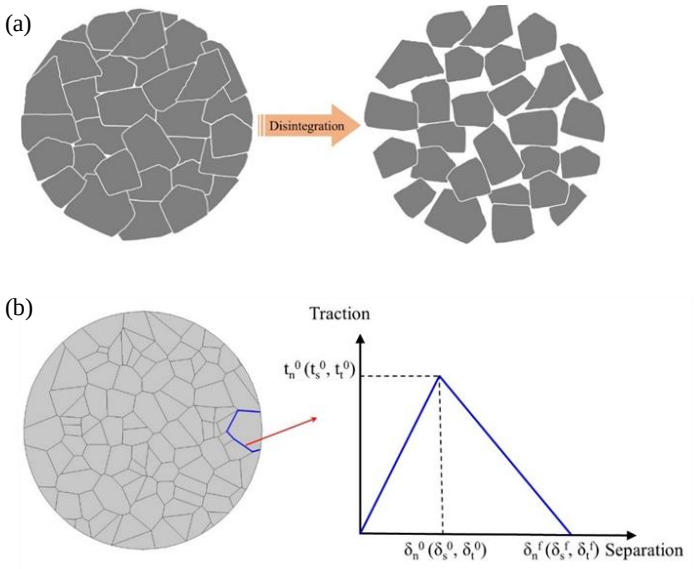

Figure 5.1. (a) Disintegration of secondary particles constitutes the major mechanical failure in NMC cathode materials. (b) The model of a spherical NMC secondary particle consisting of irregular primary particles. Cohesive zone model is used to simulate the interfacial fracture between the primary particles [190].

5.2 Experimental methods

5.2.1 Electrode preparation

As-received $LiNi_{0.5}Mn_{0.3}Co_{0.2}O_2$ (NMC532, referred as NMC in the following text, Toda America) powders, polyvinylidene fluoride, (Solvay, 5130), carbon black (Denka, powder grade), and N-methylpyrrolidone (Sigma Aldrich) were used to prepare the NMC cathodes by slot-die coating, which consist of 90 wt% NMC532, 5 wt% PVDF, and 5 wt% carbon black. Detailed

fabrication method can be found in a previous work [188]. The areal loading of the NMC cathode was 12.5 mg/cm^2. The as-coated NMC electrodes were calendered to the final porosity using a rolling miller (Model 6514H, International Rolling Mills) at 80 °C. After pressing, the porosity of the electrodes is 30.8%, which is close to the commercial NMC electrodes. To remove water, as-prepared electrodes were dried in a vacuum oven overnight at 80 °C before use.

5.2.2 Coin cell assembling

The microstructure of NMC electrodes before electrochemical cycles was imaged using SEM (T330, JEOL). Several different regimes were marked as reference for the comparison of microstructural features before and after electrochemical cycles. Next, the electrodes were transferred into a glovebox under a dry argon atmosphere (moisture and oxygen levels less than 0.5 ppm) for coin cell assembling. NMC electrodes, Li foils, and Celgard-2502 membranes were used as the cathode, anode, and separators in the CR-2032 type coin cells, respectively. The electrolyte was composed of 1 M $LiPF_6$ salt dissolved in ethylene carbonate / diethyl carbonate of 1:1 volume ratio (EC/DEC, 1:1). All assembled cells were placed to rest for about 6 h to ensure complete wetting before the electrochemical cycle. After cycling, the coin cells were disassembled. The NMC electrodes were washed several times with dimethyl carbonate (DMC) and dried overnight in a vacuum oven at room temperature.

5.2.3 Electrochemical measurement

Galvanostatic electrochemical cycles were performed using the battery test system (BT-2043, Arbin). Cyclic tests were designed to investigate the influence of two main factors on the electrode degradation: the voltage window and the C-rate. To evaluate the influence of the voltage window, a fixed lower cut-off voltage was used (3 V versus Li/Li^+), while different tests were set to the upper cut-off voltages of 4.3, 4.5, and 4.8 V, respectively. Next, to evaluate the influence of

the charging rate, different cells were cycled at the C-rates of 2C or C/2. The first charge and discharge was performed at C/20, followed by 100 cycles at a specific rate. Electrochemical impedance spectroscopy (EIS) measurements were carried out using the impedance analyzer (Versa STAT 3, Princeton Applied Research) with an amplitude voltage of 5 mV and a frequency range between 0.1 Hz and 100 kHz. All cells were discharged to the same voltage before EIS measurement. All electrochemical measurements were conducted at room temperature.

5.3 Numerical modeling

Li diffusion and stresses in the NMC secondary particles are simulated. Li transport in the porous conductive matrix and the mechanical interactions between the electrodes and the surrounding media are neglected [36]. To reveal the interfacial fracture of the secondary particles, 3D particles are simplified into a more tractable 2D model, where the secondary particle is represented by a circular domain composed of multiple primary particles of random sizes and shapes, Figure 5.1b. The polygonal primary particles are generated using the Voronoi tessellation [191]. The kinetics of Li diffusion is described by the Fick's law and the displacement field in the active material is governed by the equations of mechanical equilibrium, presented in Chapter 2.1. The governing equations for the kinematics of deformation and the kinetics of diffusion are solved simultaneously at every time step in COMSOL Multiphysics (V5.0, COMSOL). The built-in time-dependent solver MUMPS (MUltifrontal Massively Parallel sparse direct Solver) is used to solve the evolution of Li concentration and stress field. Disintegration of the primary particles is simulated using ABAQUS (V6.11, Dassault Systèmes), where the Li concentration induced mismatch strain is imported as a predefined thermal strain field in ABAQUS.

The boundary conditions are prescribed as follows. A zero-displacement condition is prescribed at the center of the secondary particle during the lithiation cycles to prevent the rigid

motion. For the diffusion boundary condition, a nominal flux $\boldsymbol{J}$ is imposed on the surface of the secondary particle with a constant value J_0 that is determined through the relationship $VC_{\max} = SJ_0\tau$, where V is volume of the NMC secondary particle, $C_{\max}$ the maximum concentration of Li, S the surface area of the particle, and τ the time to fully lithiate/delithiate the particle.

The nucleation and propagation of microcracks at the interface of primary particles during the lithiation cycles are modeled using the cohesive zone model. When the lithiation induced stresses normal to the interface reach the cohesive strength, cracks initiate and propagate. This interfacial failure can be simulated by the progressive damage of the cohesive element layer assigned in between the individual primary particle [192]. The damage response of the cohesive element is presented in terms of the traction-separation relationship in Figure 5.1b where t_n^0, t_s^0, and t_t^0 represent the interfacial strength when the deformation is either normal to the interface or in the first or the second shear direction, respectively. Likewise, δ_n^0, δ_s^0, and δ_t^0 represent the corresponding interfacial separations (displacement jumps across the interface). The initial response of the cohesive element is assumed to be linear. Once the maximum traction reaches the interfacial strength t_n^0, t_s^0, or t_t^0, damage is assumed to initiate and thus the traction response starts to drop. New crack is formed once the traction is reduced to zero or the critical separation δ_n^f, δ_s^f, and δ_t^f is reached, where the area under the traction-separation curve gives the interfacial fracture toughness G_c. The interfacial strength t_n^0 is set as 100 MPa. Since the experimental observation shows that the crack opening constitutes the major fracture behavior of NMC secondary particles [193], mode I (crack opening mode) is believed to be the dominating fracture mode. Therefore, the t_s^0 and t_t^0 are set as infinite to ignore the shear damage at the interface. The fracture toughness G_c is set as 0.11 J/m^2 [133].

5.4 Results and discussion

The electrochemical performance of the NMC cathode under different cyclic conditions is first examined. Figure 5.2a shows the capacity and Coulombic efficiency of the coin cells at 0.5C galvanostatic charging rate with different voltage windows of 3-4.3V, 3-4.5V, and 3-4.8V. The corresponding discharge capacities in the first cycle are 160.5, 170.6, and 184.6 $mAhg^{-1}$, respectively. As the cycles proceed, the coin cells maintain 84.9%, 70.7%, and 66.2% of their initial capacity at the three voltage windows after 50 cycles. The large capacity fade at a high voltage is mainly due to the accelerated surface reconstruction of highly delithiated NMC through interfacial reactions with the electrolyte, leading to the large irreversible capacity and voltage fade [194-196]. Figure 5.2b shows the electrochemical performance of the half cells at different C-rates and a fixed potential window of 3-4.3V. The cells cycled at 0.5C maintain 84.9% of the capacity after 50 cycles, which is considerably higher than that at the 2C charging rate. The lower capacity at the fast charging condition is mainly due to the slow kinetics of Li diffusion. The slow charging rate allows more Li intercalation and benefits the capacity retention over cycles.

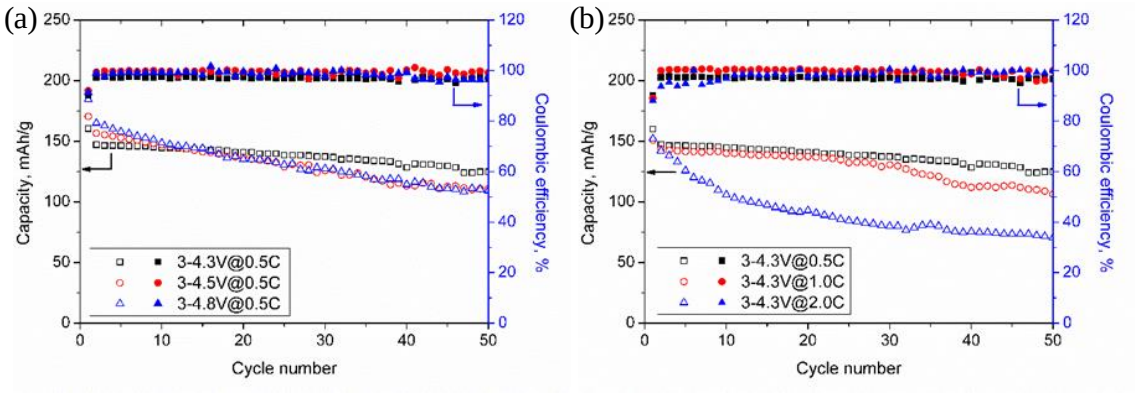

Figure 5.2. Capacity and Coulombic efficiency of half cells using NMC cathode under two different cyclic conditions: (a) 0.5C charging rate with different voltage windows; (b) different cyclic rates with the voltage window 3-4.3V.

The observed dependence of the electrochemical behaviors of NMC on the charging rate and voltage window is consistent with many prior studies [194, 197]. However, the mechanical degradation associated with the different electrochemical conditions has not been explored. Microstructural evolution at the local regimes is tracked before and after cycles to determine the controlling factor of the mechanical disintegration of NMC materials. Figure 5.3 shows the SEM images of the uncompressed sample, compressed sample, and compressed sample with complete electrolyte wetting within the coin cells, respectively. The shape of the NMC secondary particles before compression is spherical in nature and the primary particles are closely packed without obvious gaps in between. After compression, the secondary particles near the surface slightly change the shape while the packing of the primary particles remains intact. Figure 5.3c represents the reference state of the NMC electrodes right before electrochemical cycles with the experience of coin cell assembling, disassembling, and rinsing of electrodes. The comparison of Figure 5.3b and c shows that no additional structural changes are induced by the mechanical operations of assembling and disassembling of coin cells and the electrolyte wetting.

Figure 5.3d, e, and f show the morphologies of NMC electrodes after 100 cycles at 0.5C and voltage windows of 3-4.3V, 3-4.5V and 3-4.8V, respectively. It is ensured that those local views are representative to the overall microstructural feature of the composite electrodes. Compared to Figure 5.3c, it is evident that severe disintegration of the NMC particles occurs that a significant fraction of the initially closed-packed primary particles lose contact with each other. There is no clear difference for the electrodes cycled at different voltage windows, probably because (i) the upper cutoff voltage 4.3V is sufficient to induce severe fragmentation of the secondary particles and (ii) a higher cutoff voltage causes more capacity fade (Figure 5.2b) but

less Li insertion/extraction in the cycles such that the mechanical deformation and degradation are not necessarily deteriorated at the high cyclic voltages.

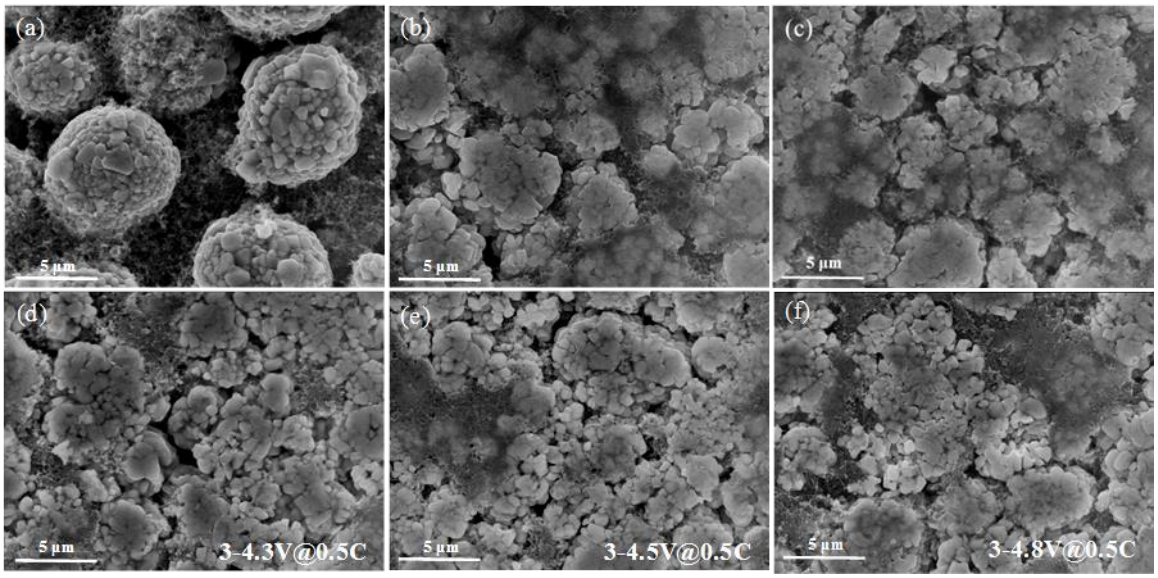

Figure 5.3. SEM images showing the microstructural changes of NMC electrodes before (a, b, c) and after (d, e, f) electrochemical cycles. (a)-(c) show the morphology of uncompressed sample, compressed sample, and compressed sample with complete electrolyte wetting in the coin cells, respectively. (c)-(e) show the microstructure of NMC electrodes after 100 cycles with the voltage windows of 3-4.3V, 3-4.5V, and 3-4.8V, respectively. The decohesion of primary particles results in the loss of connectivity and increase of electrical and thermal resistance of the cells.

Figure 5.4 shows the direct comparison of structural integrity of different marked regimes within the NMC electrodes before and after electrochemical cycles. The cells are cycled with the same charging rate 0.5C and the voltage window 3-4.3V. Before cycles, a small crack within the NMC electrode is manually induced. Then, several regimes with different distances from the crack tip are tracked to view the evolution of local structural features. It is noteworthy that few prior studies reported point to point comparison of the microstructural morphology before and after lithiation cycles [187, 189]. The blue circles in a, c and e show the local view of several regimes before cycles and the red circles in b, d, and f highlight the disintegration of NMC secondary

particles in the same regimes after 100 cycles. It is clear that the given charging rate and cyclic voltage induces extensive fragmentation of the secondary particles in the form of decohesion of the constituent primary particles. The mechanical degradation in relatively fast charging of the cells is further explored.

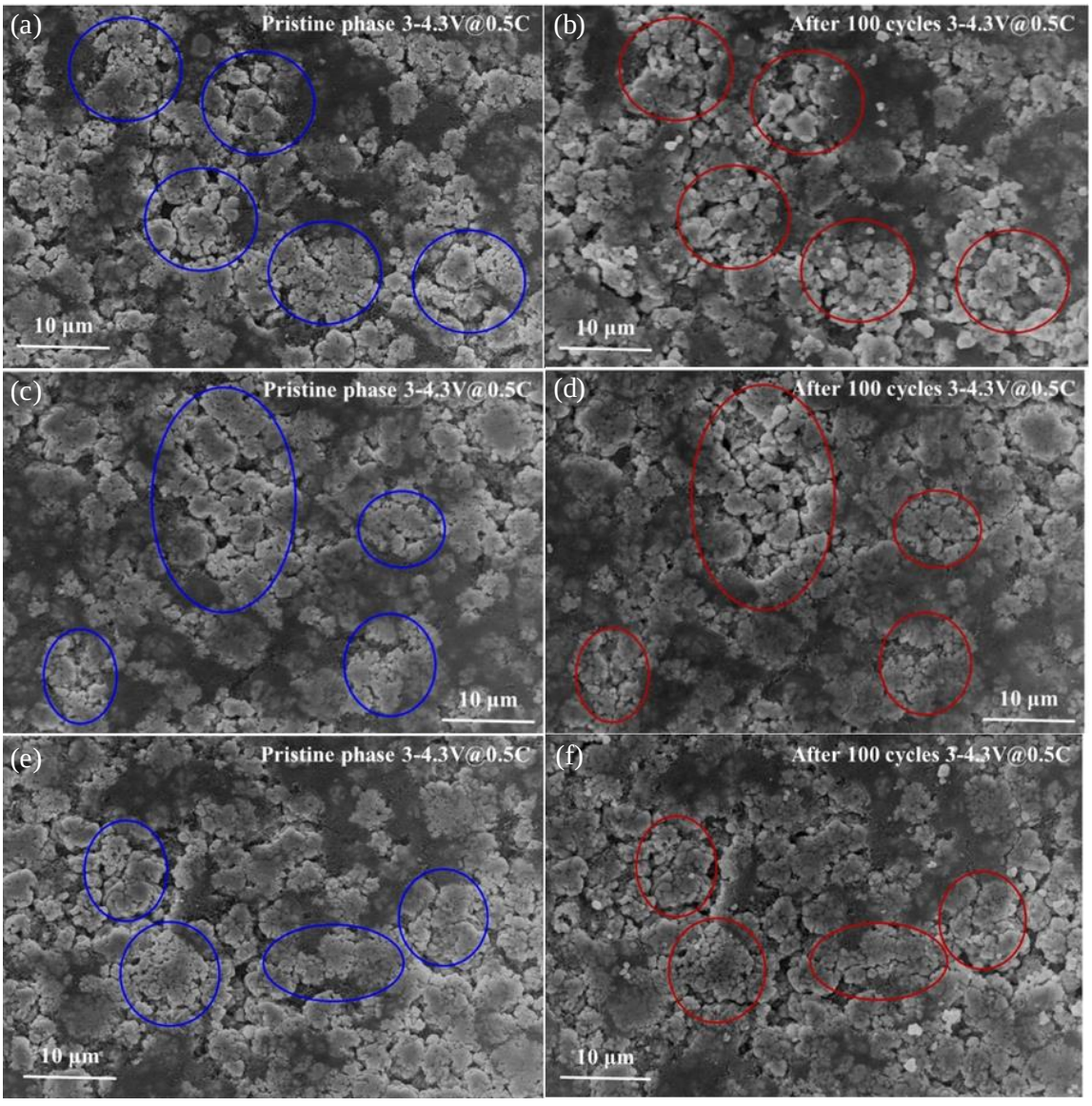

Figure 5.4. Direct comparison of the microstructural integrity of different regions within the NMC electrode before (a, c, e) and after (b, d, f) electrochemical cycles with the same charging rate 0.5C and voltage window 3-4.3V. The blue and red circles highlight the local regimes where severe particle disintegration occurs.

Figure 5.5 shows an exemplary comparison of a local regime before and after 100 cycles with the charging rate of 2C and the same voltage range 3-4.3V. From the post-mortem analysis, the only damaged regime is shown by the blue and red circles. Mechanical disintegration of the NMC secondary particles caused by fast charging is less obvious. This observation is not immediately intuitive. Several papers have reported that the high C-rate usually promotes particle fracture during electrochemical cycles [187, 198]. However, if one considers that higher C-rates limit the total amount of Li inserted into the electrodes in a given electrochemical window, it is conceivable that the proportionally lower volumetric change will likely induce less damage to the microstructure and thus lower extent of disintegration of secondary particles. This again draws the difference between the single homogeneous particles versus the aggregated secondary particles as the weak cohesion of the primary particles is more vulnerable to the mechanical deformation during Li intercalation.

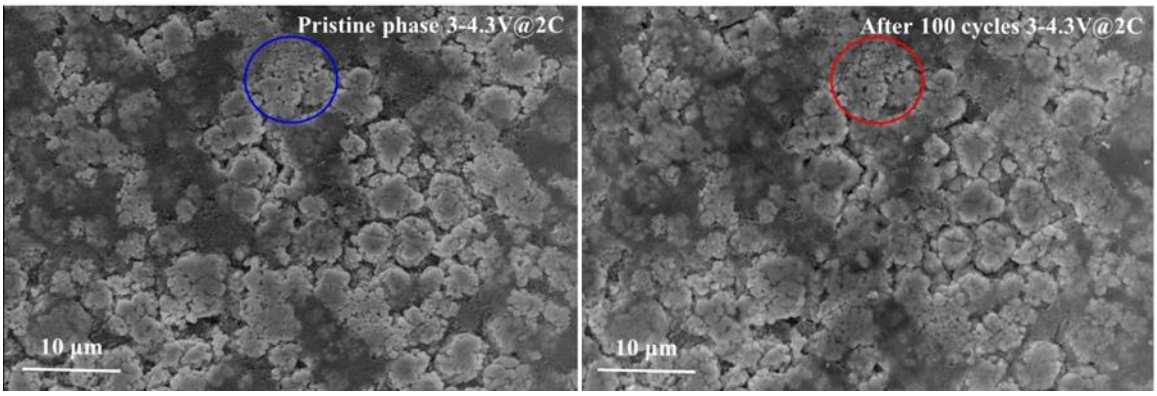

Figure 5.5. A microstructural comparison of NMC electrodes before (a) and after 100 cycles (b) with the charging rate 2C and voltage window 3-4.3V. The fast charging rate causes less disintegration of secondary particles.

The supporting information Figure 5.6, Figure 5.7, and Figure 5.8 show the mechanical disintegration of uncompressed NMC532, NMC442, and NMC622 electrodes, respectively. All

the NMC electrodes are coated with the same conditions described in the experimental section. In addition to the aforementioned fragmentation of the secondary particles, some particles in the uncompressed samples are entirely detached from the conductive matrix after the electrochemical cycles. It indicates that the binding of the NMC particles with the porous matrix is rather weak in the uncompressed electrodes. Calendering of the as-coated NMC electrodes may enhance the mechanical integrity by increasing the contact of the active particles with the conductive media, however, the disassembling of the weakly-packed primary particles remains a common mechanism of failure in various NMC compositions.

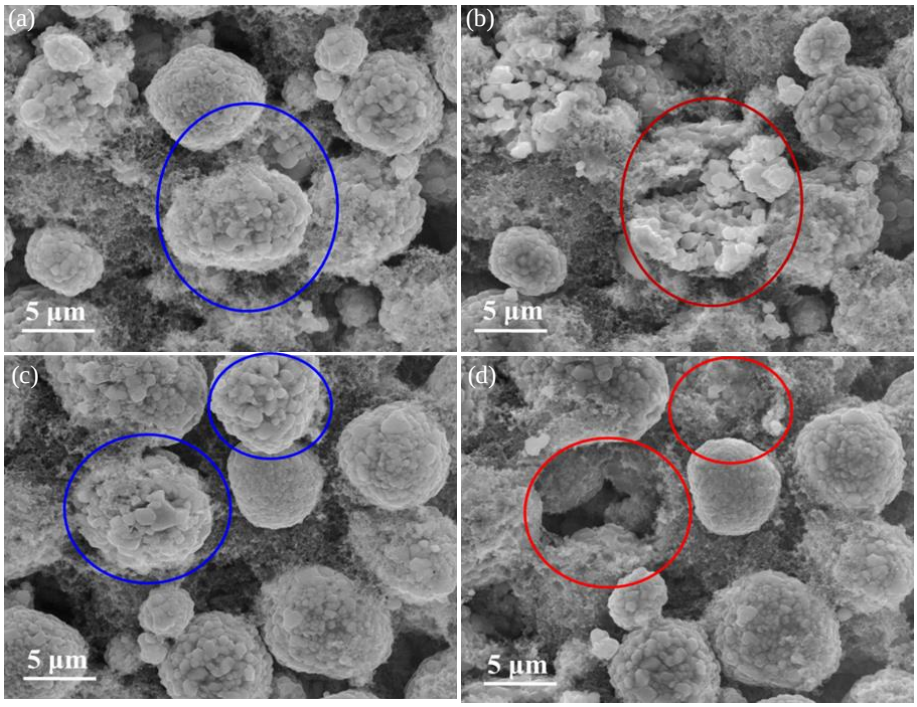

Figure 5.6. Fragmentation of NMC particles (a, b) and particle detachment from the conductive matrix (c, d) of uncompressed NMC532 electrodes before (a, c) and after (b, d) 100 cycles with the charging rate 0.5C and voltage window 3-4.3V. The blue and red circles highlight the local regimes where the particle disintegration and detachment occur.

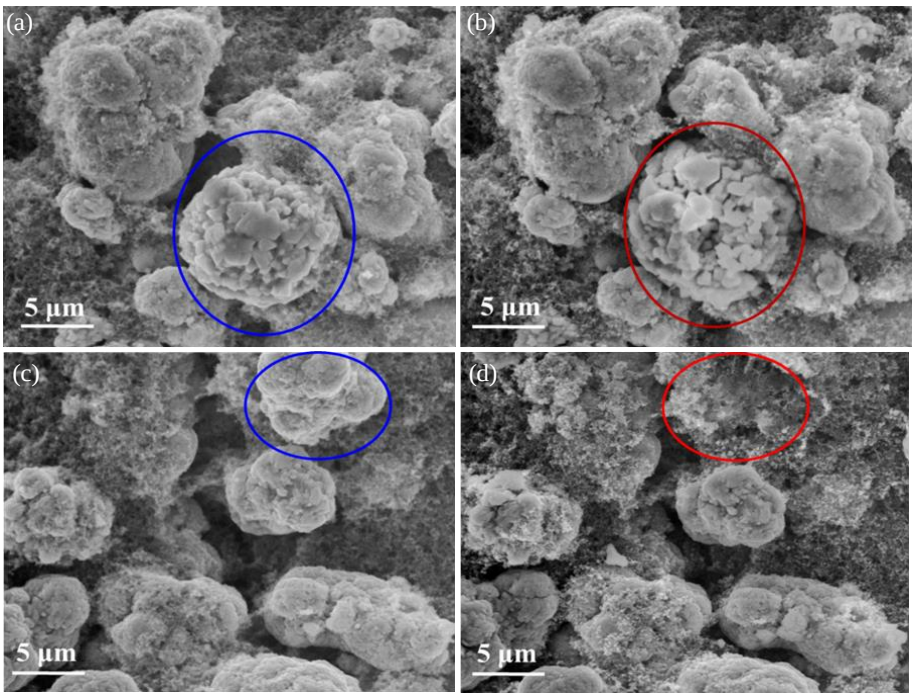

Figure 5.7. Fragmentation of NMC particles (a, b) and particle detachment from conductive matrix (c, d) of uncompressed NMC442 electrodes before (a, c) and after (b, d) 16 cycles. Blue and red circles highlight the local regimes where particle disintegration and detachment occur.

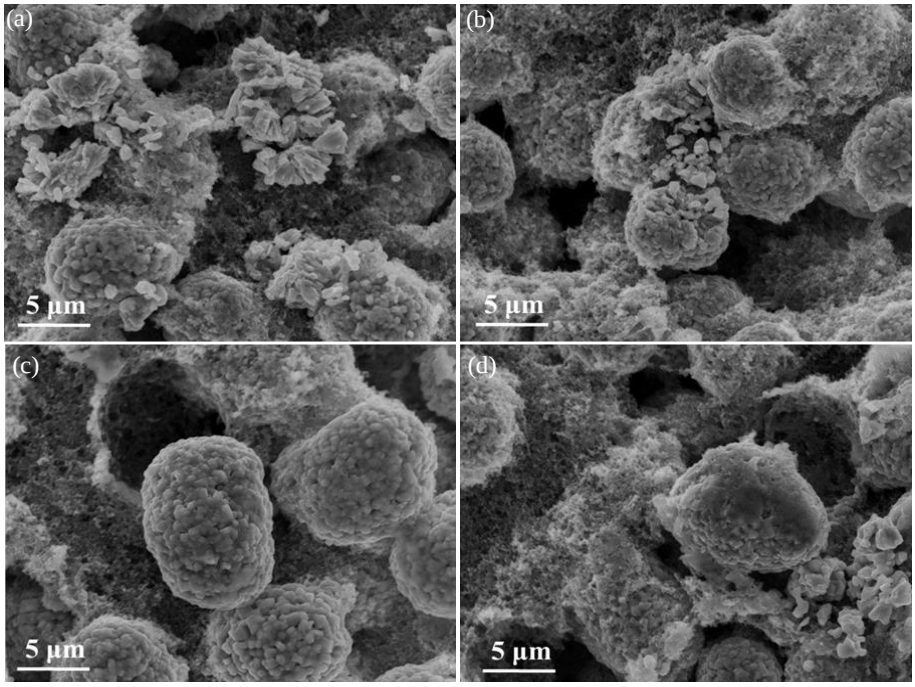

Figure 5.8. Microstructural integrity (a, b) and particle detachment (c, d) of uncompressed NMC622 electrodes after electrochemical cycles.

Electrochemical impedance spectroscopy measurements are conducted to investigate the effect of the fragmentation of NMC particles on the impedance of the cells. Figure 5.9 shows the Nyquist plots for the half cells upon electrochemical cycles with different voltage windows and C-rates. Figure 5.9a, b and c compare the evolutions of the impedance profiles for the cells cycled at 0.5C and different voltage ranges 3-4.3V, 3-4.5V, and 3-4.8V, respectively. Figure 5.9d plots the impedance profile at the fully delithiated state after 100 cycles with different C-rates. All the Nyquist plots show two typical semicircles in which the first semicircle is attributed to the Li diffusion through the surface layer and the second semicircle is assigned to the charge-transfer reactions [199]. Electrochemical impedance can be extracted by fitting the Nyquist plots with an equivalent circuit model shown in Figure 5.9e, in which R_{ohmic} represents the ohmic resistance from the electrolyte, cell hardware, cable, connection between cable and coin cells, $R_{SEI}//CPE_{SEI}$ the impedance for Li diffusion in the solid electrolyte interface of NMC cathode, $R_{ct}//CPE_{ct}$ the impedance for surface charge transfer, and Z_w the Warburg impedance describing the Li diffusion in the bulk electrode material. Table 5.1, Table 5.2 and Table 5.3 summarize the fitted impedance parameters in different cycle numbers with various voltage windows and charging rates. As shown in Table 5.1, R_{ohmic} slightly increases as the cycle number extends indicating that the ohmic resistance from the electrolyte, hardware and connection remains relatively stable. Both R_{SEI} and R_{ct} significantly increase upon the electrochemical cycles because of the formation of extra SEI films on the surface of fractured NMC secondary particles which induce large resistance of electronic and ionic conduction through the SEI layer and slow kinetics of charge transfer. Table 5.2 shows the influence of the cutoff voltage on the electrochemical impedances of cells after 100 cycles. Higher cutoff voltage correlates with a larger charge transfer impedance - R_{ct} of the electrode cycled with 3-4.8V (793.4 Ω) is more than ten times larger than that with 3-4.3V (70.6

Ω). This agrees with previous studies showing that a high cutoff voltage would accelerate the surface reconstruction of NMC materials with the formation of the rock-salt phase NiO which leads to a notable increase of charge-transfer resistance. In comparison, R_{SEI} of the electrodes cycled with different voltage ranges exhibit close values, indicating little difference in the amount of extra SEI layer formed on the fractured surface of NMC secondary particles. Therefore, the extent of particle disintegration is relatively insensitive to the cyclic voltage windows as long as the charging rate remains the same. Table 5.3 shows the influence of C-rate on the electrochemical impedance of cells after 100 cycles. Both the R_{SEI} and R_{ct} for 0.5C are significantly larger than those for 2C. The slow charging rate induces more mechanical disintegration of the NMC particles as is evident in the local SEM views in Figure 5.4 and Figure 5.5. The increase of R_{SEI} and R_{ct} is most likely due to the addition of the resistance layer formed on the new surface of fractured particles. The above conclusions revealed by the EIS measurements are in excellent agreement with the previous observations in Figure 5.2, Figure 5.3 and Figure 5.4, that is, (i) large capacity fade for the electrodes cycled at high cutoff voltages is due to the large charge transfer resistance, and (ii) the extent of fragmentation of NMC secondary particles is mainly dependent on the charging rate and is relatively insensitive to the selected voltage windows.

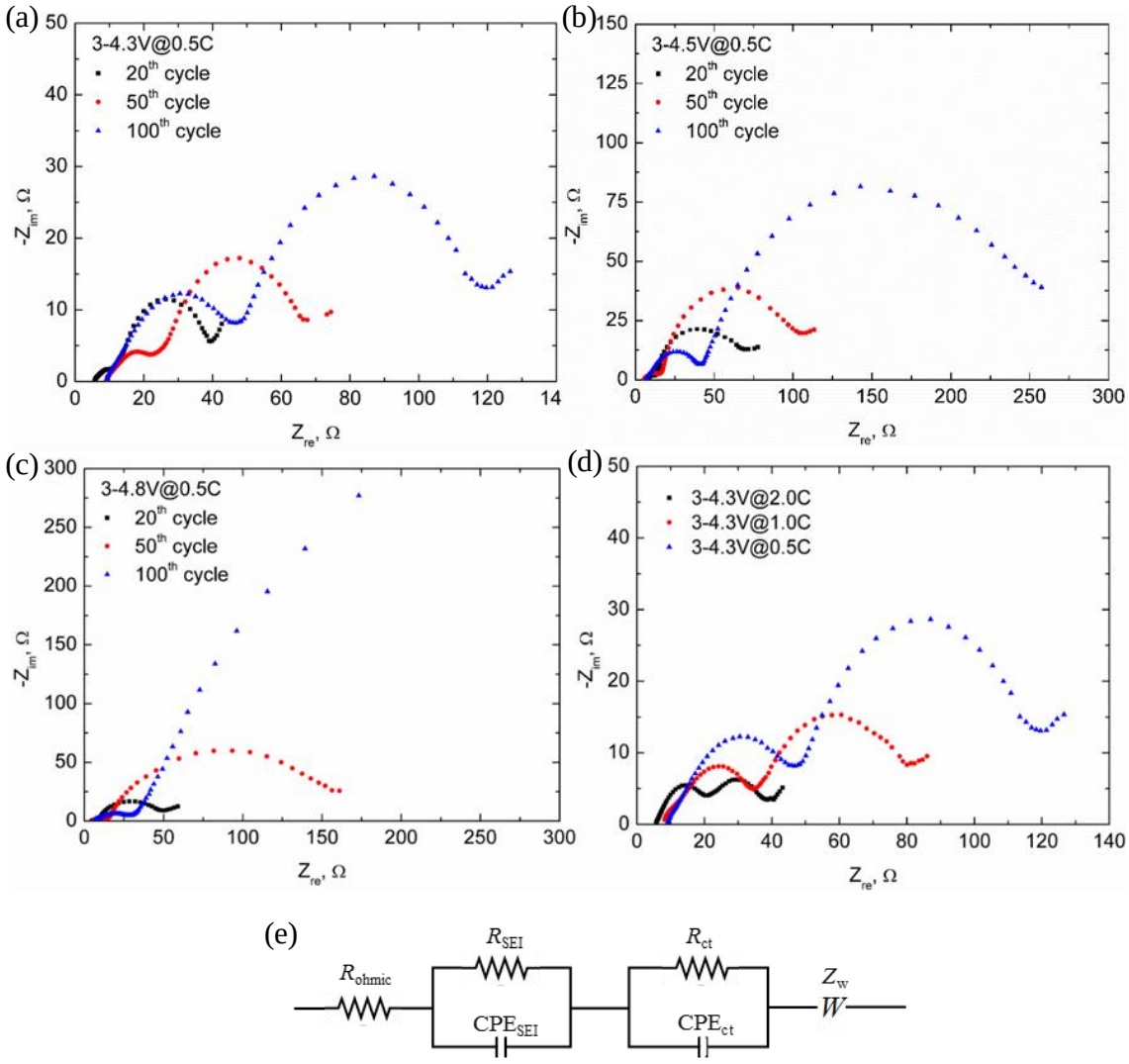

Figure 5.9. Nyquist plots for NMC electrodes after electrochemical cycles with different voltage windows and charging rates: (a) 3-4.3 V and 0.5C; (b) 3-4.5 V and 0.5C; (c) 3-4.8 V and 0.5C; (d) 3-4.3 V and different cyclic rates; (e) Equivalent circuit model to describe the Nyquist plots.

Table 5.1. Simulated parameters of EIS measurement for NMC electrodes cycled at different cycle numbers.

3-4.3V@0.5C	R_{ohmic}/Ω	R_{SEI}/Ω	R_{ct}/Ω
20^{th}	7.2	5.4	27.0
50^{th}	11.6	12.7	40.4
100^{th}	11.7	30.9	70.6

Table 5.2. Simulated parameters of EIS measurement for NMC electrodes cycled at different cutoff voltages.

100th	R_{ohmic}/Ω	R_{SEI}/Ω	R_{ct}/Ω
3-4.3V@0.5C	11.7	30.9	70.6
3-4.5V@0.5C	9.4	29.7	129.9
3-4.8V@0.5C	9.0	24.3	793.4

Table 5.3. Simulated parameters of EIS measurement for NMC electrodes cycled at different cyclic rates.

100th	R_{ohmic}/Ω	R_{SEI}/Ω	R_{ct}/Ω
3-4.3V@0.5C	11.7	30.9	70.6
3-4.3V@1.0C	11.6	22.9	42.5
3-4.3V@2.0C	7.6	13.3	17.7

Mechanical disintegration of NMC electrodes and its dependence on the charging rate is simulated using numerical modeling. Li diffusion, stress field, and crack formation within the NMC secondary spherical particles are modeled. The diameter of the NMC secondary particle is set as 11 μm and the constituent primary particles have various sizes around 1 μm. For NMC, an elastic constitutive behavior is adopted and the mechanical properties are considered to be independent of Li composition. Material properties are set as, Young's modulus E = 140 GPa, Poisson's ratio υ = 0.3, Li diffusivity $D = 10^{-15}$ m^2/s, and partial molar volume of Li in NMC $\Omega = 1.3\times10^{-30}$ m^3 [102, 172, 173]. The volumetric strains of NMC materials upon full lithiation are in the range of 4% ~ 10% [173]. The volumetric strain at the fully lithiated state is set as 5% and assumed to be linearly proportional to Li concentration. The maximum Li concentration can be calculated as $C_{max} = 0.05/\Omega$. When Li concentration on the surface of the particle reaches C_{max}, lithiation terminates and delithiation starts. At the C-rate τ =1 h (1C), the nominal flux $J_0 = 5.54\times10^{-5}$ mol/m^2.

The evolutions of the stress field and Li concentration within the NMC secondary particle at different dimensionless time steps t/τ are shown in Figure 5.10. The solid lines represent the Li distributions and stress profiles during Li insertion and the dashed lines represent those during delithiation. Figure 5.10a shows the distribution of Li concentration along the radius of the NMC particle at the charging rate 0.5C and Figure 5.10b shows the corresponding profile of the hoop stress. Li is inhomogeneously distributed because of the high charging rate relative to Li diffusion. This inhomogeneity is also visualized in the contour plot of Li distribution within the secondary particle upon full lithiation and delithiation in Figure 5.10e and f, respectively. Li insertion results in a compressive hoop stress field near the surface (Li rich) and tensile stresses at the center (Li poor) of the particle, while Li extraction unloads the stresses and induces a tensile hoop stress near the outer surface and compressive stresses at the center as shown in Figure 5.10b. The development of the tensile stresses may cause crack initiation and decohesion of the primary particles. In comparison, Figure 5.10c and d show the profiles of Li concentration and the hoop stress within the particle at the charging rate 2C. At the elevated C-rate, Li distributes more inhomogeneously, where a large amount of Li accumulates at the outer shell of the secondary particle and Li concentration at the center remains a small fraction of $C_{\max}$ at the fully lithiated state. Such a steep gradient of Li concentration reduces stresses within the particle because of the accumulation of Li near the outer shell regime while a large fraction of the spherical particle remains unlithiated. This is evident that the hoop stress (0.33 GPa) at 2C in the delithiated state is less than half of the hoop stress at 0.5C (0.85 GPa). This correlation between stresses and the charging rate explains the experimental observation that the slow charging rate 0.5C induces much more mechanical damage of the NMC secondary particles than the 2C fast charging case.

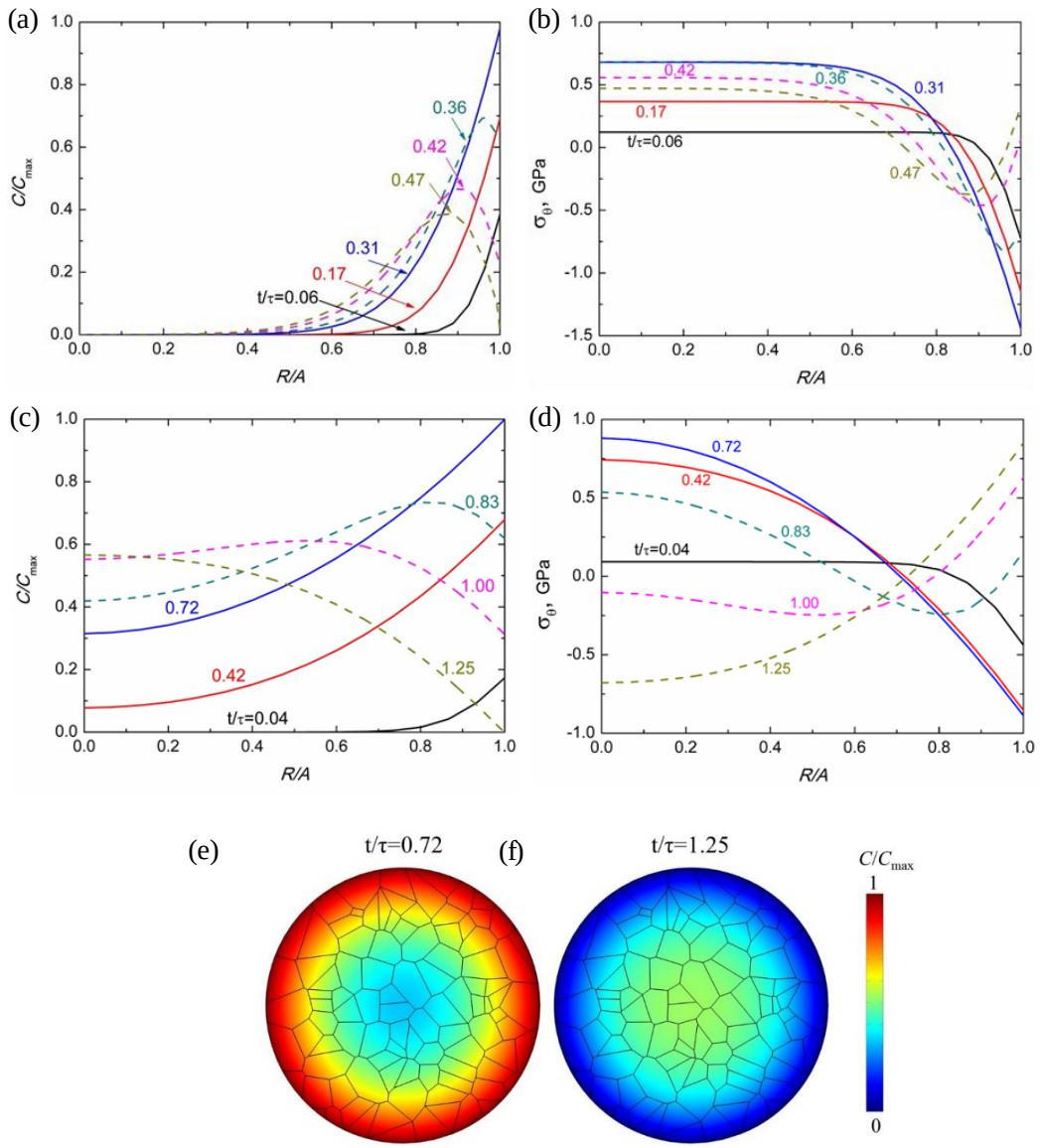

Figure 5.10. Distributions of (a) Li concentration and (b) hoop stress along the radius of a NMC secondary particle cycled at 0.5C charging rate. After delithiation, the outer shell experiences a large tensile stress caused by the inhomogeneous expansion of the particle. Distributions of (c) Li concentration and (d) hoop stress along the radius of a NMC particle cycled at 2C. The tensile stress induced near the surface shows a smaller value at the fast charging rate. Contour plots of Li concentration within the particle cycled at 0.5C upon full (e) lithiation, and (f) delithiation.

Maximum hoop stress and normalized capacity (the total amount of Li within the particle) as a function of the dimensionless charging rate $A^2/D\tau$ are plotted in Figure 5.11a. As a reference, 0.5C corresponds to the normalized charging rate $A^2/D\tau = 4.2$ and 2C corresponds to

$A^2/D\tau$=16.8. The normalized capacity monotonically decreases as the C-rate increases as expected, while the stress magnitude reaches maximum at an intermediate charging rate because of the competition between the overall mismatch strain and localized strain – stresses are minimum at the extremely slow charging rate because of homogeneous distribution of Li and absence of mismatch strain, as well as at the extremely high charging rate because of the highly concentrated Li in the outer shell regime and localized strains.

Crack initiation and propagation along the interface of the primary particles are simulated using the cohesive zone model in ABAQUS. A thermal strain field, equal to the concentration induced mismatch strain in NMC, is imported in ABAQUS and the resulting stress field and crack evolution are simulated. Figure 5.11b shows that a number of cracks initiate near the surface of the NMC secondary particle and propagate toward the center along the "grain" boundaries in the course of lithiation cycles at 0.5C, while Figure 5.11c shows that much fewer cracks grow from the surface regime at the 2C charging rate. It is noted that cracks also tend to initiate from the center in the fast charging case because of the developed large tensile stress in the interior core regime. The fracture pattern depends on the particular choices of the interfacial strength and fracture toughness in the cohesive zone model. Nevertheless, the qualitative observation that less fragmentation of the secondary particles at the fast charging rate remains valid.

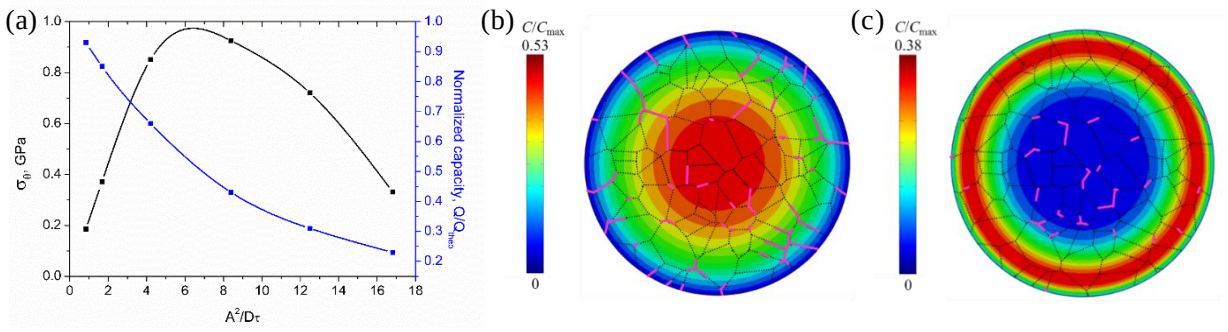

Figure 5.11. (a) The maximum hoop stress and normalized capacity of the NMC electrodes as a function of the normalized charging rate $A^2/D\tau$. The normalized capacity monotonously decreases as the charging rate increases, while the magnitude of the hoop stress reaches maximum at an intermediate charging rate. (b) A number of microcracks initiate near the surface of NMC particle and propagate toward the center during delithiation at a 0.5C charging rate. (c) Much fewer cracks grow within the particle at the 2C charging rate.

5.5 Conclusions

This chapter investigates the particle disintegration which attributes to the major mechanical degradation in NMC cathode materials. Microstructural evolution in the local regimes of NMC electrodes is tracked before and after electrochemical cycles. Controlled experiments are performed at different cycles with various voltage windows and charging rates. It is found that the slow charging rate results in severe disintegration of the NMC secondary particles while fast charging causes less damage. Electrochemical impedance spectroscopy (EIS) analysis confirms that the charging rate is a controlling factor on the mechanical disintegration of NMC particles and quantifies the effect of particle decohesion on the impedance of the cells. A numerical model is used to investigate the Li diffusion and stress evolution within the NMC secondary particles. The stresses reach maximum at an intermediate charging rate. Cohesive zone model is employed to interpret the crack formation and propagation in the weakly packed NMC secondary particles. The numerical results are in good agreement with the experimental observations. It is difficult to quantify the influence of the mechanical disintegration on the capacity fade of the cells given the

complexity of the electrochemical system, nevertheless, the post-mortem analysis on the microstructural features and direct comparison with the pristine state provide mechanistic understanding of the electrochemical behavior of Li-ion batteries and will promote engineering design of NMC materials for enhanced mechanical stability.

6. MECHANICAL AND STRUCTURAL DEGRADATION OF $LINI_XMN_YCO_ZO_2$ CATHODE IN LI-ION BATTERIES: AN EXPERIMENTAL STUDY

6.1 Introduction

$LiNi_xMn_yCo_zO_2$ ($x+y+z=1$) is among the best cathode materials for the electrification of automobile vehicles given its advantages in high capacity, electrochemical stability, and cost effectiveness [153, 200-202]. NMC is formed by partially replacing Co in $LiCoO_2$ by Ni and Mn to achieve the improved electrochemical performance while reducing the material cost. The composition of Ni, Mn, and Co can be largely tuned to optimize the capacity, rate performance, structural stability, and cost of Li-ion batteries [173, 203].

The structural stability is a key factor plaguing the cyclic performance of NMC materials [61, 63, 85, 179, 187]. Recent experiments have shown that the class of NMC, albeit of only ~ 5% volumetric change upon lithiation, suffers from heavy structural disintegration and mechanical failure after a number of cycles which significantly increase the ionic and electric impedance of batteries [35, 189, 204, 205]. Distinct from the conventional form of particle fracture in Si and $LiCoO_2$ for instance [39, 46, 47], as-synthesized NMC active materials have a hierarchical *meatball* structure that small primary particles of submicron size aggregate via van der Waals interactions and form secondary particles of tens of micrometers [102]. The interface between primary particles is rather weak and vulnerable to mechanical failure. By tracking the local morphological evolution, it is found that decohesion of primary particles constitutes the major mechanical degradation in NMC [204]. Figure 6.1 illustrates the interrelationships of mechanical, structural, and electrochemical degradation of NMC cathodes. The electrochemical cycle induces damage accumulation, such as cavitation and particle fracture [35], and deteriorates the mechanical

stability of NMC materials. The degradation of mechanical strength promotes the structural decohesion of NMC secondary particles. Consequently, the cracked particles result in the loss of the active materials and capacity fade in batteries. More importantly, the particle disintegration generates extra fresh surface and facilitates surface construction of the resistance layer which inhibits the ionic and electric conduction, reduces the cyclic efficiency, and ultimately leads to the failure of batteries [177, 178, 187, 198].

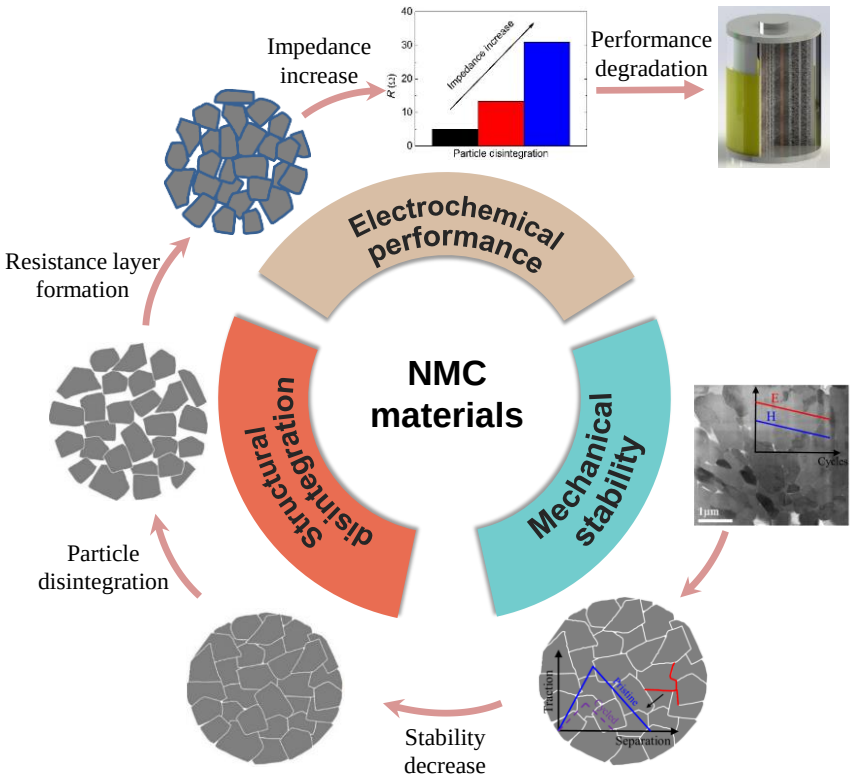

Figure 6.1. Schematics of the mechanical, structural, and electrochemical degradation of NMC cathode materials. Electrochemical cycles induce damage accumulation and deteriorate the mechanical stability of NMC particles. The mechanical degradation promotes the structural decohesion of NMC secondary particles. Consequently, the cracked particles facilitate the formation of resistance layer on the fresh surface which increases the ionic and electric impedance and ultimately leads to the failure of batteries. The cavitation figure is reproduced with permission from Kim *et al.*[35]

The mechanical properties of NMC used in practical batteries are widely unknown. Experimental characterization of the structural and mechanical stability of NMC is a challenge, partially because of the difficulty of mechanical measurement for air-sensitive battery materials, and partially because of the heterogeneity of NMC hierarchical particles at the micron scale [36, 206]. A couple of recent papers reported elastic modulus and hardness of NMC thin films and pellets [207, 208], nevertheless, the mechanical behavior of NMC of a meatball structure, dominated by the interface between the primary particles, largely differs from that of the condensed format of thin films or pellets. Likewise, the fracture toughness (cohesive strength) of the weakly bonded NMC secondary particles should be much lower than the intrinsic material properties measured in the bulk materials. Further challenges associated with the mechanical characterization of NMC particles include (I) the requirement of the measurement in an inert environment, (II) the local mapping of the highly heterogeneous composite electrodes at the microscopic level, and (III) the dynamic evolution of the chemomechanical properties of electrodes at different states of charge and after a number of lithiation cycles – no data is thus far available for complete characterization of the mechanical stability of NMC in the course of Li reactions.

This chapter reports a systematic measurement of the elastic modulus E, hardness H, and interfacial fracture toughness K_c of NMC as a function of the state of charge (SOC) and cyclic number. Instrumented nanoindentation in an inert environment is employed to probe the local mechanical properties of an example $LiNi_{0.5}Mn_{0.3}Co_{0.2}O_2$ (NMC532, referred as NMC in the following text) electrode. The mechanical properties largely depend on the lithiation state, albeit the layered crystal lattice is maintained during Li insertion and extraction, and further degrade as the electrochemical cycles proceed. The quantitative results of the elastoplastic (E, H) and

interfacial (K_c) properties of NMC help understanding of the chemomechanical behavior of NMC materials and will aid the design of composite electrodes of enhanced mechanical and structural stability.

6.2 Experimental methods

6.2.1 Sample preparation

Commercial NMC cathodes (MTI Co.) consisting of 94.2 wt% active materials, 3.0 wt% carbon black and 2.8 wt% PVDF are used as the pristine sample. The coating thickness of the NMC cathode is 45 μm ± 6 μm and the areal loading is 121 g/m^2. To remove moisture, as-received electrodes are dried in a vacuum oven overnight at 80 °C and then stored in a glovebox in dry argon atmosphere (moisture and oxygen levels less than 1.0 ppm) for several days before use. Next, electrodes are assembled into coin cells for electrochemical cycles. The NMC electrode, Li foil, and Celgard-2502 membrane are used as the cathode, anode, and separator in the CR-2032 type coin cells. The electrolyte is composed of 1 M $LiPF_6$ salt dissolved in ethylene carbonate/diethyl carbonate of 1:1 volume ratio (EC/DEC, 1:1, Sigma Aldrich). All assembled cells are placed to rest overnight to ensure complete wetting before electrochemical tests.

6.2.2 Electrochemical characterization

Galvanostatic cycling (BT-2043, Arbin) is performed. Cyclic tests are designed to investigate the influence of two major factors, state of charge and cycle number, on the mechanical properties of NMC particles. To evaluate the influence of SOC, first batch of cells are charged with C/20 charging rate and 3-4.3 V voltage window until cells reach 33%, 66%, and 100% of SOC, respectively. To examine the effect of cycle number, second batch of cells are initially charged and discharged at C/20, followed by 30, 50, and 100 cycles at C/5 charging rate. After

cycles, coin cells are disassembled in the glovebox. Cycled NMC electrodes are carefully taken out from the coin cells, washed several times with dimethyl carbonate (DMC, Sigma Aldrich), and dried overnight in a vacuum oven at room temperature.

Both pristine and cycled electrodes are polished (EcoMet 3000, Buehler) before indentation. Samples are mounted on the Al holder and the top surface is polished using micro diamond compounds (LECO Co.). Grit sizes of 3 and 1 μm are used for the initial polishing and then 0.05 μm colloidal silica suspension is used for final polishing until a mirror-like finish is obtained. Samples are cleaned with isopropyl alcohol after final polishing and delivered into glovebox for nanoindentation.

To measure the intrinsic properties of NMC in the bulk form, dense pellets are also prepared. The as-received NMC powders (secondary particles, MTI Co.) are first ball milled into primary particles of submicron size. Then, 2 g of milled powders (primary particles) are pressed into a die (13 mm diameter) under an applied uniaxial compressive stress of 180 MPa (Model 4350, Carvar). Compressed pellets are sintered at 1000 °C for 10 h with a heating rate of 10 °C/min and are left in the furnace until cooled. As-synthesized NMC pellets are initially polished by silicon carbide sandpaper and then by diamond polishing pads.

6.2.3 Mechanical characterization

The elastic modulus E, hardness H, and interfacial fracture toughness K_c are measured using the instrumented nanoindentation (G200, Keysight) in the argon-filled glovebox. Targeted indentation [209-212] is performed at the center of the NMC secondary particles of the diameter over 10 μm. The maximum impression size is typically less than 1 μm, and the distance between the indents and the adjacent matrix is large enough to avoid the influence of the surrounding medium. E and H are measured with Berkovich indenter using the Oliver-Pharr method [125], as

presented in Chapter 2.2. Indentations with maximum indentation load of 1 mN are conducted on 15 different secondary particles in each batch. The loading, holding, and unloading times are 10 s, 5 s, and 10 s, respectively. The load-displacement curves indicate that no detectable cracks are formed during the tests. A series of additional tests are performed to ensure the convergence of the measured results.

Another series of indentations are conducted on the same samples to measure the interfacial fracture toughness K_c. Cube-corner indenter with a sharp semiapex angle (apical face angle 35.3°) is used to initiate radial cracks between the primary particles. The crack length, the indentation load, and the hardness to modulus ratio are combined to calculate the fracture toughness, as presented in Chapter 2.2. The maximum load P_{max} for the indentations varies from 1 to 5 mN. The continuity of the load-displacement responses at low loads (1-2 mN), indicate that there is no detectable pop-in (i.e. crack formation) at this load range. Therefore, they are fitted for the anticipated loading curve in the hypothetical absence of pop-in using a second-order polynomial function. The load-displacement responses with pop-in at higher loads (3-5 mN) are used to calculate the h_x, h_m and c.

6.2.4 Material characterization

The microstructure of NMC is imaged using scanning electron microscopy (SEM, T330, JEOL). The average sizes of NMC secondary and primary particles, Figure 6.2a and b, are 10 and 1 μm, respectively. The SEM image in Figure 6.2c shows the surface morphology of sintered NMC pellet where no obvious pores and cracks are present. The fractured surface of NMC pellet in Figure 6.2d indicates that the average grain size of NMC pellets is around 10 μm. X-ray diffraction (XRD) is performed using a diffractometer (D-8 Focus, Bruker) with Cu K-alpha radiation in a 2θ range of 12–90° at 100 mA and 40 kV. XRD Bragg peaks of the NMC particles as well as the

sintered NMC pellets are shown in Figure 6.2e. The similar XRD patterns confirm that the sintered NMC pellet has same elemental composition as the pristine NMC electrode. Post atomic force microscopy (AFM) topography images (Dimension 3100, Veeco Instruments) are acquired to examine the accuracy of the crack length calculated from the pop-in method. Scan size 3.35 μm and scan rate 0.5 Hz are used to obtain the height image of the indentation impression. AFM-based crack length is obtained by carefully measuring the distance from indentation center to the crack tip, and then is compared with the crack length calculated from the pop-in method.

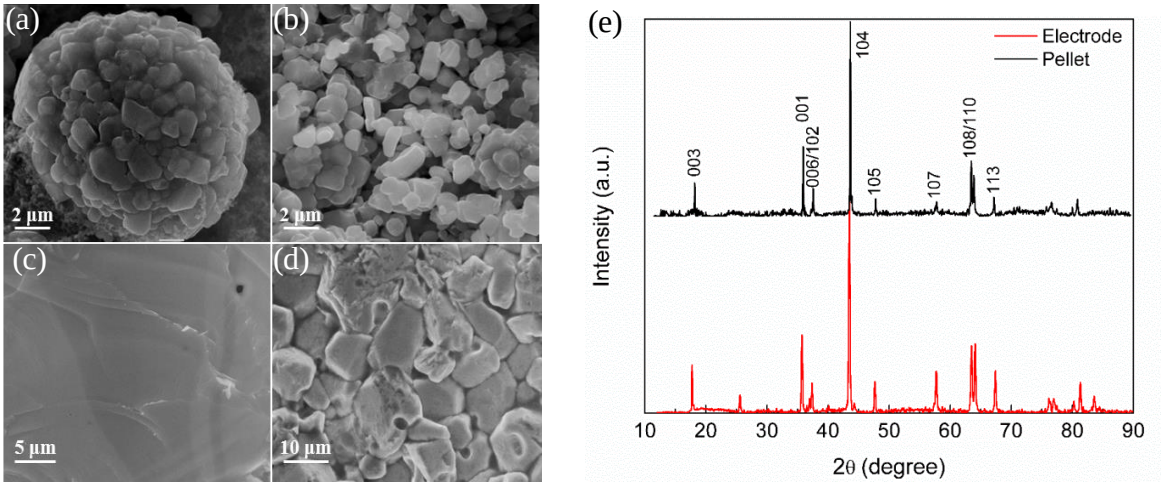

Figure 6.2. SEM images of (a) a NMC secondary particle, (b) NMC primary particles, (c) surface of the sintered NMC pellet, (d) fractured surface of sintered NMC pellet. (e) XRD profiles of NMC electrode and sintered pellets. The additional peak at $2\theta = 26.8°$ for NMC electrode is induced by the carbon black contained in the electrode. The XRD patterns show that the NMC particles in electrode and pellets have the same chemical compositions.

6.3 Results and discussion

NMC cathode in half cells are cycled and then performed nanoindentation at given states of charge and after specific cyclic numbers. Figure 6.3a shows the charge-discharge curves at the 1^{th}, 50^{th}, and 100^{th} cycles by a galvanostatic test of C/5 charging rate and 3-4.3 V voltage window. The corresponding discharge capacities are 160.5, 150.4, and 134.9 mAh/g, respectively. Figure

6.3b presents the discharge capacity and coulombic efficiency of the coin cells as a function of cycle number. As the cycles proceed, the half cells retain 93.7% and 84.1% of their initial capacity after 50 (sample I) and 100 (Sample II) cycles, respectively. The coulombic efficiency in the initial cycle is 84.3% and remains over 97.5% in the subsequent cycles. The electrochemical behavior of NMC electrodes is consistent with the literature report [187, 213]. The SEM images in the inset of Figure 6.3b show the microstructure of the local regimes where no apparent damages are present and nanoindentation is performed.

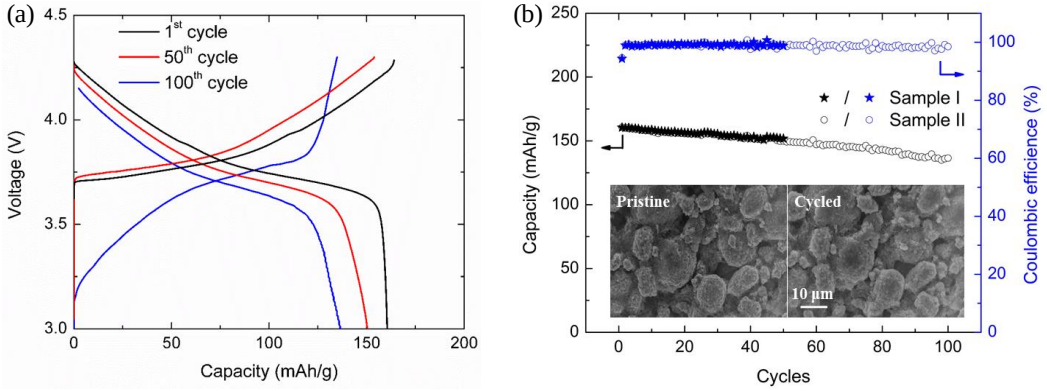

Figure 6.3. (a) Charge/discharge curves of the NMC/Li half-cell in the 1st, 50th, and 100th cycles. (b) Specific discharge capacity and Coulombic efficiency of NMC cathode as a function of the cycles. Insets show the microstructure of the local regions where indentation tests are performed.

NMC samples are polished before nanoindentation to eliminate the influence of surface roughness. The exemplary morphology of a pristine NMC electrode before and after polishing is shown in Figure 6.4a and b. The shape of the NMC secondary particles before polishing is spherical in nature and primary particles are closely packed without obvious gaps in between. After polishing, the packing of primary particles remains intact, and most secondary particles show a flat cross section which suits the indentation. It is worth noting that nanoporosity may exist along the grain boundaries which are inherited from the material synthesis procedure [35]. In the

indentation experiments, NMC particles without apparent voids or cracks are selected. Nevertheless, the presence of the microscopic defects is part of the morphological nature of the NMC particles, and their influence on the mechanical strength of NMC is embedded in the experimental results. Figure 6.4c shows the surface morphology of an indented particle where the indentation site is located at the center of the spherical particle. The impression is much smaller than the particle size. No detectable damage except the impression is observed, Figure 6.4c. The load-displacement is continuous and is solely determined by the mechanical response of NMC secondary particles as shown in the inset of Figure 6.4.

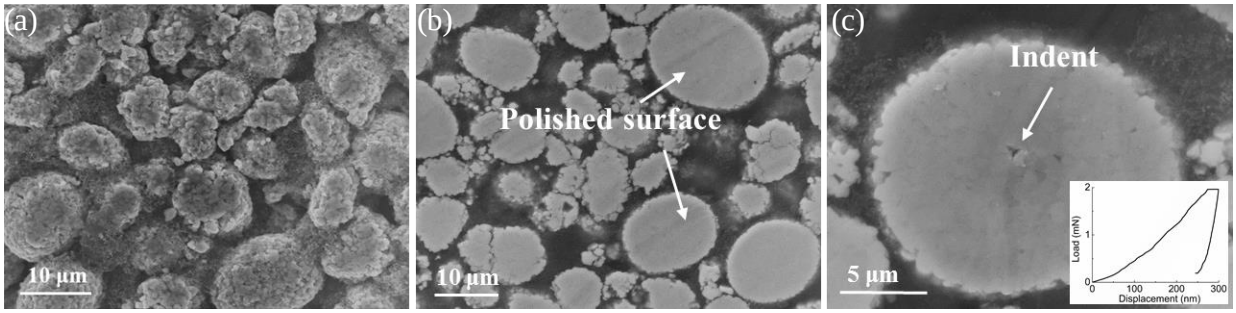

Figure 6.4. SEM images showing the surface morphologies of the NMC particles (a) before and (b) after polishing. (c) Local view of a NMC secondary particle after nanoindentation. Inset shows the load-displacement response of indentation.

Instrumented nanoindentation is widely used to measure the mechanical properties of bulk materials at small scales. Nevertheless, nanoindentation of composite materials of microscopic heterogeneity remains technically challenging and requires careful calibration. The composite electrodes consist of NMC active particles embedded in a porous matrix of carbon black conductive agents and polymer binders. The constituents have vastly different mechanical properties. Factors influencing the nanoindentation results include (I) the indentation site, (II) the substrate (surrounding matrix) effect, and (III) the applied indentation load. The effect of the above

factors is examined by conducting a series of control experiments. The targeted indentation with a precise selection of the indentation site is employed to obtain the properties of the single phase of NMC secondary particles in the composite configuration.

The sensitivity of the mechanical measurement on the indentation site is first evaluated. Tests performed near the interface between NMC particles and the surrounding matrix will deviate from the results of pure NMC materials. Elastic modulus E is measured at various locations across two NMC secondary particles of different diameters. The maximum applied load is 1 mN. Figure 6.5a plots the dependence of E on the normalized position of the indentation site, where 0 and 1 represent the interface between NMC and the matrix, 0.5 represents the center of NMC particles, and values smaller than 0 or larger than 1 represent the matrix regime. As expected, the modulus measured in the matrix is much lower (< 15 GPa) than that within NMC particles (~145 GPa), and the results close to the interface lie in between these two values. For the regions away from the interface, $0.25 < y/d < 0.75$, the measured modulus is consistent and represents the property of pure NMC particles. The blue dashed line dictates the average E measured at the center of 15 different NMC particles which is about 145 GPa. Furthermore, the convergence of E in the two different NMC particles shows the same trend which confirms that the results of targeted indentation are independent of the particle size as long as the indentation site is far away from the interface. The location of nanoindentation at the center of NMC secondary particles is selected to avoid the interference of the interface and the surrounding matrix.

Next, the substrate effect is examined because the porous conductive matrix is considerably compliant than the NMC particles. Mechanical properties of NMC cathode embedded in two different matrices are measured - one in the conventional mixture of carbon black and PVDF binders and the other in a much stiffer polymer matrix (Phenolic resin, PR). The elastic modulus

E and hardness H of PR (10.1 ± 0.8 GPa and 1.1 ± 0.2 GPa, respectively) are one order of magnitude higher than that of the conventional conductive matrix (1.78 ± 0.35 GPa and 0.043 ± 0.01 GPa, respectively). The volume fractions of NMC active particles in the two composites are close as shown in Figure 6.5b. The red and black columns in Figure 6.5b show the modulus and hardness of NMC measured in the two matrices – the values are very close, E = 142.5 ± 11.33 GPa and H = 8.58 ± 1.3 GPa for NMC in CB+PVDF, and E = 146.6 ± 9.81 GPa and H = 8.65 ± 1.02 GPa for NMC in PR. This comparison indicates that the selection of the matrix surrounding and underlying NMC particles has little effect on the indentation results because the indentation depth and the impression size are considerably smaller than the particle size.

The maximum indentation load is another important parameter for the test. A low indentation load sacrifices the experimental accuracy due to the resolution limitation, while a high load may introduce undesired effects of cracking or particle sink-in. Both the quasi-static (QS) and continuous stiffness measurement (CSM) methods are employed to find the optimal indentation load. The CSM method allows a continuous measure of the dynamic material stiffness during loading using a low magnitude oscillating force [214]. Figure 6.5c plots the modulus E measured under different indentation loads. Two regions are identified. In region I, where the indentation load is smaller than 2 mN, E is independent of the applied load and converges to the intrinsic value of NMC secondary particles. In region II, E measured by the QS method monotonously decreases as the indentation load increases. The CSM results show several sudden drops at certain indentation loads. These drops correspond to the formation and propagation of cracks, which are readily induced by indentation in brittle materials. The cracking features are also represented by the pop-in events on the load-displacement curves, as shown in the inset of Figure 6.5c. The sharp increase of the indenter penetration causes overestimation of the indentation depth and the contact

area; therefore, the measured values are lower than the intrinsic properties of NMC particles. With further increase of indentation load over 10 mN, *E* continuously decreases because of interface cracking and particle sink-in which renders the Oliver-Pharr method unsuitable in determining the mechanical properties of the measured samples [209]. Herein maximum applied load is set to be 1 mN, well below the threshold (2 mN) to induce cracks in the NMC secondary particles.

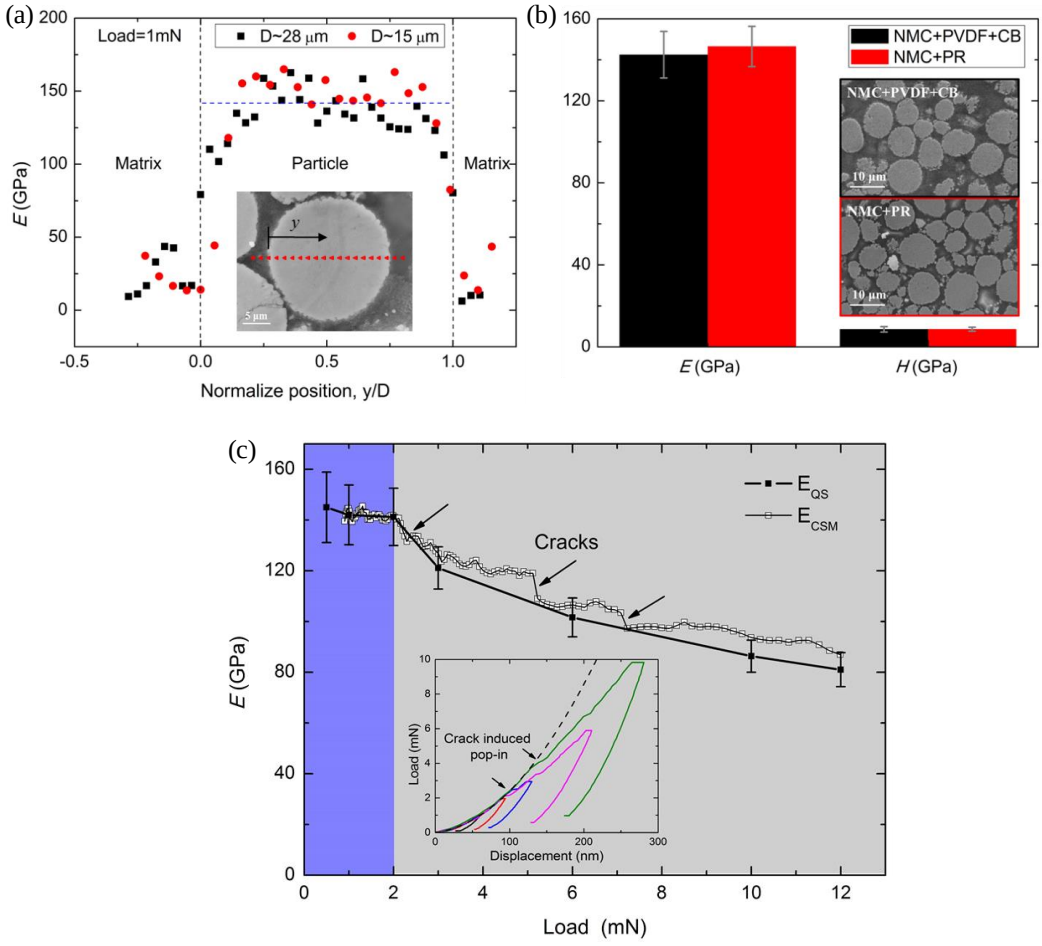

Figure 6.5. (a) Young's modulus *E* measured at different locations across the NMC secondary particles. The measurement is independent of the particle size and the indentation location as long as the indentation sites are away from the particle/matrix interface. (b) Young's modulus and hardness of NMC secondary particles measured in two types of matrixes: PVDF+CB and PR. The small-scale measurement of mechanical properties is insensitive to the selection of the matrix material. (c) Young's modulus of NMC extrapolated from different indentation loads using both the quasi-static and CSM methods. The load-displacement curves in the inset show that the reduction of *E* at high load is due to the cracks induced by indentation.

The elastic modulus E and hardness H of pristine NMC secondary particles are 142.5 ± 11.3 GPa and 8.6 ± 1.3 GPa, respectively. Table 6.1 shows the mechanical properties of the NMC secondary particles and sintered NMC pellets. Both the modulus and hardness of the NMC segregated particles are considerably lower than that measured in the NMC condensed pellets (177.5 ± 19.5 GPa and 12.6 ± 1.4 GPa, respectively). The pellet measurement agrees well with other reports in recent literature [203, 207] and represent the properties of NMC in the bulk form. The lower values of E and H of NMC secondary particles are attributed to the weak interface dictated by van der Waals interactions between primary particles. The size of the nanoindentation impression is around hundreds of nanometers which is comparable with the size of NMC primary particles. The mechanical response of NMC is largely influenced by the "grain boundaries". The interface sliding and defects propagation underneath the indenter significantly reduce the mechanical strength of the NMC composites. Compared to the bulk properties, the behaviors of the segregated particles are more informative on the mechanical and structural stability of NMC electrodes in real batteries.

Table 6.1. Experimental values of mechanical properties of NMC particles and pellets.

Material properties	NMC particles	NMC pellets
Modulus E (GPa)	142.5 ± 11.3	177.5 ± 19.5
Hardness H (GPa)	8.6 ± 1.3	12.6 ± 1.4
Fracture toughness K_c (MPa-m$^{1/2}$)	0.102 ± 0.03	0.309 ± 0.04

The mechanical properties of NMC largely depend on the state of charge and degrade as the electrochemical cycles proceed. Figure 6.6a shows the elastic modulus E and hardness H as a

function of SOC during the first delithiation, where 0% represents the pristine NMC and 100% represents $Li_{0.5}Ni_xMn_yCo_zO_2$. Delithiation of NMC results in a significant reduction of the mechanical properties. The modulus and hardness of fully charged NMC (111.6 ± 6.4 GPa and 7.1 ± 0.8 GPa, respectively) are about 77% and 80% of the values for pristine NMC particles. Figure 6.6b shows the degradation of the mechanical properties of NMC over cycles. The most dramatic reduction of the elastic modulus and hardness occur after the first lithiation cycle. This may be due to the loss of crystallinity of NMC after the initial electrochemical cycle [35]. Complete understanding of the microstructural change associated with early lithiation cycles is to be explored in future studies. After the first cycle, the elastic modulus and hardness of fully lithiated NMC steadily decrease and reduce to 107.3 ± 13.3 GPa and 6.5 ± 0.9 GPa, 74% and 73% of their initial values in pristine NMC, after 100 cycles. The loss of the mechanical properties over cycles is likely due to the formation and accumulation of nano- and micro-sized voids at the interface between primary particles. Upon electrochemical cycles, the repetitive Li insertion and extraction induce constant volume expansion and contraction. The volumetric change generates mechanical stresses that facilitate the formation of defects concentrated at the grain boundaries. The interfacial defects accumulate and reduce the mechanical strength of the segregated particles while nanoindentation probes. An evidence supporting this scenario is the observation by Kim *el al.* on the accumulation of damages in the course of lithiation cycles using scanning transmission electron microscopy (STEM) [35]. It should be noted that the generation of the nano- or micro-defects does not necessarily cause disintegration of primary particles or macroscopic damages, however, the population of the defects and interfacial sliding can significantly weaken the overall mechanical performance of NMC secondary particles. The microstructural damage alone may not fully account for the degraded mechanical properties of Li transition metal oxides over cycles [212].

Another factor contributing to the reduction may be due to the atomic structural evolution of NMC upon lithiation cycles. Specifically, when Li ions are extracted from the lattice of a layered structure, the TMs ions of a similar size of Li^+ (mostly Ni^{2+}) can occupy the vacant Li sites. This cation mixing results in lattice distortion and thus destabilize the layered structure, leading to the degradation of the mechanical strength of NMC materials [207]. The quantitative mapping of the mechanical properties of NMC on the state of charge as well as the cycle number provide useful input for computational modeling of chemomechanical behaviors of batteries and shed insight on the damage accumulation in NMC materials over cycles. The evolution of the elastic property of NMC has been explained by a prior work on first-principles theoretical modeling [133]. In this work [133], cohesive energy, defined as the energy to break the lattice into isolated free atoms, is used to represent the strength of atomic bonding and correlate with the elastic property of materials. The cohesive energy shows the similar linearly decreasing trend when Li is extracted. As shown by the evolution of atomic structure, the reduction of the cohesive energy of NMC during delithiation is attributed to (I) the Jahn-Teller distortion, (II) the decrease of electrostatic interaction between Li-O, and (III) the reduction of the TM-O polarization [203, 215].

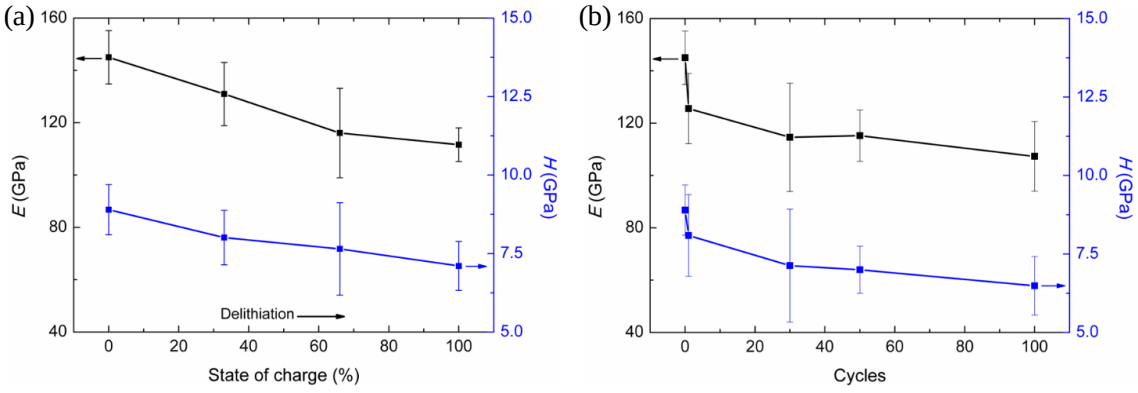

Figure 6.6. Young's modulus and hardness of NMC secondary particles as a function of (a) the state of charge and (b) cycle number.

Next, Interfacial fracture toughness K_c of NMC secondary particles is measured using cube-corner indenter in a series of indentation experiments. Post AFM topography is employed to analyze the crack patterns within NMC particles after nanoindentation. Figure 6.7a sketches the interface between primary particles (black dashed lines), radial and lateral cracks (blue lines), and indentation impression (orange lines). The inset shows the AFM image of an indent and a crack of length *c*. In general, radial cracks readily form at indentation corners and then propagate outward along the radial planes. It is observed that radial cracks mostly propagate and deflect along the interface because of the least resistance along grain boundaries. When the indenter is located well within a primary particle, the applied load may not generate radial cracks; instead, it causes ejection of a chip of materials. Previous studies showed that chip ejection in brittle materials is usually associated with lateral cracks (scallop-shape) near or directly beneath the indenter [132, 216]. The weak interface in NMC promotes the formation of lateral cracks and chip ejection in primary particles, Figure 6.7a.

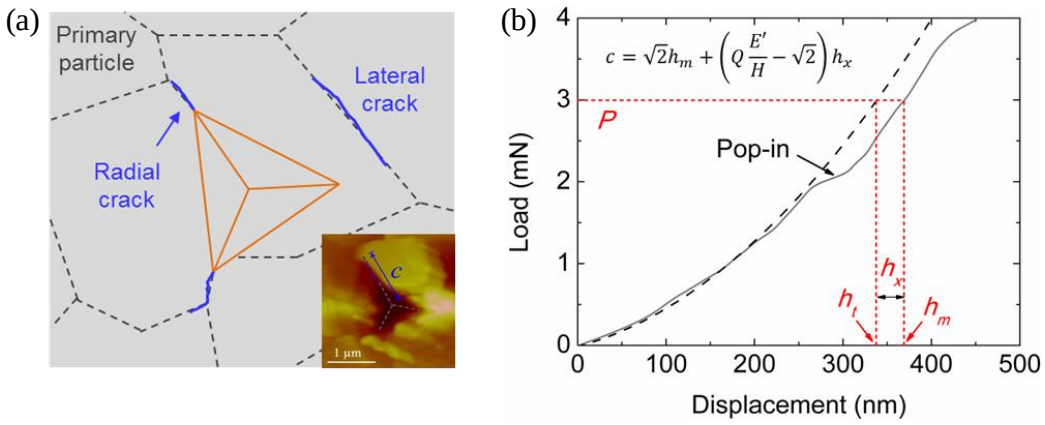

Figure 6.7. (a) Schematics of crack patterns within the NMC secondary particle after nanoindentation. Black dashed, blue, and orange lines represent the interface between the primary particles, the radial and lateral cracks, and the indentation impression, respectively. Inset shows the post AFM image of the indentation impression and the indentation-induced cracks. (b) Load-displacement curve showing the pop-in event and the h_x, h_m, h_t, and P in the calculation of K_c. (b) with the AFM measurement shown in the inset of (a).

The complex fracture modes involving crack deflection and material ejection make the optical measurement of the crack length difficult. Here the pop-in method is used to calculate the radial crack length *c*. Crack length *c* is determined from equation (5) (inset in Figure 6.7b) where the plane-strain modulus *E'* and hardness *H* are determined by previous measurements; Figure 6.7b shows the load-displacement curve with the pop-in event obtained from the nanoindentation measurement in Figure 6.7a. The pop-in depth h_x is determined from the load-displacement curves with a maximum applied load of 3-5 mN. The hypothetical load-displacement response without any crack formation (dashed line) is a fitting of the load-displacement curve at small loads of 1–2 mN following the Hertzian fitting procedure. Field *et al.* demonstrated that crack deflection or material chipping does not interfere with the calculation of crack length using the pop-in method [132]. The crack length obtained from the pop-in calculation is further compared with AFM imaging. The AFM images give slightly smaller values presumably because of the invisible radial cracks beneath the surface [212].

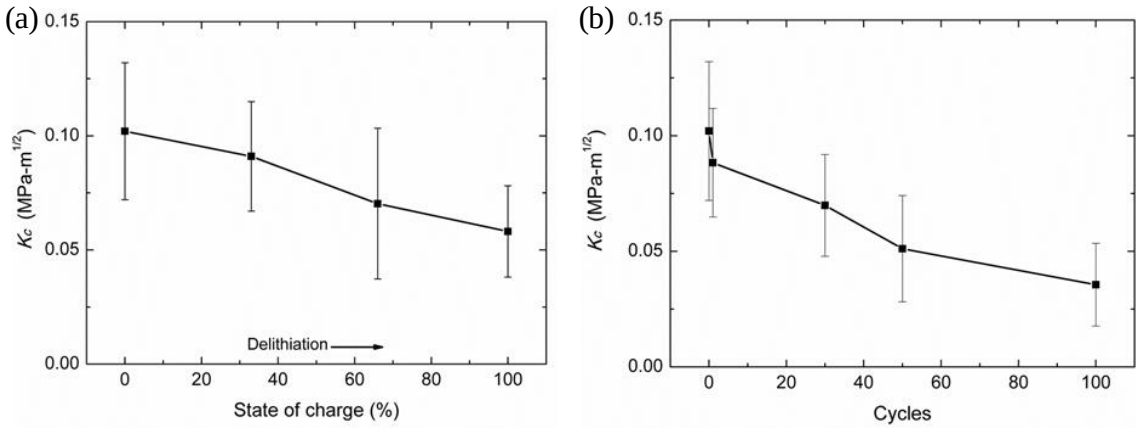

Figure 6.8. Interfacial fracture toughness K_c of NMC secondary particles as a function of (a) the state of charge and (b) cycle number.

The fracture toughness K_c is calculated using the radial crack length obtained by the pop-in method, the indentation load, and the hardness to modulus ratio. 15 indentations are conducted on each NMC sample. Among these results, 8-10 indentations are used to calculate the mean values and standard deviations of K_c, as shown in Figure 6.8. The rest of experiments showing erroneous load-displacement curves are excluded from the reports. The mean Kc for pristine NMC particles, representing the interfacial fracture toughness, is 0.102 ± 0.03 MPa-$m^{1/2}$. This value is three times lower than fracture toughness of sintered NMC pellets which is 0.309 ± 0.04 MPa-$m^{1/2}$. Figure 6.9 shows the comparison of the load-displacement responses of NMC particles versus pellets. The aggregated particles exhibit a much lower threshold of crack (~ 2 mN) than NMC pellets (> 10 mN). As-synthesized NMC particles clearly have lower structural stability than bulk pellets because of the weak interface joining the primary particles as compared to the inter-grain cohesive strength of the pellets. The fracture toughness of NMC pellets is close to the reports of other Li transition metal oxides, for instant, 0.49 ± 0.13 MPa-$m^{1/2}$ for pristine $LiMn_2O_4$ [209] and 0.9 ± 0.1 MPa-$m^{1/2}$ for $LiCoO_2$ [212]. It should be noted that grain size of the sintered pellets has a significant effect on the fracture toughness, thus, K_c of Li transition metal oxides can vary over an order of magnitude depending on the grain size of the sintered pellets [211]. The intrinsic fracture toughness of bulk NMC without any defects should be higher than that measured from the NMC pellets. Prior experiments have shown that the grain size affects the nucleation and propagation of intergranular cracks. A larger grain size provides a longer path of fracture propagation and thus decreases the material toughness. It is expected that the K_c of NMC of larger primary particles would show lower interfacial fracture strength. It will be interesting to systematically study the dependence of K_c of NMC on the grain size in future work.

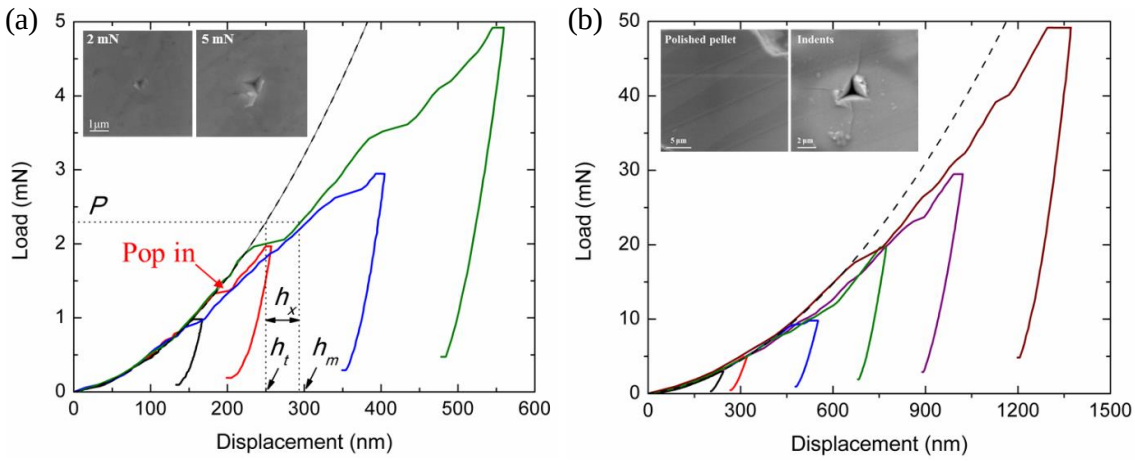

Figure 6.9. Load-displacement responses of (a) NMC secondary particles and (b) NMC pellets under different indentation loads using cube corner indenter. NMC pellets show a much higher cracking threshold than the NMC secondary particles. The inset SEM images show the indentation impression under different loads.

The impact of electrochemical cycles on the fracture properties of NMC particles is further explored. Figure 6.8a plots K_c as a function of state of charge in the first charging (delithiation) process. K_c exhibits a monotonous decrease upon Li extraction and reduces by nearly a factor of two in $Li_{0.5}Ni_{0.5}Mn_{0.3}Co_{0.2}O_2$. This reduction of fracture resistance may be caused by residual tensile stresses. Delithiation of NMC is accompanied with a volumetric contraction. The deformation is constrained by the coherence of the grain boundaries and induces a field of tensile stresses within the aggregated particles, which facilitates the formation and propagation of radial cracks during indentation tests. The stress field developed in the course of Li reactions apparently weakens the interface of primary particles and reduces the integrity of the NMC meatball structure. Figure 6.8b shows the evolution of K_c as the electrochemical cycles proceed. Similar to E and H in Figure 6.6b, K_c dramatically decreases after the first lithiation cycle. The poor retention of mechanical properties in the early lifetime is attributed to the severe microstructural damages after the first few cycles [35]. K_c steadily decreases afterwards and reaches 0.036 ± 0.018 MPa-$m^{1/2}$

after 100 cycles – over 60% of the fracture strength is lost compared to the pristine NMC. This dramatic reduction is due to the accumulation of microstructural damages at the interfaces. In the prior STEM study [35], continuous void expansion and micro-crack generation were observed along the interface as the cycle number increases, primarily induced by the repetitive volumetric change upon electrochemical cycles. The dynamic evolution of the mechanical properties of electrodes in the cyclic life illustrates that the electrochemical practice could significantly deteriorates the structural stability of NMC materials and results in potential catastrophic failure of batteries. It is also interesting to note that the different fracture behaviors of NMC segregated particles versus bulk pellets. While the interfacial fracture toughness of NMC particles is very sensitive to the presence of small-scale defects, Swallow *et al.* found that the bulk Li transition metal oxides such as $LiCoO_2$ had minor dependence on the microstructural damages in cycles [212]. This remarkable difference again draws attention on measuring the chemomechanical properties of particles in real batteries which is more informative for the design of enhanced mechanical and structural stability of battery materials.

6.4 Conclusions

Elastic modulus, hardness, and interfacial fracture toughness of NMC particles are measured using instrumented nanoindentation in an inert environment. NMC particles show considerably lower mechanical properties than sintered pellets because of the hierarchical meatball structure. The interface joining the primary particles plays a critical role in determining the mechanical behaviors of NMC cathode materials. The dynamic evolution of the mechanical properties is obtained as a function of the state of charge and the cycle number. Both the elastic modulus and hardness of NMC largely decrease when Li is extracted from the layered crystalline lattice. The mechanical properties of NMC, in particular the interfacial fracture resistance,

significantly decrease as the electrochemical cycles proceed. The loss of mechanical strength is due to the accumulation of microscopic defects and damages at the interface of the constituent primary particles. The experimental results represent the quantitative characterization of mechanical and structural stability of NMC cathode used in real batteries. The output will provide mechanistic understanding on the damage evolution in NMC materials over cycles and offer important insight on the design of composite electrodes of improved chemomechanical performance for high-capacity batteries.

7. CORROSIVE FRACTURE OF ELECTRODES IN LI-ION BATTERIES

7.1 Introduction

Mechanical degradation upon ion reactions in redox active materials is a prevalent issue causing impedance growth and performance fade in the state-of-the-art Li-ion batteries and solid-state batteries [4, 179, 217]. When Li is intercalating into the host material, electrodes deform with a characteristic volumetric strain ranging from a few percent in intercalation-type electrodes to a few hundred percent in conversion- or insertion-type materials [36]. Fracture is a consequence of the repetitive deformation and contributes to a major mechanism of aging in a wide spectrum of materials over cycles [60, 61, 63, 139, 179], including fracture of the redox active materials [39, 41, 46], crack of inactive conductive matrix [42], debonding of composite films from the current collector [218], shedding of the solid electrolyte interface (SEI) [45], and structural disintegration of aggregated particles [35, 193, 204] in both anode and cathode. Mechanical degradation and the constant disruption of the solid interfaces result in Li depletion, increase of the ohmic and thermal resistance, and steady fade of the cyclic efficiency, while the isolation of the active materials from the conductive network causes a mostly immediate loss of capacity of batteries.

Fracture is an overwhelming issue in electrodes of intrinsically large deformation associated with Li reactions [39, 219]. The formation of extensive cracks in the early state of the electrochemical reactions causes catastrophic failure of batteries. Limited success so far has been achieved to mitigate such mechanical degradation in high-capacity electrodes [60, 179, 220]. Less recognized is mechanical failure in electrodes of relatively small volumetric deformation (<10%) such as $LiNi_xMn_yCo_zO_2$ (NMC, x+y+z=1), $LiCoO_2$ and $LiMn_2O_4$ cathode [46, 47, 193, 204]. Mechanical stresses in the small-volumetric-change materials also induce extensive materials defects including dislocations [221], cavitation [35], intragranular and intergranular cracks [41].

There have been tremendous efforts to analyze and predict fracture of electrodes caused by diffusion-induced stresses [32-34, 36, 99, 180, 222, 223]. Most of the early studies focus on the fracture analysis using either a stress criterion [32, 139] or the Griffith fracture mechanics [33, 34, 222] to predict the onset of crack. It has been revealed that the particle size and the charging rate significantly influence the fracture behavior of electrodes which was soon confirmed by several experiments [39, 219, 224]. The later development of continuum theories of coupled diffusion and finite deformation allows to examine the close interactions between the diffusion kinetics and mechanical stresses in batteries and to explore the dynamics of crack growth coupled with Li transport near the crack tip. [85, 92, 141, 225].

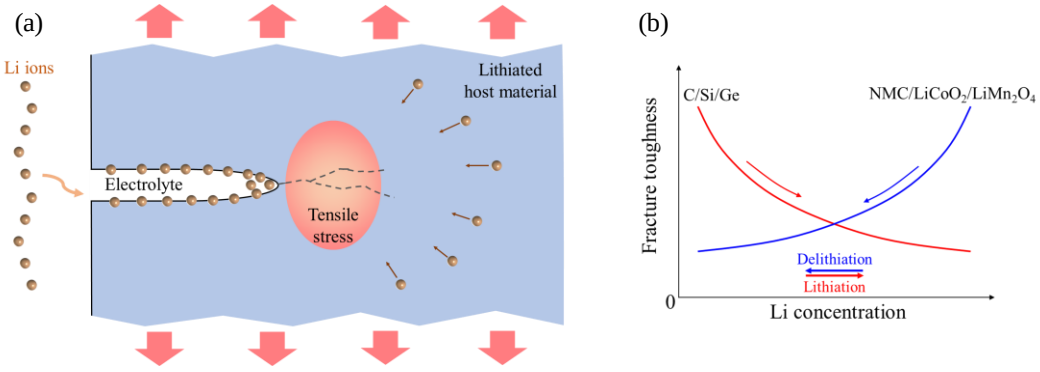

Figure 7.1. (a) Schematic of corrosive fracture of electrodes in Li-ion batteries. Tensile stress field develops at the crack tip in the electrode under far-field strain. Li diffuses rapidly on the crack surface and accumulates at the crack tip. Li reaction causes embrittlement of the host material and growth of the crack. (b) Sketch of experimental observations of Li embrittlement in anode and cathode materials. Fracture toughness of anode materials usually decreases upon Li insertion while fracture toughness of cathodes decreases during Li extraction.

Fracture in electrochemical systems is often corrosive in nature. Mechanical stresses regulate Li diffusion and the crack propagation is tightly coupled with the redistribution of Li. Figure 7.1a sketches the interactions between the stress field at the crack tip and the Li profile. The chemical load is applied by supplying a field of Li concentration or Li flux. Li diffuses rapidly

along the crack path because of the high surface diffusivity and accumulates at the crack tip because of the stress concentration ahead of the crack. This phenomenon is analogous to the diffusion of hydrogen and oxygen in fractured metals where the solute is trapped ahead of the crack tip [106, 226, 227]. Li accumulation appends an extra lithiation-induced dilatational strain at the crack tip which reduces the stress field and the driving force for crack growth. This shielding effect caused by Li accumulation is a reminiscence of crack shielding in the stress-induced martensitic transformation in ceramics [228]. Prior studies have elaborated in detail the intimate relation between the crack driving force and Li redistribution at crack tip [89, 106, 108, 229]. Li redistribution does not only modulate the stress field around the crack tip, but also alter the fracture toughness of the host material, which results in a competition between the driving force and the resistance of fracture upon Li reactions. While many studies have investigated the dependence of mechanical properties of electrodes on Li composition, such as elastic modulus and hardness at different states of charge [230, 231], fracture toughness is relatively less explored. A few recent novel experiments are developed to determine the evolution of fracture toughness upon Li reactions [103, 133, 212]. Figure 7.1b illustrates the experimental observations of fracture toughness for a variety of active materials as a function of Li concentration. Li reactions cause embrittlement of the host material. In anodes, such as the alloying-type materials C, Si and Ge, fracture toughness generally decreases during Li inserts [103, 232, 233]. The lithiation induced embrittlement is mainly due to the atomic bond breakage of the host materials upon Li insertion and the formation of weaker bonds between Li and the host atom which deteriorate the mechanical strength [72, 105]. In cathodes, such as the intercalation-type materials NMC, $LiCoO_2$ and $LiMn_2O_4$, fracture toughness usually reduces upon Li extraction [133, 212, 234]. The loss of fracture resistance upon delithiation is likely due to (i) the depolarization of the transition metals

(TM)-oxygen ionic bonding when Li extracts, (ii) the Jahn-Teller (JT) distortion when the transition metals transit from JT-inactive to JT-active states during delithiation, (iii) the structural destabilization caused by cation mixing in which TM ions of a similar size of Li^+ occupy the vacant Li sites [235], and (iv) the formation of nano-sized voids within the electrodes resulted from the volumetric contraction during Li extraction [35]. The generation of material defects does not necessarily cause macroscopic damage; however, the population and evolution of the defects will weaken the fracture toughness of redox materials. Overall, the fracture behavior of electrodes is a result of the interactions among the Li transport, the electrochemical conditions, the stress field, and the Li embrittlement effect. Whether the stress-diffusion coupling facilitates or suppresses fracture growth depends on the type of materials as well as the chemomechanical load conditions. This scenario shares similar features of corrosive fracture of metals assisted by oxygen or moisture [236, 237]. However, different from oxygen, Li might be a more corrosive species because the formation of oxides at the crack tip may shield further oxygen transport and protect unstable crack propagation, while lithiated active materials do not usually have such an effect [238].

The goal of this chapter is to study the corrosive fracture of electrodes under concurrent mechanical and chemical load. A continuum theory of coupled diffusion and large deformation is implemented into finite element program to investigate the fracture behavior that is determined by diffusion kinetics and Li embrittlement effect. The competition between energy release rate and fracture resistance as crack grows during both Li insertion and extraction is examined in detail. A phase diagram can be constructed to delineate the unstable, arrested, and delayed fracture zones in the variable space of material properties and the load conditions. The corrosive fracture model is also employed to simulate the intergranular fracture in NMC aggregated particles which constitutes the major mechanical degradation of the state-of-the-art cathode material for vehicle

applications. The structural decohesion is induced by the mismatch strain at the grain boundaries. The evolving interfacial strength at different states of charge and different cycle numbers measured by the in-situ nanoindentation is implemented in the numerical simulation. The corrosive behavior of intergranular cracks in NMC during delithiation as well as upon Li cycles are simulated and compared with experiments. This chapter is organized as follows. Chapter 7.2 presents a numerical method to determine the energy release rate of crack growth, and variation of the fracture toughness due to the evolution of the chemical composition. A cohesive zone model (CZM) integrated in commercial software COMSOL is utilized to model the crack propagation and Li transport coupled with crack generation. Chapter 7.3 presents the numerical modeling of corrosive fracture of electrodes under concurrent mechanical load and chemical (de)lithiation. The evolutions of the energy release rate are compared with the material fracture toughness as the Li reaction proceeds and crack grows. A phase diagram is constructed to delineate the unstable, arrested, and delayed fracture zones in the plane spanned by the chemical load condition and the fracture toughness. The effects of the stress regulated Li diffusion and Li insertion induced material embrittlement on the fracture behavior are carefully evaluated. This corrosive fracture model is also utilized to simulate the intergranular fracture in NMC particles. The evolving interfacial strength at different states of charge and different cycles is considered, and the numerical results are compared with the recent experimental observations.

7.2 Theory and numerical modeling

The theory and numerical modeling of coupled diffusion and elastic deformation is presented in Chapter.2.1, and the governing equations for the kinematics of deformation and kinetics of diffusion are listed from the Equation (2.1) to (2.36) in Chapter.2.1. For small-

volumetric-change electrodes such as layered NMC, the plastic contribution from the irreversible shape change can be ignored.

7.2.1 Energy release rate

In fracture mechanics, the *J*-integral is a convenient way to calculate the energy release rate *G* for linear elastic materials or materials of small-scale yielding at the crack tip. Consider an arbitrary counterclockwise path around the crack tip Υ, Figure 7.2a, the two-dimensional path-independent *J*-integral is defined as

$$J = \int_{\Upsilon} \left(W dX_2 - \mathbf{T} \cdot \frac{\partial \mathbf{u}}{\partial X_1} ds \right), \tag{7.1}$$

where W is the strain energy density, $\mathbf{T}$ is the traction vector on the contour Υ of the outward normal $\mathbf{N_0}$. ds is an element length along Υ, and X_1 and X_2 are the coordination directions.

In an electrochemical system with solid state diffusion, prior work proved that the conventional *J*-integral is no longer path-independent [89, 229, 239]. Recall that the *J*-integral includes the total energy within the closed contour and the energy passing through the contour line. When diffusion involves in the system, the free energy within the contour around the crack tip will not only include the elastic strain energy but also contains the energy associated with solute diffusion and distribution. Furthermore, both mechanical work done by tractions and free energy conveyed by solid state diffusion should be accounted in the energy along the contour line. Here a modified *J*-integral proposed in the earlier work is utilized [89],

$$J = \int_{\Upsilon} \left(\phi dX_2 - \mathbf{T} \cdot \frac{\partial \mathbf{u}}{\partial X_1} ds \right) - \int_{\Lambda} \mu \cdot \frac{\partial C}{\partial X_1} d\Lambda, \tag{7.2}$$

where Λ is the area enclosed by the contour Υ. The first linear integral accounts for the total energy inside the closed contour, the second linear integral represents the mechanical work done by the

tractions passing through the contour line, and the third area integral represents the change of free energy within the area of the contour Υ which is equal to the energy conveyed by solid state diffusion. With the definition of chemical potential μ and free energy ϕ in Equation (2.31), Equation (7.2) is recast into the following form via Green's theorem,

$$J = \int_{\Upsilon} \left(W dX_2 - \mathbf{T} \cdot \frac{\partial \mathbf{u}}{\partial X_1} ds\right) + \int_{\Lambda} (\Omega \sigma_m) \frac{\partial C}{\partial X_1} d\Lambda \,. \tag{7.3}$$

Equation (7.3) is path-independent in the chemomechanical system involving both Li diffusion and mechanical deformation, and can be used to evaluate energy release rate *G* for crack growth. It should be noted that the simplified form Equation (7.3) includes the assumption that the volumetric change due to elastic deformation is small and the elastic constants are independent on the Li composition. Gao and Zhou have evaluated the effect of these two factors in their prior work [89]. Equation (7.3) is implemented into the numerical simulation using the energy domain integral method originally proposed by Shih *et al*. [240] and subsequently elaborated by Gao and Zhou [89].

7.2.2 Crack growth

For a chemomechanical system under both mechanical and chemical load, Li profile and the stress field dynamically evolve due to the stress-diffusion coupling. Li diffusion is usually much slower than mechanical equilibrium such that the system is not always in the chemical equilibrium state especially during the crack growth. Here the dynamic stress evolution and Li diffusion coupled with crack propagation are simulated using a standard cohesive zone model (CZM) which permits the material planes in potential fracture zones to separate using a predefined traction–separation law [241, 242]. It is assumed that the preexisting crack propagates along its crack plane without any deflection. Therefore, cohesive elements are assigned in front of the initial

crack along the path of potential crack propagation, Figure 7.2b. The history-dependent traction–separation relation of the cohesive element is plotted in Figure 7.2c. The power law criterion is used here for the final failure

$$\left(\frac{\mathrm{G}_I}{\Gamma_I}\right)^{\eta} + \left(\frac{\mathrm{G}_{II}}{\Gamma_{II}}\right)^{\eta} = 1 \tag{7.4}$$

where the exponent η is called the mode mixity exponent. G_I and Γ_I are the energy release rate and fracture toughness for *i* mode, respectively. In this work, the mode mixity exponent η is set as 1 such that the power law failure criterion in Equation (7.4) is reduced to $\mathrm{G}_I/\Gamma_I + \mathrm{G}_{II}/\Gamma_{II} = 1$. If the shear induced damage in the host material is ignored, the failure criterion can be further reduced to $\mathrm{G}_I = \Gamma_I$.

The Chapter 6 shows that the fracture toughness of electrodes is largely dependent on Li composition. Therefore, the traction-separation relation of the cohesive element should be a function of the Li concentration. Here the pristine fracture toughness is set as Γ_0 and the fracture toughness of lithiated (delithiated) state is set as $\Gamma(C)$. According to the two types of Li embrittlement effects shown in Figure 7.1b, the expression $\Gamma(C)$ can be written in the following form based on the recent experimental measurements [133],

$$\begin{cases} \Gamma(C)/\Gamma_0 = 0.9(1 - C/C_{\max})^n + 0.1 & \text{Lithiation embrittlement} \\ \Gamma(C)/\Gamma_0 = 0.9(C/C_{\max})^n + 0.1 & \text{Delithiation embrittlement} \end{cases} \tag{7.5}$$

where *n* is the exponent denoting the degree of the Li-assisted embrittlement. Higher *n* indicates severer embrittlement effect due to the Li reaction. The first formula in Equation (7.5) represents the Li insertion induced embrittlement of anode materials, such as graphite and carbon nanomaterials. The normalized Li concentration $C/C_{\max}$ varies from 0 to 1, altering the fracture toughness of active material $\Gamma(C)$ from Γ_0 to $0.1\Gamma_0$. Similarly, the second formula in Equation (7.5) represents the Li extraction induced embrittlement of cathode materials upon Li extraction, such

as $LiCoO_2$ and NMC. The normalized Li concentration $C/C_{\max}$ varies from 1 to 0 and alter the fracture toughness $\Gamma(C)$ from Γ_0 to $0.1\Gamma_0$. The ranges of the variation of fracture toughness upon lithiation or delithiation agree well with the experiment results [133, 212, 233]. By appropriately selecting the fracture toughness of the pristine host material Γ_0, Li embrittlement effect can be well described by Equation (7.5).

The modified *J*-integral in Equation (7.3) is used to evaluate the driving force (energy release rate) of crack growth in the chemomechanical system. The values of modified *J*-integral are calculated from three rectangular contours enclosing the crack tip. The path-independence of the modified *J*-integral is verified by checking the convergence of the values of the modified *J*-integral from the three independent contours, Figure 7.2d. The mesh around the crack tip is refined and the mesh sensitivity has been checked, Figure 7.2e. Apart from the analysis on the onset of crack propagation using the modified *J*-integral, an independent numerical calculation is conducted to investigate the corrosive fracture behavior via utilizing the CZM described in Chapter 7.2.2. It is assumed that the preexisting crack propagates along its predefined crack plane without any deflection. Cohesive elements are preset in front of the initial crack along its cracking plane and used to simulate the crack initiation and propagation, as shown in Figure 7.2b. The size of the cohesive elements (0.05 μm) is much smaller than the characteristic size of the initial pre-existing crack (1 μm).

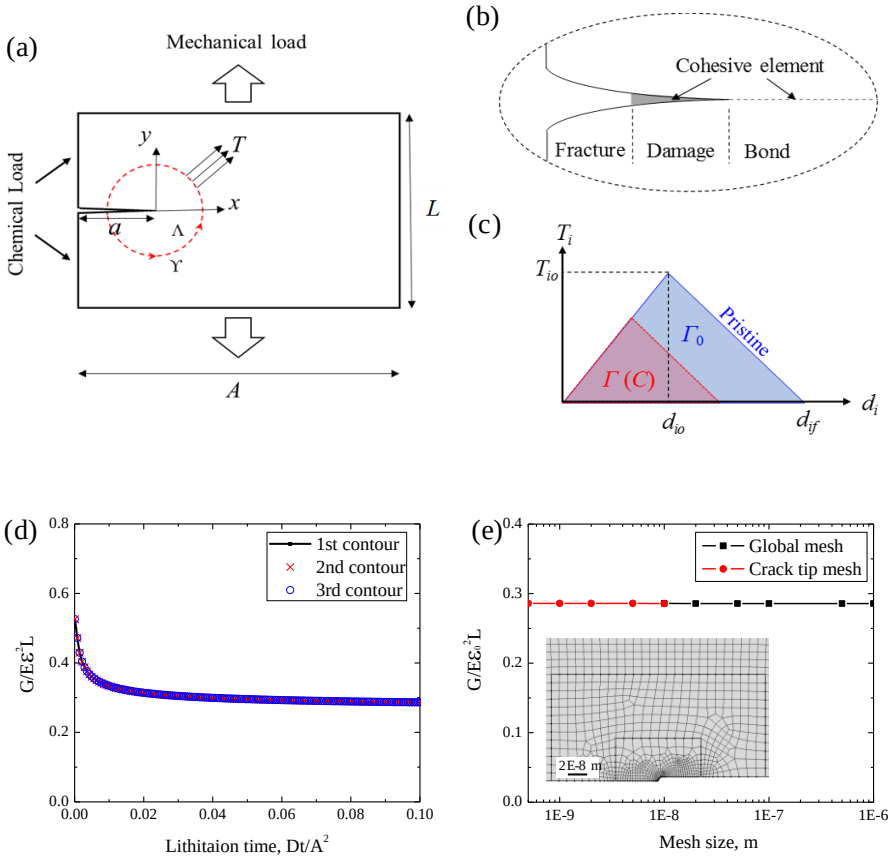

Figure 7.2. (a) A model subject to the concurrent chemical and mechanical load. The red dashed circle represents the contour ϒ for calculating the energy release rate. (b) Schematic of the cohesive zone model (CZM) for simulating the crack growth in the chemomechanical system. (c) the (de)lithiation-dependent constitute law of the cohesive element. (d) The values of modified J-integral calculated from the three independent contours around the crack tip in a system under concurrent chemical and mechanical load. (e) The mesh sensitivity check for the global mesh and crack tip refine mesh

7.3 Results and discussion

7.3.1 Corrosive fracture in Li insertion and extraction

Corrosive fracture of electrodes under concurrent chemical and mechanical load includes two successive cracking behaviors – crack initiation and following propagation. The competition between energy release rate and fracture resistance upon lithiation (delithiation) is first examined for predicting the onset of crack. Then the dynamic stress evolution and Li diffusion coupled with crack propagation after crack initiates is simulated. A model system of a simplified plane-strain

condition embedded with a pre-existing crack is used, Figure 7.2a, where A and L are the length and thickness of the model, respectively. The crack with a length of a is modeled as a notch with a small but finite tip radius of $\rho/a = 10^{-3}$. The system is subject to both mechanical and chemical load. Mechanical load is set as a constant strain boundary condition ε_0 to mimic the electrodes experiencing a lithiation (delithiation) induced mismatch strain brought by the phase boundaries, constrained grain boundaries, or the mismatch between the active redox material with the conductive matrix and current collectors. Chemical load is set as a constant Li concentration C_0 at the left surface of the model as well as at the crack surface, Figure 7.2a. It is assumed that the mechanical load, stress evolution, and crack growth are much faster than Li diffusion such that the system remains in mechanical equilibrium state while the chemical equilibrium is determined by Li transport.

The results of Li insertion and extraction will be discussed in separate sub-sections. Chapter 7.3.1.1 focuses on the corrosive fracture due to lithiation. The chemical boundary condition drives Li insertion and the lithiated product exhibits a lower fracture resistance as quantitively determined in Equation (7.5). Chapter 7.3.1.2 examines the corrosive fracture upon delithiation. The description of delithiation embrittlement in Equation (7.5) is adopted to represent the loss of fracture resistance when Li extracts. The material properties for graphite active material are used in the two sections [32, 243], Young's modulus $E = 15\ GPa$, Poisson's ratio $\upsilon = 0.3$, Li diffusivity $D = 3.9 \times 10^{-14}\ m^2/s$, partial molar volume of Li in graphite $\Omega = 3.65 \times 10^{-6}\ m^3/mol$, and maximum Li concentration $C_{\max} = 26580\ mol/m^3$. To focus on the fracture behavior, the elastic modulus and Li diffusivity are assumed to not vary with the Li concentration. The study on the variation of the elastic modulus can be found in earlier papers [89, 244]. Here the same set of material properties except the difference in the fracture toughness are used in lithiation and

delithiation – apparently one material cannot experience embrittlement in both Li insertion and extraction. To make the analysis be general, a group of dimensionless parameters is used to avoid the dependence of results on the specific choice of material properties. The dimensionless parameters are identified as follows: Li concertation $C/C_{\max}$, diffusion time Dt/A^2, stress $\sigma/E\varepsilon_0$, energy release rate $G/E\varepsilon_0^2 L$, fracture toughness $\Gamma/E\varepsilon_0^2 L$, crack length a/A, and the embrittlement effect Γ/Γ_0. Γ/Γ_0 is set to follow Equation (7.5) with an exponent n=2. The effect of the embrittlement exponent (i.e. n = 1, 2 and 3) will be also discussed in the numerical results.

7.3.1.1 Li insertion induced material embrittlement and corrosive fracture

The model system contains a pre-existing crack and is subject to the concurrent mechanical and chemical load as described earlier. At the beginning, the crack growth simulation using CZM is not considered. Instead, the energy release rate of the pre-existing crack is calculated by the modified J-integral and used to investigate the evolution of the crack driving force during the lithiation. The mechanical load is prescribed by a remote strain field $\varepsilon_0 = 2\Delta L/L = 0.04$ where ΔL is the displacement applied at the upper and lower surfaces. During lithiation, the remote tensile strain is set always larger than the lithiation-induced linear strain (i.e. $\varepsilon_{Li} = 1/3\log(1+\Omega C)$) so that the crack closing will not occur. The mechanical boundary condition generates a field of tensile stresses which reduce the chemical potential of Li (Equation (2.34)) and promotes Li insertion into the host material. By solving the coupled stress-diffusion equations, Figure 7.3a plots the distribution of Li concentration along the *x*-direction ahead of the crack at different lithiation times. The system is initially Li-free (i.e. initial Li concertation $C_{\mathrm{i}} = 0$). Lithiation starts upon applying the chemical load $C_0/C_{\max} = 0.5$, and is terminated when the system reaches the chemical equilibrium. As shown in Figure 7.3a, the surface regime is quickly saturated with Li because of the short diffusion length and the inner region is continually lithiated as the normalized

diffusion time Dt/A^2 increases. Li concentration along the diffusive direction (x-direction) does not show a typical distribution of smooth gradient. Instead, a high concentration field of Li exists ahead of the crack tip and the concentration of the singular Li field is much higher than the overall Li concentration within the system. Figure 7.3b shows Li accumulation ahead of the crack tip and the contour plot of tensile stress at $Dt/A^2 = 0.03$ and $Dt/A^2 = 1.5$, respectively. The inhomogeneous distribution of Li originates from the modulation of the stress field on Li diffusion. Since Li insertion is initiated after applying a tensile load to the system, the mechanical load reduces Li chemical potential and drives Li insertion. The stress concentration ahead of the crack tip absorbs Li toward the crack region. The extra Li driven by the stress field appends a volumetric dilation at the crack tip which reduces the driving force for crack growth. As lithiation proceeds, Li concentration within the system continually increases while the tensile stress field diminishes, as shown in the stress profiles in Figure 7.3b. Li insertion-induced volumetric expansion counterbalances the tensile strain supplied by the external mechanical load, and thus, the overall tensile stresses are reduced. As expected, a higher Li concentration boundary condition contributes to a lower tensile stress field and consequently a lower driving force for crack growth. This stress relaxation behavior is revealed when a larger chemical load C_0 is applied. Figure 7.3c presents the contour profiles of Li concentration and tensile stresses near the crack tip under different chemical boundary conditions C_0/C_{max} = 0.25, 0.5, 0.75 and 0.9, respectively. When C_0 increases, more Li atoms are pumped into the system which eliminates the average tensile stress in the system as well as the stress singularity near the crack tip.

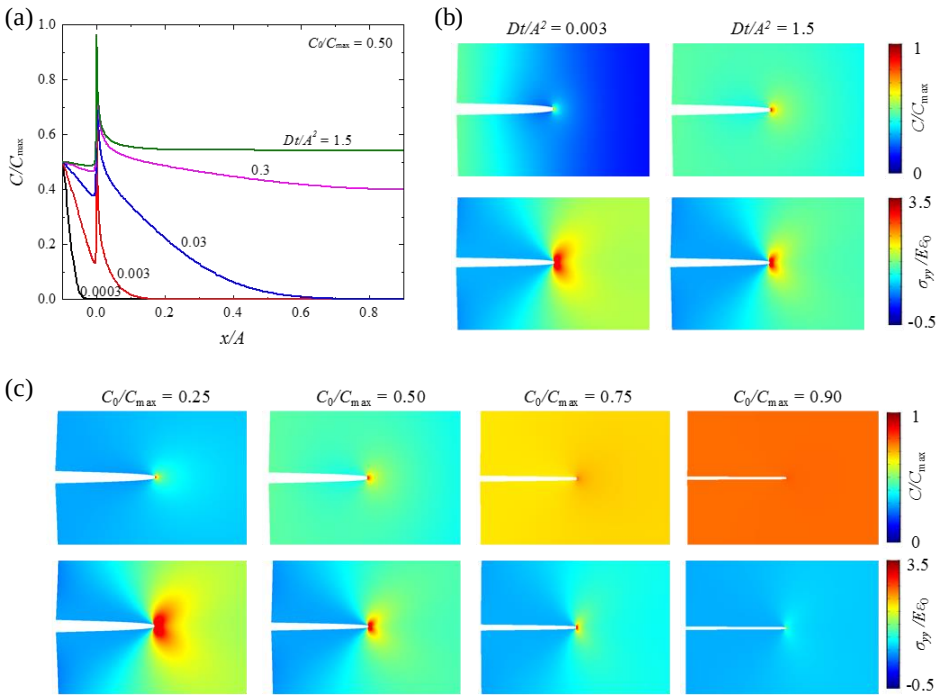

Figure 7.3. (a) Li concentration along the crack path in the *x*-direction with the chemical boundary condition C_0/C_{max} = 0.5. (b) The contour profiles of Li concentration and tensile stress near the crack tip at the dimensionless times Dt/A^2 = 0.003 and 1.5. (c) The contour profiles of Li concentration and tensile stress near the crack tip under various chemical load C_0/C_{max} = 0.25, 0.5, 0.75 and 0.9. The contour profiles are plotted at the time when lithiation is terminated.

Upon the decrease of the stress field during lithiation, the driving force of crack growth (i.e. energy release rate G) is reduced. Energy release rate due to pure external mechanical load is denoted as G_0. According to prior work, G_0 is calculated as $G_0/E\varepsilon_0^2L$=0.52. The energy release rate G for the crack under both mechanical and chemical load can be expressed as $G = G_0 + \Delta G$, where ΔG is the change of the energy release rate induced by the lithiation reaction. Since Li insertion reduces the tensile stress field, ΔG is a negative quantity which is determined by two factors: (i) The extra amount of Li accumulated around the crack tip, and (ii) the volumetric dilation which counterbalances the applied far-field tensile strain. Figure 7.4 plots the energy release rate $G = G_0 + \Delta G$ (black lines) as a function of the lithiation time. Two types of chemical load conditions are calculated: C_0/C_{max} = 0.02 in Figure 7.4a and C_0/C_{max} = 0.20 in Figure 7.4b.

As expected, G gradually decreases upon lithiation from the initial value G_0 and reaches a minimum value when lithiation is completed. In Griffith criterion, the onset of crack growth depends on the relative values of the energy release rate and the material fracture toughness. By assuming a constant fracture toughness of the lithiated phase, a crack during lithiation will be less likely to propagate. Nevertheless, the fracture behavior is more complicated when both the stress-diffusion coupling and Li embrittlement effect are considered. The stress singularity at the crack tip makes the local Li concentration near the crack tip much higher than the concentration boundary condition prescribed by C_0, as is evident in the evolution of Li concentration at the crack tip (blue line) in Figure 7.4. Unlike the stress singularity, Li accumulation around the crack tip will not be eliminated when lithiation proceeds. Figure 7.4a and b show that Li concentration near the tip monotonically increases with the lithiation time Dt/A^2. Two factors account for the holding of high Li concentration at the crack tip during the lithiation. First, an early paper proved that when a material with a pre-existing crack is subject to both mechanical and chemical load, Li concentration has a $e^{r^{-\frac{1}{2}}}$ singularity around the crack tip which is much higher than the stress singularity $r^{-\frac{1}{2}}$ [106]. Therefore, a high Li concentration will be maintained despite the reduction of the stress singularity at the crack tip. Second, although the continuous lithiation eliminates the stress singularity which subsequently reduces the stress-regulated Li accumulation, the overall Li concentration within the host still increases which yields a monotonic increase of Li concentration at the crack tip. As a result, if the Li embrittlement described in Equation (7.5) holds, the fracture toughness of the host material continuously decreases as lithiation proceeds. Figure 7.4 shows the evolutions of the fracture toughness (red lines) as a function of the lithiation time, in which the initial fracture toughness of the pristine material is set as $\Gamma_0/E\varepsilon_0^2 L = 0.8$ and the Li concentration-dependent fracture toughness $\Gamma/E\varepsilon_0^2 L$ is calculated from Equation (7.5) by choosing the Li

embrittlement exponent n = 2. Figure 7.4 demonstrates that, although both the energy release rate G and fracture toughness Γ drop upon lithiation, the decrease rate in fracture toughness is larger than that for the energy release rate because of the higher singularity of Li concentration at crack tip. This comparison indicates that crack propagation during lithiation will be triggered more easily, which is a contrary conclusion in the case where the fracture toughness is assumed to be a constant.

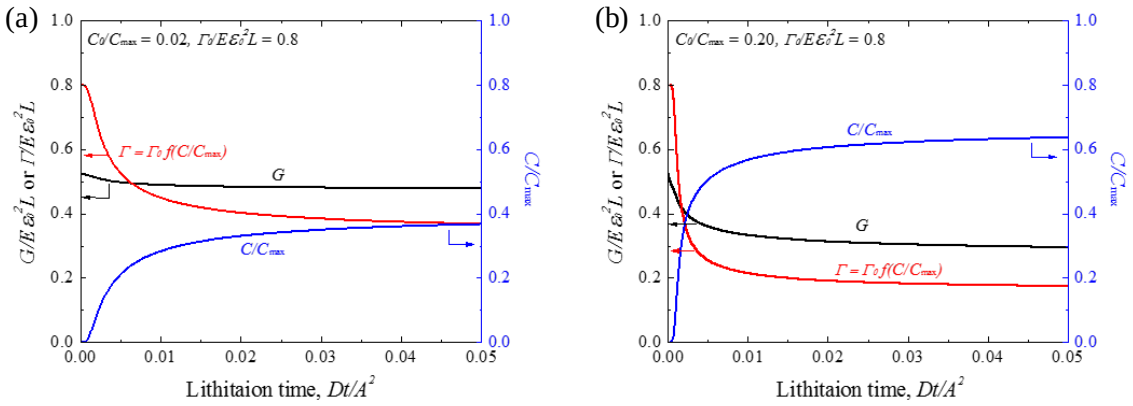

Figure 7.4. The evolving Li concentration C/C_{max} at the crack tip (blue line), energy release rate $G/E\varepsilon_0^2L$(black line), and fracture toughness $\Gamma = \Gamma_0 \cdot f(C/C_{max})$ (red line) during lithiation under two chemical load conditions, (a) C_0/C_{max} = 0.02, and (b) C_0/C_{max} = 0.20.

In the following discussion, the critical time for the onset of crack growth is defined as the time when the energy release rate G equals the fracture toughness Γ, that is $\tau_c = (Dt/A^2)_{G=\Gamma}$. As shown in Figure 7.4a, for chemical load condition C_0/C_{max} = 0.02, τ_c is about 0.006 if the host material has a pristine fracture toughness $\Gamma_0/E\varepsilon_0^2L = 0.8$. τ_c will be larger for the host material of a higher pristine fracture toughness Γ_0, and vice versa. In Figure 7.4, a higher value Γ_0 shifts up the red curve and results in a larger value of time for the energy release rate curve intersects with the fracture toughness. Certainly, for a material of sufficiently large Γ_0, fracture toughness Γ can be always higher than the energy release rate G and crack growth is suppressed upon the entire lithiation. In general, the fracture toughness of the host material Γ_0 and its evolution law $\Gamma =$

$\Gamma_0 f(C/C_{\max})$ provides the threshold of crack growth and determines the overall crack behavior. Comparing Figure 7.4a and b, the critical time for crack growth τ_c seems to be dependent on the chemical boundary condition $C_0/C_{\max}$. Specifically, τ_c for the crack under chemical load $C_0/C_{\max}$ = 0.02 is around 0.006, while τ_c for $C_0/C_{\max}$ = 0.25 is around 0.002. Although a larger chemical load tends to eliminate the tensile stress field and thus decrease the energy release rate for crack growth, the fracture toughness drops at a much faster rate because of the higher-order singularity of Li concentration at the crack tip as shown in Figure 7.4b. In the limiting case that the chemical load is zero, the energy release rate G is constant ($G/E\varepsilon_0^2 L$=0.52) and the fracture resistance of the host material remains the initial value ($\Gamma/E\varepsilon_0^2 L$=0.8), there will be no intersection of the energy release rate with the fracture toughness; thus, the onset time of crack growth is infinity. Overall, the results in Figure 7.4 demonstrate that the fracture toughness of pristine host material Γ_0, the Li embrittlement function $\Gamma = \Gamma_0 f(C/C_{\max})$, and the chemical load condition $C_0/C_{\max}$ all together determine the fracture behavior of the chemomechanical system.

The above analysis indicates that a crack in a host tends to grow if the material has lower fracture toughness and is subject to a larger chemical load. Crack growth may exhibit two different behaviors: stable and unstable cracking, depending on how the energy release rate G and fracture toughness Γ evolve with the crack extension a [127]. To understand the stable and unstable crack growth, it is convenient to compare the crack driving force curve (i.e. energy release rate G with respect to the crack extension a) and the resistance curve or R curve (i.e. fracture toughness Γ with respect to the crack extension a). The condition for stable cracking can be expresses as $G = \Gamma$ and $dG/da \leq d\Gamma/da$ within a finite crack extension da, while the unstable cracking occurs when $G = \Gamma$ and $dG/da > d\Gamma/da$. For the system subject to the only mechanical load of a constant far-field strain, the energy release rate $G/E\varepsilon_0^2 L$=0.52 is nearly independent of crack extension and the

fracture toughness also remains as its initial value. Once the energy release rate G exceeds the fracture toughness Γ, crack would propagate unstably because the driving force is always higher than the resistance of crack growth. However, for the chemomechanical system under both mechanical and chemical load, the driving force and the resistance curves both evolve with the crack extension and should be carefully analyzed. Figure 7.5a plots the normalized energy release rate $G/E\varepsilon_0^2 L$ as a function of crack extension upon lithiation with a chemical load C_0/C_{max}=0.5. According to the Li concentration distribution in Figure 7.3a, the crack extension shifts the crack tip from the Li-rich to the Li-poor region, recovering the high tensile stress around the crack tip and the associated driving force for crack growth. Therefore, energy release rate G increases as crack propagates for the entire lithiation time, Figure 7.5a. The fracture behavior at a specific time $Dt/A^2 = 0.03$ is analyzed and the Griffith fracture criterion $G = \Gamma$ is assumed to be satisfied. The energy release rate curve at this time $Dt/A^2 = 0.03$ is shown as the red curve in Figure 7.5a. To obtain the resistance curve, the Li distribution C/C_{max} near the crack tip when the crack propagates a distance of da is first determined. The corresponding Li profile is shown in the upper graph of Figure 7.5b. Then, using the Li embrittlement formula in Equation (7.5), the fracture toughness $\Gamma/E\varepsilon_0^2 L$ of the host material near the crack tip can be estimated and is shown in the lower graph of Figure 7.5b. The early discussion has demonstrated that crack propagation during lithiation is triggered more easily. Before the crack grows, Li accumulation at the crack tip always exists owing to the tensile stress singularity at crack tip. Once the fracture toughness of host material at the tip drops to be lower than the driving force for crack growth, crack propagates by a characteristic length da. Since the crack propagation is much faster than the Li diffusion, the crack tip would be immediately shifted away from the region of Li accumulation, as shown in the Li profile in Figure 7.5b. Without the Li embrittlement at the Li-concentrated regime, the fracture toughness Γ at the

fresh crack tip recovers to a higher level, as shown in the lower panel of Figure 7.5b. By comparing the driving force curve in Figure 7.5a and the resistance curve in Figure 7.5b, the conditions for stable cracking $G = \Gamma$ and $dG/da \leq d\Gamma/da$ are indeed met. Therefore, the crack will propagate by a small distance, and then is arrested until the fracture strength of the host material at the fresh crack tip is weakened again by the following Li redistribution. In this case, the corrosive fracture behaves as a typical delayed fracture of the feature of the "wait and go" behavior – the "wait" depends on the Li transport and the supply of Li at the crack tip, and the "go" depends on the Li embrittlement of the host [63, 72].

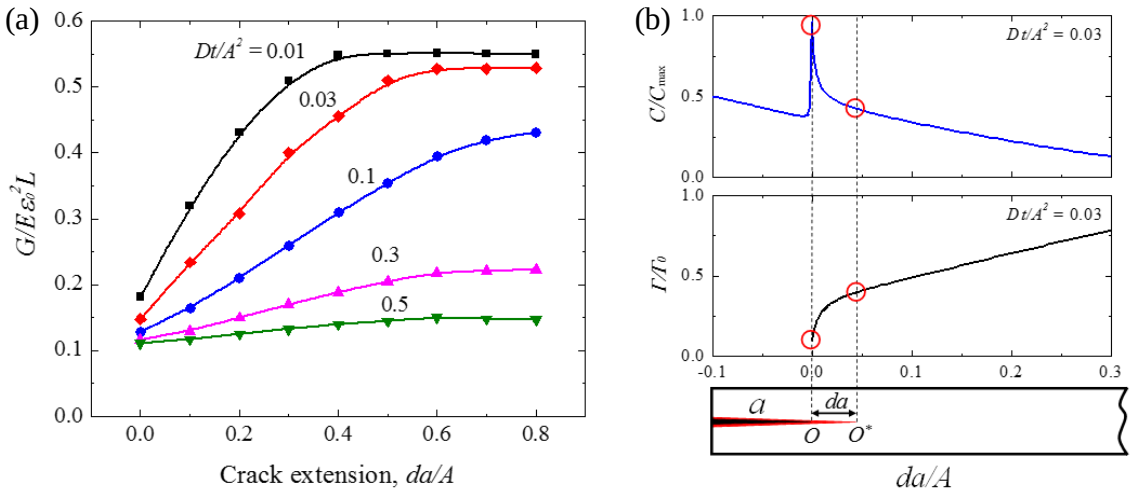

Figure 7.5. Plots of crack driving force G and crack resistance Γ. (a) Energy release rate $G/E\varepsilon_0^2 L$ as a function of the normalized crack extension da/A at different lithiation times. G increases as crack extends because the crack tip migrates from the Li-rich zone to the Li-poor regime. (b) Li concentration C/C_{max} (upper figure) and fracture toughness $\Gamma_0/E\varepsilon_0^2 L$ (lower figure) near the crack tip at $Dt/A^2 = 0.03$. When the crack tip propagates from O to O*, fracture toughness Γ of the host material at the fresh crack tip recovers to a larger value and resists further growth of the crack. Crack growth resumes after Li accumulates around the new crack by diffusion.

The delayed fracture is a dynamic process that does not only include the crack initiation upon lithiation but also involves the co-evolution of stress field and Li diffusion after the crack grows. To capture the dynamic, the CZM method is used to simulate the dynamic crack

propagation as well as the stress and diffusion fields. The crack starts propagation once the energy release rate exceeds the Li concentration-dependent fracture toughness of the cohesive elements which are preset along the cracking plane. The time scale for crack growth and stress generation is much faster than that for Li redistribution, thus, the system is in a chemical transition state unless lithiation is completed or the crack penetrates through the system.

As discussed above, the pristine fracture toughness of the host material Γ_0 and the chemical load C_0/C_{max} are the key parameters determining the fracture behavior. Here different fracture behaviors are identified on a plane spanned by C_0/C_{max} (the chemical boundary condition) and $\Gamma_0/E\varepsilon_0^2 L$ (the normalized pristine fracture toughness). In Figure 7.6a, each point in the plane represents one complete simulation with a given set of values of C_0/C_{max} and $\Gamma_0/E\varepsilon_0^2 L$. The phase diagram in Figure 7.6a delineates three types of fracture behaviors: the unstable, arrested, and delayed fracture zones. For the chemomechanical system composed of a host of a high pristine fracture toughness and is loaded by small Li concentration (i.e. upper left region), the pre-existing crack remains arrested during the entire lithiation process. In this safe regime, the material flaws will not expand due to the high fracture resistance and low chemical load. On the other side, when the pristine fracture toughness is relatively low and a sufficient Li source is supplied (upper right region), crack propagates when the energy release rate exceeds the fracture toughness, then stops and waits for the Li to reaccumulate at the new crack tip, giving the delayed fracture upon lithiation. The boundary between the regions of arrested fracture and delayed fracture are estimated by connecting the neighboring simulation points in-between the two regimes. As expected, the boundary starts from the material toughness $\Gamma_0/E\varepsilon_0^2 L = 0.52$ and the chemical condition C_0/C_{max}=0 where the fracture toughness is identical to the energy release rate $G_0/E\varepsilon_0^2 L$=0.52 applied by the external mechanical load as discussed in the Figure 7.4. If the pristine fracture

toughness is below this critical value, no matter whether the system is subject to the chemical load, the energy release rate G_0 induced by the far-field mechanical load already exceeds the fracture resistance and causes unstable cracking, as shown by the regime with the dashed line boundary $\Gamma_0/E\varepsilon_0^2 L = 0.52$. This fracture behavior due to the pure mechanical load is referred as unstable fracture (i.e. lower region).

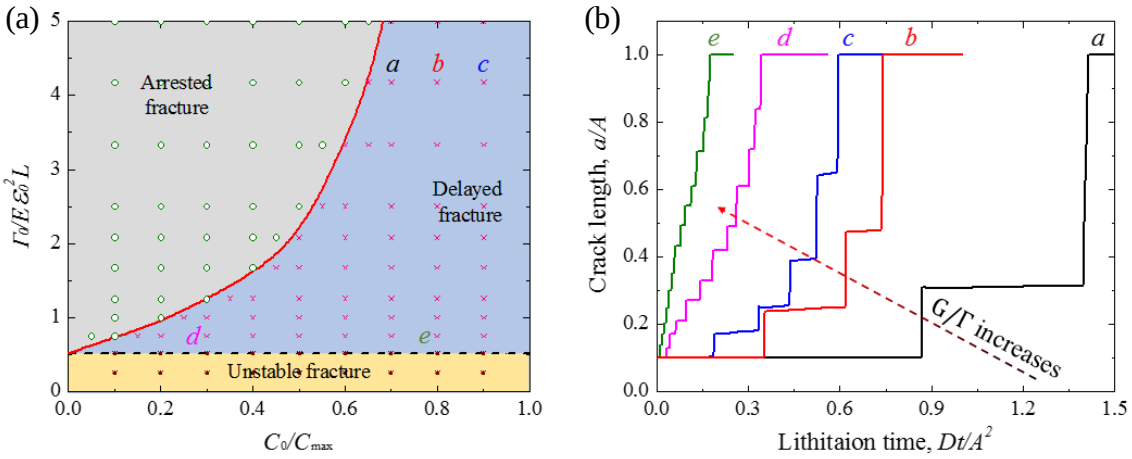

Figure 7.6. (a) The phase diagram of corrosive fracture composed of unstable fracture, arrested fracture, and delayed fracture on the plane spanned by the fracture toughness of the pristine host material $\Gamma_0/E\varepsilon_0^2 L$ and the chemical load C_0/C_{max}. Each single point in the diagram represents one complete simulation with given values of C_0/C_{max} and $\Gamma_0/E\varepsilon_0^2 L$. Boundaries delineating different regimes are estimated by connecting the neighboring points. (b) The evolution of crack length as a function of the lithiation time for various combinations of $\Gamma_0/E\varepsilon_0^2 L$ and C_0/C_{max} in the delayed fracture zone. Different lines correspond to the points *a*-*e* in (a). The ratio of the energy release rate to the fracture toughness increases from *a* to *e* which induces the transition from the "wait-and-go" behavior to the unstable fracture.

Among the three types of fracture behaviors, the delayed fracture that involves the co-evolution of stress field and Li transport is of particular interest. Figure 7.6b plots the evolution of the crack length as a function of the lithiation time for different sets of $\Gamma_0/E\varepsilon_0^2 L$ and C_0/C_{max}, marked as the points *a*, *b*, *c*, *d*, and *e* in the delayed fracture zone in the phase diagram. In the comparison from *a* to *c* of the same fracture resistance, the time of "wait" depends on the supply

of Li and a smaller chemical load allows for a longer time for crack to wait until the next jump in crack length. Overall, the ratio of the energy release rate to the fracture toughness increases from point *a* to point *e* that induces a transition from the "wait and go" delayed crack to the unstable cracking behavior.

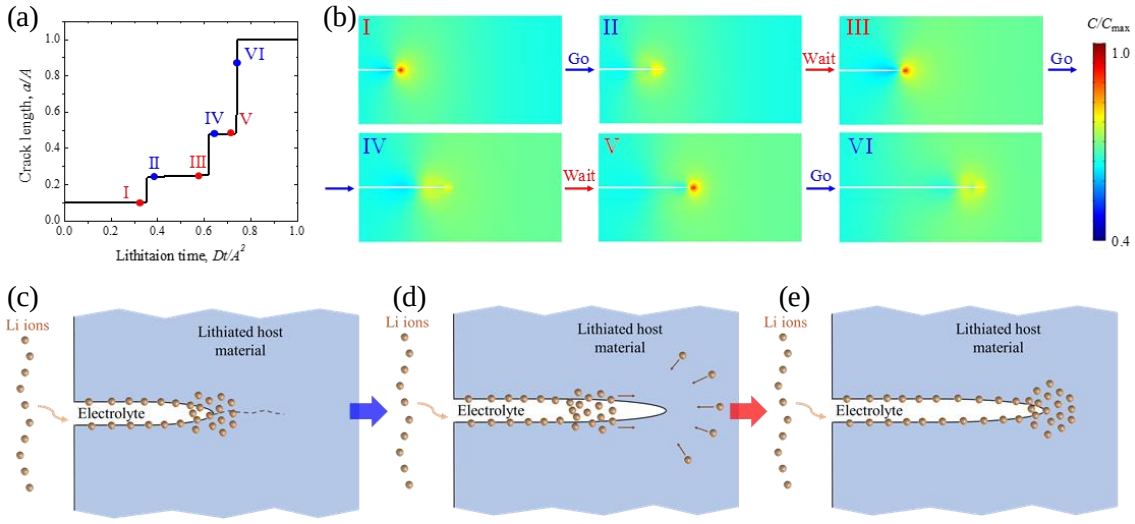

Figure 7.7. (a) The plot of crack length upon lithiation for $C_0/C_{max} = 0.8$ and $\Gamma_0/E\varepsilon_0^2 L = 4.2$ (point *b* in Figure 7.6a). The crack propagation is a typical "wait-and-go" behavior in which the crack "goes" at the transition of I-II, III-IV, and V-VI, and "waits" at II-III and IV-V. (b) The corresponding profiles of Li concentration at the lithiation times I-VI. (c-e) Schematics of delayed fracture due to the concurrent Li diffusion, Li embrittlement, and crack growth. (c) While the crack "waits", the crack remains in a steady state. Li accumulates around the crack tip due to the stress concentration and weakens the fracture strength of the host material. (d) When the fracture resistance is below the energy release rate, crack propagates and creates fresh surfaces without Li. Without the Li embrittlement effect, the fracture resistance increases and crack stops. (e) The "go" and "wait" repeat while Li diffuses and crack grows.

Figure 7.7a shows the details of the crack evolution as a function of lithiation time for $C_0/C_{max} = 0.8$ and $\Gamma_0/E\varepsilon_0^2 L = 4.2$ (point *b* in the phase diagram). The crack propagates by a "go and wait" behavior in which the crack "goes" at the transition of I-II, III-IV, and V-VI, and "waits" at II-III and IV-V. The "go" state represents the rapid crack propagation such that the crack length versus lithiation time exhibits a pulsed jump in Figure 7.7a. The slow redistribution of Li cannot

catch the fast crack propagation, resulting in the recovery of fracture toughness at the fresh crack tip and the temporary arrest of the crack growth. The corresponding Li concentration profiles before and after the "go" state are shown in Figure 7.7b. Followed each rapid growth of crack is the "wait" state during which the crack is arrested and the crack length remains a constant. As shown in Figure 7.7b, Li gradually accumulates at the crack tip in the "wait" state until the fracture toughness drops below the energy release rate again. Figure 7.7c-e shows the schematics of delayed fracture due to the concurrent Li diffusion, Li embrittlement, and crack growth. While the crack "waits", the crack remains a steady state. Li accumulates around the crack tip due to the stress concentration which weakens the fracture strength of the host material. When the fracture resistance is below the energy release rate, crack propagates and creates fresh surfaces without Li. Without the Li embrittlement effect, the fracture resistance increases and crack stops. The "go" and "wait" repeat while Li diffuses and crack grows. It is noted that the surface diffusion on new crack surface is not explicitly modeled in the examples, partially because there is no experimental measurement of surface diffusivity to my best knowledge, and partially because the phase diagram in Figure 7.6, which delineates different fracture behaviors, will not be altered if surface diffusion is added. In Figure 7.6, the fracture behavior depends on the final states of mechanical equilibrium and diffusion equilibrium, and is insensitive to the transient state of Li transport. Nevertheless, the waiting time in the "wait-and-go" plot in Figure 7.7 will be shortened if the fast surface diffusion on new crack surface is considered.

In the phase diagram of corrosive fracture, it is demonstrated that the fracture toughness and the chemical load play the major role in regulating the fracture behavior of the chemomechanical system. The two factors both originate from the stress modulated Li diffusion and Li-assisted embrittlement. Next, the effect of stress-diffusion coupling and Li embrittlement

is explored in detail by evaluating each factor separately. The sensitivity of the degree of Li embrittlement on the phase diagram will be first examined. As written in Equation (7.5), the degree of embrittlement is represented by the exponent n where a larger value of n indicates severer embrittlement due to Li insertion. Figure 7.8a shows the fracture toughness of the host material as a function of the Li concentration for three different embrittlement exponents n=1, 2, and, 3. It is clear that the fracture toughness of the host material reduces as Li inserts and a higher exponent n induces more degradation of the fracture strength except the setting values at the initial and the final Li concentrations. Using the same procedure in Figure 7.6a, the phase diagram of the three different embrittlement exponents is constructed in Figure 7.8b. With a different set of embrittlement function, the border lines separating the different fracture zones are largely shifted. Comparing to the phase diagram for n=2, a severer Li embrittlement (n=3) reduces the size of the arrested fracture regime (safe region) and the delayed fracture occupies most space of the variable plane. In this case, the chemomechanical system becomes more sensitive to the material defects and flaws and the mechanical integrity is vulnerable upon lithiation. On the other side, when the Li embrittlement is less severe (n=1), the region of arrested fracture is enlarged such that the pre-existing flaws is less likely to propagate during the Li reaction.

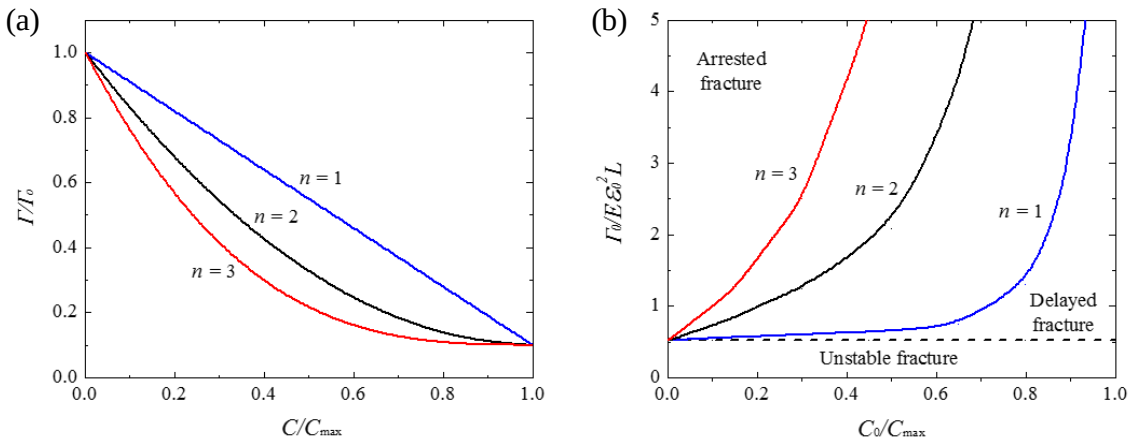

Figure 7.8. (a) Fracture toughness of the host material as a function of the Li concentration for different embrittlement exponents n = 1, 2, and 3. A larger value of n represents a severer Li embrittlement effect. (b) Phase diagram of corrosive fracture with a variation of the embrittlement exponent. When the embrittlement exponent increases, the size of the arrested fracture zone is reduced while the region of delayed fracture is enlarged.

Next, the influence from the stress-regulated Li diffusion on the corrosive fracture behavior will be examined. Equation (2.34) is rewritten by introducing a non-dimensional parameter χ that represents the degree of the stress effect on Li diffusion,

$$\mu = \mu_0 + kT\ln\left(\frac{C}{C_{\max} - C}\right) - \chi\Omega\sigma_m\,. \tag{7.6}$$

Specifically, χ can be varied from 0 to 1 in which $\chi = 1$ includes the stress effect on Li diffusion for the isotropic-expansion host during Li insertion, and $\chi = 0$ ignores the stress-diffusion coupling. Figure 7.9 plots the comparison of the phase diagrams with ($\chi = 1$) and without ($\chi = 0$) considering the stress effect on Li diffusion. When the stress effect is accounted ($\chi = 1$), the high tensile stress near the crack tip promotes Li embrittlement by regulating the Li accumulation near the crack tip. As a result, the region of the arrested fracture (safe region) shrinks in size and the delayed fracture is more dominant on the variable space. It seems that the stress-diffusion coupling acts like a catalyst which accelerates the Li transport and expediates the corrosive fracture of the host material. Conversely, in the hypothetical scenario that Li is only supplied by the chemical

boundary condition and is not influenced by the local stress field ($\chi = 0$), the delayed fracture is much less likely to occur.

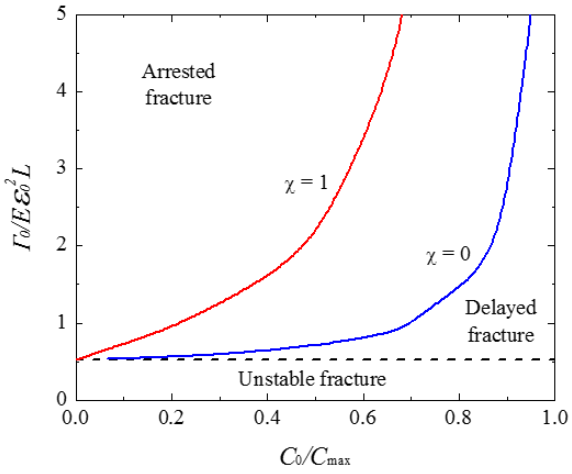

Figure 7.9. Comparison of the phase diagrams with (χ = 1) and without (χ = 0) considering the stress effect on Li diffusion. By considering the stress-diffusion coupling (χ = 1), the stress field near the crack tip regulates Li accumulation and promotes embrittlement. Therefore, the arrested fracture zone (safe region) shrinks in size and delayed fracture zone increases.

7.3.1.2 Li extraction induced material embrittlement and corrosive fracture

The delithiation-induced fracture in electrodes has been extensively studied [34, 99, 180]. Li extraction is usually accompanied with a volumetric contraction of electrodes which induces a field of tensile stress and causes crack formation. To examine the corrosive fracture during the delithiation process, it is assumed that the host is initially at the fully lithiated state (i.e. initial Li concertation $C_{\mathrm{i}} = C_{\max}$). Delithiation starts upon applying the chemical load $C_0/C_{\max} = 0.5$, and is terminated when the system reaches chemical equilibrium. During delithiation, the system is free of the external mechanical load ($\varepsilon = 0$) so that the stress field is solely due to the delithiation induced volumetric contraction. This type of chemomechanical boundary condition was widely used to simulate the delithiation of spherical active particles or thin film electrodes constrained by a substrate.

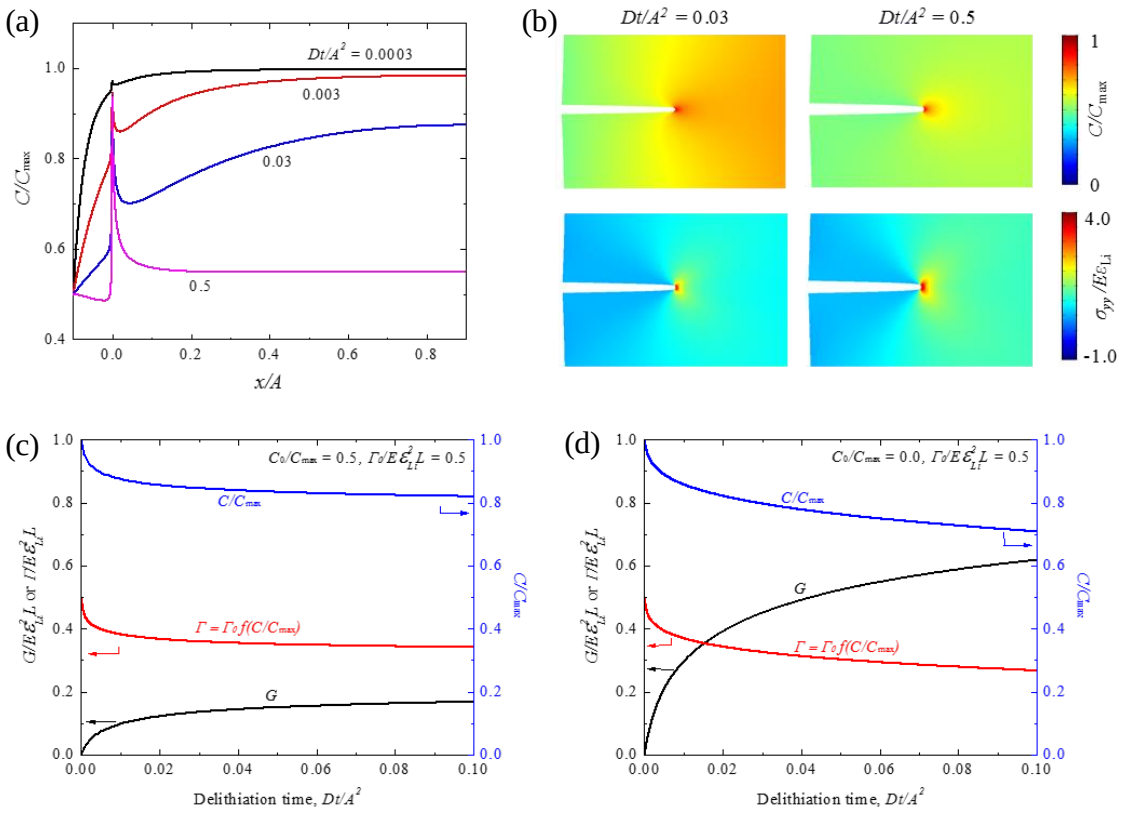

Figure 7.10. (a) The distribution of Li concentration along the crack path in the *x*-direction during delithiation with the chemical boundary condition C_0/C_{max} = 0.5. (b) The contour profiles of Li concentration and tensile stress near the crack tip at Dt/A^2 = 0.03 and 0.5. (c, d) The evolving of Li concentration C/C_{max} at the crack tip (blue line), energy release rate $\Gamma_0/E\varepsilon_{Li}^2L$ (black line), and fracture toughness $\Gamma = \Gamma_0 \cdot f(C/C_{max})$ (red line) for the chemical load C_0/C_{max} = 0.5, and (d) C_0/C_{max} = 0.

Figure 7.10a shows the distribution of Li concentration along the crack path in the *x*-direction in the course of delithiation. Li close to the surface is quickly depleted while the Li concentration in the inner regime remains high. The mismatch strain generates a field of tensile stress in the Li-poor regime near the surface and compressive stresses in the Li-rich regime. Once delithiation proceeds toward the inner regime, a stress singularity at the crack tip emerges which attracts Li accumulation at the crack zone, Figure 7.10a. Even though the average Li concentration in the system decreases during delithiation, Li concentration near the crack tip remains a large value as seen in Figure 7.10a and b. Li retention at crack tip is attributed to the tensile stress in the

host, especially near the crack tip, which continuously increases upon delithiation that traps Li via the stress regulated Li distribution.

In addition to modulating Li accumulation around the crack tip, the growing stress singularity upon delithiation also increases the driving force for crack growth. Figure 7.10c plots the energy release rate $G/E\varepsilon_0^2L$ (black line) as a function of the delithiation time with a chemical load $C_0/C_{max} = 0.5$. Energy release rate starts from zero (i.e. $G_0 = 0$) since no mechanical force is applied, and monotonously increases as delithiation proceeds. The fracture toughness (red line) at the crack tip is determined by the local Li concentration (blue line), Figure 7.10c. Li retention at the crack tip remains higher than 80% of C_{max} during the entire delithiation. Considering the delithiation-induced embrittlement described in Equation (7.5), the average fracture toughness of the system significantly drops as Li depletes, however, the fracture toughness near the crack tip remains a high value because the Li accumulation at the crack tip which prevents the host from the embrittlement effect. As the energy release rate G increases and the fracture toughness of the delithiated phase reduces, delithiation generally promotes crack growth. Nevertheless, the shielding effect from the stress regulated Li accumulation may postpone the crack propagation as shown in Figure 7.10c. Similarly, Figure 7.10d shows the Li concentration (blue line) at the crack tip, energy release rate (black line), and fracture toughness (red line) of the host at the crack tip in terms of the delithiation time for a larger chemical load, $C_0/C_{max} = 0$. A larger chemical load results in a higher energy release rate for crack growth and a lower fracture toughness of the host which causes crack growth during delithiation.

Growth behavior of the crack after it starts propagating will be next examined. Figure 7.11a plots the driving force of crack growth in which the energy release rate $G/E\varepsilon_{Li}^2L$ at various delithiation times Dt/A^2 are plotted as a function of the normalized crack extension da/A. During

delithiation, the regime away from the surface is less delithiated such that the magnitude of the tensile stress in the inner regime is smaller. Once the crack growth initiates, crack migrates from the Li-poor regime of high tensile stresses to the inner Li-rich regime of low tensile stresses which reduces the energy release rate, Figure 7.11a. Without considering the Li embrittlement, the fracture toughness of the system would remain constant during Li extraction. In this case, the condition for stable crack growth will be satisfied, i.e. $dG/da < d\Gamma/da$, once the crack starts to propagate. Therefore, the system behaves as a delayed fracture [108]. If the fracture toughness is determined by the Li concentration via the embrittlement effect, the fracture toughness (lower graph, Figure 7.11b) can be calculated based on the Li concentration distribution near the crack tip (upper graph, Figure 7.11b). Here it is assumed that the driving force and fracture resistance satisfy the Griffith's criterion $G = \Gamma$ at the time $Dt/A^2 = 0.03$. Once the crack starts to propagate, crack tip immediately migrates away from the Li-accumulated regime. At the fresh crack tip, the material fracture toughness decreases. In this scenario, the growth of crack stops when $dG/da \leq d\Gamma/da$ within a finite crack extension da and resumes when the energy release rate overcomes the fracture resistance. This behavior is also a typical "go and wait" delayed fracture.

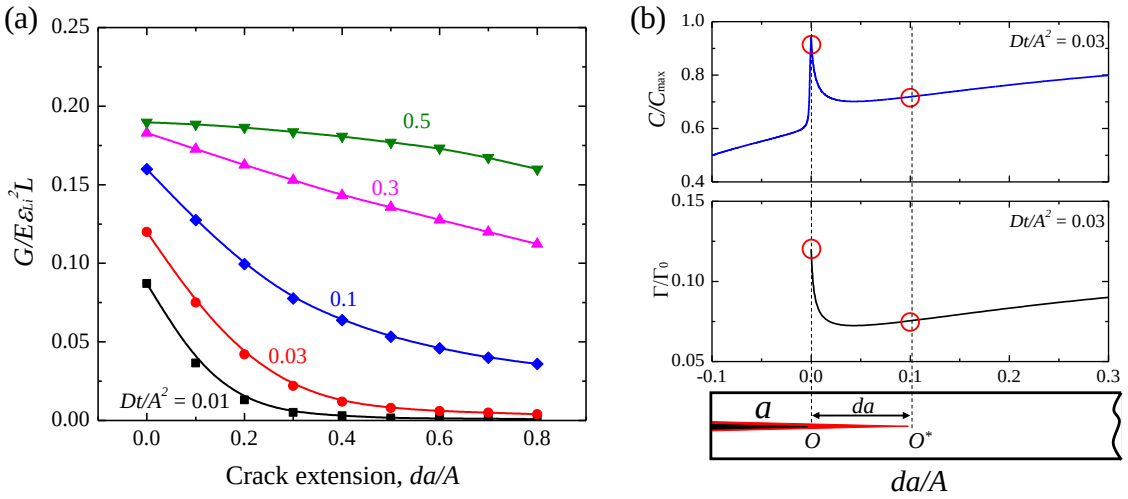

Figure 7.11. Energy release rate G and crack resistance Γ during Li extraction. (a) Energy release rate $G/E\varepsilon_{Li}^2L$ as a function of the normalized crack extension da/A at different delithiation times. G decreases as crack extends because the crack tip migrates from the Li-poor zone to the Li-rich regime. (b) Li concentration C/C_{max} (upper figure) and fracture toughness Γ/Γ_0 (lower figure) near the crack tip at $Dt/A^2 = 0.03$. When the crack tip propagates from O to O*, fracture toughness Γ of the host material at the new crack tip decreases. Crack growth stops when $dG/da \leq d\Gamma/da$ and resumes when the energy release rate overcomes the fracture resistance.

Cohesive element modeling is performed to construct the phase diagram of corrosive fracture upon delithiation, Figure 7.12. Since there is no external mechanical load, only two types of fracture behaviors are identified: arrested and delayed fracture. The effect of the Li embrittlement on the corrosive fracture of the chemomechanical system will be first examined. The phase diagrams in Figure 7.12a in terms of C_0/C_{max} and $\Gamma_0/E\varepsilon_0^2L$ are obtained with and without considering the Li embrittlement effect. C_0/C_{max} are selected from 1 to 0 to represent the degree of delithiation from low to high, respectively. The Li embrittlement enlargers the size of the delayed fracture (lower right zone) which increases the potential of crack propagation upon delithiation. This demonstrates that Li embrittlement makes the chemomechanical system more vulnerable to defects and flaws, and thus deteriorates the mechanical integrity upon delithiation.

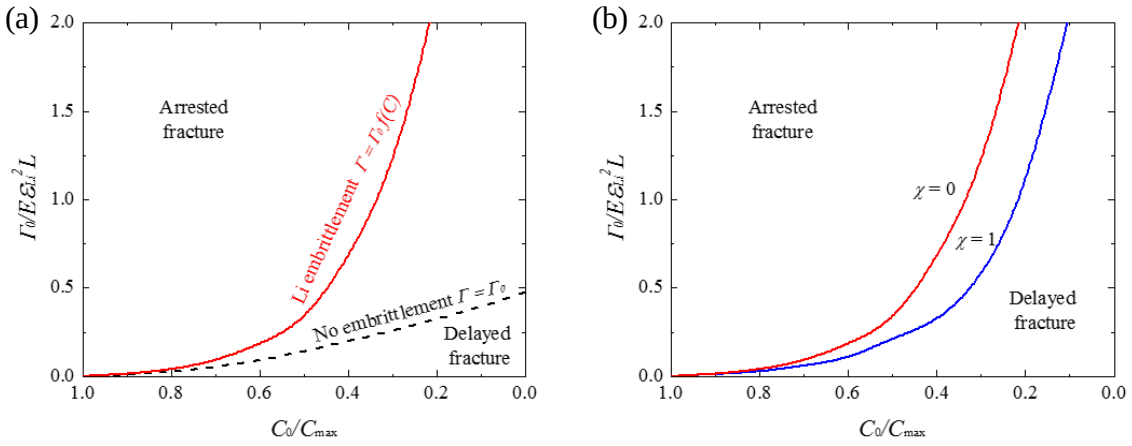

Figure 7.12. (a) Comparison of the phase diagrams of corrosive fracture with (red line) and without (black dashed line) considering the Li embrittlement effect. (b) The comparison with (χ = 1) and without (χ = 0) considering the stress-diffusion coupling.

Then, the effect of stress regulated diffusion on the corrosive fracture during delithiation is investigated. Figure 7.12b plots the phase diagrams with (χ=1) and without (χ=0) considering the stress effect on Li diffusion. As discussed in Figure 7.9, stress-regulated diffusion upon lithiation acts like a catalyst that promotes Li embrittlement and deteriorates the mechanical integrity of the system. Conversely, the stress-regulated diffusion during delithiation provides a shielding effect on Li embrittlement because the local tensile stress traps Li around the crack tip such that the host material retains a high local Li concentration upon Li extraction. Therefore, when the coupling effect between stress and diffusion is considered (χ=1), the arrested fracture zone expands in its size while the delayed fracture regime shrinks, Figure 7.12b.

7.3.2 Corrosive fracture in NMC cathode

The corrosive fracture model is used to simulate the intergranular fracture in NMC cathode materials. NMC is the state-of-the-art cathode for the application of electric vehicles, owing to its low cost, excellent cyclic stability, and tunable electrochemical properties [203]. The synthesis process results in a hierarchical microstructure in NMC where small primary particles of

submicron size aggregate via weak interactions and form secondary particles of tens of micrometers [35]. The cohesion strength of the primary particles is weak, thus the grain boundaries is subject to intergranular cracks generated by the mismatch strains among the primary particles during Li reactions. Specifically, experiments have shown that NMC secondary particles can easily disintegrate into isolated clusters over cycles which mechanically degrades the electrodes and deteriorates the electrochemical performance of batteries. Figure 7.13a and b show the experimental observation and sketch of the structural disintegration of the NMC particles. Nanoindentation is used to determine that the interfacial strength of NMC particles is largely dependent on the state of charge and the cycle number [133]. The interfacial fracture toughness between primary particles decreases upon delithiation and steadily fades as the electrochemical cycles proceed, presumably because of the accumulation of microscopic defects and damages at the interfaces between the constituent primary particles.

In this section, corrosive behavior of intergranular cracks in an NMC secondary particle upon Li cycles are simulated and compared with experiments. The spherical 3D particles are simplified into a more tractable 2D plane-strain model with a radius $R = 5\,\mu m$. The NMC secondary particle is represented by a circular domain composed of multiple primary particles of random sizes and shapes, Figure 7.13c. The polygonal primary particles are generated using the Voronoi tessellation. To reduce the computational cost, a quarter of the spherical particle is used in the numerical modeling. Every primary particle within the model has its own grain orientation and the orientation of *c*-axis is indicated by the arrows in Figure 7.13c. NMC has a layered structure where Li, O, and transition metals occupy alternating atomic layers. The lattice strain associated with Li reactions is highly anisotropic. $LiNi_{0.6}Mn_{0.2}Co_{0.2}O_2$ (NMC622) is used as a model system and simulate the delithiation process from $LiNi_{0.6}Mn_{0.2}Co_{0.2}O_2$ to

$Li_{0.5}Ni_{0.6}Mn_{0.2}Co_{0.2}O_2$. The strains in the *a*-axis (b-axis) and *c*-axis are set to be -2% (compressive) and 1% (tensile), respectively, according to the Bragg peak shifting in *in-situ* XRD scanning experiments [193]. The magnitude of the anisotropic strain during Li extraction is assumed to be proportional to Li concentration. The experimental results of Li embrittlement on the interfacial fracture toughness are implemented into the numerical simulation. The evolving interfacial strength at different states of charge and different cycle numbers is fitted to the experimental values [133], Figure 7.13d. The material properties for NMC622 are selected as follows: Young's modulus $E = 140$ GPa [133], Poisson's ratio $\upsilon = 0.3$, Li diffusivity $D = 7 \times 10^{-15}$ m^2/s [238] and $C_{\max} = 35164$ mol/m^3. Several dimensionless quantities are identified: Li concentration $C/C_{\max}$, diffusion time Dt/R^2, fracture toughness $\Gamma/E\varepsilon_{Li}^2 R$, and crack length a/R. ε_{Li} is set as the lattice strain 2% (-2%) along the *a*-axis upon lithiation (delithiation).

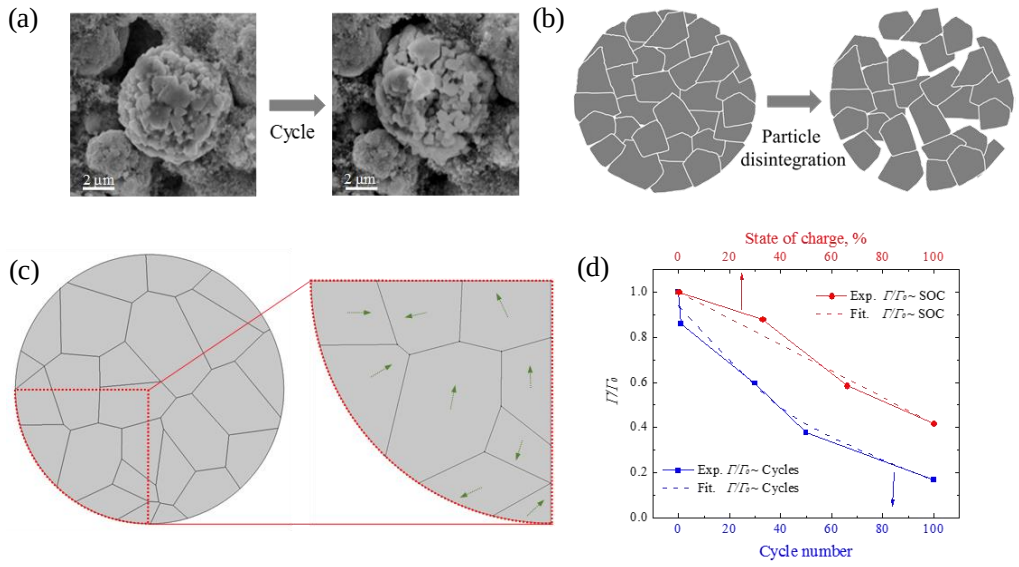

Figure 7.13. (a) SEM images and (b) schematics showing heavy intergranular fracture in NMC cathode materials. (c) A model of a spherical NMC secondary particle consisting of irregular primary particles. A quarter of the spherical particle is used in the modeling of intergranular fracture induced by Li reactions. The arrows indicate the *c*-axis orientation within each grain. (d) Fracture strength of NMC is highly dependent on the state of charge and the cycle number. The experimental values are measured by nanoindentation [133].

7.3.2.1 Intergranular cracks in NMC upon delithiation

Corrosive behavior of intergranular cracks in NMC in the initial delithiation is first investigated. The NMC particle is at the fully lithiated state (C_i/C_{max}=1) before delithiation starts. A constant chemical load C_0/C_{max} = 0.5 is applied on the surface of the NMC aggregated particle to mimic the delithiation process from the initial state $LiNi_{0.6}Mn_{0.2}Co_{0.2}O_2$ to the final product $Li_{0.5}Ni_{0.6}Mn_{0.2}Co_{0.2}O_2$. This chemical boundary condition of Li exchange is analogous to a potentiostatic operation of a battery cell. Delithiation terminates when a homogeneous Li concentration C/C_{max} = 0.5 within the particle is reached. Figure 7.14a plots the radial distribution of Li concentration in the NMC secondary particle during delithiation. The outer shell is delithiated much sooner than the inner region and the chemical potential gradient of Li drives Li diffusion from the center toward the surface. Figure 7.14b plots the contour profiles of Li concentration and delithiation-induced strain along the *x*-direction at the delithiation times Dt/R^2=0.0048, 0.024, and 0.24, respectively. At the early state of delithiation, the grains close to the surface experience a larger tensile strain owing to their low Li concentration. The mismatch strain from adjacent grains of different grain orientations can trigger intergranular cracks near the surface regime and drive the crack propagation toward the center of the NMC particle.

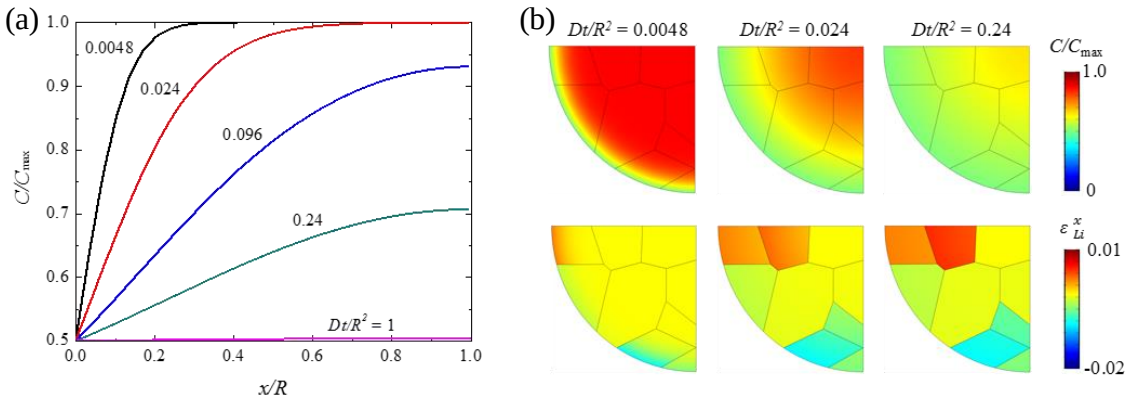

Figure 7.14. (a) Radial distribution of Li concentration in the NMC secondary particle under the delithiation load $C_0/C_{max} = 0.5$. (b) The contour profiles of Li concentration and delithiation-induced strain at delithiation times Dt/R^2=0.0048, 0.024 and 0.24, respectively.

Intergranular cracks initiate and propagate when the energy release rate for crack growth exceeds the fracture resistance of the interface between primary particles. Figure 7.15 plots the crack length as a function of the delithiation time for the NMC particle of pristine interfacial fracture toughness $\Gamma_0/E\varepsilon_{Li}^2 L = 0.045$. The insets show the contour plots of the first principal stress at various delithiation times and their corresponding crack morphologies. The figures I-V show the crack patterns with the arrows indicating the crack growth path. Without considering the Li embrittlement effect, the NMC secondary particle has a constant interfacial fracture toughness upon Li reactions and the initiation of intergranular cracks is solely dependent on the development of tensile stress near the surface. Once an intergranular crack starts growing, the tensile stress and associated strain energy behind the crack tip are effectively released which prohibits initiation of another intergranular crack from the surface. The triggered crack propagates along the grain boundary and toward the center of the NMC particle as the field of mechanical stresses evolve upon delithiation, Figure 7.15a. The intergranular crack will eventually meet the joints of the grain boundaries which will force the crack to deflect. The deflection of crack requires a higher driving force for a continuous growth which retards or even stagnates the propagation of the intergranular

crack in NMC. Overall, without considering the Li embrittlement effect, it is observed that a single intergranular crack and its dynamics dominates the failure of NMC particles. This morphology is somewhat different from the experimental observations in which the NMC particles are often disintegrated by multiple intergranular cracks and generation of several isolated clusters of primary particles [193]. This adds another motivation to examine the fracture behavior of NMC by including the Li embrittlement on the interfacial strength. Figure 7.15b shows a similar plot of the evolution of the crack length upon Li extraction and snapshots of crack patterns and stress profiles at various times. At the stage I, an intergranular crack initiates from the surface and starts propagation. This intergranular crack initiates at an earlier time and propagates more quickly due to the Li embrittlement to the interface. After the initial crack growth, although the tensile stress and the strain energy behind the crack tip are released, nucleation of new cracks elsewhere are still probable because the fracture resistance dramatically drops as the delithiation proceeds. When one intergranular crack encounters the joints of grain boundaries that deflect the crack, other cracks are still in propagation, as seen in the snapshots from IV to V in Figure 7.15b. As a result, multiple cracks co-exist and co-evolve in NMC particle and this fracture behavior is in good agreement with the experimental observations of crack morphologies in NMC during the initial delithiation [193, 245].

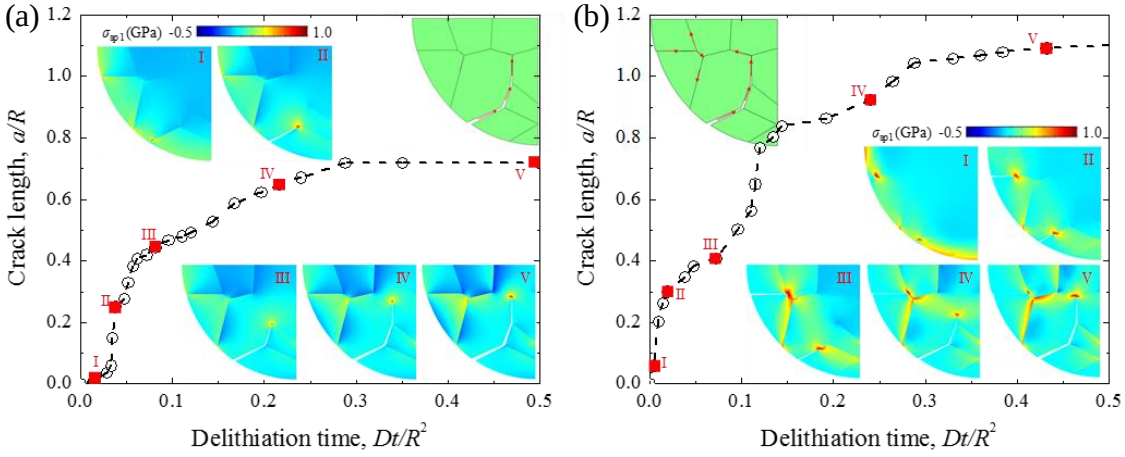

Figure 7.15. The evolution of intergranular cracks in NMC cathode during delithiation without (a) and with (b) Li embrittlement effect. Insets show the contour plots of the first principal stress at various delithiation times and their corresponding crack morphologies. The arrows indicate the crack growth paths. For a better view, the deformation of the interfacial cracks has been amplified by a factor of 3.

As previously discussed in Chapter 7.3.1, the corrosive fracture of electrodes is largely dependent on the fracture toughness of the pristine host material $\Gamma_0/E\varepsilon_{Li}^2 L$. Here the effect of $\Gamma_0/E\varepsilon_{Li}^2 L$ on the intergranular crack of NMC secondary particles can be evaluated. The length of the intergranular crack in a 3D configuration is plotted in terms of the delithiation time Dt/R^2 and the pristine fracture toughness $\Gamma_0/E\varepsilon_{Li}^2 L$, Figure 7.16. In both cases with and without considering the Li embrittlement, the initial fracture toughness determines the time of crack initiation as well as the final crack length. In the case without Li embrittlement, no intergranular crack would occur for a high pristine fracture toughness $\Gamma_0/E\varepsilon_{Li}^2 L = 0.06$, while the same value of pristine fracture toughness is apparently insufficient to suppress the intergranular crack when considering the Li embrittlement effect. For $\Gamma_0/E\varepsilon_{Li}^2 L = 0.03$ and 0.045 in Figure 7.16a, the crack length remains a plateau in the later state of delithiation because the intergranular crack hits the joints of grain boundaries and the driving force is not sufficient to overcome the resistance for crack deflection without Li embrittlement. In comparison, $\Gamma_0/E\varepsilon_{Li}^2 L = 0.045$ in Figure 7.16b shows that, when the

interfacial fracture toughness degrades in delithiation, the delithiation-induced mechanical stresses can cause the crack deflection and continuous growth. In general, whether the crack deflection will occur or not depends on the competition between the energy dissipation of crack deflection and Li embrittlement. If the energy dissipation of crack deflection is sufficiently small, crack deflection can still occur even though Li embrittlement is ignored, as indicated by the sudden increase of crack length for $\Gamma_0/E\varepsilon_{Li}^2 L = 0.015$ in Figure 7.16a.

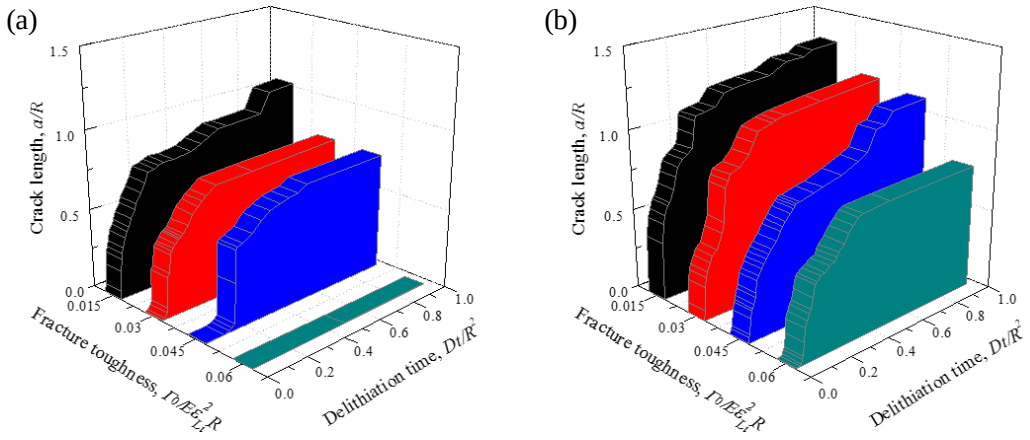

Figure 7.16. 3D plots of intergranular crack length as a function of the delithiation time Dt/A^2 and pristine fracture toughness of NMC $\Gamma_0/E\varepsilon_{Li}^2 L$ without (a) and with (b) considering the Li embrittlement effect.

7.3.2.2 Intergranular cracks in NMC upon Li cycles

The dynamic evolution of corrosive intergranular cracks in NMC during Li cycles is also modeled. Previous experiments have shown that the electrochemical cycle deteriorates the interfacial strength of NMC particles due to the surface reconstruction and the accumulation of microscopic defects at the interface of the primary particles [133]. In the simulation of lithiation and delithiation cycles, delithiation starts first, as described in Chapter 7.3.2.1. Once delithiation is finished, lithiation will continue by applying a chemical load $C_0/C_{max} = 1$ on the surface of the NMC secondary particle. The delithiation and lithiation processes will repeat and the interfacial

fracture toughness of NMC secondary particles is set as a function of the cycle number as shown in Figure 7.13d. The variation of the fracture toughness within a cycle has been ignored, for the purpose to focus on the dynamic fracture growth induced by the electrochemical cycles.

If Li embrittlement induced by the electrochemical cycles is not accounted, the fracture resistance remains constant as the Li cycle proceeds. In this case, even though a cyclic chemical load is applied to the NMC particle, the crack length will remain the same over cycles. In another word, either no crack forms if the interfacial fracture toughness is sufficiently high or the intergranular crack remains stagnation in the subsequent cycles if the crack stops growth in the first cycle. This scenario is contradictory to the typically observation in experiments that intergranular cracks in NMC steadily grows over cycle [35, 193]. This fatigue-like damage accumulation in NMC upon electrochemical cycles is mainly due to the Li embrittlement effect. Figure 7.17a plots the evolution of intergranular cracks in NMC secondary particles where the crack length grows during Li cycles until the crack penetrates through the entire secondary particle. Specifically, the crack dynamics shows a "grow-stagnate-grow" behavior where the fast crack growth in the early cycles is induced by the Li embrittlement on the interfacial strength, the following crack stagnation is due to crack kinking at the joints of the grain boundaries, and the later stage of crack growth is because of the significant decrease of the fracture resistance after a large number of cycles that reduces the energy for crack deflection. To compare with the experimental observation of the crack morphology, a recent transmission electron microscopy (TEM) study [35] showed similar accumulation of damage in that most damage occurred within the first 10 cycles while the rate of damage accumulation in the following 10^{th} to 100^{th} cycle is much slower. In addition, Figure 7.17b presents the contour plots of the first principal stress at various cycle numbers and their corresponding crack morphologies. The simulated crack

morphologies caused by Li cycles qualitatively agree with the intergranular crack patterns in NMC observed by the scanning electron microscopy (SEM) and TEM, as shown in Figure 7.17c and d, respectively [193].

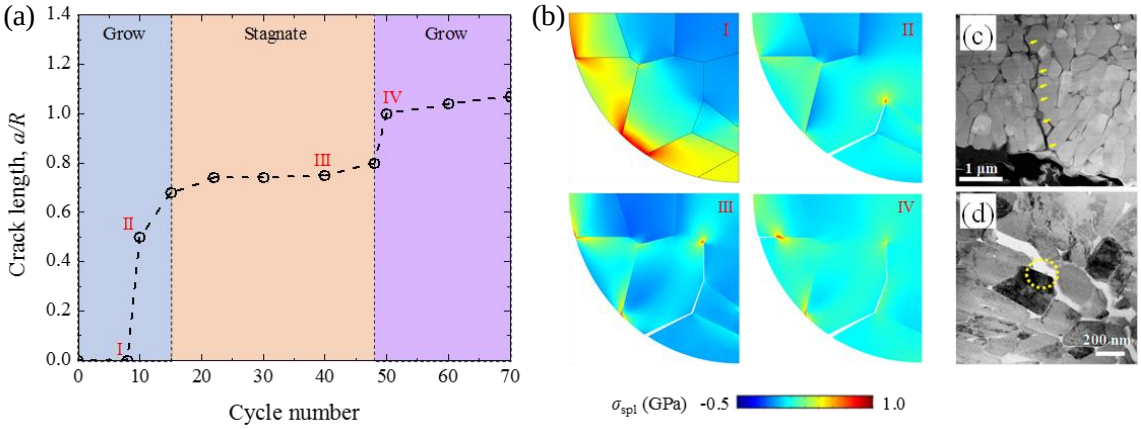

Figure 7.17. (a) The growth of intergranular cracks in NMC secondary particles upon Li cycles. Crack stagnation is because of a larger driving force required to deflect the interfacial cracks at the joints of the grain boundaries. (b) The contour plots of the first principal stress at various cycle numbers and their corresponding crack morphologies. (c) SEM and (d) TEM images showing the intergranular cracks in NMC upon electrochemical cycles. Figures are reproduced from the work of Ryu et al. [193]

7.4 Conclusions

Corrosive fracture of electrodes under concurrent mechanical and chemical load is investigated. Li acts like a corrosive species that deteriorates the mechanical strength and toughness of the host electrodes upon Li cycles. A developed finite element program based on a continuum theory of coupled diffusion and large deformation is utilized to investigate the fracture behavior that is dependent on the chemomechanical load, diffusion kinetics, Li embrittlement/ toughening effect, and material properties. The competition between energy release rate and fracture resistance as crack grows during both Li insertion and extraction is examined in detail. A

phase diagrams is constructed to delineate the unstable, arrested, and delayed fracture zones in the variable space of material properties and the load conditions.

In the case of Li embrittlement during the insertion reaction, Li accumulation at the crack tip appends a local dilatational strain which reduces the stress field and thus the driving force for crack growth. Meanwhile, Li concentration at the crack tip also reduces the fracture toughness which promotes crack initiation. Crack propagates as a typical delayed fracture of the feature of "wait and go" – the "wait" depends on the Li transport and supply of Li at the crack tip, and the "go" depends on the Li embrittlement of the host. The pristine fracture toughness of the host material and the chemical load are the key parameters that determine the crack behavior. In the parametric studies, it is found that the stress regulated Li diffusion promotes Li embrittlement through trapping Li at the crack tip, and a severer Li embrittlement effect facilitates delayed fracture.

For Li extraction induced material embrittlement which is typically observed in cathodes, the driving force for crack growth is entirely due to the delithiation induced volumetric contraction. The continuous Li extraction increases the energy release rate and reduces the fracture toughness of the host material which facilitates crack formation upon delithiation. Without an external mechanical load, the corrosive fracture shows two distinct behaviors: arrested and delayed fracture. In this case, the stress regulated Li diffusion provides a shielding effect at the crack tip which retards crack growth.

During the battery cycles, the mismatch strain at the grain boundaries often induces the structural decohesion which constitutes the major mechanical degradation in NMC cathode materials. The corrosive fracture model is used to simulate the intergranular fracture in NMC aggregated particles. It is found that Li embrittlement accelerates the initiation and growth of

intergranular cracks in an NMC particle. Furthermore, Li embrittlement is a reason for the propagation of multiple intergranular cracks and crack deflection through the grain boundaries. The numerical modeling of crack growth and patterns agrees well with the experimental observations by recent TEM and SEM studies.

8. CONCLUSIONS AND OUTLOOK

8.1 Summary and concluding remarks

This thesis studies the couplings between mechanics and electrochemistry in Li-ion batteries using integrated theories and experiments. A continuum model coupling the diffusion and large elasto-plastic deformation is established. The continuum model provides a theoretical framework to understand the concurrent mechanics (stresses, plasticity, fracture) and electrochemical processes (mass transport, charge transfer, potential and capacity of batteries) in Li-ion batteries. This continuum model is implemented into a computational program which is particularly useful to model the complex microstructures of the real electrodes and simulate the influence of mechanics phenomena on the electrochemical behaviors in batteries. This thesis includes a setup of the *in operando* electro-chemo-mechanical quantification platform that integrates a nanoindenter and an electrochemical station in an Argon-filled glovebox. This platform can simultaneously detect the electrochemical and mechanical responses from the electrode materials under real battery working conditions. The coordinated approaches of continuum modeling and experiments can inform and guide each other, offering complete mechanistic understanding on the tightly coupled mechanics and electrochemistry in Li-ion batteries. The main conclusions in the previous chapters are summarized here.

- Chemomechanical behaviors of three-dimensional composite electrodes are model and the intimate coupling between the lithiation kinetics and mechanical stresses is explored. It is found that the Li profiles and stress states in multiple active particles constrained by a matrix are significantly different from that in a free-standing configuration. The mechanical interactions regulate Li chemical potential in Si nanowires and transform the isotropic deformation to an anisotropic behavior and vice versa. The modeling highlights

the strong coupling between the electrochemistry of lithiation and mechanical stresses in the composite electrodes and provides important insight on the design of resilient batteries.

- Reconstructed models for commercial batteries are employed to study the co-evolution of mechanical stresses and Li storage. It is found that the state of charge in the active particles is highly inhomogeneous regulated by the stress field. Significant capacity loss is possible due to the mechanical confinement of the inactive matrix and particles contact. A multi-dimensional space of design is open for the optimization of the mechanical and electrochemical performance of composite electrodes by the selection of the geometry, network, and properties of the active particles and the surrounding medium.
- Particle disintegration which attributes to the major mechanical degradation in NMC cathode materials is investigated. The microstructural evolution in the local regimes of NMC electrodes is tracked before and after electrochemical cycles. It is found that the slow charging rate results in severe disintegration of the NMC secondary particles while fast charging causes less damage. Electrochemical impedance spectroscopy (EIS) analysis confirms that the charging rate is a controlling factor on the mechanical disintegration of NMC particles and quantifies the effect of particle decohesion on the impedance of the cells. A numerical model is used to investigate the Li diffusion and stress evolution within the NMC secondary particles. The numerical results are in good agreement with the experimental observations.
- Elastic modulus, hardness, and interfacial fracture toughness of NMC particles are measured using instrumented nanoindentation in an inert environment. NMC particles show considerably lower mechanical properties than sintered pellets because of the hierarchical meatball structure. The dynamic evolution of the mechanical properties is

obtained as a function of the state of charge and the cycle number. Both the elastic modulus and hardness of NMC largely decrease when Li is extracted from the layered crystalline lattice. The mechanical properties of NMC, in particular the interfacial fracture resistance, significantly decrease as the electrochemical cycles proceed. The loss of mechanical strength is due to the accumulation of microscopic defects and damages at the interface of the constituent primary particles.

- Corrosive fracture of electrodes under concurrent mechanical and chemical load is studied. A continuum theory of coupled diffusion and large deformation is implemented into finite element program to investigate the fracture behavior that is dependent on the chemomechanical load, diffusion kinetics, Li embrittlement effect, and material properties.
    - In the case of Li embrittlement during the insertion reaction, Crack propagates as a typical delayed fracture of the feature of "wait and go" – the "wait" depends on the Li transport and supply of Li at the crack tip, and the "go" depends on the Li embrittlement of the host. In the parametric studies, it is found that the stress regulates Li diffusion promotes Li embrittlement through trapping Li at the crack tip, and a severer Li embrittlement effect facilitates delayed fracture.
    - For Li extraction induced material embrittlement, the driving force for crack growth is entirely due to the delithiation induced volumetric contraction. Without an external mechanical load, the corrosive fracture shows two distinct behaviors: arrested and delayed fracture. In this case, the stress regulated Li diffusion provides a shielding effect at the crack tip which retards crack growth.
    - The theory is used to model the intergranular fracture in NMC aggregated particles. The evolving interfacial strength at different states of charge and different cycle

numbers is implemented in the numerical simulation. It is found that Li embrittlement accelerates the initiation and growth of intergranular cracks in an NMC particle. Furthermore, Li embrittlement is a reason for the propagation of multiple intergranular cracks and crack deflection through the grain boundaries.

8.2 Outlook of future work

This thesis focuses on the mechanical phenomena and electrochemical processes within the electrode materials of Li-ion batteries. Recently, mechanical issues and electro-chemo-mechanical couplings are frequently observed at the interface between electrode and electrolyte of Li-ion batteries [246, 247]. Furthermore, the electro-chemo-mechanical study on other battery systems such as Li-sulfur (S) battery and sodium (Na) -ion battery is still at the early stage [248]. Beyond the work in this thesis, various interesting topics need to explore in future work.

- The degradation processes of electrode materials still need to be further explored. Various novel experimental techniques enable people to characterize microstructural evolutions during battery cycling [220]. These *in situ* microstructural characterizations provide a mechanistic understanding on the damage initiation and accumulation caused by Li reaction. Furthermore, the atomic scale characterizations can probably reveal the underlying mechanisms for the evolution of macroscopic mechanical properties of electrode materials, which is helpful for the design of Li-ion batteries with an excellent mechanical resilience.
- The intimate coupling between mechanics and electrochemistry does not only influence the kinetics of Li diffusion within the electrodes, it also affects the thermodynamics of electrochemical reaction at the interface between electrode and electrolyte. A few recent works have explored the stress effect on the surface charge transfer at electrode/electrolyte

interface. However, very little work attempts to investigate the electrochemical response of batteries by considering the stress effect on both surface charge transfer at the interface and Li bulk diffusion within the electrodes. As shown in Figure 1.9b, the stress may regulate the short-term and long-term responses of batteries via affecting the surface charge transfer and Li bulk diffusion, respectively.

- All solid-state batteries (ASSB) recently attract a lot of research interest due to its unique advantages of excellent stability and high safety. Nevertheless, the mechanical issues in ASSB, especially the contact issue at the interface between solid electrolyte and electrodes, hinder the large-scale development of such batteries. For instance, the poor mechanical contact would result in a high interfacial resistance ranging from 10^2–10^3 $\Omega \cdot cm^2$ and inhomogeneous current distribution, which significantly deteriorates the electrochemical performance of ASSB [249]. While the performance decrease caused by mechanical issues in ASSB has been extensively observed, a complete understanding on the origin and evolution of these mechanical issues associated with ASSB operation is still missing. Several interesting topics need to be further explored, such as how the mechanical contact at the interface evolves upon the repetitive electrochemical reactions, or how the mechanical properties of electrodes and electrolyte can be tuned to obtain a better interfacial contact and thus high electrochemical performance.
- Li-S battery and Na-ion battery are attracting considerable attention for large-scale energy storage owing to their high safety and low cost. The widespread implementation of Li-S battery and Na-ion battery is limited by several mechanical issues, particularly the large volume changes of host material during electrochemical reactions (i.e. ~80% for S electrode in Li-S battery and 420% for Sn electrode in Na-Sn battery). Such a huge volume

change may induce mechanical damage and associated electrochemical degradations. There is a lack of studies on the electro-chemo-mechanical behaviors in Li-S battery and Na-ion battery.

REFERENCES

[1] J. Newman and K. E. Thomas-Alyea, *Electrochemical systems*, John Wiley & Sons, 2012.

[2] J. Murrell, A very brief history of thermodynamics, *Sussex University*, 2009.

[3] R. Huggins, *Advanced batteries: materials science aspects*, Springer Science & Business Media, 2008.

[4] J. M. Tarascon and M. Armand, *Issues and challenges facing rechargeable lithium batteries*, Co-Published with Macmillan Publishers Ltd, UK, 2012.

[5] C. Martin, Driving change in the battery industry, *Nature Nanotechnology*, 9: 327, 2014.

[6] J. B. Goodenough, H. Abruna, and M. Buchanan, *Basic Research Needs for Electrical Energy Storage. Report of the Basic Energy Sciences Workshop on Electrical Energy Storage, April 2-4, 2007*, DOESC (USDOE Office of Science (SC)), 2007.

[7] B. K. Bose, Global warming: Energy, environmental pollution, and the impact of power electronics, *IEEE Industrial Electronics Magazine*, 4: 6-17, 2010.

[8] A. Kwade, W. Haselrieder, R. Leithoff, A. Modlinger, F. Dietrich, and K. Droeder, Current status and challenges for automotive battery production technologies, *Nature Energy*, 3: 290, 2018.

[9] J. R. Croy, A. Abouimrane, and Z. Zhang, Next-generation lithium-ion batteries: The promise of near-term advancements, *MRS Bulletin*, 39: 407-415, 2014.

[10] B. Scrosati and J. Garche, Lithium batteries: Status, prospects and future, *Journal of Power Sources*, 195: 2419-2430, 2010.

[11] M. Winter and R. J. Brodd, What are batteries, fuel cells, and supercapacitors?, *Chemical Reviews*, 104: 4245-4270, 2004.

[12] M. M. Thackeray, C. Wolverton, and E. D. Isaacs, Electrical energy storage for transportation-approaching the limits of, and going beyond, lithium-ion batteries, *Energy & Environmental Science*, 5: 7854-7863, 2012.

[13] B. Kang and G. Ceder, Battery materials for ultrafast charging and discharging, *Nature*, 458: 190, 2009.

[14] M. Endo, C. Kim, K. Nishimura, T. Fujino, and K. Miyashita, Recent development of carbon materials for Li ion batteries, *Carbon*, 38: 183-197, 2000.

[15] I. Hadjipaschalis, A. Poullikkas, and V. Efthimiou, Overview of current and future energy storage technologies for electric power applications, *Renewable and Sustainable Energy Reviews*, 13: 1513-1522, 2009.

[16] M. R. Palacín and A. de Guibert, Why do batteries fail?, *Science,* 351: 1253292, 2016.

[17] J. Vetter, P. Novak, M. R. Wagner, C. Veit, K. C. Möller, J. Besenhard, M. Winter, M. Wohlfahrt Mehrens, C. Vogler, and A. Hammouche, Ageing mechanisms in lithium-ion batteries, *Journal of Power Sources,* 147: 269-281, 2005.

[18] A. Barré, B. Deguilhem, S. Grolleau, M. Gérard, F. Suard, and D. Riu, A review on lithium-ion battery ageing mechanisms and estimations for automotive applications, *Journal of Power Sources,* 241: 680-689, 2013.

[19] S. Zhang, M. S. Ding, K. Xu, J. Allen, and T. R. Jow, Understanding solid electrolyte interface film formation on graphite electrodes, *Electrochemical and Solid-State Letters,* 4: A206-A208, 2001.

[20] L. Gireaud, S. Grugeon, S. Laruelle, B. Yrieix, and J. M. Tarascon, Lithium metal stripping/plating mechanisms studies: A metallurgical approach, *Electrochemistry Communications,* 8: 1639-1649, 2006.

[21] O. Dolotko, A. Senyshyn, M. J. Mühlbauer, K. Nikolowski, and H. Ehrenberg, Understanding structural changes in NMC Li-ion cells by in situ neutron diffraction, *Journal of Power Sources,* 255: 197-203, 2014.

[22] J. Groot, State-of-health estimation of li-ion batteries: Cycle life test methods, *Chalmers Univeristy,* 2012.

[23] H. M. Cheng, F. M. Wang, J. P. Chu, R. Santhanam, J. Rick, and S. C. Lo, Enhanced cycleabity in lithium ion batteries: Resulting from atomic layer depostion of Al_2O_3 or TiO_2 on $LiCoO_2$ electrodes, *The Journal of Physical Chemistry C,* 116: 7629-7637, 2012.

[24] I. D. Scott, Y. S. Jung, A. S. Cavanagh, Y. Yan, A. C. Dillon, S. M. George, and S. H. Lee, Ultrathin coatings on nano-$LiCoO_2$ for Li-ion vehicular applications, *Nano Letters,* 11: 414-418, 2010.

[25] X. Li, J. Liu, M. N. Banis, A. Lushington, R. Li, M. Cai, and X. Sun, Atomic layer deposition of solid-state electrolyte coated cathode materials with superior high-voltage cycling behavior for lithium ion battery application, *Energy & Environmental Science,* 7: 768-778, 2014.

[26] L. Chen, K. Wang, X. Xie, and J. Xie, Effect of vinylene carbonate (VC) as electrolyte additive on electrochemical performance of Si film anode for lithium ion batteries, *Journal of Power Sources,* 174: 538-543, 2007.

[27] N. S. Choi, K. H. Yew, K. Y. Lee, M. Sung, H. Kim, and S. S. Kim, Effect of fluoroethylene carbonate additive on interfacial properties of silicon thin-film electrode, *Journal of Power Sources,* 161: 1254-1259, 2006.

[28] M. Ulldemolins, F. Le Cras, B. Pecquenard, V. Phan, L. Martin, and H. Martinez, Investigation on the part played by the solid electrolyte interphase on the electrochemical performances of the silicon electrode for lithium-ion batteries, *Journal of Power Sources,* 206: 245-252, 2012.

[29] S. Dalavi, P. Guduru, and B. L. Lucht, Performance enhancing electrolyte additives for lithium ion batteries with silicon anodes, *Journal of the Electrochemical Society,* 159: A642-A646, 2012.

[30] P. Arora, R. E. White, and M. Doyle, Capacity fade mechanisms and side reactions in lithium-ion batteries, *Journal of the Electrochemical Society,* 145: 3647-3667, 1998.

[31] K. Zhao, M. Pharr, S. Cai, J. J. Vlassak, and Z. Suo, Large plastic deformation in high-capacity lithium-ion batteries caused by charge and discharge, *Journal of the American Ceramic Society,* 94: 2011.

[32] J. Christensen and J. Newman, Stress generation and fracture in lithium insertion materials, *Journal of Solid State Electrochemistry,* 10: 293-319, 2006.

[33] K. Zhao, M. Pharr, L. Hartle, J. J. Vlassak, and Z. Suo, Fracture and debonding in lithium-ion batteries with electrodes of hollow core-shell nanostructures, *Journal of Power Sources*, 218: 6-14, 2012.

[34] K. Zhao, M. Pharr, J. J. Vlassak, and Z. Suo, Fracture of electrodes in lithium-ion batteries caused by fast charging, *Journal of Applied Physics,* 108: 073517, 2010.

[35] N. Y. Kim, T. Yim, J. H. Song, J.-S. Yu, and Z. Lee, Microstructural study on degradation mechanism of layered $LiNi_{0.6}Co_{0.2}Mn_{0.2}O_2$ cathode materials by analytical transmission electron microscopy, *Journal of Power Sources,* 307: 641-648, 2016.

[36] R. Xu, L. S. Vasconcelos, and K. Zhao, Computational analysis of chemomechanical behaviors of composite electrodes in Li-ion batteries, *Journal of Materials Research,* 31: 2715-2727, 2016.

[37] Y. Hu, X. Zhao, and Z. Suo, Averting cracks caused by insertion reaction in lithium–ion batteries, *Journal of Materials Research,* 25: 1007-1010, 2010.

[38] S. P. Nadimpalli, R. Tripuraneni, and V. A. Sethuraman, Real-time stress measurements in germanium thin film electrodes during electrochemical lithiation/delithiation cycling, *Journal of the Electrochemical Society,* 162: A2840-A2846, 2015.

[39] X. H. Liu, L. Zhong, S. Huang, S. X. Mao, T. Zhu, and J. Y. Huang, Size-dependent fracture of silicon nanoparticles during lithiation, *ACS Nano,* 6: 1522-1531, 2012.

[40] Y. Qi, Q. Xu, and A. Van der Ven, Chemically induced crack instability when electrodes fracture, *Journal of the Electrochemical Society,* 159: A1838-A1843, 2012.

[41] L. Mu, R. Lin, R. Xu, L. Han, S. Xia, D. Sokaras, J. D. Steiner, T. C. Weng, D. Nordlund, M. M. Doeff, Y. Liu, K. Zhao, H. L. Xin, and F. Lin, Oxygen release induced chemomechanical breakdown of layered cathode materials, *Nano Letters,* 18: 3241-3249, 2018.

[42] G. Ning, B. Haran, and B. N. Popov, Capacity fade study of lithium-ion batteries cycled at high discharge rates, *Journal of Power Sources,* 117: 160-169, 2003.

[43] J. Maranchi, A. Hepp, A. Evans, N. Nuhfer, and P. Kumta, Interfacial properties of the a-Si⁄ Cu: active–inactive thin-film anode system for lithium-ion batteries, *Journal of the Electrochemical Society,* 153: A1246-A1253, 2006.

[44] C. Yu, X. Li, T. Ma, J. Rong, R. Zhang, J. Shaffer, Y. An, Q. Liu, B. Wei, and H. Jiang, Silicon thin films as anodes for high-performance Lithium-ion batteries with effective stress relaxation, *Advanced Energy Materials,* 2: 68-73, 2012.

[45] H. Sun, G. Xin, T. Hu, M. Yu, D. Shao, X. Sun, and J. Lian, High-rate lithiation-induced reactivation of mesoporous hollow spheres for long-lived lithium-ion batteries, *Nature Communications,* 5: 4526, 2014.

[46] H. Wang, Y. I. Jang, B. Huang, D. R. Sadoway, and Y. M. Chiang, TEM study of electrochemical cycling-induced damage and disorder in $LiCoO_2$ cathodes for rechargeable lithium batteries, *Journal of the Electrochemical Society,* 146: 473-480, 1999.

[47] X. Hao, X. Lin, W. Lu, and B. M. Bartlett, Oxygen vacancies lead to loss of domain order, particle fracture, and rapid capacity fade in lithium manganospinel ($LiMn_2O_4$) batteries, *ACS Applied Materials & Interfaces,* 6: 10849-10857, 2014.

[48] H.-H. Sun and A. Manthiram, Impact of microcrack generation and surface degradation on a nickel-rich layered $Li[Ni_{0.9}Co_{0.05}Mn_{0.05}]O_2$ cathode for lithium-ion batteries, *Chemistry of Materials,* 29: 8486-8493, 2017.

[49] J. Cannarella and C. B. Arnold, Stress evolution and capacity fade in constrained lithium-ion pouch cells, *Journal of Power Sources,* 245: 745-751, 2014.

[50] L. Baggetto, D. Danilov, and P. H. Notten, Honeycomb-Structured Silicon: Remarkable Morphological Changes Induced by Electrochemical (De) Lithiation, *Advanced Materials,* 23: 1563-1566, 2011.

[51] C. K. Chan, H. Peng, G. Liu, K. McIlwrath, X. F. Zhang, R. A. Huggins, and Y. Cui, *High-performance lithium battery anodes using silicon nanowires*, World Scientific, 2011.

[52] H. Kim, B. Han, J. Choo, and J. Cho, Three-dimensional porous silicon particles for use in high-performance lithium secondary batteries, *Angewandte Chemie,* 120: 10305-10308, 2008.

[53] N. Liu, H. Wu, M. T. McDowell, Y. Yao, C. Wang, and Y. Cui, A yolk-shell design for stabilized and scalable Li-ion battery alloy anodes, *Nano Letters,* 12: 3315-3321, 2012.

[54] L. F. Cui, L. Hu, J. W. Choi, and Y. Cui, Light-weight free-standing carbon nanotube-silicon films for anodes of lithium ion batteries, *ACS Nano,* 4: 3671-3678, 2010.

[55] M. Yamada, A. Ueda, K. Matsumoto, and T. Ohzuku, Silicon-based negative electrode for high-capacity lithium-ion batteries:"SiO"-carbon composite, *Journal of the Electrochemical Society,* 158: A417-A421, 2011.

[56] A. Magasinski, P. Dixon, B. Hertzberg, A. Kvit, J. Ayala, and G. Yushin, High-performance lithium-ion anodes using a hierarchical bottom-up approach, *Nature Materials,* 9: 353, 2010.

[57] X. Chen, K. Gerasopoulos, J. Guo, A. Brown, C. Wang, R. Ghodssi, and J. N. Culver, A patterned 3D silicon anode fabricated by electrodeposition on a virus-structured current collector, *Advanced Functional Materials,* 21: 380-387, 2011.

[58] H. Haftbaradaran, X. Xiao, M. W. Verbrugge, and H. Gao, Method to deduce the critical size for interfacial delamination of patterned electrode structures and application to lithiation of thin-film silicon islands, *Journal of Power Sources,* 206: 357-366, 2012.

[59] S. K. Soni, B. W. Sheldon, X. Xiao, M. W. Verbrugge, A. Dongjoon, H. Haftbaradaran, and G. Huajian, Stress mitigation during the lithiation of patterned amorphous Si islands, *Journal of the Electrochemical Society,* 159: A38-A43, 2011.

[60] M. T. McDowell, S. Xia, and T. Zhu, The mechanics of large-volume-change transformations in high-capacity battery materials, *Extreme Mechanics Letters,* 9: 480-494, 2016.

[61] K. Zhao and Y. Cui, Understanding the role of mechanics in energy materials: A perspective, *Extreme Mechanics Letters,* 9: 347-352, 2016.

[62] B. W. Sheldon, S. K. Soni, X. Xiao, and Y. Qi, Stress contributions to solution thermodynamics in Li-Si alloys, *Electrochemical and Solid-State Letters,* 15: A9-A11, 2011.

[63] R. Xu and K. Zhao, Electrochemomechanics of electrodes in Li-ion batteries: A review, *Journal of Electrochemical Energy Conversion and Storage,* 13: 030803, 2016.

[64] F. Spaepen, A survey of energies in materials science, *Philosophical Magazine,* 85: 2979-2987, 2005.

[65] K. Zhao, M. Pharr, Q. Wan, W. L. Wang, E. Kaxiras, J. J. Vlassak, and Z. Suo, Concurrent reaction and plasticity during initial lithiation of crystalline silicon in lithium-ion batteries, *Journal of the Electrochemical Society,* 159: A238-A243, 2012.

[66] Y. Gao and M. Zhou, Strong stress-enhanced diffusion in amorphous lithium alloy nanowire electrodes, *Journal of Applied Physics,* 109: 014310, 2011.

[67] J. Pan, Q. Zhang, J. Li, M. J. Beck, X. Xiao, and Y. T. Cheng, Effects of stress on lithium transport in amorphous silicon electrodes for lithium-ion batteries, *Nano Energy,* 13: 192-199, 2015.

[68] B. Lu, Y. Song, Q. Zhang, J. Pan, Y. T. Cheng, and J. Zhang, Voltage hysteresis of lithium ion batteries caused by mechanical stress, *Physical Chemistry Chemical Physics,* 18: 4721-4727, 2016.

[69] H. Yang, S. Huang, X. Huang, F. Fan, W. Liang, X. H. Liu, L. Q. Chen, J. Y. Huang, J. Li, and T. Zhu, Orientation-dependent interfacial mobility governs the anisotropic swelling in lithiated silicon nanowires, *Nano Letters,* 12: 1953-1958, 2012.

[70] Y. Zhang, Y. Li, Z. Wang, and K. Zhao, Lithiation of SiO_2 in Li-ion batteries: in situ transmission electron microscopy experiments and theoretical studies, *Nano Letters,* 14: 7161-7170, 2014.

[71] Y. Zhang, Z. Wang, Y. Li, and K. Zhao, Lithiation of ZnO nanowires studied by in-situ transmission electron microscopy and theoretical analysis, *Mechanics of Materials,* 91: 313-322, 2015.

[72] X. Huang, H. Yang, W. Liang, M. Raju, M. Terrones, V. H. Crespi, A. C. T. van Duin, and S. Zhang, Lithiation induced corrosive fracture in defective carbon nanotubes, *Applied Physics Letters,* 103: 153901, 2013.

[73] R. Xu and K. Zhao, Corrosive fracture of electrodes in Li-ion batteries, *Journal of the Mechanics and Physics of Solids,* 121: 258-280, 2018.

[74] S. Prussin, Generation and distribution of dislocations by solute diffusion, *Journal of Applied Physics,* 32: 1876-1881, 1961.

[75] F. Larché and J. W. Cahn, A linear theory of thermochemical equilibrium of solids under stress, *Acta Metallurgica,* 21: 1051-1063, 1973.

[76] F. Larché and J. W. Cahn, A nonlinear theory of thermochemical equilibrium of solids under stress, *Acta Metallurgica,* 26: 53-60, 1978.

[77] J. C. M. Li, Physical chemistry of some microstructural phenomena, *Metallurgical Transactions A,* 9: 1353-1380, 1978.

[78] G. B. Stephenson, Deformation during interdiffusion, *Acta Metallurgica,* 36: 2663-2683, 1988.

[79] J. Christensen and J. Newman, A mathematical model of stress generation and fracture in lithium manganese oxide, *Journal of the Electrochemical Society,* 153: A1019-A1030, 2006.

[80] Y. T. Cheng and M. W. Verbrugge, Evolution of stress within a spherical insertion electrode particle under potentiostatic and galvanostatic operation, *Journal of Power Sources,* 190: 453-460, 2009.

[81] Y. T. Cheng and M. W. Verbrugge, Diffusion-induced stress, interfacial charge transfer, and criteria for avoiding crack initiation of electrode particles, *Journal of the Electrochemical Society,* 157: A508-A516, 2010.

[82] S. Golmon, K. Maute, S. H. Lee, and M. L. Dunn, Stress generation in silicon particles during lithium insertion, *Applied Physics Letters,* 97: 033111, 2010.

[83] H. Haftbaradaran, J. Song, W. Curtin, and H. Gao, Continuum and atomistic models of strongly coupled diffusion, stress, and solute concentration, *Journal of Power Sources,* 196: 361-370, 2011.

[84] Y. T. Cheng and M. W. Verbrugge, The influence of surface mechanics on diffusion induced stresses within spherical nanoparticles, *Journal of Applied Physics,* 104: 083521, 2008.

[85] R. Xu and K. Zhao, Mechanical interactions regulated kinetics and morphology of composite electrodes in Li-ion batteries, *Extreme Mechanics Letters,* 8: 13-21, 2016.

[86] P. Barai and P. P. Mukherjee, Stochastic analysis of diffusion induced damage in lithium-ion battery electrodes, *Journal of the Electrochemical Society,* 160: A955-A967, 2013.

[87] C. F. Chen, P. Barai, and P. P. Mukherjee, Diffusion induced damage and impedance response in lithium-ion battery electrodes, *Journal of the Electrochemical Society,* 161: A2138-A2152, 2014.

[88] P. Barai and P. P. Mukherjee, Mechano-electrochemical stochastics in high-capacity electrodes for energy storage, *Journal of the Electrochemical Society,* 163: A1120-A1137, 2016.

[89] Y. F. Gao and M. Zhou, Coupled mechano-diffusional driving forces for fracture in electrode materials, *Journal of Power Sources,* 230: 176-193, 2013.

[90] V. A. Sethuraman, V. Srinivasan, A. F. Bower, and P. R. Guduru, In situ measurements of stress-potential coupling in lithiated silicon, *Journal of the Electrochemical Society,* 157: A1253-A1261, 2010.

[91] D. M. Piper, T. A. Yersak, and S.-H. Lee, Effect of compressive stress on electrochemical performance of silicon anodes, *Journal of the Electrochemical Society,* 160: A77-A81, 2013.

[92] A. F. Bower, P. R. Guduru, and V. A. Sethuraman, A finite strain model of stress, diffusion, plastic flow, and electrochemical reactions in a lithium-ion half-cell, *Journal of the Mechanics and Physics of Solids,* 59: 804-828, 2011.

[93] S. Kim, S. J. Choi, K. Zhao, H. Yang, G. Gobbi, S. Zhang, and J. Li, Electrochemically driven mechanical energy harvesting, *Nature Communications,* 7: 10146, 2016.

[94] X. H. Liu, H. Zheng, L. Zhong, S. Huang, K. Karki, L. Q. Zhang, Y. Liu, A. Kushima, W. T. Liang, and J. W. Wang, Anisotropic swelling and fracture of silicon nanowires during lithiation, *Nano Letters,* 11: 3312-3318, 2011.

[95] P. Limthongkul, Y. I. Jang, N. J. Dudney, and Y. M. Chiang, Electrochemically-driven solid-state amorphization in lithium-silicon alloys and implications for lithium storage, *Acta Materialia,* 51: 1103-1113, 2003.

[96] M. T. McDowell, I. Ryu, S. W. Lee, C. Wang, W. D. Nix, and Y. Cui, Studying the kinetics of crystalline silicon nanoparticle lithiation with in situ transmission electron microscopy, *Advanced Materials,* 24: 6034-6041, 2012.

[97] D. J. Liu, J. D. Weeks, and D. Kandel, Current-induced step bending instability on vicinal surfaces, *Physical Review Letters,* 81: 2743, 1998.

[98] A. Udupa, S. Sadasiva, and G. Subbarayan, A framework for studying dynamics and stability of diffusive-reactive interfaces with application to Cu_6Sn_5 intermetallic compound growth, *Proceedings of the Royal Society A,* 472: 20160134, 2016.

[99] I. Ryu, J. W. Choi, Y. Cui, and W. D. Nix, Size-dependent fracture of Si nanowire battery anodes, *Journal of the Mechanics and Physics of Solids,* 59: 1717-1730, 2011.

[100] S. W. Lee, H. W. Lee, W. D. Nix, H. Gao, and Y. Cui, Kinetics and fracture resistance of lithiated silicon nanostructure pairs controlled by their mechanical interaction, *Nature Communications,* 6: 2015.

[101] V. A. Sethuraman, M. J. Chon, M. Shimshak, N. Van Winkle, and P. R. Guduru, In situ measurement of biaxial modulus of Si anode for Li-ion batteries, *Electrochemistry Communications,* 12: 1614-1617, 2010.

[102] L. S. Vasconcelos, R. Xu, J. Li, and K. Zhao, Grid indentation analysis of mechanical properties of composite electrodes in Li-ion batteries, *Extreme Mechanics Letters,* 9: 495-502, 2016.

[103] M. Pharr, Z. Suo, and J. J. Vlassak, Measurements of the fracture energy of lithiated silicon electrodes of Li-ion batteries, *Nano Letters,* 13: 5570-7, 2013.

[104] R. Grantab and V. B. Shenoy, Pressure-gradient dependent diffusion and crack propagation in lithiated silicon nanowires, *Journal of the Electrochemical Society,* 159: A584-A591, 2012.

[105] H. Yang, X. Huang, W. Liang, A. C. T. van Duin, M. Raju, and S. Zhang, Self-weakening in lithiated graphene electrodes, *Chemical Physics Letters,* 563: 58-62, 2013.

[106] F. Yang, B. Liu, and D. N. Fang, Interplay between fracture and diffusion behaviors: Modeling and phase field computation, *Computational Materials Science,* 50: 2554-2560, 2011.

[107] R. Xu, X. L. Fan, W. X. Zhang, and T. Wang, Interfacial fracture mechanism associated with mixed oxides growth in thermal barrier coating system, *Surface and Coatings Technology,* 253: 139-147, 2014.

[108] M. Klinsmann, D. Rosato, M. Kamlah, and R. M. McMeeking, Modeling crack growth during Li insertion in storage particles using a fracture phase field approach, *Journal of the Mechanics and Physics of Solids,* 92: 313-344, 2016.

[109] L. Anand, A Cahn-Hilliard-type theory for species diffusion coupled with large elastic-plastic deformations, *Journal of the Mechanics and Physics of Solids,* 60: 1983-2002, 2012.

[110] J. Lubliner, *Plasticity theory*, Courier Corporation, 2008.

[111] A. F. Bower and P. R. Guduru, A simple finite element model of diffusion, finite deformation, plasticity and fracture in lithium ion insertion electrode materials, *Modelling and Simulation in Materials Science and Engineering,* 20: 045004, 2012.

[112] F. Larché and J. W. Cahn, Overview no. 41 the interactions of composition and stress in crystalline solids, *Acta Metallurgica*, 33: 331-357, 1985.

[113] E. Bohn, T. Eckl, M. Kamlah, and R. McMeeking, A model for lithium diffusion and stress generation in an intercalation storage particle with phase change, *Journal of the Electrochemical Society*, 160: A1638-A1652, 2013.

[114] F. Yin, G. J. Cheng, R. Xu, K. Zhao, Q. Li, J. Jian, S. Hu, S. Sun, L. An, and Q. Han, Ultrastrong nanocrystalline stainless steel and its Hall-Petch relationship in the nanoscale, *Scripta Materialia,* 155: 26-31, 2018.

[115] F. Yin, Y. Liu, R. Xu, K. Zhao, A. Partin, and Q. Han, Nanograined surface fabricated on the pure copper by ultrasonic shot peening and an energy-density based criterion for peening intensity quantification, *Journal of Manufacturing Processes,* 32: 656-663, 2018.

[116] B. W. Deng, R. Xu, K. J. Zhao, Y. F. Lu, S. Ganguli, and G. J. Cheng, Composite bending-dominated hollow nanolattices: A stiff, cyclable mechanical metamaterial, *Materials Today,* 21: 467-474, 2018.

[117] F. Yin, R. Xu, S. Hu, K. Zhao, S. Yang, S. Kuang, Q. Li, and Q. Han, Enhanced Mechanical and Biological Performance of an Extremely Fine Nanograined 316L Stainless Steel Cell–Substrate Interface Fabricated by Ultrasonic Shot Peening, *ACS Biomaterials Science & Engineering*, 4: 1609-1621, 2018.

[118] Q. Sun, X. Liu, Q. Han, J. Li, R. Xu, and K. Zhao, A comparison of AA2024 and AA7150 subjected to ultrasonic shot peening: Microstructure, surface segregation and corrosion, *Surface and Coatings Technology,* 337: 552-560, 2018.

[119] Q. Sun, Q. Han, R. Xu, K. Zhao, and J. Li, Localized corrosion behaviour of AA7150 after ultrasonic shot peening: Corrosion depth vs. impact energy, *Corrosion Science,* 130: 218-230, 2018.

[120] Z. Hu, G. Tong, Q. Nian, R. Xu, M. Saei, F. Chen, C. Chen, M. Zhang, H. Guo, and J. Xu, Laser sintered single layer graphene oxide reinforced titanium matrix nanocomposites, *Composites Part B: Engineering,* 93: 352-359, 2016.

[121] Y. Hu, P. Kumar, R. Xu, K. Zhao, and G. J. Cheng, Ultrafast direct fabrication of flexible substrate-supported designer plasmonic nanoarrays, *Nanoscale,* 8: 172-182, 2016.

[122] G. Pharr and W. Oliver, Measurement of thin film mechanical properties using nanoindentation, *MRS Bulletin,* 17: 28-33, 1992.

[123] G. Pharr, Measurement of mechanical properties by ultra-low load indentation, *Materials Science and Engineering: A,* 253: 151-159, 1998.

[124] K. Technologies, Nanoindentation, scratch, and elevated temperature testing of cellulose and PMMA films *Keysight Technologies Application Note,* 2014.

[125] W. C. Oliver and G. M. Pharr, An improved technique for determining hardness and elastic modulus using load and displacement sensing indentation experiments, *Journal of Materials Research,* 7: 1564-1583, 1992.

[126] W. C. Oliver and G. M. Pharr, Measurement of hardness and elastic modulus by instrumented indentation: Advances in understanding and refinements to methodology, *Journal of Materials Research,* 19: 3-20, 2004.

[127] T. L. Anderson, *Fracture mechanics: fundamentals and applications,* CRC Press, 2017.

[128] X.-K. Zhu and J. A. Joyce, Review of fracture toughness (G, K, J, CTOD, CTOA) testing and standardization, *Engineering Fracture Mechanics,* 85: 1-46, 2012.

[129] S. Chiang, D. Marshall, and A. Evans, The response of solids to elastic/plastic indentation. I. Stresses and residual stresses, *Journal of Applied Physics,* 53: 298-311, 1982.

[130] E. Yoffe, Elastic stress fields caused by indenting brittle materials, *Philosophical Magazine A,* 46: 617-628, 1982.

[131] M. Nastasi, D. M. Parkin, and H. Gleiter, *Mechanical properties and deformation behavior of materials having ultra-fine microstructures,* 233, Springer Science & Business Media, 2012.

[132] J. Field, M. Swain, and R. Dukino, Determination of fracture toughness from the extra penetration produced by indentation-induced pop-in, *Journal of Materials Research,* 18: 1412-1419, 2003.

[133] R. Xu, H. Sun, L. S. Vasconcelos, and K. Zhao, Mechanical and structural degradation of $LiNi_xMn_yCo_zO_2$ cathode in Li-ion batteries: An experimental study, *Journal of the Electrochemical Society,* 164: A3333-A3341, 2017.

[134] L. Beaulieu, K. Eberman, R. Turner, L. Krause, and J. Dahn, Colossal reversible volume changes in lithium alloys, *Electrochemical and Solid-State Letters,* 4: A137-A140, 2001.

[135] X. H. Liu, S. Huang, S. T. Picraux, J. Li, T. Zhu, and J. Y. Huang, Reversible nanopore formation in Ge nanowires during lithiation–delithiation cycling: An in situ transmission electron microscopy study, *Nano Letters,* 11: 3991-3997, 2011.

[136] K. Zhao, W. L. Wang, J. Gregoire, M. Pharr, Z. Suo, J. J. Vlassak, and E. Kaxiras, Lithium-assisted plastic deformation of silicon electrodes in lithium-ion batteries: a first-principles theoretical study, *Nano Letters,* 11: 2962-2967, 2011.

[137] K. Zhao, G. A. Tritsaris, M. Pharr, W. L. Wang, O. Okeke, Z. Suo, J. J. Vlassak, and E. Kaxiras, Reactive flow in silicon electrodes assisted by the insertion of lithium, *Nano Letters,* 12: 4397-4403, 2012.

[138] H. Yang, W. Liang, X. Guo, C. M. Wang, and S. Zhang, Strong kinetics-stress coupling in lithiation of Si and Ge anodes, *Extreme Mechanics Letters,* 2: 1-6, 2015.

[139] X. Zhang, W. Shyy, and A. Marie Sastry, Numerical Simulation of Intercalation-Induced Stress in Li-Ion Battery Electrode Particles, *Journal of the Electrochemical Society,* 154: A910, 2007.

[140] M. W. Verbrugge and B. J. Koch, Modeling lithium intercalation of single-fiber carbon microelectrodes, *Journal of the Electrochemical Society,* 143: 600-608, 1996.

[141] L. Brassart, K. Zhao, and Z. Suo, Cyclic plasticity and shakedown in high-capacity electrodes of lithium-ion batteries, *International Journal of Solids and Structures,* 50: 1120-1129, 2013.

[142] Z. Cui, F. Gao, and J. Qu, Interface-reaction controlled diffusion in binary solids with applications to lithiation of silicon in lithium-ion batteries, *Journal of the Mechanics and Physics of Solids,* 61: 293-310, 2013.

[143] Y. An and H. Jiang, A finite element simulation on transient large deformation and mass diffusion in electrodes for lithium ion batteries, *Modelling and Simulation in Materials Science and Engineering,* 21: 074007, 2013.

[144] P. Stein and B. Xu, 3D Isogeometric Analysis of intercalation-induced stresses in Li-ion battery electrode particles, *Computer Methods in Applied Mechanics and Engineering,* 268: 225-244, 2014.

[145] H. Yang, F. Fan, W. Liang, X. Guo, T. Zhu, and S. Zhang, A chemo-mechanical model of lithiation in silicon, *Journal of the Mechanics and Physics of Solids,* 70: 349-361, 2014.

[146] K. Higa and V. Srinivasan, Stress and Strain in Silicon Electrode Models, *Journal of the Electrochemical Society*, 162: A1111-A1122, 2015.

[147] E. K. Rahani and V. B. Shenoy, Role of plastic deformation of binder on stress evolution during charging and discharging in lithium-ion battery negative electrodes, *Journal of The Electrochemical Society*, 160: A1153-A1162, 2013.

[148] N. Ding, J. Xu, Y. Yao, G. Wegner, X. Fang, C. Chen, and I. Lieberwirth, Determination of the diffusion coefficient of lithium ions in nano-Si, *Solid State Ionics*, 180: 222-225, 2009.

[149] T. Song, J. Xia, J. H. Lee, D. H. Lee, M. S. Kwon, J. M. Choi, J. Wu, S. K. Doo, H. Chang, and W. I. Park, Arrays of sealed silicon nanotubes as anodes for lithium ion batteries, *Nano Letters*, 10: 1710-1716, 2010.

[150] Y. Yao, M. T. McDowell, I. Ryu, H. Wu, N. Liu, L. Hu, W. D. Nix, and Y. Cui, Interconnected silicon hollow nanospheres for lithium-ion battery anodes with long cycle life, *Nano Letters*, 11: 2949-2954, 2011.

[151] S. W. Lee, M. T. McDowell, J. W. Choi, and Y. Cui, Anomalous shape changes of silicon nanopillars by electrochemical lithiation, *Nano Letters*, 11: 3034-3039, 2011.

[152] M. Armand and J.-M. Tarascon, Building better batteries, *Nature*, 451: 652, 2008.

[153] M. S. Whittingham, Materials challenges facing electrical energy storage, *MRS Bulletin*, 33: 411-419, 2008.

[154] N. Nitta, F. Wu, J. T. Lee, and G. Yushin, Li-ion battery materials: present and future, *Materials Today*, 18: 252-264, 2015.

[155] A. Mukhopadhyay and B. W. Sheldon, Deformation and stress in electrode materials for Li-ion batteries, *Progress in Materials Science*, 63: 58-116, 2014.

[156] M. Thackeray, Structural considerations of layered and spinel lithiated oxides for lithium ion batteries, *Journal of the Electrochemical Society*, 142: 2558-2563, 1995.

[157] V. Malavé, J. Berger, H. Zhu, and R. J. Kee, A computational model of the mechanical behavior within reconstructed Li_xCoO_2 Li-ion battery cathode particles, *Electrochimica Acta*, 130: 707-717, 2014.

[158] I. A. Courtney and J. Dahn, Electrochemical and in situ X-ray diffraction studies of the reaction of lithium with tin oxide composites, *Journal of the Electrochemical Society*, 144: 2045-2052, 1997.

[159] J. W. Choi, J. McDonough, S. Jeong, J. S. Yoo, C. K. Chan, and Y. Cui, Stepwise nanopore evolution in one-dimensional nanostructures, *Nano Letters*, 10: 1409-1413, 2010.

[160] G. Sandu, L. Brassart, J. F. Gohy, T. Pardoen, S. Melinte, and A. Vlad, Surface coating mediated swelling and fracture of silicon nanowires during lithiation, *ACS Nano,* 8: 9427-9436, 2014.

[161] T. Hutzenlaub, S. Thiele, R. Zengerle, and C. Ziegler, Three-dimensional reconstruction of a $LiCoO_2$ Li-ion battery cathode, *Electrochemical and Solid-State Letters,* 15: A33-A36, 2011.

[162] T. Hutzenlaub, S. Thiele, N. Paust, R. Spotnitz, R. Zengerle, and C. Walchshofer, Three-dimensional electrochemical Li-ion battery modelling featuring a focused ion-beam/scanning electron microscopy based three-phase reconstruction of a $LiCoO_2$ cathode, *Electrochimica Acta,* 115: 131-139, 2014.

[163] M. Ebner and V. Wood, Tool for tortuosity estimation in lithium ion battery porous electrodes, *Journal of the Electrochemical Society,* 162: A3064-A3070, 2015.

[164] M. Chung, J. Seo, X. Zhang, and A. Sastry, Implementing realistic geometry and measured diffusion coefficients into single particle electrode modeling based on experiments with single $LiMn_2O_4$ spinel particles, *Journal of the Electrochemical Society,* 158: A371-A378, 2011.

[165] J. Hun, M. Chung, M. Park, S. Woo, X. Zhang, and A. Marie, Generation of realistic particle structures and simulations of internal stress: A numerical/AFM study of LiMn2O4 particles, *Journal of the Electrochemical Society,* 158: A434-A442, 2011.

[166] S. A. Roberts, V. E. Brunini, K. N. Long, and A. M. Grillet, A framework for three-dimensional mesoscale modeling of anisotropic swelling and mechanical deformation in lithium-ion electrodes, *Journal of The Electrochemical Society,* 161: F3052-F3059, 2014.

[167] H. Mendoza, S. A. Roberts, V. E. Brunini, and A. M. Grillet, Mechanical and electrochemical response of a $LiCoO_2$ cathode using reconstructed microstructures, *Electrochimica Acta,* 190: 1-15, 2016.

[168] M. Ebner, F. Marone, M. Stampanoni, and V. Wood, Visualization and quantification of electrochemical and mechanical degradation in Li ion batteries, *Science,* 342: 716-720, 2013.

[169] M. Ebner, F. Geldmacher, F. Marone, M. Stampanoni, and V. Wood, X-ray tomography of porous, transition metal oxide based lithium ion battery electrodes, *Advanced Energy Materials,* 3: 845-850, 2013.

[170] J. Joos, T. Carraro, A. Weber, and E. Ivers-Tiffée, Reconstruction of porous electrodes by FIB/SEM for detailed microstructure modeling, *Journal of Power Sources,* 196: 7302-7307, 2011.

[171] P. R. Shearing, L. E. Howard, P. S. Jørgensen, N. P. Brandon, and S. J. Harris, Characterization of the 3-dimensional microstructure of a graphite negative electrode from a Li-ion battery, *Electrochemistry Communications,* 12: 374-377, 2010.

[172] Y. Wei, J. Zheng, S. Cui, X. Song, Y. Su, W. Deng, Z. Wu, X. Wang, W. Wang, and M. Rao, Kinetics tuning of Li-ion diffusion in layered Li $(Ni_xMn_yCo_z)O_2$, *Journal of the American Chemical Society,* 137: 8364-8367, 2015.

[173] Y. Koyama, I. Tanaka, H. Adachi, Y. Makimura, and T. Ohzuku, Crystal and electronic structures of superstructural $Li_{1-x}[Co_{1/3}Ni_{1/3}Mn_{1/3}]O_2(0\leqslant x\leqslant 1)$, *Journal of Power Sources,* 119: 644-648, 2003.

[174] N. Qaiser, Y. J. Kim, C. S. Hong, and S. M. Han, Numerical modeling of fracture-resistant Sn micropillars as anode for lithium ion batteries, *The Journal of Physical Chemistry C,* 120: 6953-6962, 2016.

[175] M. Winter and J. O. Besenhard, Electrochemical lithiation of tin and tin-based intermetallics and composites, *Electrochimica Acta,* 45: 31-50, 1999.

[176] R. E. Garcıa, Y.-M. Chiang, W. C. Carter, P. Limthongkul, and C. M. Bishop, Microstructural modeling and design of rechargeable lithium-ion batteries, *Journal of the Electrochemical Society,* 152: A255-A263, 2005.

[177] P. Verma, P. Maire, and P. Novák, A review of the features and analyses of the solid electrolyte interphase in Li-ion batteries, *Electrochimica Acta,* 55: 6332-6341, 2010.

[178] N. Liu, Z. Lu, J. Zhao, M. T. McDowell, H. W. Lee, W. Zhao, and Y. Cui, A pomegranate-inspired nanoscale design for large-volume-change lithium battery anodes, *Nature Nanotechnology,* 9: 187, 2014.

[179] S. Zhang, Chemomechanical modeling of lithiation-induced failure in high-volume-change electrode materials for lithium ion batteries, *npj Computational Materials,* 3: 7, 2017.

[180] W. H. Woodford, Y. M. Chiang, and W. C. Carter, "Electrochemical shock" of intercalation electrodes: A fracture mechanics analysis, *Journal of the Electrochemical Society,* 157: A1052, 2010.

[181] S. P. Nadimpalli, V. A. Sethuraman, D. P. Abraham, A. F. Bower, and P. R. Guduru, Stress evolution in lithium-ion composite electrodes during electrochemical cycling and resulting internal pressures on the cell casing, *Journal of the Electrochemical Society,* 162: A2656-A2663, 2015.

[182] J. Sheth, N. K. Karan, D. P. Abraham, C. C. Nguyen, B. L. Lucht, B. W. Sheldon, and P. R. Guduru, In situ stress evolution in $Li_{1+x}Mn_2O_4$ thin films during electrochemical cycling in Li-ion cells, *Journal of the Electrochemical Society,* 163: A2524-A2530, 2016.

[183] K. Y. Chung and K. B. Kim, Investigation of structural fatigue in spinel electrodes using in situ laser probe beam deflection technique, *Journal of the Electrochemical Society,* 149: A79-A85, 2002.

[184] C. Daniel, D. Mohanty, J. Li, and D. L. Wood, Cathode materials review, *AIP Conference Proceedings,* 1597: 26-43, 2014.

[185] J. Li, C. Daniel, and D. Wood, Materials processing for lithium-ion batteries, *Journal of Power Sources*, 196: 2452-2460, 2011.

[186] D. J. Miller, C. Proff, J. Wen, D. P. Abraham, and J. Bareño, Observation of microstructural evolution in Li battery cathode oxide particles by in situ electron microscopy, *Advanced Energy Materials,* 3: 1098-1103, 2013.

[187] G. Li, Z. Zhang, Z. Huang, C. Yang, Z. Zuo, and H. Zhou, Understanding the accumulated cycle capacity fade caused by the secondary particle fracture of $LiNi_{1-x-y}Co_xMn_yO_2$ cathode for lithium ion batteries, *Journal of Solid State Electrochemistry,* 2016.

[188] J. Li, C. Daniel, S. J. An, and D. Wood, Evaluation residual moisture in lithium-ion battery electrodes and its effect on electrode performance, *MRS Advances,* 1: 1029-1035, 2016.

[189] G. H. Sun, T. Sui, B. H. Song, H. Zheng, L. Lu, and A. M. Korsunsky, On the fragmentation of active material secondary particles in lithium ion battery cathodes induced by charge cycling, *Extreme Mechanics Letters,* 9: 449-458, 2016.

[190] Abaqus v6.11, *Dassault Systèmes,* France: 2011.

[191] D. Reem, An algorithm for computing Voronoi diagrams of general generators in general normed spaces, *2009 Sixth International Symposium on Voronoi Diagrams,* 144-152, 2009.

[192] X. Fan, R. Xu, W. Zhang, and T. Wang, Effect of periodic surface cracks on the interfacial fracture of thermal barrier coating system, *Applied Surface Science,* 258: 9816-9823, 2012.

[193] H. H. Ryu, K. J. Park, C. S. Yoon, and Y. K. Sun, Capacity fading of Ni-Rich $Li[Ni_xCo_yMn_{1-x-y}]O_2$ ($0.6 \leqslant x \leqslant 0.95$) cathodes for high-energy-density lithium-ion batteries: Bulk or surface degradation?, *Chemistry of Materials,* 30: 1155-1163, 2018.

[194] B. R. Lee, H. J. Noh, S. T. Myung, K. Amine, and Y. K. Sun, High-voltage performance of $Li[Ni_{0.55}Co_{0.15}Mn_{0.30}]O_2$ positive electrode material for rechargeable Li-ion batteries, *Journal of the Electrochemical Society,* 158: A180-A186, 2011.

[195] B. Song, Z. Liu, M. O. Lai, and L. Lu, Structural evolution and the capacity fade mechanism upon long-term cycling in Li-rich cathode material, *Physical Chemistry Chemical Physics,* 14: 12875-12883, 2012.

[196] D. Mohanty, S. Kalnaus, R. A. Meisner, K. J. Rhodes, J. Li, E. A. Payzant, D. L. Wood III, and C. Daniel, Structural transformation of a lithium-rich $Li_{1.2}Co_{0.1}Mn_{0.55}Ni_{0.15}O_2$ cathode during high voltage cycling resolved by in situ X-ray diffraction, *Journal of Power Sources,* 229: 239-248, 2013.

[197] J. Li, L. E. Downie, L. Ma, W. Qiu, and J. Dahn, Study of the failure mechanisms of $LiNi_{0.8}Mn_{0.1}Co_{0.1}O_2$ cathode material for lithium ion batteries, *Journal of the Electrochemical Society,* 162: A1401-A1408, 2015.

[198] S. Watanabe, M. Kinoshita, T. Hosokawa, K. Morigaki, and K. Nakura, Capacity fading of $LiAl_yNi_{1-x-y}Co_xO_2$ cathode for lithium-ion batteries during accelerated calendar and cycle life tests (effect of depth of discharge in charge–discharge cycling on the suppression of the micro-crack generation of $LiAl_yNi_{1-x-y}Co_xO_2$ particle), *Journal of Power Sources,* 260: 50-56, 2014.

[199] S. Zhang, K. Xu, and T. Jow, EIS study on the formation of solid electrolyte interface in Li-ion battery, *Electrochimica Acta,* 51: 1636-1640, 2006.

[200] P. He, H. Yu, and H. Zhou, Layered lithium transition metal oxide cathodes towards high energy lithium-ion batteries, *Journal of Materials Chemistry,* 22: 3680-3695, 2012.

[201] M. S. Whittingham, Lithium batteries and cathode materials, *Chemical Reviews,* 104: 4271-4302, 2004.

[202] D. Andre, S. J. Kim, P. Lamp, S. F. Lux, F. Maglia, O. Paschos, and B. Stiaszny, Future generations of cathode materials: an automotive industry perspective, *Journal of Materials Chemistry A,* 3: 6709-6732, 2015.

[203] H. Sun and K. Zhao, Electronic structure and comparative properties of $LiNi_xMn_yCo_zO_2$ cathode materials, *The Journal of Physical Chemistry C,* 121: 6002-6010, 2017.

[204] R. Xu, L. S. Vasconcelos, J. Shi, J. Li, and K. Zhao, Disintegration of meatball electrodes for $LiNi_xMn_yCo_zO_2$ cathode materials, *Experimental Mechanics,* 58: 549-559, 2017.

[205] M. Lang, M. S. D. Darma, K. Kleiner, L. Riekehr, L. Mereacre, M. Á. Pérez, V. Liebau, and H. Ehrenberg, Post mortem analysis of fatigue mechanisms in $LiNi_{0.8}Co_{0.15}Al_{0.05}O_2$–$LiNi_{0.5}Co_{0.2}Mn_{0.3}O_2$–$LiMn_2O_4$/graphite lithium ion batteries, *Journal of Power Sources,* 326: 397-409, 2016.

[206] M. Ebner, D. W. Chung, R. E. García, and V. Wood, Tortuosity anisotropy in lithium-ion battery electrodes, *Advanced Energy Materials,* 4: 1301278, 2014.

[207] D. Kim, H. C. Shim, T. G. Yun, S. Hyun, and S. M. Han, High throughput combinatorial analysis of mechanical and electrochemical properties of $Li[Ni_xCo_yMn_z]O_2$ cathode, *Extreme Mechanics Letters,* 9: 439-448, 2016.

[208] E. J. Cheng, K. Hong, N. J. Taylor, H. Choe, J. Wolfenstine, and J. Sakamoto, Mechanical and physical properties of $LiNi_{0.33}Mn_{0.33}Co_{0.33}O_2$ (NMC), *Journal of the European Ceramic Society,* 37: 3213-3217, 2017.

[209] H. Y. Amanieu, D. Rosato, M. Sebastiani, F. Massimi, and D. C. Lupascu, Mechanical property measurements of heterogeneous materials by selective nanoindentation: Application to $LiMn_2O_4$ cathode, *Materials Science and Engineering: A,* 593: 92-102, 2014.

[210] J. Nohava, P. Haušild, Š. Houdková, and R. Enžl, Comparison of isolated indentation and grid indentation methods for HVOF sprayed cermets, *Journal of Thermal Spray Technology,* 21: 651-658, 2012.

[211] M. Qu, W. H. Woodford, J. M. Maloney, W. C. Carter, Y. M. Chiang, and K. J. Van Vliet, Nanomechanical quantification of elastic, plastic, and fracture properties of $LiCoO_2$, *Advanced Energy Materials,* 2: 940-944, 2012.

[212] J. G. Swallow, W. H. Woodford, F. P. McGrogan, N. Ferralis, Y. M. Chiang, and K. J. Van Vliet, Effect of electrochemical charging on elastoplastic properties and fracture toughness of Li_XCoO_2, *Journal of the Electrochemical Society,* 161: F3084-F3090, 2014.

[213] D. Mohanty, E. Hockaday, J. Li, D. Hensley, C. Daniel, and D. Wood, Effect of electrode manufacturing defects on electrochemical performance of lithium-ion batteries: Cognizance of the battery failure sources, *Journal of Power Sources,* 312: 70-79, 2016.

[214] X. Li and B. Bhushan, A review of nanoindentation continuous stiffness measurement technique and its applications, *Materials Characterization,* 48: 11-36, 2002.

[215] A. Van der Ven, M. Aydinol, G. Ceder, G. Kresse, and J. Hafner, First-principles investigation of phase stability in Li_xCoO_2, *Physical Review B,* 58: 2975, 1998.

[216] A. Miserez, J. C. Weaver, P. J. Thurner, J. Aizenberg, Y. Dauphin, P. Fratzl, D. E. Morse, and F. W. Zok, Effects of laminate architecture on fracture resistance of sponge biosilica: Lessons from nature, *Advanced Functional Materials,* 18: 1241-1248, 2008.

[217] M. R. Palacin and A. de Guibert, Why do batteries fail?, *Science,* 351: 1253292, 2016.

[218] J. P. Maranchi, A. F. Hepp, A. G. Evans, N. T. Nuhfer, and P. N. Kumta, Interfacial properties of the a-Si/Cu: Active-inactive thin-film anode system for lithium-ion batteries, *Journal of The Electrochemical Society,* 153: A1246, 2006.

[219] S. W. Lee, I. Ryu, W. D. Nix, and Y. Cui, Fracture of crystalline germanium during electrochemical lithium insertion, *Extreme Mechanics Letters,* 2: 15-19, 2015.

[220] S. Zhang, K. Zhao, T. Zhu, and J. Li, Electrochemomechanical degradation of high-capacity battery electrode materials, *Progress in Materials Science,* 89: 479-521, 2017.

[221] P. Yan, J. Zheng, M. Gu, J. Xiao, J. G. Zhang, and C. M. Wang, Intragranular cracking as a critical barrier for high-voltage usage of layer-structured cathode for lithium-ion batteries, *Nature Communications,* 8: 14101, 2017.

[222] R. A. Huggins and W. D. Nix, Decrepitation model for capacity loss during cycling of alloys in rechargeable electrochemical systems, *Ionics,* 6: 57-63, 2000.

[223] T. K. Bhandakkar and H. Gao, Cohesive modeling of crack nucleation under diffusion induced stresses in a thin strip: Implications on the critical size for flaw tolerant battery electrodes, *International Journal of Solids and Structures,* 47: 1424-1434, 2010.

[224] C. K. Chan, H. Peng, G. Liu, K. McIlwrath, X. F. Zhang, R. A. Huggins, and Y. Cui, High-performance lithium battery anodes using silicon nanowires, *Nature Nanotechnology,* 3: 31-5, 2008.

[225] A. F. Bower, E. Chason, P. R. Guduru, and B. W. Sheldon, A continuum model of deformation, transport and irreversible changes in atomic structure in amorphous lithium–silicon electrodes, *Acta Materialia,* 98: 229-241, 2015.

[226] P. Sofronis and R. M. McMeeking, Numerical analysis of hydrogen transport near a blunting crack tip, *Journal of the Mechanics and Physics of Solids,* 37: 317-350, 1989.

[227] M. Z. Alam and D. K. Das, Effect of cracking in diffusion aluminide coatings on their cyclic oxidation performance on Ti-based IMI-834 alloy, *Corrosion Science,* 51: 1405-1412, 2009.

[228] A. G. Evans, *Fracture in ceramic materials. Toughening mechanisms, machining damage, shock*, Noyes Publications,Park Ridge, NJ; Dept. of Materials Science and Mineral Engineering, Univ. of California, Berkeley, 1984.

[229] H. Haftbaradaran and J. Qu, A path-independent integral for fracture of solids under combined electrochemical and mechanical loadings, *Journal of the Mechanics and Physics of Solids,* 71: 1-14, 2014.

[230] L. S. Vasconcelos, R. Xu, and K. Zhao, Operando nanoindentation: A new platform to measure the mechanical properties of electrodes during electrochemical reactions, *Journal of The Electrochemical Society,* 164: A3840-A3847, 2017.

[231] L. A. Berla, S. W. Lee, Y. Cui, and W. D. Nix, Mechanical behavior of electrochemically lithiated silicon, *Journal of Power Sources,* 273: 41-51, 2015.

[232] M. Pharr, Y. S. Choi, D. Lee, K. H. Oh, and J. J. Vlassak, Measurements of stress and fracture in germanium electrodes of lithium-ion batteries during electrochemical lithiation and delithiation, *Journal of Power Sources*, 304: 164-169, 2016.

[233] Y. Liu, H. Zheng, X. H. Liu, S. Huang, T. Zhu, J. Wang, A. Kushima, N. S. Hudak, X. Huang, and S. Zhang, Lithiation-induced embrittlement of multiwalled carbon nanotubes, *ACS Nano,* 5: 7245-7253, 2011.

[234] M. Sebastiani, K. Johanns, H. Amanieu, and G. Pharr, Effects of lithiation on the fracture toughness and mechanical properties of $LiMn_2O_4$ cathode battery materials, 2015.

[235] P. Yan, J. Zheng, D. Lv, Y. Wei, J. Zheng, Z. Wang, S. Kuppan, J. Yu, L. Luo, and D. Edwards, Atomic-resolution visualization of distinctive chemical mixing behavior of Ni, Co, and Mn with Li in layered lithium transition-metal oxide cathode materials, *Chemistry of Materials*, 27: 5393-5401, 2015.

[236] R. Molins, G. Hochstetter, J. Chassaigne, and E. Andrieu, Oxidation effects on the fatigue crack growth behaviour of alloy 718 at high temperature, *Acta Materialia,* 45: 663-674, 1997.

[237] A. Barnoush and H. Vehoff, Recent developments in the study of hydrogen embrittlement: Hydrogen effect on dislocation nucleation, *Acta Materialia,* 58: 5274-5285, 2010.

[238] S. Cui, Y. Wei, T. Liu, W. Deng, Z. Hu, Y. Su, H. Li, M. Li, H. Guo, Y. Duan, W. Wang, M. Rao, J. Zheng, X. Wang, and F. Pan, Optimized temperature effect of Li-ion diffusion with layer distance in $Li(Ni_xMn_yCo_z)O_2$ cathode materials for high performance Li-ion battery, *Advanced Energy Materials,* 6: 1501309, 2016.

[239] M. Zhang, J. Qu, and J. R. Rice, Path independent integrals in equilibrium electro-chemo-elasticity, *Journal of the Mechanics and Physics of Solids,* 107: 525-541, 2017.

[240] C. Shih, B. Moran, and T. Nakamura, Energy release rate along a three-dimensional crack front in a thermally stressed body, *International Journal of Fracture,* 30: 79-102, 1986.

[241] K. Roe and T. Siegmund, An irreversible cohesive zone model for interface fatigue crack growth simulation, *Engineering Fracture Mechanics,* 70: 209-232, 2003.

[242] M. Elices, G. Guinea, J. Gomez, and J. Planas, The cohesive zone model: advantages, limitations and challenges, *Engineering Fracture Mechanics,* 69: 137-163, 2002.

[243] X. Lin, J. Park, L. Liu, Y. Lee, A. Sastry, and W. Lu, A comprehensive capacity fade model and analysis for Li-ion batteries, *Journal of the Electrochemical Society,* 160: A1701-A1710, 2013.

[244] A. Sarkar, P. Shrotriya, and A. Chandra, Fracture modeling of lithium-silicon battery based on variable elastic moduli, *Journal of the Electrochemical Society,* 164: E3606-E3612, 2017.

[245] S. Y. Park, W. J. Baek, S. Y. Lee, J. A. Seo, Y. S. Kang, M. Koh, and S. H. Kim, Probing electrical degradation of cathode materials for lithium-ion batteries with nanoscale resolution, *Nano* Energy, 49: 1-6, 2018.

[246] G. Bucci, T. Swamy, Y. M. Chiang, and W. C. Carter, Modeling of internal mechanical failure of all-solid-state batteries during electrochemical cycling, and implications for battery design, *Journal of Materials Chemistry A,* 5: 19422-19430, 2017.

[247] K. Guo, P. A. Tamirisa, B. W. Sheldon, X. Xiao, and H. Gao, Pop-Up Delamination of Electrodes in Solid-State Batteries, *Journal of the Electrochemical Society*, 165: A618-A625, 2018.

[248] Y. Zhang, Y. Luo, C. Fincher, S. McProuty, G. Swenson, S. Banerjee, and M. Pharr, In-situ measurements of stress evolution in composite sulfur cathodes, *Energy Storage Materials,* 2018.

[249] Q. Liu, Z. Geng, C. Han, Y. Fu, S. Li, Y. b. He, F. Kang, and B. Li, Challenges and perspectives of garnet solid electrolytes for all solid-state lithium batteries, *Journal of Power Sources,* 389: 120-134, 2018.

VITA

Rong Xu

Ph.D. candidate, Purdue University
585 Purdue Mall, Room 3179, West Lafayette, IN 47907-2088, US

EDUCATION

08/2014-12/2018: Ph.D. in Mechanical Engineering, Purdue University, West Lafayette, IN.
Advisor: Kejie Zhao

09/2011-07/2014: Master in Engineering Mechanics, Xi'an Jiaotong University, Xi'an, China.
Advisor: Tiejun Wang

09/2007-07/2011: Bachelor in Engineering Mechanics, Xi'an Jiaotong University, Xi'an, China.

RESEARCH INTERESTS

Nanomechanical testing (Nanoindentation)
Numerical modeling for multiphase systems (Finite Element Method)
Electrochemistry and mechanics in Li-ion batteries
Fracture mechanics in film/substrate structure

RESEARCH EXPERIENCES

PhD Thesis - Theories and Experiments on the Electro-Chemo-Mechanics of Battery Materials *(08/2014-Present, Purdue)*

- Established theoretical framework to study couplings between electrochemistry and mechanics.
- Employed numerical simulation to predict stress evolution and crack formation in electrodes.
- Fabricated electrodes using state-of-art electrode materials NMC & Si/NPs.
- Designed the *in-operando* nanoindetation experiments to characterize the electrochemical and mechanical performance of electrode materials.

Multiple Surface/Interface Cracking Behavior of Film/Substrate System
(01/2011-12/2013, XJTU, China & 08/2016-Present, Purdue)

- Conducted *in-situ* experiments to observe surface/interface cracking in film/substrate system under extreme working conditions (high temperature or high load).
- Built FEM model to investigate the failure mechanisms in film/substrate system.
- Parametrically designed the applications of film/substrate system such as thermal barrier coatings and thin film electrode to achieve the optimized mechanical resilience.

Experimental Characterization of Enhanced Mechanical Performances of Alloy Fabricated by Ultrasonic Shot Peening (USP) *(05/2016-Present, Purdue)*

- Coordinated the cooperation between two research groups in the Schools of ME and MET.
- Designed nanomechanical experiments (micropillar compression and nanoindentation) to characterize the mechanical performance of the nanostructured surfaces fabricated by USP.
- Analyzed the mechanisms of nanograin enhanced mechanical performance and constructed the constitutive model for mechanical response of USP enhanced alloy.

TEACHING EXPERIENCES

Lambert Fellow Instructor: *ME323 Mechanics of Material* *(08/2017-05/2018, Purdue)*
TA: *ME323 Mechanics of Material & ME570 Machine Design* *(08/2015-05/2016, Purdue)*

HONORS & AWARDS

Outstanding Research Award from the College of Engineering, Purdue, 2018
Ward A. Lambert Graduate Teaching Fellowship, Purdue, 2018.
Drs. Helen and Marvin Adelberg Fellowship, Purdue, 2017.
Outstanding abstract for the 2016 MRS Spring conference, Phoenix, 2016.
Outstanding graduate award, Xi'an Jiaotong University, China, 2014.
National scholarship, Xi'an Jiaotong University, China, 2008, 2009 & 2013.

PUBLICATIONS (Citations: 327, h-index: 12)

1. **Rong Xu**, Kejie Zhao, Corrosive fracture of electrodes in Li-ion batteries. *Journal of the Mechanics and Physics of Solids*. 121, 258-280 (2018).
2. **Rong Xu**, Luize Scalco de Vasconcelos, Junzhe Shi, Jianlin Li, Kejie Zhao. Disintegration of meatball electrodes for $LiNi_xMn_yCo_zO_2$ cathode materials. *Experimental Mechanics*. 58, 549-559 (2018).
3. **Rong Xu**, Hong Sun, Luize Scalco de Vasconcelos, Kejie Zhao. Mechanical and structural degradation of $LiNi_xMn_yCo_zO_2$ cathode in Li-ion batteries: An experimental study. *Journal of the Electrochemical Society*. 164, A3333-A3341 (2017).
4. **Rong Xu**, Luize Scalco de Vasconcelos, Kejie Zhao. Computational analysis of chemo-mechanical behaviors of composite electrodes in Li-ion batteries. *Journal of Materials Research*. 31, 2715-2727 (2016).
5. **Rong Xu**, Kejie Zhao. Electro-chemo-mechanics of electrodes in Li-ion batteries: A review. *Journal of Electrochemical Energy Conversion and Storage*. 13, 030803 (2016).
6. **Rong Xu**, Kejie Zhao. Mechanical interactions regulated kinetics and morphology of composite electrodes in Li-ion batteries. *Extreme Mechanics Letters*. 8, 13-21 (2016).
7. **Rong Xu**, Xueling Fan, TJ Wang. Mechanisms governing the interfacial delamination of thermal barrier coating system with double ceramic layers. *Applied Surface Science*. 370, 394-402 (2016).
8. **Rong Xu**, Xueling Fan, Weixu Zhang, TJ Wang. Interfacial fracture mechanism associated with mixed oxides growth in thermal barrier coating system. *Surface and Coatings Technology*. 253, 139-147 (2014).
9. **Rong Xu**, Xueling Fan, Weixu Zhang, Yan Song, TJ Wang. Effects of geometrical and material parameters of top and bond coats on the interfacial fracture in thermal barrier coating system. *Materials & Design*. 47, 566-574 (2013).
10. Luize Scalco de Vasconcelos, Nikhil Sharma, **Rong Xu**, Kejie Zhao. In-situ nanoindentation measurement of local mechanical behavior of composite electrodes in liquid electrolyte. Submitted.
11. Qingqing Sun, **Rong Xu**, Qingyou Han, Kejie Zhao, Xingtao Liu, Ian McAdams, Ruiji Sun, Wilson Xu, Jie Li, Fei Yin, Jianyue Zhang, Licong An. Chemical gradient induced by surface nanocrystallization. Submitted.
12. Biwei Deng, **Rong Xu**, Kejie Zhao, Yongfeng Lu, Sabyasachi Ganguli, Gary J. Cheng. Composite bending dominated hollow nanolattices: A stiff, cyclable mechanical metamaterials. *Materials Today*. 21, 467-474 (2018).
13. Linqin Mu, Ruoqian Lin, **Rong Xu**, Lili Han, Dimosthenis Sokaras, James D. Steiner, Tsu-Chien Weng, Dennis Nordlund, Marca M. Doeff, Yijin Liu, Kejie Zhao, Huolin L. Xin, Feng Lin. Oxygen release induced chemomechanical breakdown of layered cathode materials. *Nano Letters*. 18, 3241-3249 (2018).

14. Guanghui Zhang, Xueling Fan, **Rong Xu**, Luochuan Su, TJ Wang. Transient thermal stress due to the penetration of calcium-magnesium-alumino-silicate in EB-PVD thermal barrier coating system. *Ceramics International*. 44, 12655-12663 (2018).
15. Fei Yin, Gary J. Cheng, **Rong Xu**, Kejie Zhao, Qiang Li, Jie Jian, Shan Hu, Qingyou Han. Ultrastrong nanocrystalline stainless steel and its Hall-Petch relationship in the nanoscale. *Scripta Materialia*. 155, 26-31 (2018).
16. Fei Yin, Yanfei Liu, **Rong Xu**, Kejie Zhao, Austin Partina, Qingyou Han. Nanograined surface fabricated on the pure copper by ultrasonic shot peening and an energy-density based criterion for peening intensity quantification. *Journal of Manufacturing Processes*. 32, 656-663 (2018).
17. Luize Scalco de Vasconcelos, **Rong Xu**, Kejie Zhao. Operando nanoindentation: A new platform to measure the mechanical properties of electrodes during electrochemical reactions. *Journal of the Electrochemical Society*. 164, A3840-A3847 (2017).
18. Fei Yin, **Rong Xu**, Shan Hu, Kejie Zhao, Shiqi Yang, Shihuan Kuang, Qiang Li, Xinghang Zhange, Qingyou Han. Enhanced mechanical and biological performances of an extremely dine nanograined cell-substrate interface fabricated by ultrasonic shot peening. *ACS Biomaterials Science & Engineering*. 4, 1609-1621 (2018).
19. Ze Liu, Benxin Wu, **Rong Xu**, Kejie Zhao, Yung Shin. Microhole drilling by double laser pulses with different pulse energies. *Journal of Manufacturing Science and Engineering*. 140, 091015 (2018).
20. Qingqing Sun, Xingtao Liu, Qingyou Han, Jie Li, **Rong Xu**, Kejie Zhao. A comparison of AA2024 and AA7150 subjected to ultrasonic shot peening: Microstructure, surface segregation and corrosion. *Surface and Coatings Technology*. 337, 552-560 (2018).
21. Qingqing Sun, Qingyou Han, **Rong Xu**, Kejie Zhao, Jie Li. Localized corrosion behavior of AA7150 after ultrasonic shot peening: corrosion depth vs. impact energy. *Corrosion Science*. 130, 218-230 (2017).
22. Qiming Chen, **Rong Xu**, Zitao He, Kejie Zhao, Liang Pan. Printing 3D gel polymer electrolyte in lithium-ion microbattery using stereolithography. *Journal of the Electrochemical Society*. 164, A1852-A1857 (2017).
23. Ze Liu, Benxin Wu, Avik Samanta, Ninggang Shen, Hongtao Ding, **Rong Xu**, Kejie Zhao. Ultrasound-assisted water-confined laser micromachining (UWLM) of metals: Experimental study and time-resolved observation. *Journal of Materials Processing Technology*. 245, 259-269 (2017).
24. Luize Scalco de Vasconcelos, **Rong Xu**, Jianlin Li, Kejie Zhao. Grid indentation analysis of mechanical properties of composite electrodes in Li-ion batteries. *Extreme Mechanics Letters*. 9, 495-502 (2016).
25. Yaowu Hu, Prashant Kumar, **Rong Xu**, Kejie Zhao, Gary J. Cheng. Ultrafast direct fabrication of flexible substrate-supported designer plasmonic nanoarrays. *Nanoscale*. 8, 172-178 (2016).
26. Zengrong Hu, Guoquan Tong, Qiong Nian, **Rong Xu**, Mojib Saei, Feng Chen, Changjun Chen, Min Zhang, Huafeng Guo, Jiale Xu. Laser sintered single layer graphene oxide reinforced titanium matrix nanocomposites. *Composites Part B: Engineering*. 93, 352-359 (2016).
27. Bowen Lv, Hua Xie, **Rong Xu**, Xueling Fan, Weixu Zhang, TJ Wang. Effects of sintering and mixed oxide growth on the interface cracking of air-plasma-sprayed thermal barrier coating system at high temperature. *Applied Surface Science*. 360, 461-469 (2016).
28. Xueling Fan, **Rong Xu**, TJ Wang. Interfacial delamination of double-ceramic-layer thermal barrier coating system. *Ceramics International*. 40, 13793-13802 (2014).

29. Xueling Fan, Wei Jiang, Jianguo Li, Tao Suo, TJ Wang, **Rong Xu**. Numerical study on interfacial delamination of thermal barrier coatings with multiple separations. *Surface and Coatings Technology*. 244, 117-122 (2014).
30. Xueling Fan, **Rong Xu**, M. Kikuchi. Fracture of thermal barrier coating with multiple surface cracks and delaminations: Interlayer effect. *Journal of Central South University*. 21, 2579-2583 (2014).
31. Xueling Fan, **Rong Xu**, Weixu Zhang, TJ Wang. Effect of periodic surface cracks on the interfacial fracture of thermal barrier coating system. *Applied Surface Science*. 258, 9816-9823 (2012).

CONFERENCE TALKS

1. 2018 Midwest Society of Experimental Mechanics Student Conference, March 2018, West Lafayette, IN
2. 2017 ASME International Mechanical Engineering Congress&Exposition, November 2017, Tampa, FL.
3. 2017 MRS spring conference, April 2017, Phoenix, AZ.
4. 53rd SES annual conference. October 2016, College Park, MD.
5. 2nd Midwest Mechanics of Materials and Structures workshop, August 2016, Evanston, IL.
6. 1st Midwest Mechanics of Materials and Structures workshop, August 2015, Champaign, IL.
7. 2nd Students Seminar on Mechanical Engineering, November 2013, Kenting, Taiwan.
8. 13th International Conference on Fracture, June 2013, Beijing, China.
9. 9th International Conference on Fracture & Strength of Solids, June 2013, Jeju, Korea.

SYNERGISTIC ACTIVITIES

Symposium Co-chair:

2018 Midwest Society of Experimental Mechanics Student Conference, Purdue University.
2017 Prospective Graduate Student Visitation Research Posters Session, Purdue University.

Journal Reviewer:

Nature Communications, Journal of Applied Physics, The Journal of Physical Chemistry, Extreme Mechanics Letters, Electrochimica Acta, Materials and Design, AIP Advances, Journal of Materials Science, Vacuum, International Journal of Computational Materials Science and Surface Engineering.